INFORMATION TO USERS

This manuscript has been reproduced from the microfilm master. UMI films the text directly from the original or copy submitted. Thus, some thesis and dissertation copies are in typewriter face, while others may be from any type of computer printer.

The quality of this reproduction is dependent upon the quality of the copy submitted. Broken or indistinct print, colored or poor quality illustrations and photographs, print bleedthrough, substandard margins, and improper alignment can adversely affect reproduction.

In the unlikely event that the author did not send UMI a complete manuscript and there are missing pages, these will be noted. Also, if unauthorized copyright material had to be removed, a note will indicate the deletion.

Oversize materials (e.g., maps, drawings, charts) are reproduced by sectioning the original, beginning at the upper left-hand corner and continuing from left to right in equal sections with small overlaps. Each original is also photographed in one exposure and is included in reduced form at the back of the book.

Photographs included in the original manuscript have been reproduced xerographically in this copy. Higher quality 6" x 9" black and white photographic prints are available for any photographs or illustrations appearing in this copy for an additional charge. Contact UMI directly to order.

.

Tectonic Deformation in Western Washington State from Global Positioning System Measurements

by

Giorgi Khazaradze

A dissertation submitted in partial fulfillment
of the requirements for the degree of

Doctor of Philosophy

University of Washington

1999

Program Authorized to Offer Degree: Geophysics Program

UMI Number: 9936437

Copyright 1999 by
Khazaradze, Giorgi

UMI
300 North Zeeb Road
Ann Arbor, MI 48103

Doctoral Dissertation

In presenting this thesis in partial fulfillment of the requirements for the Doctoral degree at the University of Washington, I agree that the Library shall make its copies freely available for inspection. I further agree that extensive copying of the dissertation is allowable only for scholarly purposes, consistent with "fair use" as prescribed in the U.S. Copyright Law. Requests for copying or reproduction of this dissertation may be referred to UMI Dissertation Services, 300 North Zeeb Road, P.O. Box 1346, Ann Arbor, MI 48106-1346, to whom the author has granted "the right to reproduce and sell (a) copies of the manuscript in microform and/or (b) printed copies of the manuscript made from microform."

Signature_____

Date_____3/29/1999_____
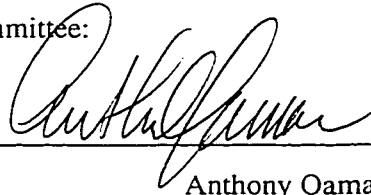
University of Washington

Graduate School

This is to certify that I have examined this copy of a doctoral
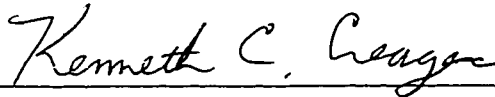dissertation by

Giorgi Khazaradze

and have found that it is complete and satisfactory in all respects,

and that any and all revisions required by the final

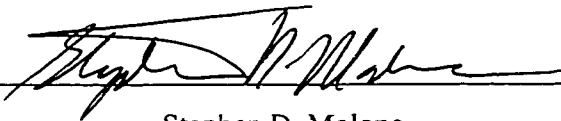examining committee have been made.

Chair of Supervisory Committee:

_____

Anthony Qamar

Reading Committee:

_____

Kenneth C. Creager

_____

Stephen D. Malone

Date: June 8, 1999

University of Washington

Abstract

Tectonic Deformation in Western Washington State from Global Positioning System Measurements

by Giorgi Khazaradze

Chairperson of the Supervisory Committee:

Professor Anthony Qamar

Graduate Program in Geophysics

Western Washington state is adjacent to the Cascadia Subduction Zone (CSZ), which stretches from northern California to southern British Columbia. More that three years of continuous and "campaign" style GPS measurements in western Washington indicate that the direction of the observed horizontal velocities is roughly parallel to the direction of relative plate convergence of the Juan de Fuca (JDF) and North America (NA) plates and that the relative plate convergence and velocities decrease away from the deformation front. The average maximum principal strain rate for the entire study area calculated from the GPS velocities indicates compression of 0.05 ± 0.01 μstrain/yr in the direction N75°E.

Most of the observed velocities can be attributed to locking of the CSZ thrust interface causing the accumulation elastic strain as the next great subduction earthquake approaches. Three-dimensional elastic dislocation modeling results suggest that the seismogenic zone along the Washington section of the CSZ is ~10% wider than the earlier published values of 90 km; This can theoretically cause higher levels of ground shaking in the densely populated Puget basin of western Washington.

Although the subduction related signal dominates the observed GPS velocity field, there is also evidence for an additional north-south oriented compression. To isolate this signal from the subduction related signal the dislocation model predictions must be subtracted from the observed velocities, yielding a "residual" velocity field that suggests the presence of N-S oriented compression at a rate of ~4 mm/yr over a N-S distance of approximately 250 km. This signal presumably represents a more long-term deformation pattern than the periodic accumulation and release of elastic strain connected with subduction earthquakes and most likely is related to the occurrence of shallow earthquakes in western Washington, which are characterized by predominantly north-south oriented maximum principal stress directions.

Table of Contents

List of Figures

v

List of Tables

Acknowledgments

I would like to thank my advisor Tony Qamar for introducing me to GPS technology and for his continual support, guidance, help and friendship. Also I would like to thank Steve Malone for his guidance in my first years of the graduate school, while I was still aspiring to be a seismologist. I gratefully thank Herb Dragert for his tremendous help. Without Herb's willingness to share his expertise and advice with me, this work would have been impossible to complete. I would also like to thank John Booker. If not his firm support as a chair of the Geophysics Program in the usefulness of the GPS technology (and my abilities), it would have been impossible to conduct 1995, 1996 "campaigns". I would like to thank Ken Creager for keeping his office door ever open for the graduate students and his everlasting enthusiasm to discuss various scientific matters. I would like to thank Ruth Ludwin for improving my English grammar and Pete Lombard for making my life easy by keeping the computer system "healthy and happy". I would also like to thank Juergen Klotz, my new boss at the GeoForschungsZentrum Potsdam, for creating the best environment to successfully finish this dissertation.

Many thanks to:

My fellow office-mates, class-mates and friends for helpful discussions and many more: John Castle, Seth Moran, John Winchester, Joe Henton, Ronnie Ning, Jeff Johnson.

To Julie van Buren, Kim Pham and Connie Wright for helping to cope wi the state bureaucracy.

The "campaign" helpers for their enthusiasm, endurance and expertise: Jeff Schwartz, Sandra Corso, Gerrick Bergsma, Ruth Ludwin, Bill Steele, Muna Qamar, TJ Saunders, Irakli Tskhadadze, Nini Gabunia, Brant Robertson and others.

Elliot Endo and Gene Iwatsubo from the Cascades Volcano Observatory for helping us with 1996 GPS campaign and for sharing the data collected in earlier years.

Will Prescott, Jerry Svarc and Karen Wendt for sharing the USGS collected data and hosting me in their office in Menlo Park.

Geoff Blewitt, Jeff Freymueller, Roy Hyndman, Kristine Larson, Kelin Wang, Rob McCaffrey and Ray Wells. I have benefited greatly from numerous e-mail and personal conversations with them.

Paul Flück for his excellent thesis, including his code for dislocation modeling I used in this study.

GIPSY support group at JPL and in particular, to Ken Hurst; CORS people at NOAA and in particular Bill Strange

And last but not least, thanks to my numerous friends in Seattle (including the Scandinavian House), Georgia and the rest of the world for their love and friendship!

Dedication

I would like to dedicate this work to my parents, Nanuli and Otar. Without their love, support and trust it would have been impossible for me to complete this work.

I. Introduction

1.1 Objectives

The primary objective of my dissertation is to determine the nature of contemporary crustal deformation in western Washington measured by means of Global Positioning System (GPS) technology and to link these observations with the tectonic processes driving lithospheric deformation at the convergent plate margin of the Pacific Northwest United States. Specific questions I intend to answer are:

- What is the magnitude and orientation of crustal deformation rates in western Washington?

- What are the main driving forces behind the observed tectonic deformation?

- How do measured geodetic strain rates relate to the north-south oriented maximum principal stress deduced from earthquake focal mechanisms in the Puget Lowland?

- How are the geodetically determined strain rates related to the geologically and seismically determined strain rates?

I believe this study has been successful in answering most of the above questions and thus has significantly enhanced our knowledge of the regional tectonics and its implications for the earthquake potential in the Pacific Northwest United States.

1.2 Study Area

1.2.1 Introduction

My study area (shown as a box in Figure 1.1) encompasses western Washington State, which is located in the forearc of the Cascadia Subduction Zone (CSZ), the only subduction zone within the contiguous United States. This makes the CSZ, including western Washington State, an ideal "back-yard laboratory" for studies of subduction related processes, and in particular, for investigating the nature of elastic strain accumulation in the crust of the overriding North American plate. Before I describe the results and interpretations of my own investigation, it is necessary to present an overview of tectonic, geologic and seismic characteristics of the study area. Sections 1.2.2, 1.2.3 and 1.2.4 will serve this purpose. Later, in the discussion chapter of this dissertation (Chapter V) I will frequently refer to various geologic, tectonic and seismic characteristics of the study area presented in these sections.
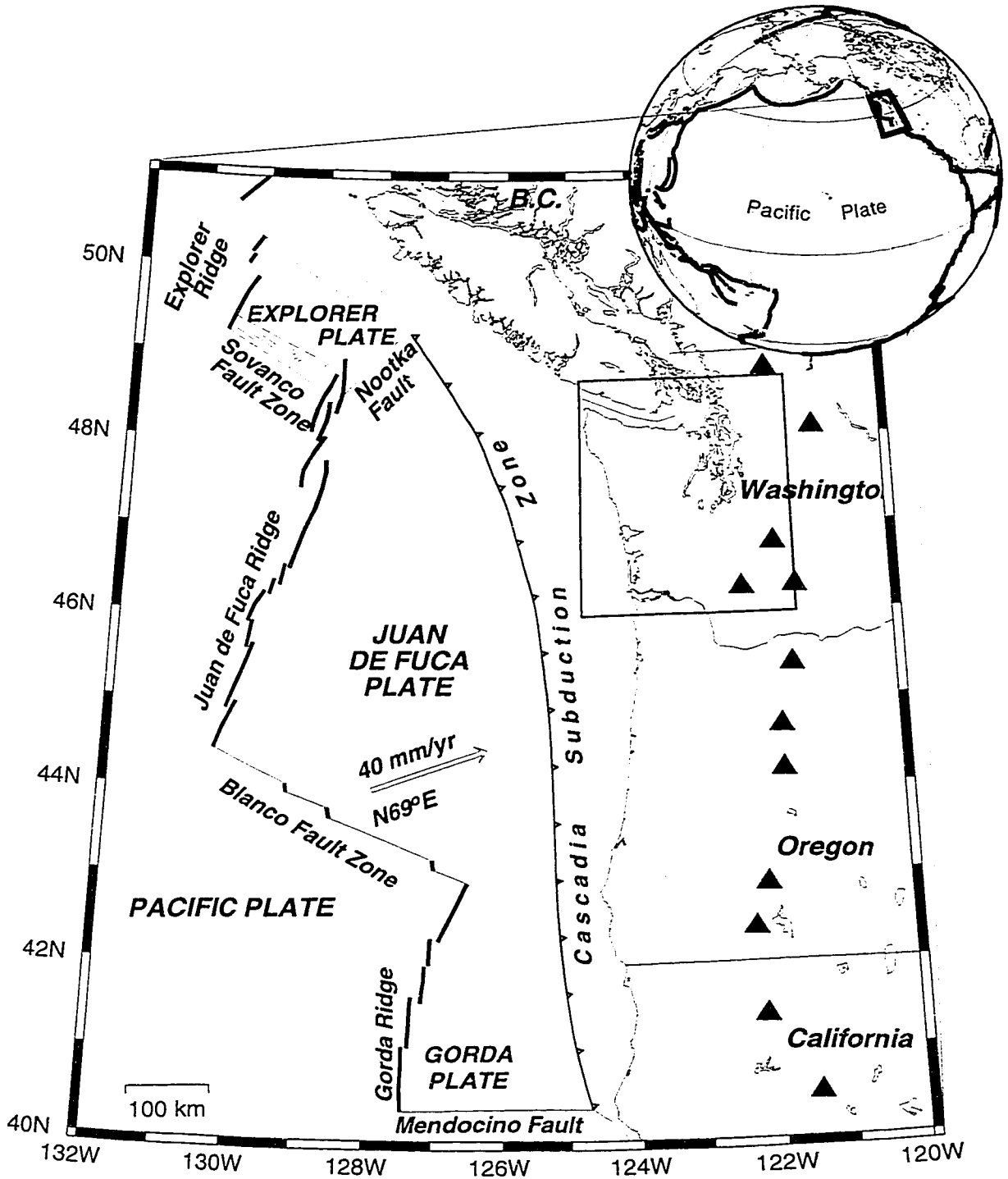
Figure 1.1: Map of the Cascadia subduction zone. Triangles indicate Cascade volcanoes. The study area is shown as a box. The inset in the upper corner of the figure shows the outline of the Circum-Pacific tectonic plates.

1.2.2 Tectonic Setting

The Cascadia Subduction Zone (CSZ) stretches from northern California to southern British Columbia (Figures 1.1 and 1.3). The CSZ is the result of oblique convergence of the Juan de Fuca (JDF) and North America (NA) plates. According to the NUVEL-1A global plate motions model (*DeMets et al.*, 1990; 1994) the convergence rate between these plates at Seattle is 40 mm/yr in the direction of N70°E. On the other hand, according to *Riddihough* (1984), the convergence rate at the same location is equal to 44 mm/yr in the direction of N62°E. Figure 1.2 shows the JDF/
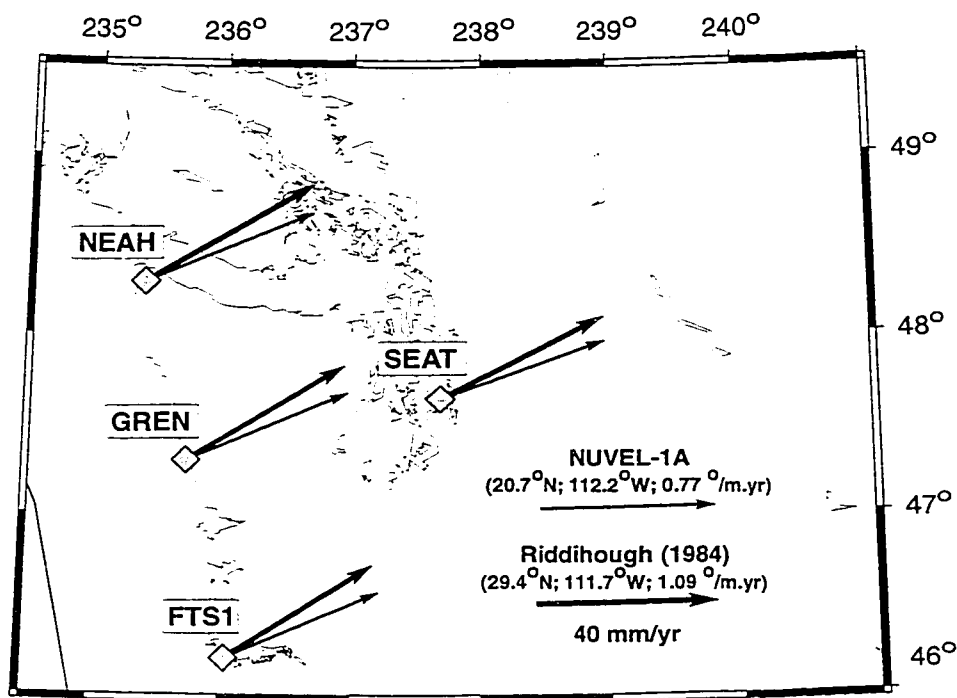
Figure 1.2: JDF and NA plate convergence vectors. Velocities predicted by the NUVEL-1A (*DeMets et al.* 1990; 1994) and *Riddihough* (1984) models at the selected GPS sites along the coast are displayed as vectors. Euler poles used to calculate velocities are listed in the figure.

NA convergence vectors predicted by two models at selected GPS stations along the coast and in the Puget Lowland.

The JDF plate is a last remnant of the Farallon plate, which has been subducting under the NA plate for more than 35 Ma (*Engebretson et al.*, 1984). Among a dozen or so known tectonic plates worldwide, the JDF plate is among the smallest. It's much smaller than the adjacent North America and the Pacific plates (PA) (see the inset of Figure 1.1). For this reason, we can not study neotectonic processes along the CSZ without taking into account the forces arising from the
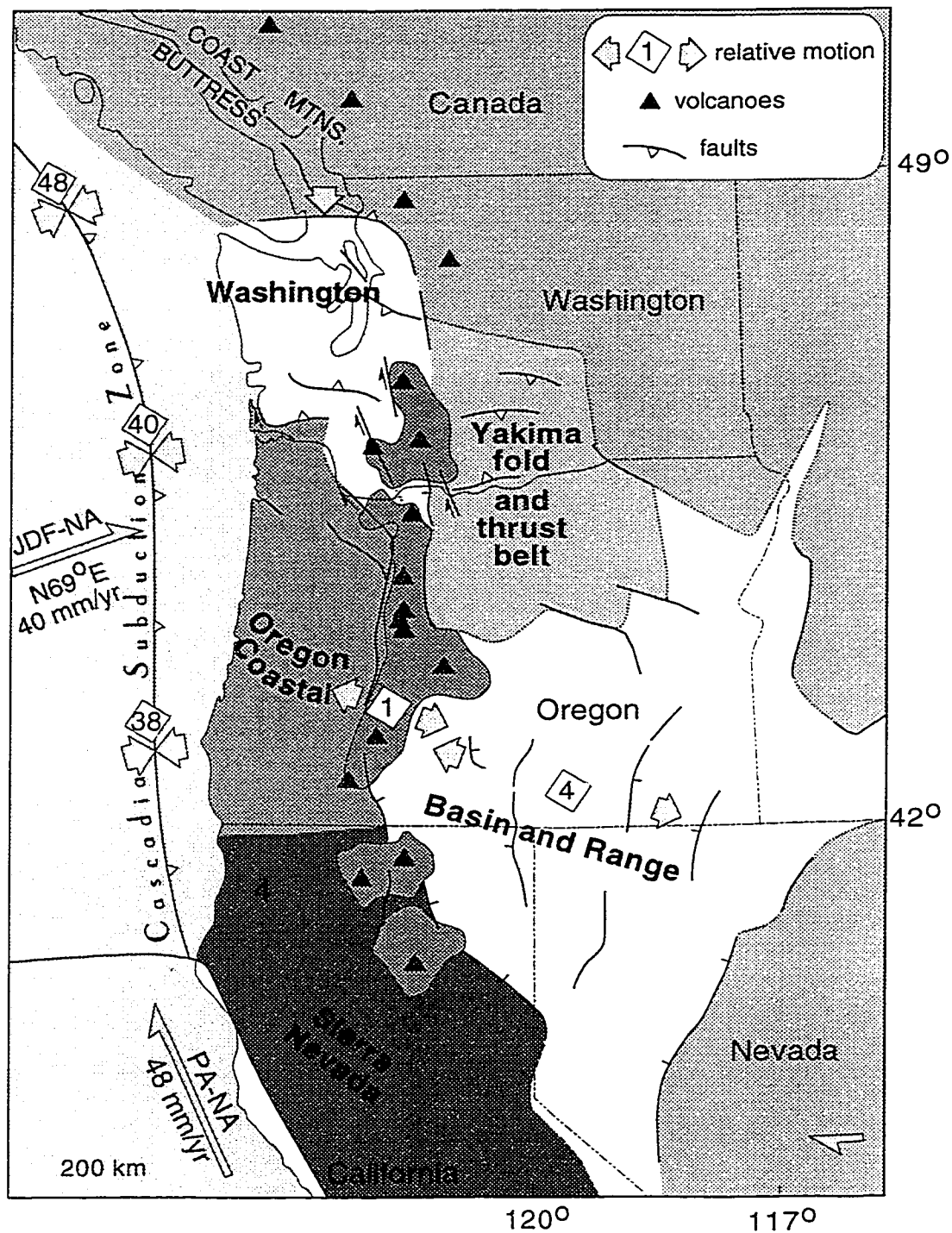
Figure 1.3: Major tectonic units along the Cascadia subduction zone. From south to north, the forearc is divided into three tectonic blocks/segments: Sierra-Nevada (SN); Oregon Coastal (OC) and Washington (W). Thick arrows indicate observed relative rates from very long baseline interferometry, paleoseismology and magmatic spreading. Figure is adopted from *Wells et al.* (1998).

PA/NA plate interaction. Due to the small size of the JDF plate, the oceanic crust produced at the Juan de Fuca ridge (Figure 1.1) does not have to travel very far before it subducts under the NA continent. Hence, the average age of the subducting slab at the deformation front is only 8 Ma, which is considerably younger than at most of the other subduction zones worldwide. The young age of the slab contributes to the following characteristics of the CSZ:

- Shallow dip angle (5°-15°) of the subducting JDF plate from the deformation front to 60 km depth landward.

- A moderate thickness (~6 km) of the JDF subducting plate (*Parsons et al.*, 1998).

- High temperature at the deformation front (~250°) (*Hyndman and Wang*, 1993).

  The latter factor is enhanced by the presence of a thick layer (~3 km) of sediments, deposited on top of the JDF plate from the adjacent NA plate. Also, due to the thick layer of sediments, the CSZ has developed an extensive accretionary wedge, reaching a maximum width of 65 km in western Washington (*Duncan*, 1982).

Based on variety of geological and geophysical evidence, including seismic and volcanic activity, uplift rates, plate boundary geometry, heat flow data and paleomagnetic studies (*Beck et al.*, 1986; *Blackwell et al.*, 1990; *Ludwin et al.*, 1991; *Mitchell et al.*, 1994; *Trehu et al.*, 1994; *Weaver and Baker*, 1988), *three* distinct segments can be identified along the CSZ (e.g. *Wells et al.*, 1998). 1) The northern segment (marked *Washington* block in Figure 1.3) is characterized by the presence of a compressional volcanic arc, high seismic activity, low magmatic extrusion rate, low heat flow, folded basement and small rotations in the forearc west of the Cascades range. 2) The central segment (marked *Oregon Coastal* block in Figure 1.3) is characterized by an extensional arc with low seismicity, high extrusion rate, large forearc rotation and the presence of an axial graben in the Cascade range. 3) The southern segment (marked *Sierra-Nevada* block in Figure 1.3) is located in northern California and it is the shortest of the three segments along the CSZ and represents a transpressive arc with high rates of seismicity, high extrusion rate and small forearc rotations.

My study area lies in the northern segment of the CSZ (shown as a box in Figure 1.1). According to the recent tectonic model proposed by *Wells et al.* (1998) this segment is characterized by the presence of a compressional volcanic arc, and is marked by several broken sub-blocks squeezed against the Canadian Coast mountains buttress in the north. This is mainly due to the northward translation of the central Oregon block caused by the Pacific/North America dextral shear that

dominates tectonics in California (*Pezzopane and Weldon*, 1993; *Wells et al.*, 1998) (see Figure 5.3). The margin-parallel translation of the forearc segments may also be due in part to the obliqueness of subduction across the CSZ (*McCaffrey*, 1992; *Wang*, 1996).

The varied tectonic regime of the Cascadia margin may be partially related to arching of the Juan de Fuca plate beneath the Olympic Mountains and Puget Sound (*Crosson and Owens*, 1987; *Weaver and Baker*, 1988). It may also reflect the inherited heterogeneity in the overlying North America plate (*Trehu et al.*, 1994). Although earthquakes only occur to depth of 100 km, there is evidence that the slab of the JDF plate penetrates to 400-600 km depth beneath Washington, but does not reach similar depths below Oregon (*Rasmussen and Humphreys*, 1988; *Bostock and VanDecar*, 1995). There is also evidence for a depressed Moho beneath the central Cascade ranges in Washington (*Crosson and Owens*, 1987; *Schultz and Crosson*, 1996).

Neogene deformation rates estimated from paleomagnetic observations (*Beck et al.*, 1986; *England and Wells*, 1991; *Magill et al.*, 1982; *Wells*, 1990; *Wells and Coe*, 1985; *Wells and Heller*, 1988; *Wells et al.*, 1998) indicate that the forearc of the CSZ rotates clockwise with respect to the interior of North America, causing the northward motion of its constituent blocks (Figure 5.3). Possible driving forces behind this motion are: 1) varying rates of oblique convergence along the Juan de Fuca plate, 2) Basin and Range spreading, or 3) right-lateral shear resulting from the Pacific/North America plate interaction (see Figures 1.1, 1.3 and 5.3) (*Pezzopane and Weldon*, 1993; *Wells and Heller*, 1988). However, the question of the relative importance of each of the above driving forces is still not resolved.

As the CSZ forearc moves northward, it encounters a resistance from the pre-Tertiary rocks of the Canadian Coastal mountains, causing the break up of the northern section of the forearc (Figure 1.3) into smaller blocks. In order to accommodate continuing north-south compression, these blocks have undergone large vertical motions, producing significant structural units, such as the Everett, Seattle, and Tacoma basins in the Puget Lowland (marked EB, SB and TB in Figure 1.5). These basins are associated with large gravity lows (Figure 1.4), indicating the presence of thick (5-10 km) low density sedimentary layers (*Blakely and Jachens*, 1990; *Finn*, 1990; *Pratt et al.*, 1997). The fact that these negative gravity anomalies are separated from the surrounding gravity highs by steep gradients, with remarkably linear geometry, led *Gower et al.* (1985) to the conclusion that these basins are separated from each other by east-west oriented faults. One of the
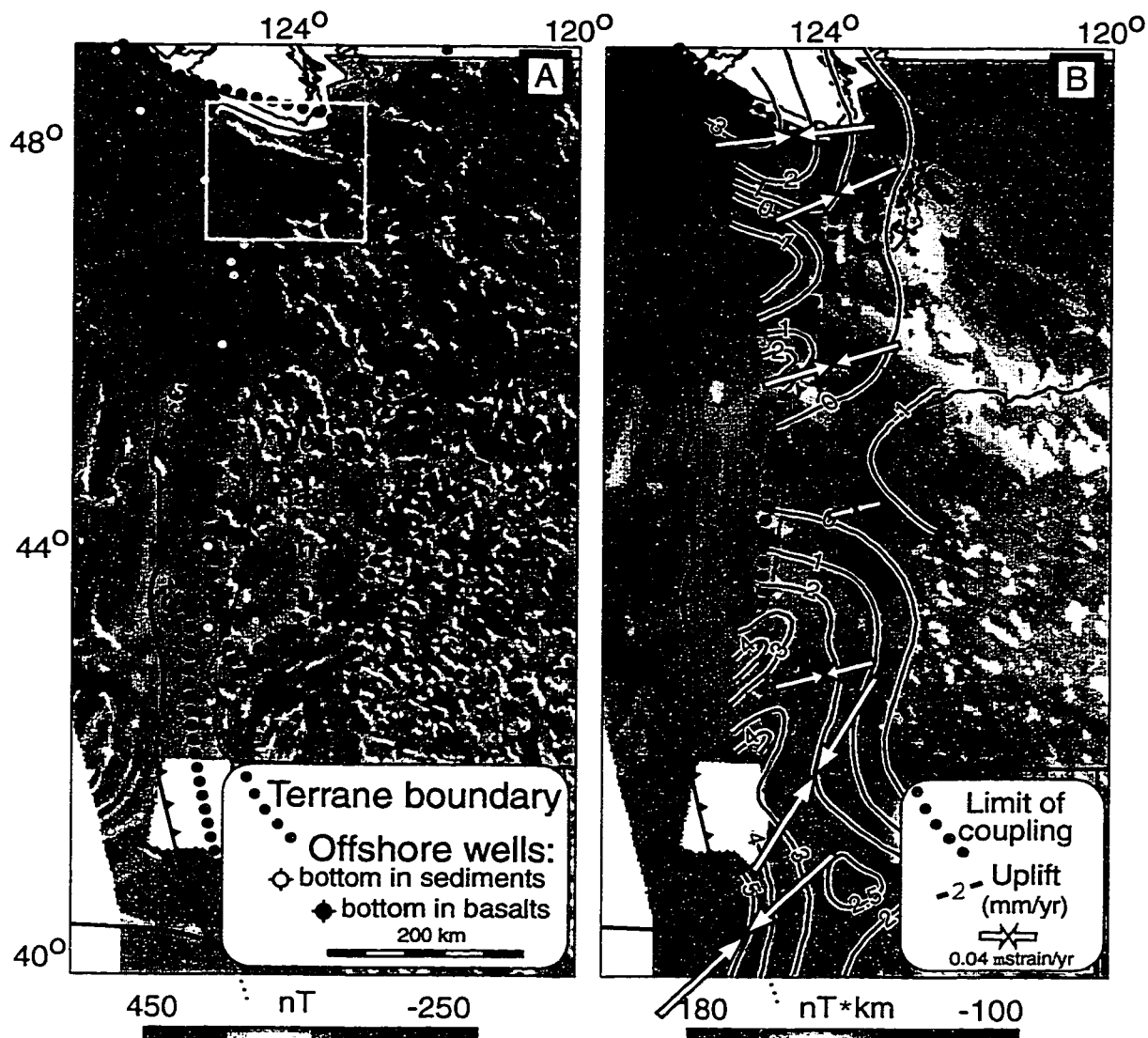
Figure 1.4: Magnetic and pseudogravity anomaly maps of the Pacific Northwest United States. A) Dotted line delineates approximate outline of main geologic terranes along th CSZ: *North America Basement* (NAB), *the Coast Range* (CR), *Cascade Volcanic Arc* (CVA) and *the Cascadia Accretionary Wedg* (CAW) including the Olympic Subduction Complex (OSC). An inset around the OSC shows location of Figure 1.6. Filled circles show location of offshore wells. Blue circles indicate wells bottoming in sediments and red circles bottoming in basalts. B) Pseudogravity anomaly (gravity that would be observed if magnetization were replaced by mass in 1:1 proportion) reflects total volume of the CR basalts and coincides with low geodetic uplift rates shown as red contour lines from *Mitchell et al.* (1994) (see Tables 1.1 and 1.2 for further details) and margin contraction (white arrows from *Murray and Lisowski* (1994)). Dotted line represents an eastward limit of coupling between the JDF and NA plates afte *Hyndman and Wang* (1995) (see Figure 4.4 for further details). Figure adopted from *Wells et al.* (1998).

major block-bounding faults is the Seattle fault (marked SF in Figure 1.5), consisting of perhaps four fault strands distributed over a 7 km wide zone (*Johnson et al.*, 1994; *Pratt et al.*, 1997).

1.2.3 Geologic Setting

The gross features of the regional geology along the Cascadia subduction zone can be divided into *four* major geologic provinces/terranes: the *North America Basement,* the *Coast Range,* the *Cascade Volcanic Arc* and the *Cascadia Accretionary Wedge* (see Figure 1.4).

The *North America Basement* (marked NAB in Figure 1.4) province represents a rigid part of the NA continent, consisting of pre-Tertiary (Mezozoic and Paleozoic) rocks sutured to NA sometime in the Jurassic and Cretaceous (*Monger et al.*, 1982). The *Coast Range* province consists of anomalously thick (2-30 km) (e.g. *Pratt et al.*, 1997) allocthonous Paleocene and Eocene oceanic basalts, straddling the CSZ along its entire length from northern California to southern British Columbia. The stratigraphic units for this province are referred to by different names, based on their geographic location: Silletz River Volcanics in Oregon, Metchosin Volcanics in southern Vancouver Island, and Crescent Formation in Washington (*Snavely*, 1987; *Tabor and Cady*, 1978). While there is a consensus regarding the timing of the Coast Range formation (it was formed sometime during the Eocene), the question of its origin is still not well known. Two main hypotheses exist. According to the first one, a seamount complex on the in-coming oceanic plate was accreted to the continent. The seamount was generated by the Yellowstone hot-spot or the re-organization of the spreading directions of the Farallon and the Kula plates (*Duncan*, 1982; *Snavely*, 1987; *Wells et al.*, 1984). The second hypothesis proposes that the Coast Range terrane was formed locally due to continental rifting (*Babcock et al.*, 1992). The Crescent formation in Washington is exposed in the eastern part of the Olympic Subduction Complex (OSC) (Figures 1.4 and 1.6) as a crescent shaped province of basaltic flows and sills, underlain by pillow basalts (*Tabor and Cady*, 1978). Due to the extensive late Cenozoic uplift and exhumation processes taking place in the Olympic Peninsula (*Brandon et al.*, 1998; *Brandon and Vance*, 1992), the Crescent Formation has tilted into a steep, east-plunging anticline, underlain by Eocene and younger subduction deposits (*Brandon and Calderwood*, 1990; *Tabor and Cady*, 1978). To the west, the Crescent formation is truncated by series of faults, such as, the Hurricane Ridge fault (marked HRF in Figure 1.5); to the east, in the Puget Lowland, it is buried under a thick layer of Quaternary sediments. Based on seismic reflection studies, *Johnson et al.* (1996) suggest the

presence of a north-south oriented, dextral strike-slip fault called Coast Range boundary fault (marked CBF in Figure 1.5), which separates the Coast Range province from the third geologic province, the *Cascades volcanic arc* (CVA). The CVA has formed as a result of continuing subduction of the JDF plate. It stretches for more than 1000 km along the CSZ, forming a chain of strato-volcanoes starting with Lassen Peak in northern California and ending with Mount Garibaldi in southern British Columbia. The formation of the CVA started approximately 38 Ma years ago (*Heller*, 1987). The most recent volcanic eruption along the CVA took place on Mount St. Helens on May 18th, 1980. Based on spatial, temporal and compositional distribution of approximately 3000 volcanic vents and their relation to the JDF subduction and the Basin and Range extension, *Guffanti and Weaver* (1988) have divided the CVA into 6 separate segments. My study area, encompasses two of their northern segments. The first segment, stretching from Mt. Garibaldi in southern British Columbia. to Glacier Peak in northern Washington, is characterized by the presence of isolated strato-volcanoes and low rates of volcanic extrusion. The second segment, stretching from Mt. Rainier to Mt. Hood, is wider and is marked by the presence of basaltic vents, located on both sides of the andesitic arc. Interestingly enough, these two segments are separated by a volcanic gap, coinciding with the north-south extent of the Puget Lowland to the west. *Guffanti and Weaver* (1988) suggest a possible link between this gap in the Cascades volcanism and the geometry of the JDF plate. According to *Weaver and Baker* (1988) the subducting JDF plate along this latitude has the smallest dip angle ($<10°$) due to the arching of the Juan de Fuca plate.

The fourth major geologic province along the CSZ is the Cascadia accretionary wedge, which formed as a result of sediment scraping from the downgoing JDF (i.e. Farallon) plate. Since the initiation of the subduction approximately 45 to 50 Ma years ago (*Duncan and LeVerne*, 1991) the CSZ has undergone a complex history of development, which affected the structure and composition of the modern accretionary wedge. The earliest evidence of accretion is found in the Olympic Mountains, a spectacular mountain range topped by Mt. Olympus (2427 meters). This part of the Cascadia accretionary wedge is usually referred to as the Olympic Subduction Complex (OSC) (Figure 1.6) (e.g. *Brandon and Vance*, 1992) or the Olympics core rocks. To the east and north respectively, the OSC is separated from the adjacent Crescent Formation and North America basement rocks by the east-dipping Hurricane Ridge thrust fault (marked HRF in Figure 1.5) and the north-dipping San Juan and Leech river faults (marked SJF and LRF in Figure 1.5).
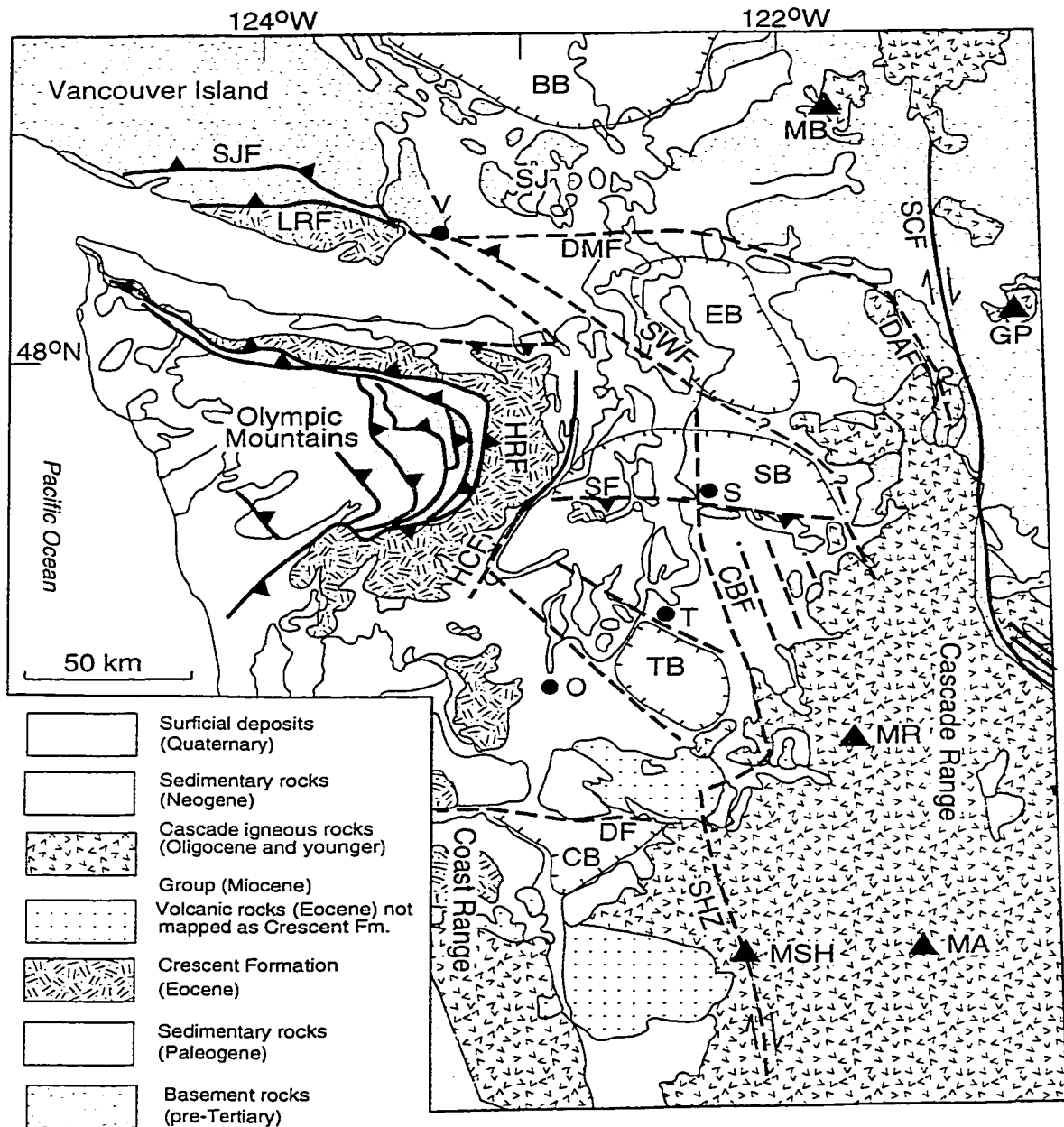
Figure 1.5: Schematic geologic map of western Washington. Abbreviations for cities (black circles): **O** = Olympia; **MP** = Mt. Persis; **S** = Seattle; **T** = Tacoma; **TM** = Tiger Mt.; **V** = Victoria. Abbreviations for faults (heavy lines): **CBF** = Coast Range boundary fault; **DAF** = Darrington fault; **DF** = Dotty fault; **DMF** = Devils Mountain fault; **HCF** = Hood Canal fault; **HRF** = Hurricane Ridge fault; **LRF** = Leech River fault; **SCF** = Straight Creek fault; **SF** = Seattle fault; **SWF** = Southern Whidbey Island fault. Abbreviations for Cenozoic sedimentary basins (enclosed hachured areas): **BB** = Bellingham basin; **CB** = Chehalis basin; **EB** = Everett basin; **SB** = Seattle basin; **TB** = Tacoma basin. Abbreviations for modern Cascade volcanoes (triangles): **GP** = Glacier peak; **MA** = Mt. Adams; **MB** = Mt. Baker; **MR** = Mt. Rainier; **MSH** = Mt. St. Helen. See Figure 1 in *Johnson et al.* (1996) for more details.
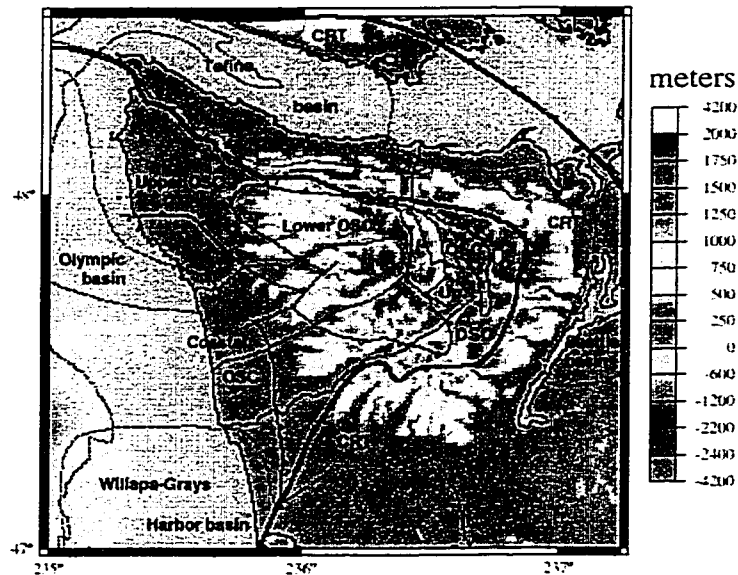
Figure 1.6: Topography and tectonic features of the Olympic Mountains. Faults are marked as solid black lines (see Figure 1.5 for more details); The dashed black lines enclose young basins surrounding the Olympic Mountains uplift; Abbreviations: CRT = Coast Range Terrane; OSC = Olympic Subduction Complex. Map reproduced from *Brandon et al.* (1998).

Using fission-track dating techniques for detrital zircons found in sandstones, *Brandon and Vance* (1992) have estimated the timing of deposition, accretion and metamorphism in the OSC. Based on their findings, *Brandon and Vance* divide the OSC into *three* lithologically distinct units (Figure 1.6). The *Upper* unit is mainly represented by Eocene clastic sediments with exposures of lower Eocene pillow basalts which are related to the Coast Range terrane. The *Lower* unit consists solely of younger (late Oligocene and early Miocene) clastic sediments. The *Coastal* unit is mainly represented by Miocene clastic sediments and minor enclosures of Eocene pillow basalts and sedimentary rocks. The origin of the latter geologic unit, is not clear. However, *Brandon et al.* (1998) label them as "exotic blocks" and suggest that they were derived by a submarine landsliding from the overlying Coast Range terrane. In terms of deformation and metamorphism, the Upper and Lower units differ distinctly from the Coastal unit. While the first two exhibit strong cleavage and prehnite-pumpellyite facies metamorphism, the Coastal unit lacks cleavage and metamorphic grade is restricted to zeolite facies.

1.2.4 Seismicity

The Cascadia subduction zone, and western Washington in particular, is subject to *three* types of earthquakes: 1) subduction earthquakes, occurring along the JDF and NA plates interface; 2) deep intra-slab earthquakes within the JDF plate; 3) shallow crustal earthquakes within the NA crust (Figure 1.7).

■ Deep earthquakes (>60 km)   ＼ Subduction earthquakes

● Shallow earthquakes (<25 km)   △/△ Cascades Volcanoes
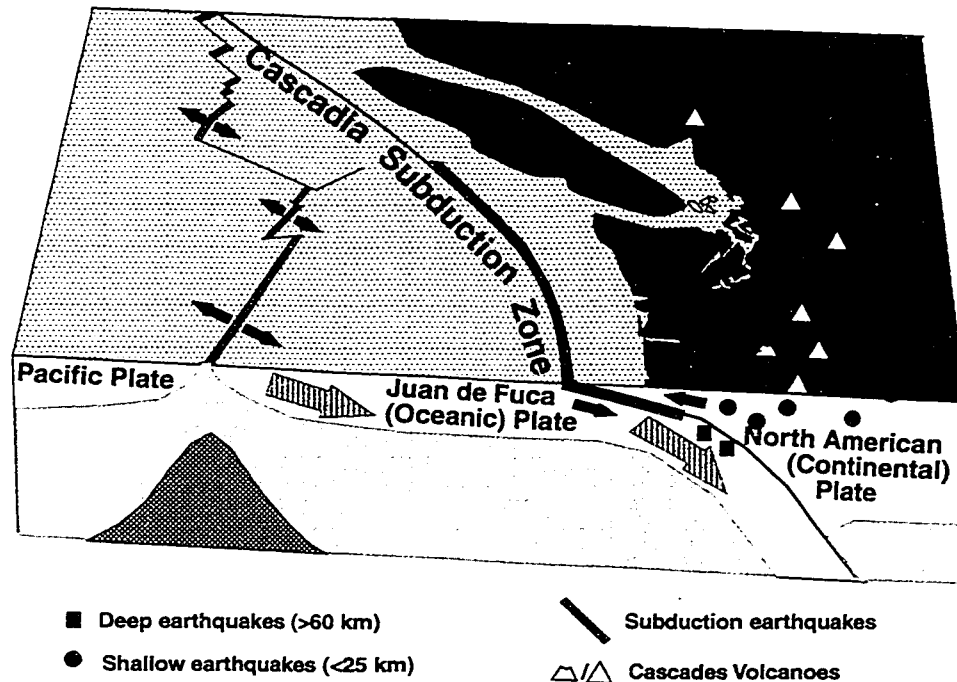
Figure 1.7: 3-D diagram of the Cascadia subduction zone. Figure is a courtesy of Dr. A. Qamar (Geophysics Program, University of Washington).

Due to the absence of historic megathrust earthquakes, the CSZ was formerly assumed to be aseismic (*Ando and Balazs*, 1979; *Crosson*, 1972). However, since *Heaton and Kanamori* (1984) first noted the similarities between the CSZ and the subduction zones in southwestern Japan and southern Chile (with a proven record of large megathrust earthquakes), the hypothesis that the CSZ could not generate large megathrust earthquakes has been questioned. The most compelling evidence for the occurrence of such earthquakes comes from paleoseismological investigations (e.g *Atwater et al.*, 1995). The main evidence for the occurrence of great subduction earthquakes along the CSZ is based on the discovery of buried tidal marshes and forest soils, indicating a sudden subsidence along the Pacific coast (*Atwater*, 1992; *Atwater*, 1996).

QUAKES | | | || | |

2000   0   2000
B.C. | A.D.
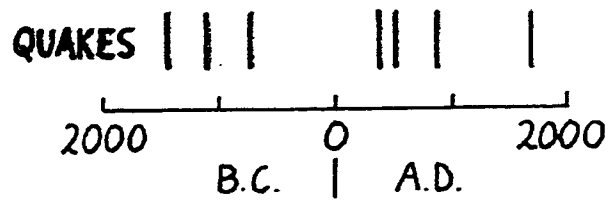
Figure 1.8: Historic earthquakes along the Cascadia subduction zone. Short vertical bars on the top indicate approximate times for the occurrence of each earthquake. Figure from Brian Atwater (University of Washington/United States Geological Survey).

Figure 1.8 shows approximate dates for the seven great subduction earthquakes (greater than magnitude 8) which probably occurred along the CSZ in the last 3500 year. Dates were constrained using radiocarbon (*Atwater et al.*, 1991) and tree ring (*Yamaguchi et al.*, 1997) dating techniques. These data suggest an average recurrence time-interval of 500 years between subduction type earthquakes along the CSZ. However, the repeat interval is highly non-uniform, varying from 400 to 1300 years. Interestingly enough, in line with the paleoseismological evidence, studies based on modeling tsunami records in Japan have suggested that the most recent earthquake on the CSZ took place in January, 1700 and measured approximately 8.9 in magnitude (*Satake et al.*, 1996). In addition to the above geologic evidence, contemporary crustal deformation and heat flow measurements, combined with elastic dislocation and thermal modeling, indicate that the thrust zone is currently locked and elastic strain is accumulating towards the next great subduction earthquake (*Dragert et al.*, 1994; *Flück et al.*, 1997; *Hyndman and Wang*, 1995; *Savage et al.*, 1991).

Although subduction type earthquakes theoretically pose the biggest hazard to the Pacific Northwest Unites States, the most damaging earthquakes in the past half a century in the study area have occurred within the subducting Juan de Fuca plate. These were the 1949 Olympia earthquake (m_b 7.1; depth 54 km) and 1965 Seattle earthquake (m_b 6.5; depth 60 km) (e.g. *Ludwin et al.*, 1991) (Figure 1.7). These types of events are referred to as intra-plate or intra-slab earthquakes. They comprise the "Wadati-Benioff" zone of seismicity (Figure 1.10) and constrain the geometry of the JDF plate beneath the North American continent.
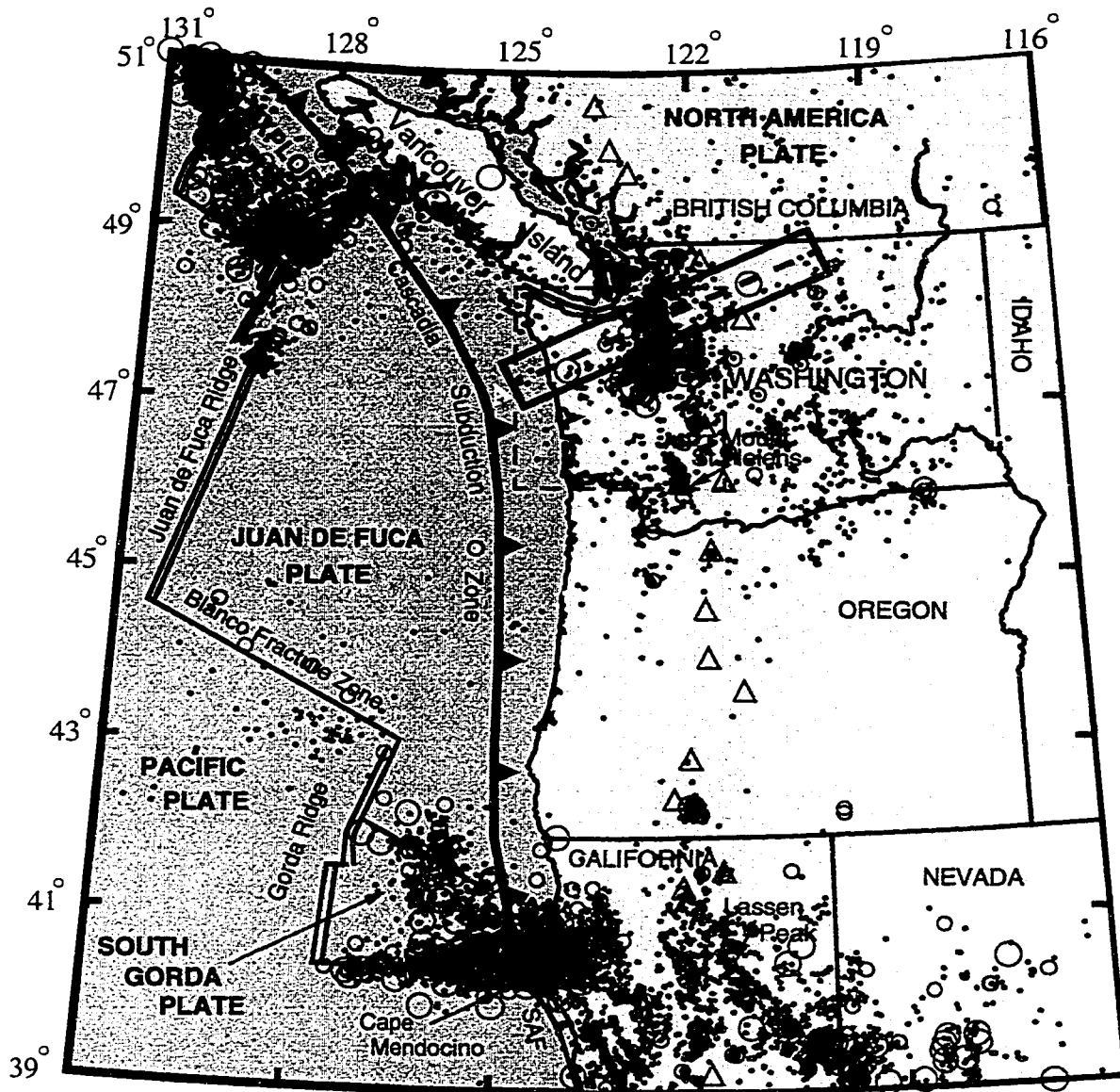
Figure 1.9: Seismicity in the Pacific Northwest United States. Green circles indicate 9339 events located within the crust of the North American plate. Red circles show 8192 events assigned to the Juan de Fuca plate. See Figure 1.10 for the cross-sectional view of earthquakes within A-A' profile. The study area is shown as a dashed box. Figure is courtesy of Karen Meagher (USGS/UW).

To further complicate the picture, the largest known earthquake in the written history of Washington and Oregon occurred in 1872 in the North Cascades earthquake (*Milne et al.,* 1978) (Figure 1.7). Based on the intensity pattern *Malone and Bor* (1979) estimated the magnitude of this earthquake to be 7.4. Although there is no clear evidence for the exact depth and location of
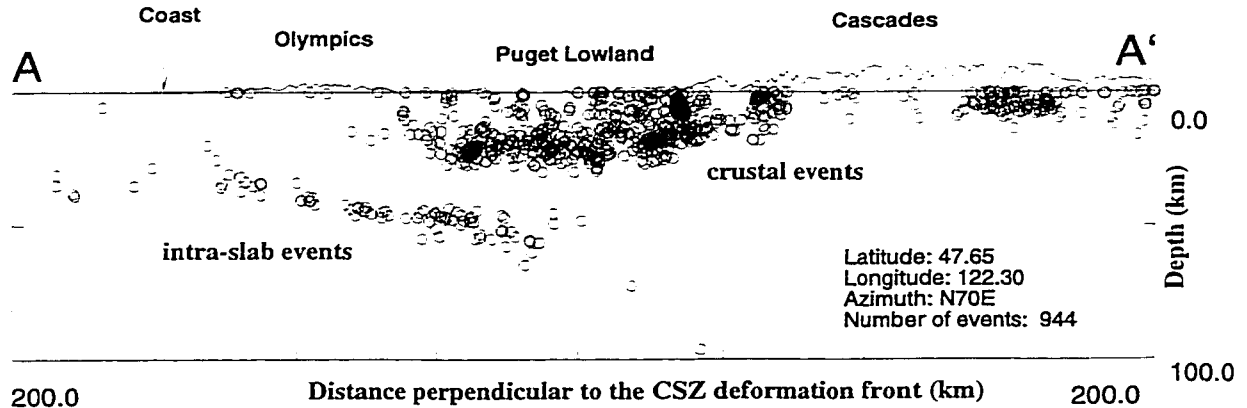
Figure 1.10: Depth distribution of earthquakes within the A-A' box shown in Figure 1.9. The box represents a 1° wide and 400 km long swath, oriented perpendicular to the CSZ deformation front and centered on Seattle. Total number of earthquakes shown is 944. 86 events between 30 and 100 km depth define the "Wadati-Benioff" zone and are presumed to take place near the top of the subducting JDF plate. Wiggly line on top of the plot represents a crude topography with 5:1 vertical to horizontal exaggeration.

the 1872 North Cascades earthquake, the number of aftershocks, the general character of current seismicity, and intensity pattern of the main shock indicate that the hypocenter of this earthquake was located within the NA crust. The most recent earthquake activity in western Washington has also been concentrated in the crust of the overriding North America plate. Geologic and recent seismological evidence suggests that there are major *shallow* faults in the crust of Washington and Oregon that may pose a more direct threat to populated regions in the conceivable future than the megathrust type earthquakes on the CSZ. Recent examples of crustal earthquakes in the Puget Lowland are the January 29, 1995 (M 5.0) Point Robinson earthquake, that occurred on an E-W thrust fault (possibly the Seattle fault) 24 km south of Seattle at a depth of 20 km (*Dewberry and Crosson*, 1996), and the June 23, 1997 (M 4.9) event that occurred at a depth of 7 km beneath Point White on southwestern Bainbridge Island. These recent events indicate that the Seattle fault remains active and raises the possibility of a repeat of the major (M > 7) earthquake that happened 1100 years ago and resulted in 7 m of uplift at Restoration Point (*Bucknam et al.*, 1992).

Further north, the South Whidbey Island fault (marked SWF in Figure 1.5) shows similar earthquake potential. The 6 to 7 km wide fault zone shows evidence of both strike-slip (right-lateral) and thrust offset (*Johnson et al.*, 1996). Like the Seattle fault, the South Whidbey Island

fault displays over 400m of offset on the base of Quaternary sediments and is estimated to be capable of generating earthquakes exceeding magnitude 7.

1.3 Previous Geodetic Investigations

1.3.1 Introduction

Previous geodetic estimates of crustal deformation in the vicinity of the study area come from tide gauge records, traditional geodetic surveys using leveling, triangulation and trilateration, and continuous GPS observations on Vancouver Island. The following two sections summarize the results obtained from these surveys. In general, most of the previous geodetic estimates of the tectonic deformation along the CSZ are consistent with subduction of the Juan de Fuca plate under North America, where the thrust fault is locked and elastic strain accumulates towards the next subduction earthquake.

1.3.2 Vertical Deformation Measurements

Previous vertical deformation rate estimates in the study area come from repeated leveling surveys and long-term trends in tide gauge records. Details of these measurements are given in tables below as well as in Figures 1.4 and 1.11.

Vertical deformation measurements (tide gauge and leveling data) in the Pacific Northwest date back to the beginning of this century (*Ando and Balazs*, 1979; *Holdahl et al.*, 1989; *Reilinger and Adams*, 1982). Although several issues still remain controversial such as the proper size of the eustatic rate of sea-level change to be applied to tide gauge data (variable γ in Table 1.1) (*Dragert et al.*, 1994; *Savage et al.*, 1991) and the computed uplift rates at specific stations (e.g. Toke Point), the overall trend of deformation is well resolved. The highest uplift rates are observed along the coast, reaching its maximum of 3.4 mm/yr at Neah Bay (Figure 1.11, Tables 1.1 and 1.2). The west to east transition from regional uplift to subsidence apparently occurs in the Puget Sound basin.

The location of the point of zero uplift (i.e. "hinge line") is important for estimating the width of the "locked" portion of the JDF and NA plate interface (*Savage et al.*, 1991). Vertical uplift rates presented as dashed contour lines in Figure 1.11 are based on results of *Mitchell* et al. (1994) who point out that the contouring they use is "crude and locally arbitrary", hence the discrepancy between the tectonic uplift rates presented in Table 1.1 and Figure 1.11. The apparent north-south

Table 1.1: Vertical uplift rates in mm/yr from tide gauge data.

Tide Gauge Station	Duration[a] (years)	Distance[b] (km)	Sea Level Rise[c] (h)	Postglacial rebound[d] (δ)	Tectonic Uplift[e] (v)	References[f]
Astoria (AS)	67	131	0.0 ± 0.2	-0.7	2.5 ± 0.2	1,2,4
Friday Harbor (FH)	49	211	0.6 ± 0.5	1.1	0.1 ± 0.5	3
Neah Bay (Nb)	58	140	-1.6 ± 0.2	0.0	3.4 ± 0.2	5
Seattle (S)	68	270	2.3 ± 0.5	-0.7	0.2 ± 0.5	1,2
Toke Point (TP)	23	133	2.1 ± 0.3	-1.0	0.7 ± 0.3	4
Toke Point (TP)	23	133	-0.2 ± 0.2	-1.0	3.0 ± 0.2	5
Victoria (V)	80	184	0.7 ± 0.1	1.0	0.1 ± 0.5	3

a. Duration of observations.
b. Approximate distance of the site from the base of the continental slope.
c. Positive values indicate upward movement of the sea level relative to land.
d. Postglacial rebound δ in mm/yr with 1σ errors calculated from ICE-3G model of *Tushingham and Peltier* (1991).
e. Tectonic uplift v in mm/yr with 1σ errors calculated using the following equation: $v=\gamma-(h+\delta)$, where h and δ are described above and γ is a constant eustatic correction of 1.8 mm/yr from *Douglas* (1991).
f. References: (1) *Holdahl et al.* (1989); (2) *Savage et al.* (1991); (3) *Dragert et al.* (1994). (4) *Mitchell et al.* (1994); (5) *Hyndman and Wang* (1995);

Table 1.2: Vertical uplift rates in western Washington from leveling surveys[a].

Leveling Lines[b]	Duration[c] (years)	Distance (km)[d]	Uplift (mm/yr)[e]	Uncertainty per 100 km	Ref.[f]
Neah Bay - Twin River (Nb - Tr)	33	160		1.2	1, 2
Twin River - Blyn (Tr - Bl)	44	193	4.0	0.9	1, 2
Westport - Aberdeen (We - Ab)	27	135		1.5	1
Aberdeen - Olympia (Ab - Ol)	55	167	4.0	0.7	1
Astoria - Rainier (AS - Ra)	21	125	3.5	3.6	1,2

a. Table is adopted from *Hyndman and Wang* (1995).
b. Location of leveling lines is shown in Figure 1.11.
c. Duration of observations.
d. Approximate distance of the site from the base of the continental slope.
e. Uplift rates between the end points relative to the most landward point.
f. References: (1) *Reilinger and Adams* (1982); (2) *Mitchell et al.* (1994).

variation in the observed uplift in Figure 1.11 is mainly due to *Mitchell* et *al.'s* interpretation of the tide gauge records from station Toke Point (TP) near Grays Harbor. *Hyndman and Wang* (1995) noted that near zero uplift rate at Toke Point presented a significant outlier and after re-examining the original tide gauge data they found that the omission of two years of intermittent

data resulted in a 3.0 mm/yr uplift rate for Toke Point. This value is also more consistent with the leveling results shown in Table 1.2.

1.3.3 Horizontal Deformation Measurements

Horizontal deformation measurements in the vicinity of the study area are based on repeated positional surveys using trilateration, triangulation and GPS methods. Within the study area five strain networks have been surveyed (shown as shaded polygons in Figure 1.11). Two main features of horizontal deformation rates along the CSZ deduced from these measurements are: 1) the observed strain rates decrease away from the coast: from 0.18 μstrain/yr in the JDF network to 0.04 μstrain/yr in the Seattle network; 2) the direction of maximum compression is roughly parallel to the relative motion of the JDF and NA plates: N68°E in the Seattle array, N59°E in the Olympic array, and N71°E in the Bellingham array (Table 1.3). Note that the strain rate estimate for the Bellingham network, which comes from the combination of GPS measurements with previous trilateration and triangulation data (*Snay and Matsikari*, 1991) is not very accurate (1σ errors are 75% of the observed signal), and therefore does not provide meaningful constraints for crustal deformation modeling.

Table 1.3: Horizontal strain measurements in western Washington State[a].

Strain Network	Duration[b] (years)	Distance[c] (km)	Shortening rate		References[f]
			ε_2[d]	Θ (1σ)[e]	
Bellingham	80	280	-0.12 ± 0.09	71 ± 21	1
Columbia	50	160	-0.09 ± 0.03	60 ± 5	2
Juan de Fuca	95	180	-0.18 ± 0.04	64 ± 5	3
Olympic	8	220	-0.09 ± 0.03	59 ± 7	4
Seattle	13	270	-0.04 ± 0.01	68 ± 6	4

a. Adopted from *Hyndman and Wang* (1995)
b. Duration of observations years.
c. Approximate distance of the site from the base of the continental slope in kilometers.
d. ε_2 Maximum principal strain rate in μstrain/yr with 1σ errors. Negative value represents compression.
e. Azimuth of ε_2 in degrees, measured clockwise from North with 1σ errors.
f. References: (1) *Snay and Matsikari*, (1991); (1991); (2) *Vincent* (1989); (3) *Lisowski et al.* (1989); (4) *Savage et al.* (1991).

The updated results of continuous GPS observations from two stations on Vancouver Island (*Dragert et al.*, 1998; *Henton et al.*, 1998) located just north of the study area, indicate that the station UCLU which is located closer to the deformation front, is moving relative to DRAO at a
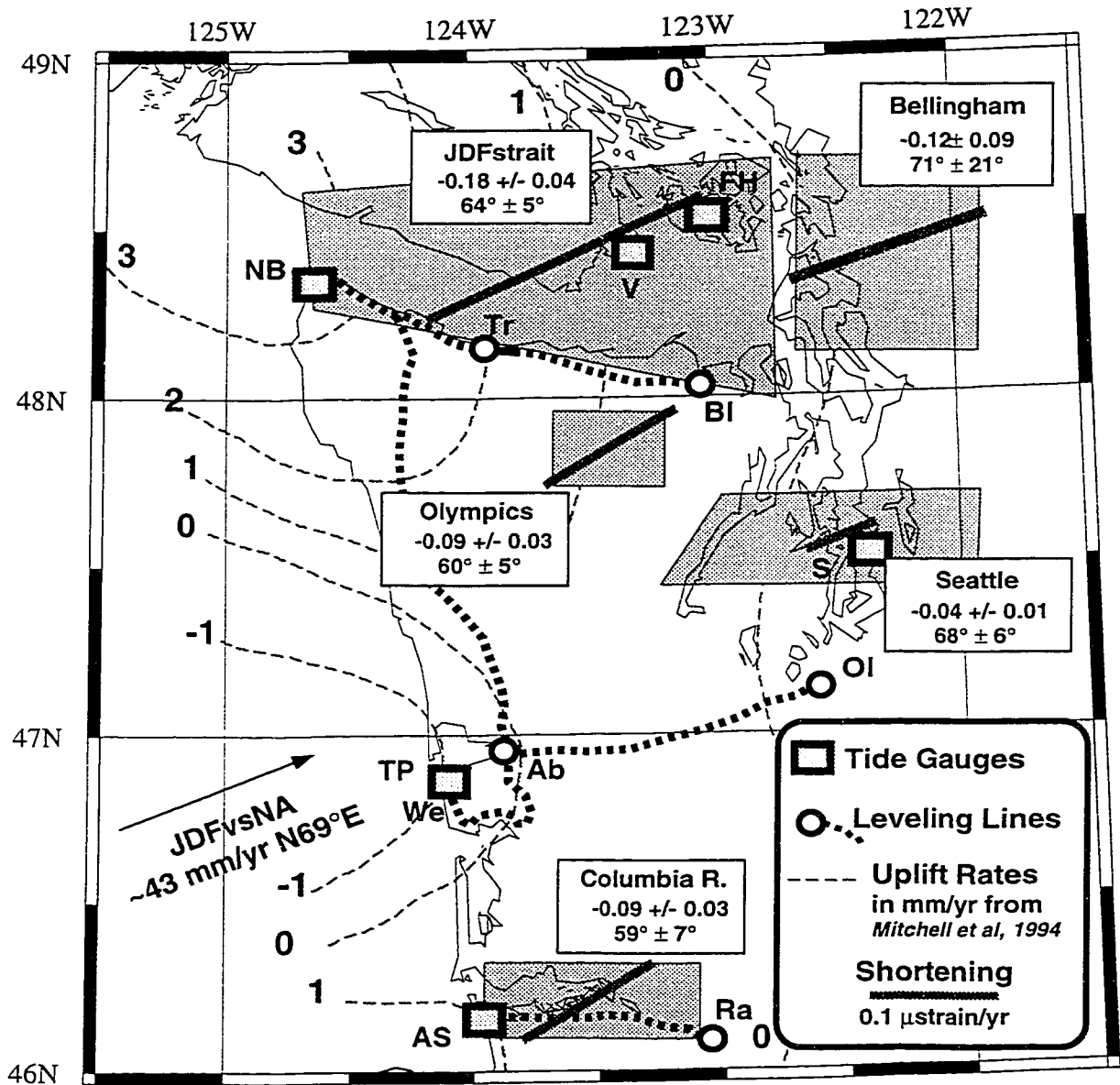
Figure 1.11: Summary of geodetic measurements in western Washington. The area covered by the horizontal strain networks are shown as shaded boxes. Thick lines within these boxes represent maximum compressive strain averaged over the shaded area and given in Table 1.3. The scale is given in the legend. Actual values of strain (in μstrain/yr) and orientation (measured clockwise from North) with 1σ uncertainties are given in boxes for each net. Dashed contour lines represent geodetic uplift rates (in mm/yr), which are also shown in Figure 1.4. See page 12,274 in *Mitchell et al.* (1994) for details regarding the construction of these contour lines. Small quadrangles show locations of tide gauge stations with station codes given in Table 1.1. Thick dashed lines indicate leveling routes listed in Table 1.2.

rate of 11.3±0.4 mm/yr in the direction N52°E±2°. Station ALBH located near Victoria, B.C., exhibits motion of 4.7±0.4 mm/yr in the direction N62°E±5° (Figure 1.12 and Table 1.4). These rates are consistent with the main features of geodetic strain accumulation deduced from earlier positional surveys (listed in Table 1.3), as well as with the findings presented in this study and discussed in the following chapters.
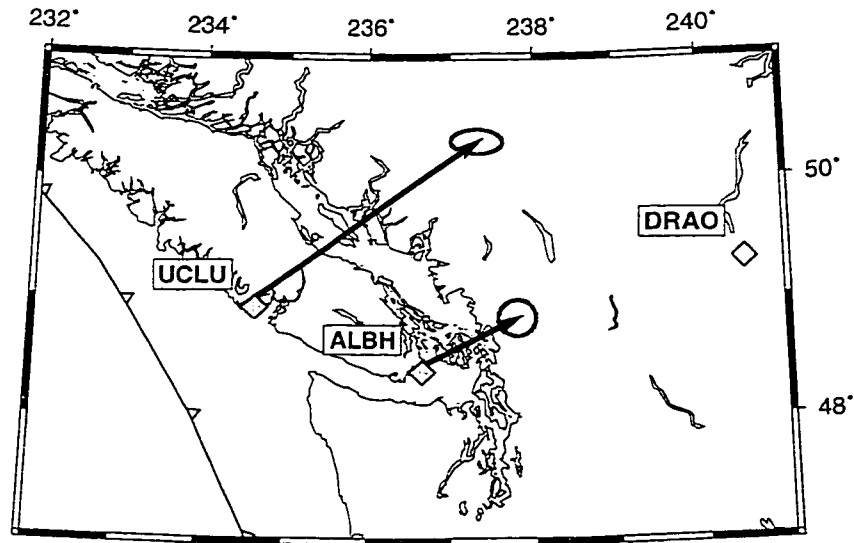
Figure 1.12: GPS horizontal velocities with respect to station DRAO in Penticton, Canada. See Table 1.4 for more details, including references.

Table 1.4: Horizontal GPS station velocities relative to DRAO.

Stations	Duration (years)	Distance[a] (km)	North[b] (mm/yr)	East (mm/yr)	Horiz. (mm/yr)	Horiz. Az. (degrees)	Ref.[c]
ALBH	~5	185	2.2 ± 0.3	4.2 ± 0.3	4.7 ± 0.4	62 ± 5	1,2
UCLU	~5	90	6.9 ± 0.2	8.9 ± 0.4	11.3 ± 0.4	52 ± 2	1,2

a. Approximate distance of the site from the base of the continental slope in kilometers.
b. Errors represent 95% estimates.
c. References: (1) *Dragert et al.* (1998); (2) *Henton et al.* (1998).

The advantage of the GPS positioning compared to classical surveying techniques (e.g. trilateration) is the ability to determine all three components of the strain rate tensor, as well as associated rigid body rotation and translation. In Chapter III I will present calculations of these parameters for several subregions located within the study area based on crustal deformation rates estimated with GPS measurements.

II. GPS Data Collection and Analysis

2.1 Introduction

The advent of Global Positioning System (GPS) technology has revolutionized our ability to determine geodetic positions and to navigate. The primary reason for GPS development by the United States Department of Defense (DoD) was to aid the military in navigation. For this purpose, the DoD has invested more than 8 billion dollars in GPS. Since the early 1990s, with the advancement of GPS technology and decreasing costs of GPS receivers, the system has started to be used in a wide range of non-military applications. The most common uses of GPS are real-time navigation (air, sea or land navigation) and position estimation (e.g. cadastral surveying, crustal deformation monitoring).

In this chapter first I will describe the main features of GPS technology (section 2.2) with the emphasis on its application to high-precision geodesy, such as crustal deformation monitoring. Detailed description of GPS technology can be found in various books published in recent years (e.g. *Leick*, 1995). Section 2.3 includes the description of the GPS data used in this study, followed by the presentation of data analysis and velocity estimation procedure (section 2.4).
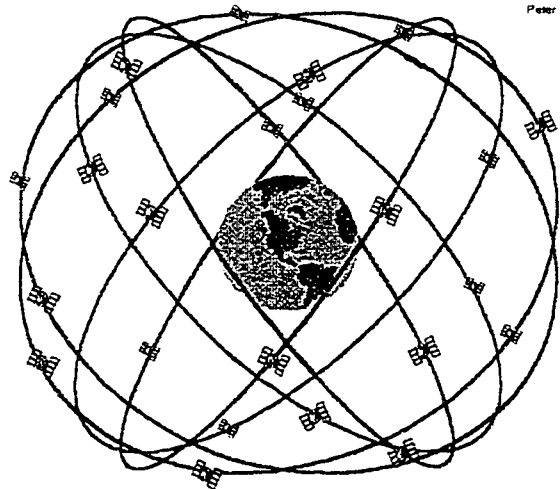
Figure 2.1: GPS satellites nominal constellation. 24 satellites orbit the earth every 12 hours at an altitude of 20,200 km. Each of 6 orbital planes, inclined at 55° to the equatorial plane, have 4 satellites. Figure from *Dana* (1998).

2.2 Overview of GPS technology

2.2.1 GPS Satellites and Signals

The first GPS satellite was launched by the DoD in 1978. However, the Initial Operational Capability (IOC) of the system was not achieved until 1993, when the full constellation of 24 satellites was in orbit (Figure 2.1). Since that time, signals from at least 4 satellites can be received at any time and place on the earth, which is the minimum number of satellites needed to estimate position.

The main principle of GPS positioning is simple: location of a point can be uniquely determined by knowing the distance to three other points (i.e. satellites) at known locations (Figure 2.2). In practice a fourth satellite is also needed to estimate the clock offset for each GPS receiver. The principle is the same one used in determining the position and origin time of earthquakes.
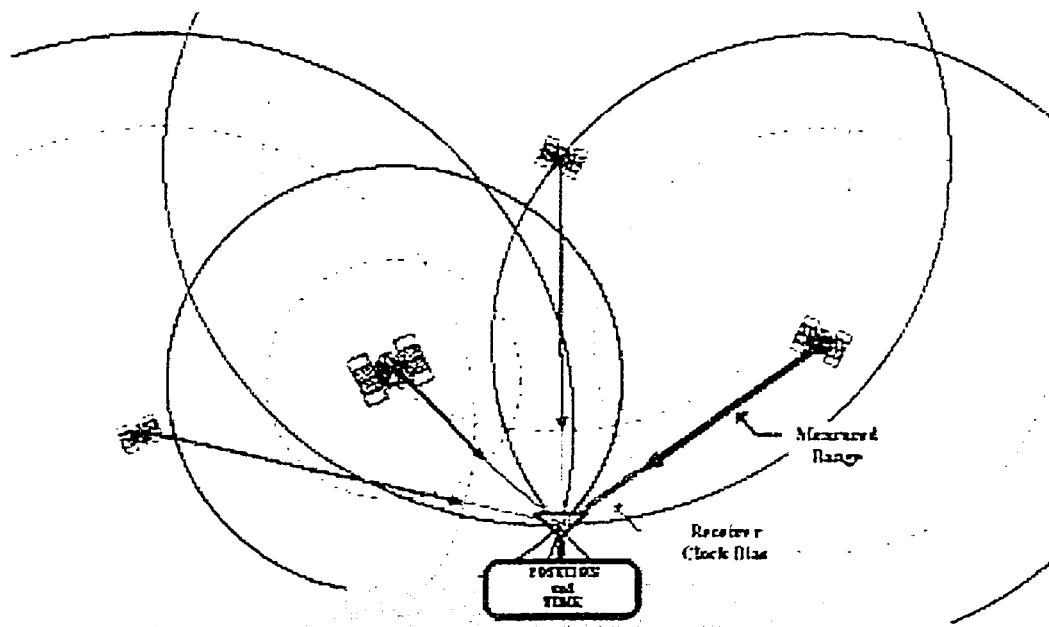
Figure 2.2: Main principle of GPS positioning. Three spheres with a radius equal to the distance from the respective satellite to the receiver antenna on the earth surface intersects within a small area, which is an estimated position of the antenna. The signal from the fourth satellite is necessary to correct for the receiver clock bias. Figure from *Dana* (1998).

The GPS satellites transmit electro-magnetic waves at two carrier frequencies, $L1$=1575.42 MHz ($\lambda^1 \approx$19 cm) and $L2$=1227.60 MHz ($\lambda \approx$24.4 cm), which are derived by multiplication of the fundamental frequency (10.23 MHz) by factors of 154 and 120, respectively. The fundamental

frequency is produced by highly stable atomic clocks on board the satellites. Carrier frequencies are modulated by precision *(P)* code and coarse-acquisition *(C/A)* codes, in order to encode date and time information. In addition, a navigation message modulates both *L1* and *L2* carrier signals (Figure 2.3). *P* code ($\lambda \approx 30$ meters) is a pseudo-random noise (PRN) code which modulates both *L1* and *L2* carrier frequencies. Since the introduction of antispoofing (AS) capabilities on new Block-II GPS satellites, *P* code can be accessed only by the military and is the basis for the Precise Positioning Service (PPS), which provides real-time positioning accuracy of approximately 25 meters *(Dana, 1998)*. Civilian users have to rely on Standard Positioning Service (SPS), based on the *C/A* code ($\lambda = 300$ meters) which modulates only the *L1* carrier frequency. The SPS provides a positioning accuracy of 100 meters with 95% confidence *(Leick,* 1995). The lower level of accuracy of the SPS compared to PPS is implemented by the DoD by introducing artificial errors in the transmitted clock and broadcast satellite ephemeris, a process collectively known as selective availability (SA). For high precision geodetic studies (e.g. tectonic deformation measurements) researchers rely on more accurate carrier phase signals in combination with precise satellite orbits (as opposed to broadcast orbits). This approach ensures the achievement of a few mm precision in horizontal and 5-8 mm in vertical positioning (see Figures 3.1 and 3.2 for precisions obtained in this study).

2.2.2 GPS Observables

There are two main observable quantities or "observables" in GPS technology: carrier phase *(L)* and pseudorange *(P)*, the apparent distance to a satellite. The carrier phase observations provide higher precision estimates of the distance between satellites and receivers than pseudorange observations but require the estimation of the integer number of cycles (n) that the wave traveled along its path (because the phase can only be determined modulo nλ). The correct estimation of n is not a trivial task, since the GPS signals travel from high-speed satellites which orbit the earth at a distance of ~20,000 km above the surface.

---

1. $\lambda = V/f = V \times T$; where λ is wavelength in meters, *f* is frequency in Hz and *T* is period in seconds, and *V* is the velocity of light.

L1 CARRIER 1575.42 MHz

C/A CODE 1.023MHz

NAV/SYSTEM DATA 50 Hz

P-CODE 10.23 MHz

L2 CARRIER 1227.6 MHz

→ **L1 SIGNAL**

$\bigotimes$ Mixer

$\bigoplus$ Modulo 2 Sum
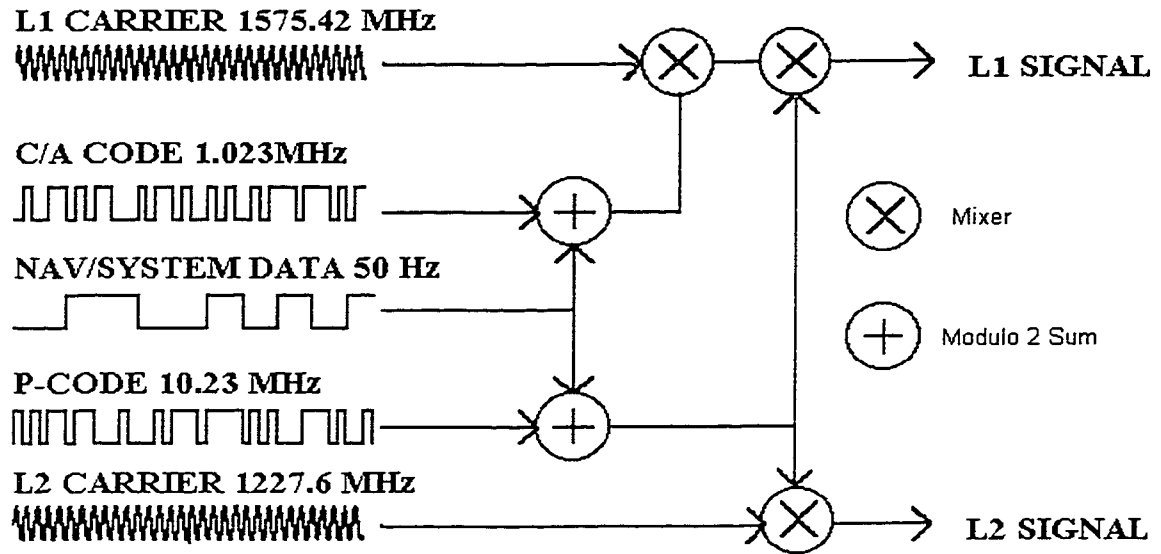
→ **L2 SIGNAL**

Figure 2.3: Schematic representation of GPS signals. Figure from *Dana* (1998).

The carrier phase observable (*L1* or *L2*) between receiver r and satellite x at time t (e.g. Leick, 1995; Zumberge et al., 1997) can be expressed using the following equation:

$$L_{rxt} = \rho_{rxt} + N_{rxt} + I_{rxt} + T_{rxt} + C_{rt} - c_{xt} + M_{rxt} + v_{rxt} \qquad \text{(EQ 2.1)}$$

All terms in Equation 2.1 are assumed to be converted to ranges in meters (i.e. T_{rxt} tropospheric time delay in seconds is multiplied by wave propagation velocity). Terms on the right hand side of Equation 2.1 are: ρ_{rxt} - is a true range between the satellite and the receiver. If the path of GPS signal were entirely in a vacuum and the travel time were known exactly then $L_{rxt} = \rho_{rxt}$. Since this in not the case, the expression for L contains 7 additional terms: N_{rxt} - integer number of phase biases; I_{rxt} - ionospheric time delay; T_{rxt} - tropospheric time delay; C_{rt} and c_{xt} - satellite and receiver clock errors; M_{rxt} - multipath effects; v_{rxt} - measurement noise. The expression for P pseudorange is essentially the same as for the carrier phase L given in Equation 2.1, except that it does not contain the bias term N_{rxt}.

N_{rxt} - integer number of phase biases

This term, unlike others in Equation 2.1 is characteristic only of carrier phase data (L). The procedure of resolving an unknown integer number of wavelengths that the wave has traveled from the source to the receiver, is most commonly called bias-fixing or ambiguity resolution. The

simplest way to estimate N_{rxt}, is by forming *double-differences* for phase or pseudorange observables, as illustrated schematically in Figure 2.4. The procedure of forming double-differenced observable involves the combination of two *single-difference* observables. The latter is the case when two different receivers record signals from the same satellite. For example, two receivers k and m observe a satellite p as shown in Figure 2.4. Since the observed carrier-phase at both receivers is affected by the same satellite clocks errors, if any, the difference of the observed phases at each receiver is independent of the satellite clock error. Thus single-differencing eliminates common satellite clock errors. Moreover, one can take two single-difference observations from different satellites and form a double-differenced observable by subtracting one from another. This procedure eliminates receiver clock error. More discussion concerning the use of double-differenced observables in estimating N_{rxt} follows in section 2.4.2. For a detailed description of algorithms used in ambiguity resolution the reader can refer to *Blewitt* (1989).

I_{rxt} - ionospheric time delay

The ionosphere, which stretches from approximately 50 to 1500 km above the earth's surface, is a dispersive medium. For this reason, the ionospheric time delay I_{rxt} has a frequency dependence, as illustrated in Equation 2.2 (*Leick*, 1995):

$$I_{rxt} = \frac{40.30 \cdot TEC}{c \cdot f^2} \qquad \text{(EQ 2.2)}$$

where f is the carrier frequency, c is the wave propagation velocity in vacuum (*m/sec*) and **TEC** is the total electron content along the wave path (*electrons/m²*) which can be expressed as:

$$TEC = \int_{path} N_e ds \qquad \text{(EQ 2.3)}$$

where N_e is a local electron density in electrons/m³. From Equation 2.2 we can see that waves (i.e. signals) with higher frequencies are delayed less in the ionosphere. By using typical values for TEC in Equation 2.2, *Leick* (1995) has estimated the range of expected ionospheric corrections for *L1* and *L2* carrier phase frequencies (Table 2.1).

From Table 2.1 we see that the TEC in the ionosphere has a profound impact on observed pseudorange values when compared to the desired precision in the range of a few millimeters.

Table 2.1: Ionospheric range corrections for L1 and L2 frequencies.

Frequency	Range Correction I_{rxt} (meters)	
	$TEC^a=10^{16}$	$TEC=10^{18}$
L1 (1575.42 MHz)	0.16	16
L2 (1227.60 MHz)	0.26	26

a. TEC: Total electron contents in electrons/m^2.

The greatest values for TEC are usually associated with observations taken during the day, during increased solar activity, and close to the equator or at high latitudes.

Fortunately, due to the dispersive character of the ionosphere, by combining phase measurements at two frequencies into an *ionosphere-free* combination observable (denoted as *LC*), it is possible to eliminate the first-order delays caused by the ionosphere:

$$LC = L1 \cdot \frac{f_1^2}{f_1^2 - f_2^2} - L2 \cdot \frac{f_2^2}{f_1^2 - f_2^2} = L1 \cdot 2.546 - L2 \cdot 1.546 \qquad (EQ\ 2.4)$$

where *LC*, *L1* and *L2* are expressed in meters, and f_1 and f_2 are 1575.42 MHz and 1227.60 MHz carrier frequencies, respectively.

Using appropriate expressions for *L1* and *L2* from Equation 2.1 in Equation 2.4 eliminates the ionospheric delay term I_{rxt}:

$$LC = \rho_{rxt} + N_{rxt} + T_{rxt} + C_{rt} - c_{xt} + M_{rxt} + v_{rxt} \qquad (EQ\ 2.5)$$

However, to take advantage of this technique, data have to be recorded with dual-frequency receivers which are considerably more expensive than single-frequency receivers.

T_{rxt} - **tropospheric time delay**

The tropospheric delay is a combined effect of the troposphere, the tropopause and the stratosphere, stretching up to a height of 40 km from the earth's surface (*Leick*, 1995). Although the thickness of this layer is only a fraction of the ionosphere thickness, signal delays it can cause are of the same magnitude as those caused by the ionosphere. Due to the non-dispersive nature of the troposphere, signals of all frequencies (e.g. *L1* and *L2*) are delayed by the same amount. Thus

forming a linear combination of observations from different signals, analogous to the ionosphere-free combination, is not effective to eliminate tropospheric time delays.

Like the ionospheric time delay expressions given in Equations 2.2 and 2.3, the tropospheric time delay (T_{rxt}) can be expressed in terms of the tropospheric index of refraction (N_T) (*Leick*, 1995):

$$T_{rxt} = \int_{path} N_T ds \qquad \text{(EQ 2.6)}$$

where the tropospheric index of refraction (N_T) is a sum of the dry (N_{Dry}) and wet (N_{Wet}) component:

$$N_T = N_{Dry} + N_{Wet} \qquad \text{(EQ 2.7)}$$

where N_{Dry} and N_{Wet} are functions of the atmospheric pressure (p), partial pressure of water vapor (e) in mbars, and the surface temperature (T) in degrees Kelvin:

$$N_{Dry} = 77.624 \cdot \frac{p}{T} \cdot 10^{-6} \qquad \text{(EQ 2.8)}$$

$$N_{Wet} = -12.92 \cdot \frac{e}{T} + 371900 \cdot \frac{e}{T^2} \cdot 10^{-6} \qquad \text{(EQ 2.9)}$$

The coefficients in Equations 2.8 and 2.9 are based on empirical observations and were calculated by *Essen and Froome* (1951). 90% of the tropospheric delay is due to the first term in Equation 2.7 (*Leick*, 1995). Thus by measuring temperature and pressure on the surface of the earth, it is possible to estimate this part of the delay. The right hand side of Equation 2.9, representing the wet component of the tropospheric delay (N_{Wet}), includes water vapor pressure (e) terms. Proper modeling of this part of the delay requires the estimation of the water vapor content along the propagation path. The latter task is hard to achieve with simple measurements of pressure and temperature on the surface. It requires either a water vapor radiometer (WVR) or a radiosonde, both tremendously expensive tools. In real life, atmospheric observations at the surface are not available either. Therefore, both dry and wet components of the tropospheric delay have to be modeled. Since the dry component of the tropospheric delay depends mainly on atmospheric pressure and temperature, it is relatively safe to model it using simple relationships for a standard atmosphere. For example the relationship between the pressure P (in bars) and station surface

elevation *h* is given by Equation 2.10 (*Blewitt*, 1993), where a typical value for *H* is 7 km (*Tralli et al.*, 1988).

$$P = 1.013 \cdot e^{-h/H}$$ (EQ 2.10)

Modeling of the wet component of the tropospheric delay is more complicated, since the water vapor pressure dependence on turbulence causes random variations in the wet component delay over a wide range of spatial and temporal scales (*Blewitt*, 1993). The most commonly used approach to model tropospheric delays is to use a mapping function for estimating delays at different elevations from the zenith (i.e. vertical) wet delay (ZWD) (e.g. *Davis et al.*, 1985; *Lanyi*, 1983). Residuals between the model and actual delays are estimated using stochastic models, such as, for example, a random walk process (e.g. *Tralli and Lichten*, 1990). With improvements in satellite orbit estimation and ground antenna and receiver designs, correct modeling of the troposphere related errors remains a major obstacle towards improving GPS precision, especially in the vertical component. However, in recent years significant advances have been achieved on this front. For example, *Bar-Sever et al.* (1998) report 19.5% and 15% average improvement in radial and horizontal site position repeatabilities, respectively, by lowering an elevation angle cutoff[2] and by including horizontal gradients in tropospheric delay modeling. This and other advances in modeling various parameters affecting GPS signal propagation, make GPS an increasingly useful tool in studying the atmosphere. For example, starting in 1998, the IGS offers a stand alone product of tropospheric delay estimates in the form of the ZWDs for more than 100 worldwide IGS GPS stations (*Gendt*, 1998). To convert ZWD into an estimate of precipitable water vapor (PWV), which is of great importance for numerical weather forecasting, climate research and atmospheric studies, one has to conduct surface meteorological observations simultaneously with recording GPS signals from space-borne satellites. For this reason, increasing number of continuous GPS stations are being equipped with surface meteorological packages. It is worthwhile to mention that both of the University of Washington continuous GPS stations used in this study (see NEAH and SEAT in Figure 2.6), have simultaneous meteorological observations (*Tad Anderson*, pers. comm) that can be utilized for atmospheric studies in the future.

---

2. In GPS data processing, data from a satellite are used only if the satellite is above the horizon by an angle that exceeds the elevation angle cutoff.

C_{rt} and c_{xt} satellite and receiver clock errors

Satellite and receiver clock errors are due to drift in clock oscillators. Receiver clock errors are especially significant, since the receivers employ less accurate quartz crystal oscillators that are subject to higher drift rates. Although GPS satellites are equipped with highly stable cesium atomic clocks (rubidium as backup), the introduction of selective availability (SA) by the DoD artificially degrades the quality of satellite clocks. Fortunately, as mentioned earlier, the method of double-differencing GPS observables eliminates most of the satellite and receiver related clock errors. The basic idea behind this method is that two receivers k and m observe two satellites p and q simultaneously (Figure 2.4).
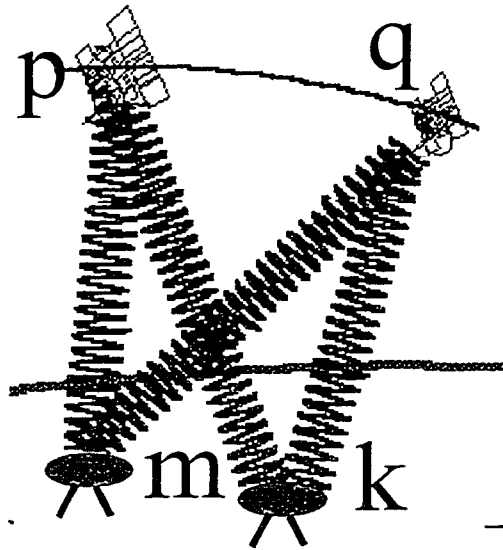
Figure 2.4: GPS double difference observations. Figure from *Dana* (1998).

Creating double differences is not the only way to eliminate clock errors. Some GPS processing software, including the GIPSY/OASIS-II analysis package used in the current study, rely on undifferenced data and instead of eliminating clock errors by forming double-differenced observables, they estimate clock errors (i.e. biases) stochastically (e.g. using a "white noise" model). See discussion by *Blewitt* (1993) for further details.

M_{rxt} - multipath effects

Multipathing effects are caused mainly by signal scattering/reflection on the ground near the receiving antenna. The outcome of this effect is that the same signal arrives at the antenna at different times due to the different paths is has traveled. Multipath effects can also arise at

satellites, although errors associated with the ground multipathing are much more significant. Since signals from satellites near the horizon are more susceptible to multipathing, GPS users have traditionally discarded data below $10°$ elevation. Much work has been applied to developing antennas that reduce multipath induced errors. Initial improvements included the use of antenna groundplanes, which are successful in preventing waves below $0°$ (i.e. ground reflected) from entering the antenna sensor. However, there are also problems associated with signals reaching the antenna via antenna edge diffraction (*Leick*, 1995). This has led to the development of choke ring antennas (*Tranquilla et al.*, 1994), the state-of-the-art of today's GPS antenna technology.

v_{rxt} - measurement noise

Measurement noise includes inherent random errors as well as systematic errors. The latter can be caused by miscalibrations of GPS antennas or by errors in the measurement of the height of the antenna above a GPS reference point (e.g. geodetic marker).

2.3 GPS Data

The GPS data used in this study to estimate crustal deformation rates in western Washington State can be divided into two categories: continuous and "campaign" style data which are discussed in sections 2.3.1 and 2.3.2, respectively.

2.3.1 Continuous GPS Stations

Since the early 1990s, with the decreasing cost of GPS receivers and sophistication in analysis techniques (*Yunck*, 1995), the geodetic community has pursued a novel approach of recording GPS data on a continuous basis. Obvious benefits of continuous recording over "campaign" style (or episodic) surveys include the increased precision of observations (due to the reduction in RMS scatter of daily position estimates, 24 hour long daily observations, elimination of setup and antenna related errors) and possible detection of short term geodetic signals from pre and post-seismic effects. A recent example of the latter was provided by GPS data from stations near the Landers, California earthquake (*Blewitt et al.*, 1993; *Bock et al.*, 1993; *Murray et al.*, 1993; *Wyatt et al.*, 1994). Today, numerous arrays of continuous GPS receivers operate worldwide. The largest and surely the most impressive one is located in Japan which consists of more than 1000 permanent GPS stations (*Kato et al.*, 1998).

IGS Worldwide Stations
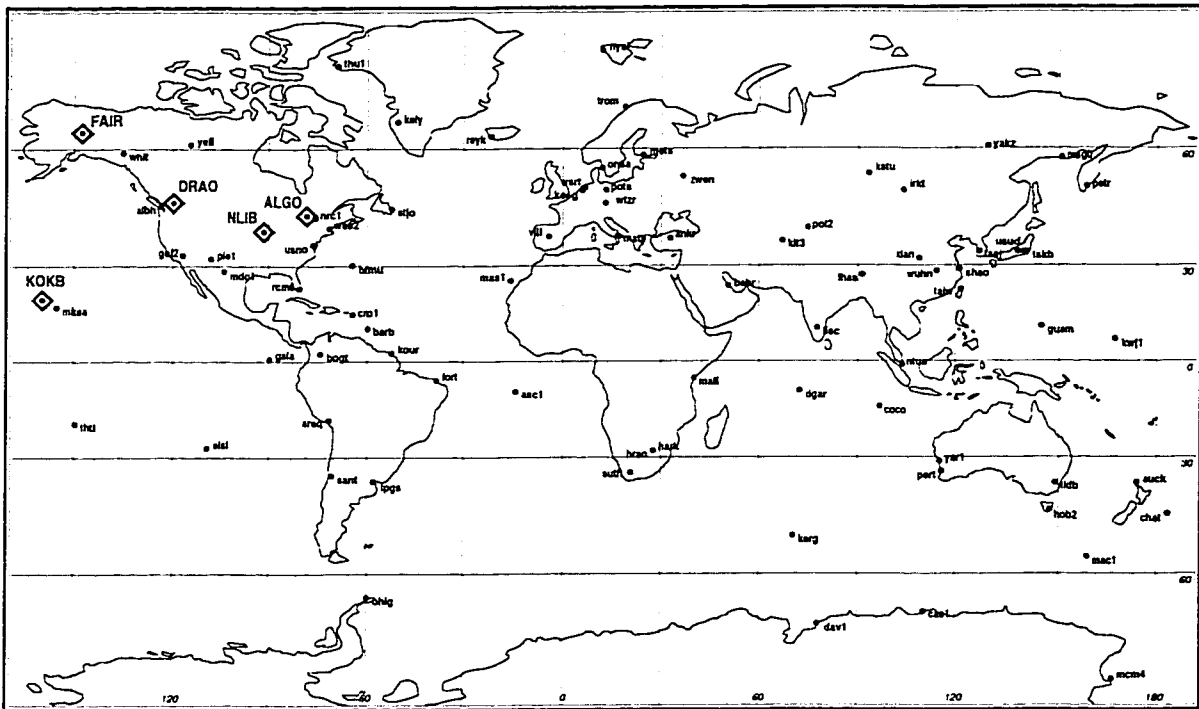
Figure 2.5: IGS worldwide network of permanent GPS trackers. Stations used in daily analysis are shown as diamonds with upper case names next to them. See Table A.1 for more details.

The establishment of a worldwide network of continuous GPS stations, under the aegis of the International GPS Service (IGS), led to a major advance in high precision GPS geodesy (*Beutler et al.*, 1994). Instead of relying on less accurate "broadcast ephemeris" transmitted from satellites with the navigation message (see section 2.2.1), 7 analysis centers located in the United States (3), Canada (1), Germany (2) and Switzerland (1), compute satellite precise orbits on a daily basis, which are later merged into combined IGS orbits available on the Internet at *http:// igscb.jpl.nasa.gov*. These orbits are crucial for achieving the high precision required for crustal deformation monitoring. The combination of positions and velocities computed with various space geodetic techniques (e.g. GPS, VLBI, SLR and DORIS) have enabled the International Earth Rotation Service (IERS) to produce a dynamic global reference frame: International Terrestrial Reference System (ITRF) (*Sillard et al.*, 1998). In the analysis, I have consistently included data from at least five IGS stations (ALGO, DRAO, FAIR, KOKB and NLIB), shown as

diamonds in Figure 2.5 and listed in Table A.1. With the exception of KOKB, all of these stations are located on the North America plate. KOKB is located in Hawaii on the Pacific Plate. The inclusion of IGS stations is necessary to ensure a reliable transformation of daily position estimates spanning several years of observations to a common reference frame (e.g. ITRF96). See the description of post-processing in section 2.4.2 for further details.

Regional Stations

One of the first permanent GPS arrays in North America was established in 1991 by the Geological Survey of Canada (GSC) in southern British Columbia; it is called the Western Canada Deformation Array (WCDA) (*Dragert et al.*, 1995). In the summer of 1995, the University of Washington, in cooperation with the GSC, installed the first continuously recording GPS stations in Washington State, located in Seattle (SEAT) and near Neah Bay (NEAH) (Figures 2.6 and 2.7) (*Khazaradze et al.*, 1995).

In early 1996, the US Coast Guard and the National Geodetic Survey established three additional permanent GPS stations in the region: at Fort Stevens (FTS1), Whidbey Island (WHD1) and Robinson Point (RPT1) (Figure 2.6). These stations are part of a nationwide network of Continuously Operating GPS Reference Stations (CORS) shown in Figure 2.8 (*Strange*, 1994). Although the antennas at these stations (due to their location on top of ~10 meters tall towers) are less stable than antennas at stations specifically designed for high precision geodetic work (e.g. NEAH), our results show that the CORS stations located in western Washington can be successfully used in crustal deformation monitoring.

Table 2.2: Number of analyzed days for the continuous GPS stations.

Station Code	ALBH	DRAO	FTS1	NEAH	RPT1	SEAT	WHD1
# of analyzed days	1023	1042	836	872	869	933	879

Crustal deformation rates presented in this study are based on data from seven regional continuously operating GPS receivers (ALBH, DRAO, FTS1, NEAH, RPT1, SEAT and WHD1) that are presently part of a larger network called the Pacific Northwest Geodetic Array (PANGA) (Figure 2.6). (*Khazaradze and Qamar*, 1997; *Miller et al.*, 1998). Detailed information regarding PANGA, including the station locations, dates of the installation and a list of responsible agencies is given in Table A.2. Each of the 7 analyzed GPS stations has at least 2.5 years of continuous
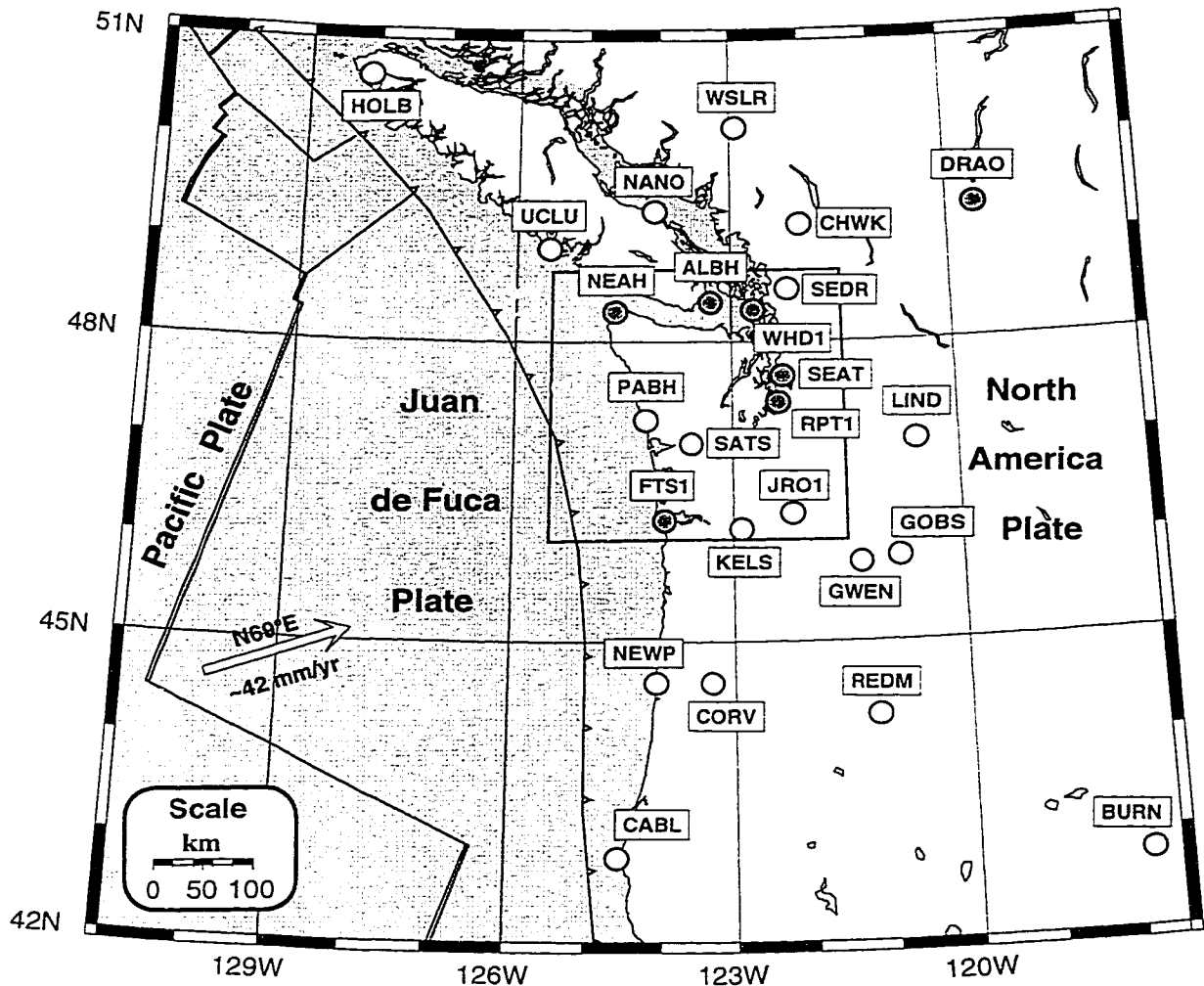
Figure 2.6: Pacific Northwest Geodetic Array (PANGA) as of January, 1999. A box shows the study area. Filled circles show stations with at least 2.5 years of continuous data that were used in this study. The white arrow shows the direction of relative motion between the Juan de Fuca and North America plates based on NUVEL-1A global plate motions model (*DeMets et al.*, 1990; 1994). Table A.2 provides more details regarding PANGA stations.

data. The number of days analyzed for each of the stations are given in Table 2.2. Newer PANGA stations shown as open circles in Figure 2.6 have been in place for substantially less time and therefore, I refrain from interpreting their velocities.

2.3.2 "Campaign" GPS Stations

Starting in 1986 the Geological Survey of Canada, the United States Geological Survey (USGS) and the National Geodetic Survey have conducted half a dozen GPS "campaigns" (i.e. surveys) in Washington State and British Columbia. Since 1994, the University of Washington (UW) has
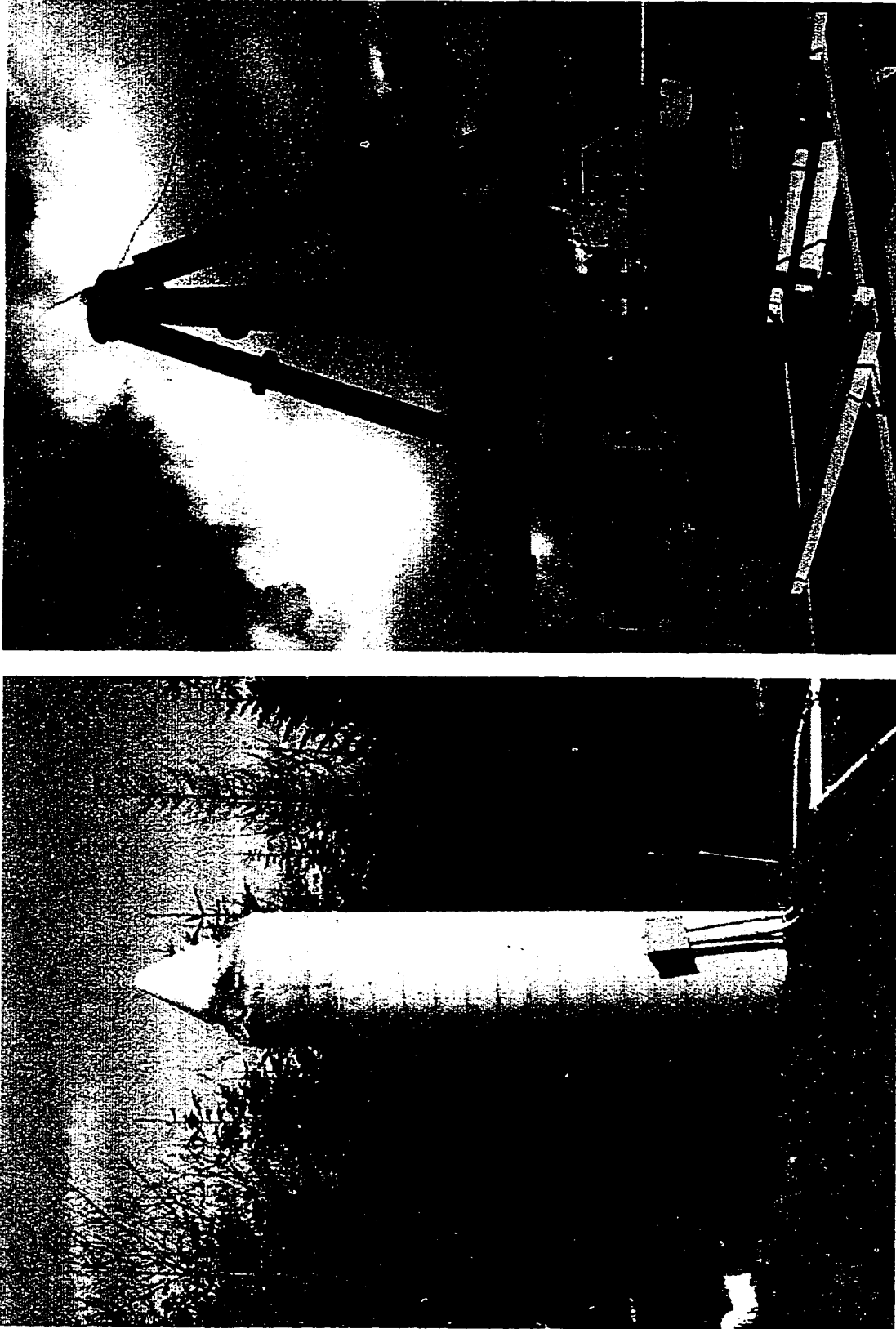
Figure 2.7: Antenna monumentations for continuous GPS stations at Neah Bay (left) and Seattle (right). For locations see NEAH and SEAT in Figure 2.6 for locations of these stations.
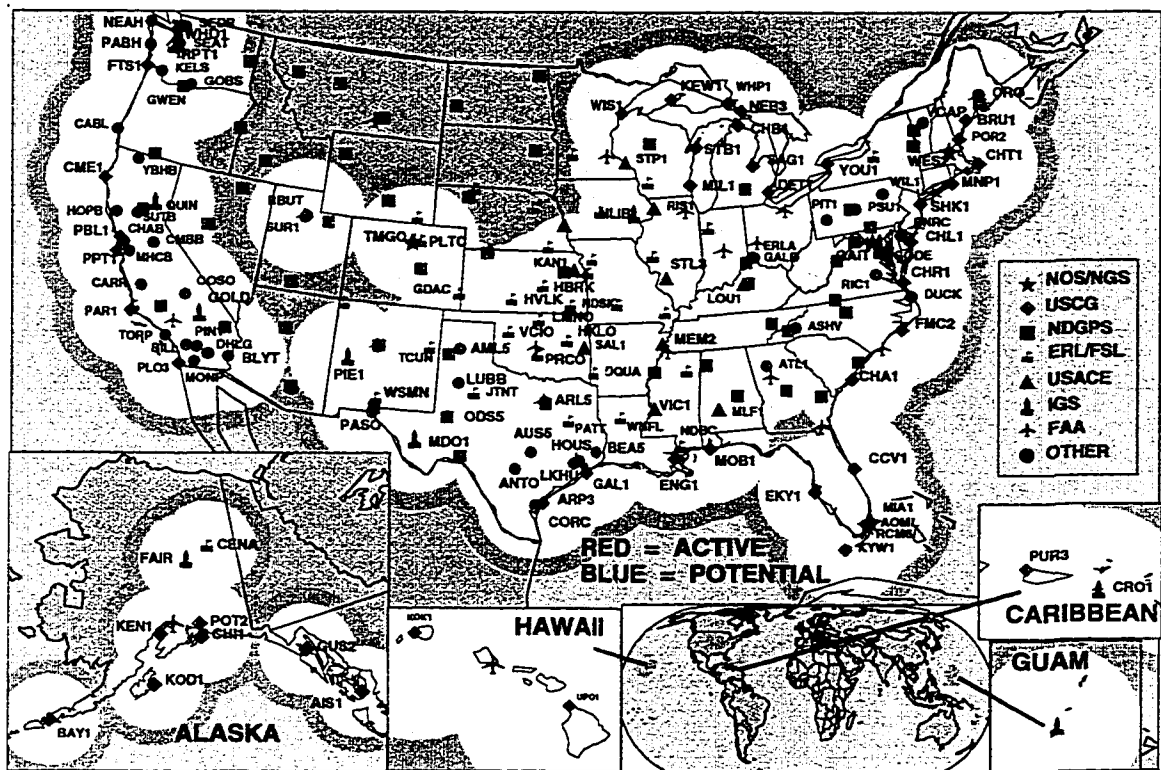
Figure 2.8: Map of Continuously Operating Reference Stations (CORS) in the United States. From the National Geodetic Survey WWW homepage at: *http://www.ngs.noaa.gov/CORS*.

joined their efforts and has carried out three independent GPS campaigns in 1995, 1996 and 1997. In 1994, the UW was a participant in a USGS survey. The 1996 campaign concentrated on establishing first-time (or zero epoch) measurements in the Puget Lowland. This survey was a collaboration between the UW and the USGS Cascades Volcano Observatory (CVO) in Vancouver, Washington. Overall, since the late 1980s, more than 150 geodetic benchmarks have been surveyed in Washington State using GPS. Although I have analyzed data from 119 of these sites (shown as circles in Figure 2.9), in this study I have chosen only 38 "campaign" stations, shown as shaded triangles in Figure 2.9 and listed in Table A.3. The main criteria for the selection of these stations were:

- Surveys were conducted in 1994, 1995, 1996 and 1997.

- Observations for each station spanned at least two years.

- Stations surveyed only in two different years had at least two occupations per year

- Stations were located within the study area.
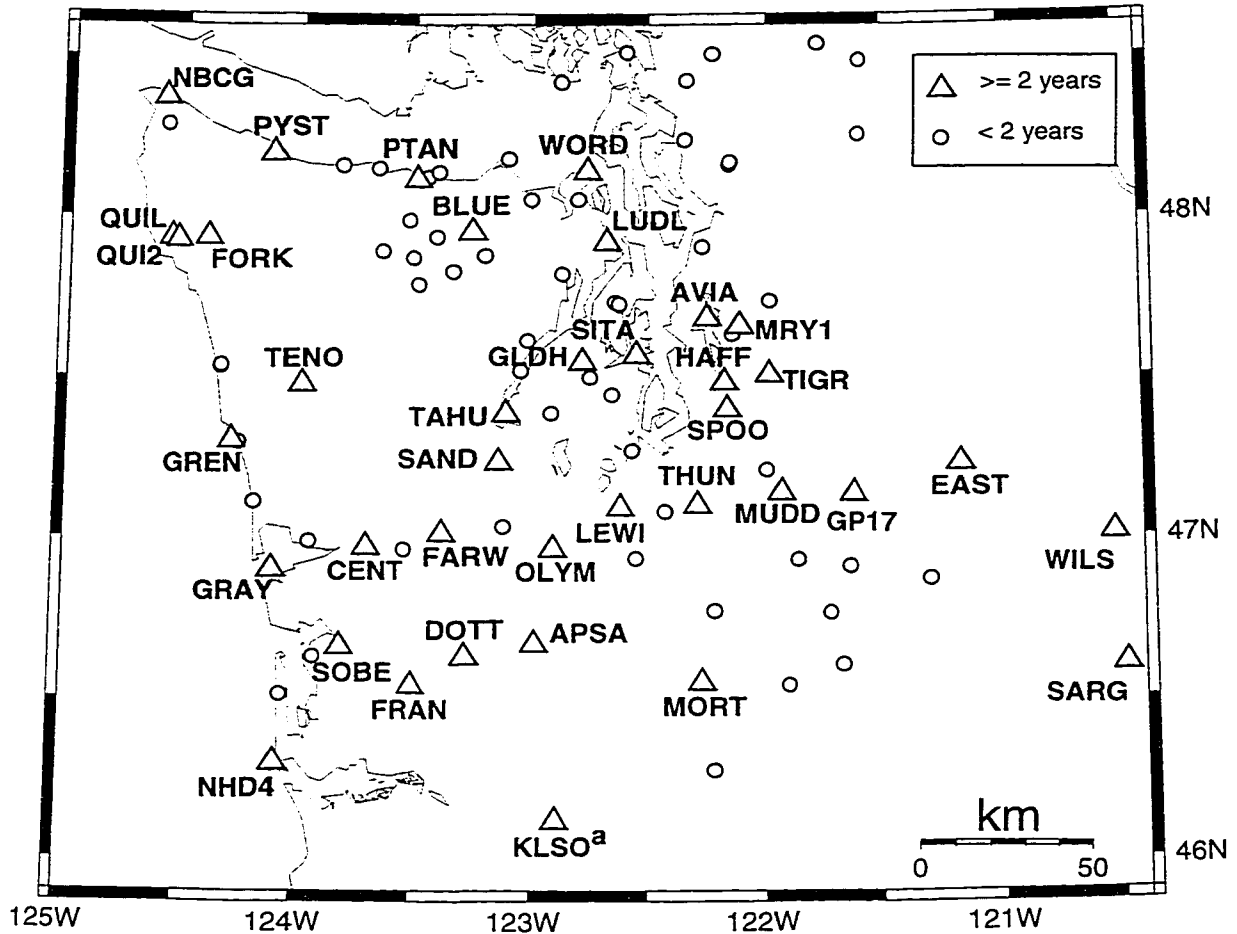
Figure 2.9: Map of geodetic benchmarks in western Washington State surveyed in GPS "campaigns" since 1994. Stations considered in this study are shown as triangles, with station codes next to them. Each of the stations were surveyed for at least two years. See Table A.3 for detailed description of analyzed stations. Stations that did not meet the selection criteria are shown as circles. Station KLSO in Kelso, Washington is operated by the Cowlitz county GIS group (George Bradford and Todd Wilson). Because the data from this station is not available on the Internet, I have analyzed KLSO data only for days during the "campaign" observations. Since 10/09/97 the UW installed an additional station 10 meters away from the original Cowlitz county tracker.

A summary of the occupation history for all of the 38 stations is given in Table 2.3. More detailed information can be found in Table A.4

As can be seen from the occupation history summary presented in Table 2.3, more than half of the analyzed data were obtained by the USGS. If not for the generosity of Will Prescott from the

Table 2.3: "Campaign" GPS station occupation summary.

Campaign Year	1994	1995	1996[c]	1997	1994-97
# of occupations by UW[a]	9	23	28	66	126
# of occupations by USGS	18	27	15	31	91
# of occupations by CVO	21	0	32	0	53
# of occupations by Cowlitz[b]	0	2	15	13	30
# of total occupations	48	52	90	110	300

a. UW: University of Washington; USGS: United States Geological Survey, Menlo Park, California; CVO: Cascades Volcano Observatory, USGS, Vancouver, Washington.

b. Since 1995 Cowlitz county GIS group (George Bradford and Todd Wilson) operates a continuous GPS station in Kelso, Washington (KLSO in Table A.3). Because the data is not available on the Internet, I have analyzed KLSO data only for days during the "campaign" observation. Since 10/09/97 the UW installed an additional station 10 meters away from the original Cowlitz county tracker (see the entry for KELS in Table A.2 for more details).

c. In 1996 the UW and CVO conducted a joint 6 day campaign from June 10th to June15th.

USGS office in Menlo Park, California and Elliot Endo from the Cascades Volcano Observatory in Vancouver, Washington in sharing their data with us, the number of stations meeting our selection criteria would have been twice as small. On the other hand, the reason we rely on the USGS data so heavily is that we have intentionally attempted to re-occupy as many of their stations as possible. This way we were able to increase the time-span of observations and ultimately reduce the errors in our velocity estimates. Unfortunately, the combination of data collected by different agencies has led to extra complications in the analysis mainly due to the need to combine data from different types of GPS receivers and antennas used by the USGS, CVO and the UW. Problems arise when various types of antennas were used at the same station during different occupations. Because of variation in antenna phase center locations (see Table 2.5), mixing of different types of antennas degrades the precision of estimated position (e.g *Wu et al.*, 1993). Such variations affect mainly the vertical component of position and can lead to errors exceeding 10 mm (*Schupler et al.*, 1994). Since the expected rates of vertical deformation (i.e. uplift) in the Cascadia subduction zone do not exceed 5 mm/yr, two or three years of GPS observations is not a sufficient time to reliably estimate vertical velocities, especially with "campaign" style intermittent observations. For this reason, in this study no attempt is made to estimate vertical velocities from GPS data.

Mixing different antenna types at the same station can also cause up to several millimeter errors in horizontal position estimates. This fact is manifested from non-zero North and East component antenna phase center offsets for six out of seven different types of GPS antennas used for the selected 38 "campaign" and 6 continuous sites (Table 2.4). In an ideal situation, when the same type of antennas exhibit identical characteristics, and they are correctly oriented to true North during the setup, mixing of antennas should not pose a significant problem. Unfortunately, in real life all of the above can be false, thus degrading the achievable precision of position (and velocity) estimation.

Table 2.4: Type of used GPS antennas and their phase center offsets[a].

#	Ant Code	Antenna Name	L1[b]			L2[c]		
			North	East	Up	North	East	Up[d]
1	ASH_CHK	Ashtech Choke Ring	0.0	0.0	110.0	0.0	0.0	128.0
2	ASH_GDP	Original Ashtech L1/L2	-2.0	5.0	78.6	-2.0	5.0	78.6
3	ASH_WHP	Ashtech Geodetic III	-0.6	0.2	83.9	1.1	-1.6	62.3
4	ASH_GD	Ashtech Geodetic III CORS	-1.2	-0.8	87.7	0.9	-1.6	59.8
5	TRIM_CGP	Trimble Geodetic L1/L2 GP	-0.1	-0.6	74.2	-0.5	2.8	70.5
6	TRIM_CHK	Trimble Choke Ring	1.2	0.5	109.8	1.2	0.6	128.0
7	TRIM_SST	Trimble 4000ST L1/L2 Geodetic	-0.7	-0.2	75.7	-1.9	-0.3	74.5

a. Phase center offsets are based on NOAA calibration results (*Mader*, 1999).
b. *L1* phase center in millimeters from the Antenna Reference Point.
c. *L2* phase center in millimeters from the Antenna Reference Point.
d. Note: Up component for *L1* and *L2* antenna phase center offsets represents an average value which has been determined for a standard elevation cutoff angle of 15 degrees. In reality, the phase center location changes with the changing direction of the signal from a satellite. As illutrated by the NGS calibration results for Trimble 4000ST L1/L2 Geodetic antenna given in Table 2.5.

Detailed information regarding individual station occupation history for the 1994, 1995, 1996 and 1997 campaigns (including the antenna height information) can be found in Tables A.5, A.6, A.7 and A.8, respectively.

Table 2.5: Vertical phase center variations for Trimble 4000ST L1/L2 Geodetic GPS antenna[a].

Satellite Angle[b]	90°	80°	70°	60°	50°	40°	30°	20°	10°	0°
L1 phase center (mm)	0	10.1	17.7	22.1	23.4	22.1	19.2	16.4	15.7	0
L2 phase center (mm)	0	1.5	3.3	4.6	5.2	4.9	4.0	3.0	2.7	0

a. Phase center offsets are based on NOAA calibration results (*Mader*, 1999). Values for L1 and L2 vertical offsets are given relative to the average values for the Trimble 4000ST L1/L2 Geodetic antenna presented in Table 2.4 and calculated using 15° elevation cutoff. The phase center elevation variations at 10° were calculated by arbitrarily constraining the L1 and L2 correction to zero at the zenith (i.e. 90°) and the horizon (i.e. 0°) and finding an interpolated value for 10° (*Mader*, 1999).

b. Satellite angle is the angle of arriving signals measured above the horizon.

2.4 Data Analysis

2.4.1 Introduction

To estimate GPS station positions and velocities I have used the GIPSY/OASIS-II analysis package developed at the Jet Propulsion Laboratory (JPL) (*Webb and Zumberge*, 1997). GIPSY stands for GPS Inferred Positioning SYstem and OASIS for Orbit Analysis and SImulation Software. While the GIPSY was designed specifically for GPS data analysis, OASIS is a more general package incorporating covariance analyses for earth orbiting and deep space missions (*Gregorius*, 1996). From here on I will refer to both modules as GIPSY.

The GIPSY analysis package uses undifferenced GPS observables, and reduces phase and pseudo-range data simultaneously. Most of the other GPS data analysis packages used for high precision geodesy rely on forming double-differences (e.g. BERNESE and GAMIT). Using undifferenced phase observations provides several advantages, such as the ability to independently estimate individual site and/or satellite specific parameters (e.g. clocks, phase residuals and tropospheric delays). This makes the task of isolating problematic receivers or satellites much easier. More in depth discussion of the advantages and disadvantages on using undifferenced versus double-differenced data can be found in *Blewitt* (1993).

2.4.2 Data Processing

GPS data analysis using the GIPSY software can be divided into three main steps: *pre-processing, processing* and *post-processing*.

The first two steps, *pre-processing* and *processing,* are performed for each day to be analyzed, which means on a daily basis for the continuous data processing. The final product of these two steps is a "stacov" file, containing the date and number of estimated station parameters followed by the estimated parameters and their covariance. The estimated parameters include individual station positions in an earth-centered, earth-fixed cartesian reference frame (ECEF). Vertical antenna phase center offset information for each station is appended to the "stacov" file. This information can be used to correct erroneous entries for the antenna heights during the post-processing, avoiding time-consuming reprocessing procedure.

The final *post-processing* step in GPS data analysis involves the transformation of daily "stacov" files to a common reference frame (e.g. ITRF96) and the creation of time series (station positions versus time) in a local North-East-Up geodetic coordinate system. These time series are used to estimate relative station velocities.

Specific models and parameter values I used in the processing of GPS data presented in this study are given in Table B.1. Below I describe each of the *three* main steps involved in the estimation of station positions and velocities.

Pre-processing

The *pre-processing* step involves translation of raw binary GPS data collected in the field into ASCII RINEX (Receiver INdependent EXchange) format files (*Gurtner et al.,* 1989). I have used a program called TEQC developed at UNAVCO (*http://www.unavco.ucar.edu*) to perform the translation. TEQC also performs an initial data quality check, which enables the identification of obvious problems in the data, such as, time gaps (e.g. due to power failure) or the presence of abnormally high number of cycle slips[3] (e.g. due to increased multipath effects near the antenna). After all the data are translated into RINEX format, four day-specific files described in Table 2.6 are obtained from JPL. These files are available via anonymous ftp from *sideshow.jpl.nasa.gov* seven to ten days after the data are recorded.

---

3. A cycle slip is usually a break in the data that prevents the receiver from keeping an accurate count of received cycles of phase data. Recall that the number of cycles between the satellite and receiver must be estimated to compute the range. For each cycle slip one must compute the number of missed cycles. Thus cycle slips add to the number of unknowns that must be estimated.

Table 2.6: JPL products used in the GPS data analysis

#	File Name	Description
1	YYYY-MM-DD.eci[a]	precise satellite orbits, fiducial[b]
2	YYYY-MM-DDtpeo.nml	time, polar motion and earth orientation information
3	YYYY-MM-DD.shad	list of satellites in passing through the earth's shadow
4	YYYY-MM-DD.tdpc	time dependent parameter file including satellite clocks

a. YYYY: year; MM: month; DD: day .

b. Fiducial orbits are obtained by constraining positions of 13 IGS stations to *a priori* value from an appropriate reference frame (e.g. ITRF96).

In the next step, pseudo-range and phase data from each station is decimated from 30 seconds to 5 minute samples using second order polynomial fit and merged into a binary QMfile. Afterwards, the TurboEdit (*Blewitt*, 1990) and PhasEdit (*Freymueller*, 1992) data editing programs are used to detect outliers and fix cycle slips for the code tracking (e.g. TurboRogue receiver manufactured by Allen Osborne and Associates) and codeless receivers (e.g. Ashtech and Trimble manufactured receivers), respectively. Both types of receivers record $L1$ and $L2$ carrier phase signals. In the absence of antispoofing, the code-tracking receivers have the capability of recording $P1$ and $P2$ code signals, while the codeless receivers can not record P code and rely on C/A code (see section 2.2.1). However, since February 1994, the DoD has permanently switched the antispoofing on and the P code can only be accessed by the authorized users with cryptographic equipment and keys and specially equipped receivers.

The *pre-processing* step also involves the elimination of signals which were recorded from "unhealthy" satellites as reported by the US Naval Observatory (agency responsible for the GPS satellite maintenance/operation). In addition, signals from satellites below a certain number of degrees above the horizon (i.e. elevation cutoff angle) are ignored. I have consistently used satellite data only if the satellites where $10°$ or more above the horizon, although default value in the GIPSY analysis package is set to $15°$. Lowering the elevation cutoff angle reduces the daily scatter in the computed vertical component of position. *Bar-Sever et al.* (1998) have suggested using $7°$ cutoff to estimate horizontal gradients of tropospheric path delay.

Processing

The *processing* step consists of *model generation* and *parameter estimation* parts. The term "model" here is used to denote all the known forces (e.g. earth rotation) which effect the estimation of various parameters of our interest (e.g. station position or satellite orbit parameters).

The *model generation* part includes *orbit* and *measurement models* (*Webb and Zumberge*, 1997). Orbit models are not used explicitly in the analysis. However, because the orbits are held fixed to the JPL estimated values, orbit models are present implicitly in the final position estimates. Schematic description of satellite orbit modeling parameters used by JPL is provided in Table B.1 as shaded cells. More information on orbit models can be found in *Gregorius* (1996).

The *measurement models* can be divided into two parts: *earth* and *observation models* (*Gregorius*, 1996). The former includes forces affecting motion of the whole earth and station position estimates: tidal effects (e.g. solid earth tides, pole tides and ocean loading), earth rotation (UT1), polar motion, precession, nutation and rotation, perturbation.

The *observation* model deals with the GPS observables and various factors affecting their propagation through the atmosphere as described in section 2.2.2. It also incorporates a database of known antenna phase center offsets from the point of reference (e.g. geodetic benchmark).

Most of the *model* parameters described above are defined in the *qregres.nml* FORTRAN namelist which is used as input to a GIPSY program called, *qregres*. Actual values used in the analysis are provided in Table B.1. Detailed description of *measurement* models, including mathematical formulations, can be found in *Sovers and Border* (1990) or *Gregorius* (1996).

As mentioned earlier, the second step in the *processing* part of the analysis is *parameter estimation*. In this step, all the parameters, such as station positions and orbit and measurement models, are estimated using a Square Root Information Filter (SRIF). SRIF is a modification of a Kalman Filter and was initially developed by *Bierman* (1977). Detailed description of its application to high-precision GPS positioning can be found in *Lichten* (1990). The GIPSY program modules which handle the parameter estimation part are: *pre-pre-filter, prefilter, filter, smapper, postfit, postbreak, edtpnt2, postfit*. For the detailed description of these programs the reader can refer to publications by *Webb and Zumberge* (1997) or *Gregorius* (1996).

At the final stage in the *processing* step, the user generally has a choice to proceed further to perform an ambiguity resolution and obtain *ambiguity-fixed* solutions or be content with somewhat lower accuracy (factor of 1.5 to 2) *ambiguity-free* solutions. Ambiguity resolution entails fixing biases to integer values by forming double-differences (see Figure 2.4) for phase (called the wide-lane combination with $\lambda{=}86.2$ cm) and pseudorange (called the narrow-lane combination with $\lambda{\approx}5.4$ cm) observables. It is performed by the GIPSY program called *ambigon2*. Detailed description of ambiguity resolution techniques used in the GIPSY is given in *Blewitt* (1989).

In the analysis of continuous and "campaign" GPS data I have performed ambiguity resolution for each of the analyzed day and all the results presented in this study are based on these solutions.

Post-processing

The main goal of the *post-processing* step of the GPS data analysis is to determine individual GPS station velocities based on daily position estimates. A summary of the steps undertaken to achieve this goal is listed below as a bulleted text. The UNIX C-shell script calling specific the GIPSY programs used in the post-processing is given in Table B.2.

- Correct for possible errors in the antenna phase center vertical offsets.

- Combine all daily non-fiducial[4] solutions (i.e. "stacov" files) into one solution with station positions, velocities and covariances (i.e. "all.stacov" file) for the specified epoch (I have used January 01, 1997).

- Apply minimal constraints to rotational, translational and scale elements in the combined non-fiducial solution file (i.e. "all.stacov" file). This procedure removes uncertainties due to the loosely defined internal reference frame (*Gregorius*, 1996) and only affects the covariance matrix and does not change station position and velocity estimates. Details regarding this procedure can be found in *Vanicek and Krakiwsky* (1986).

- Transform the combined solution to an appropriate reference frame. I have used the International Terrestrial Reference Frame ITRF96 (*Sillard et al.*, 1998). This transformation is performed by using a generalized 14 parameter (3 for rotations, 3 for translations and 1 for scale, plus the same number of parameters for the rates)

---

4. "Fiducial" means constrained. Thus non-fiducial solution stands for the daily position estimate obtained without constraining any of the analyzed station position to previously determined value. In the analysis, each station was assigned an a priori standard deviation of 100 meters. Non-fiducial approach is discussed in *Heflin et al.* (1992) and *Blewitt et al.* (1992).

Helmert transformation. The output file "final.stacov" includes individual station position and velocity estimates in earth-centered, earth-fixed, cartesian (X, Y, Z) coordinate system. It also includes the covariance matrix and nominal epoch.

Normally, the last step provides the derived estimates of station velocities. However, the GIPSY programs "stamrg", "statistics" and "heightfix" were limited to combining a maximum of 999 days of data. Since this maximum was exceeded at the two Canadian sites, the following steps were added to produce velocity estimates:

- Following the post-processing procedure described above, obtain the combined "final.stacov" solution for 999 days.

- Use "final.stacov" and the daily solutions to obtain daily time series in the ITRF96 reference frame as described in Table B.2 under the title: "# start creating time series for each daily solution".

- Plot deviations from the mean value for each station in latitude, longitude (and height for the continuous stations) as shown in Figures C.1, C.2, C.3, C.4, C.5 and C.6 (I refer to these plots as station time series).

- Estimate velocities for each station in latitude, longitude (and height for the continuous stations) by weighted least squares linear regression using the GIPSY estimated formal errors as weighting factors. Regression was carried out using the Least Squares Spectral Analysis (LSSA) program by *Pagiatakis* (1997).

- Transform estimated station velocities from an absolute (e.g. ITRF96) reference frame to a fixed North America reference frame by subtracting a no-net-rotation model of current plate velocities (NNR-NUVEL-1A)[5] by *Argus and Gordon* (1991).

The following Euler pole of rotation was used to calculate NA plate velocities at each of the GPS station locations:

Table 2.7: The NNR-NUVEL-1A Euler pole of rotation for North American plate.

Plate	Latitude (°)	Longitude (°)	ω (°/Ma clockwise)
North America	-2.5	274.0	0.21

- Finally, convert station velocities in the NA fixed reference frame to a reference frame where station DRAO in Penticton, Canada is held fixed. This step is performed in order to reduce day-to-day scatter due to common error. The choice of DRAO as a

---

5. The NNR-NUVEL-1A model is based on the assumption that there is no net rotation of the lithosphere (i.e. no-net-rotation or NNR frame). Relative plate velocities in the NNR-NUVEL-1A model are constrained to the NUVEL-1A global plate motions model values derived from sea floor spreading rates and transform fault and earthquake slip azimuths (*DeMets et al.*, 1990; 1995).

reference station is due to its location on a stable part of North American continent. The section below discusses the validity of this assumption. A detailed description of the procedure used to estimate velocities relative to DRAO is given in Table B.3.

Table 2.8: DRAO GPS station velocity relative to stable NA continent.

#	Reference	Method[a]	Velocity[b] (mm/yr)
1	*Argus and Heflin*, 1995	GPS	2.0±4.0
2	*Argus and Gordon*, 1996	VLBI	2.0±5.2
3	this study	ALGO	2.8±3.4
4		NLIB	2.0±4.5

a. Entries 1 and 2 show DRAO velocities relative to the stable NA continent, where the latter is defined as a combination of 9 sites assigned to the NA continent (*Argus and Heflin*, 1995; *Argus and Gordon*, 1996). Errors represent 95% confidence limits.

b. Entries 3 and 4 show DRAO velocities relative to the stable NA continent, where the latter is assumed to be fixed to ALGO and NLIB, respectively. Errors represent 95% confidence limits computed by adding (in quadrature) 5 mm/yr systematic error to each station velocity divided by the duration of observations following the procedure adopted by *Argus and Heflin* (1995) and *Argus and Gordon* (1996).

DRAO Velocity relative to the "stable" North American Continent

Plate motion estimates based on the analysis of globally distributed GPS (*Argus and Heflin*, 1995) and VLBI (*Argus and Gordon*, 1996) stations show insignificant motion of DRAO relative to the stable NA continent (Table 2.8). I have tested whether this observation is also supported by the results of this study. This task was relatively simple to achieve, since I have systematically used 5 IGS stations in the daily analysis, including two stations located on the stable NA continent: ALGO and NLIB (Table A.1). Therefore, by inspecting estimated velocities at these stations relative to DRAO, I was able to check the assumption of DRAO stability. The computed velocities at stations ALGO (located in Ontario, Canada) and NLIB (located in Iowa, USA) relative to DRAO are equal to 2.8±3.4 and 2.0±4.5 mm/yr, respectively (Table 2.8 and Figure 2.10). Where errors represent 95% confidence limits calculated as described in footnote *b* to Table 2.8. Thus, according to my analysis, station DRAO in Penticton, Canada exhibits insignificant

motion relative to stable NA continent, which is consistent with the earlier published observations presented in Table 2.8 for comparison.
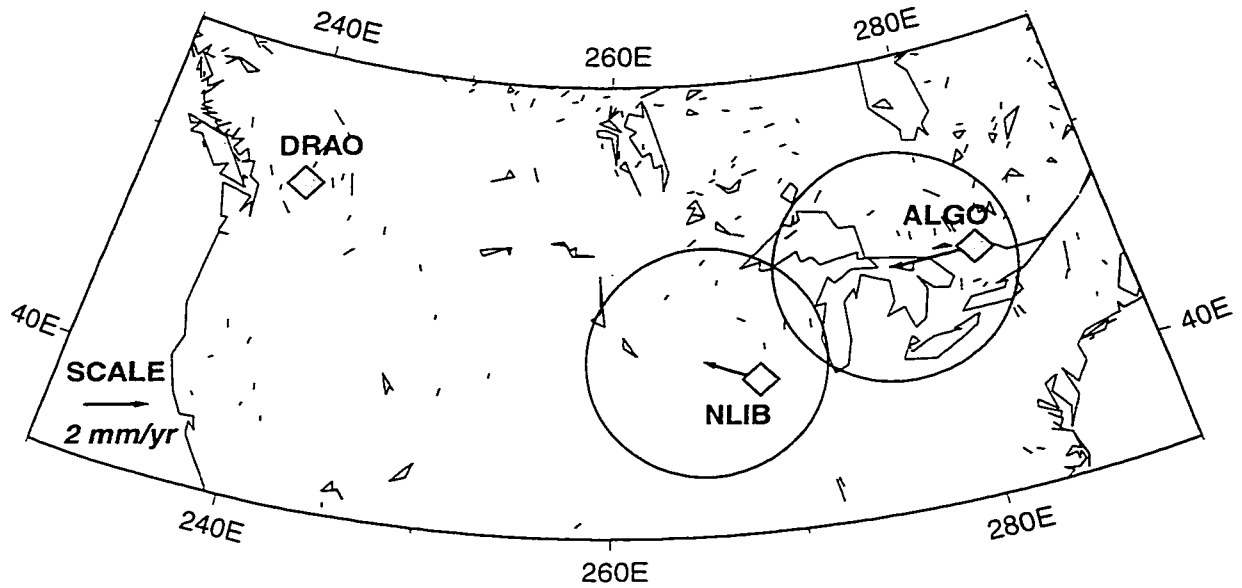
Figure 2.10: Velocities of IGS stations on "stable" North American plate relative to station DRAO in Penticton, Canada. Ellipses represent 95% confidence limits. See Table 2.8 for more information.

According to the above described *post-processing* procedure I have estimated velocities for the entire set of 44 continuous and "campaign" GPS stations which are presented as tables in Appendix D and as vectors in chapter III.

III. Results of GPS Measurements

3.1 Introduction

This chapter consists of *three* main sections. The *first* section includes a discussion of the precision of computed station positions and velocities. The *second* section outlines the main results by presenting the actual velocity field for the entire set of 44 continuous and "campaign" stations. And finally, the *third* section includes the calculation of the strain rate tensors for the entire study area as well as several subregions.

3.2 Precision of GPS Measurements

Before presenting velocity estimates for GPS stations, representing tectonic deformation, it is important to evaluate the achieved precision of the GPS measurements.

Precision describes how exact a measurement parameter is (e.g. station position coordinate) and it can be estimated by the scatter of individual measurements around their mean value. Long term precision of GPS measurements S_{line} (Equation 3.1) is defined as the weighted root mean square (wrms) about the best fitting line (*Larson et al.*, 1991). The same quantity is often referred to as the "daily repeatability" (e.g. *Blewitt*, 1989). This measure of precision assumes that tectonic deformation rates are constant and best estimated via linear regression of the positional time series. Non-linear transients, whether caused by physical events (e.g. nearby earthquakes or groundswell due to groundwater influx) or by instrumental effects (e.g. change in antenna or change in multipath environment), will affect not only the velocity estimate but also the measure of precision.

$$S_{line} = \sqrt{\frac{\frac{N}{N-2}\sum_{i=1}^{N}(y_i - (a + bt_i))^2/\sigma_i^2}{\sum_{i=1}^{N}1/\sigma_i^2}}$$

(EQ 3.1)

Variables on the right hand side of Equation 3.1 are defined as follows: y_i is an estimate of an unknown parameter (e.g. latitude or longitude) at a site that may be computed daily, N is the total number of y_i, σ_i represents an estimated standard error of y_i^1, a is the intercept and b is the slope

of the best fitting line (i.e. North, East and Vertical velocity), t_i is the time at which y_i is estimated.
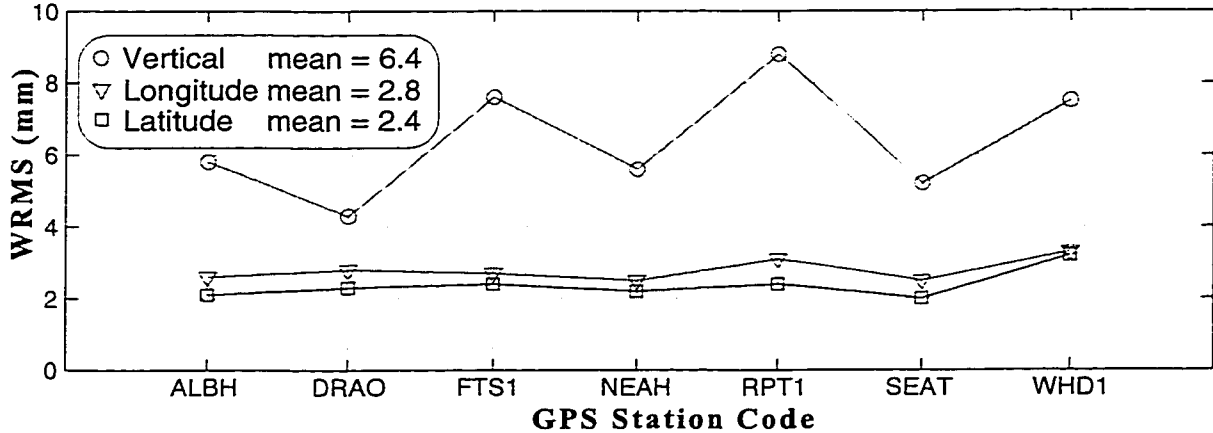
Figure 3.1: Precision of position estimates for the continuous GPS stations. Wrms values were calculated using Equation 3.1. Number of independent measurements (N) for each station is given in Table 2.2. Table D.1 contains wrms values for individual stations.

The average precision achieved for the continuous GPS station position estimates for the north-south and east-west components is equal to 2.4 and 2.8 mm, respectively (Figure 3.1). Slightly higher scatter in the east-west (i.e. longitudinal) component is due to more north-south oriented ground-tracks of the GPS satellites, which cause less advantageous geometry for the east-west component determination (e.g. *Dixon*, 1991). The achieved precision for the vertical component is a factor of two worse (~6 mm) than for the horizontal component (~3 mm). This is a common result for GPS investigations and is mainly caused by: 1) the fact that ground receivers can see satellites only above the horizon and not below; 2) the vertical component is a factor of three more sensitive than horizontal components to errors in tropospheric models (e.g. *Dixon*, 1991).

Also noteworthy in Figure 3.1 is the fact that the CORS stations (FTS1, RPT1 and WHD1) have the highest rms scatter, especially in the vertical component. As mentioned earlier in section 2.3.1, antennas at these stations are located on top of ~10 meters tall towers, which are presumably less stable than monuments used at other continuous GPS stations analyzed in this study. However, since the rms scatter for the horizontal components of the CORS stations is

---

1. I have used formal errors estimated by the GIPSY GPS data analysis package, which were calculated by propagating the standard deviation of the carrier-phase and pseudo-range data through the variance-covariance matrix. They depend on apriori weights assigned to phase and pseudo-range data in the *wash.nml* FORTRAN namelist and were set to 10 and 1000 mm, respectively.

comparable to the other stations, most likely the stability of the monument itself is not a cause for the observed higher scatter in the vertical component. It's probably due to the lower quality antennas used at the CORS sites. Unlike other continuous GPS stations analyzed in this study, which are equipped with choke ring antennas, the CORS sites use Ashtech manufactured antennas (noted as ASH_GD in Table 2.4) which are more prone to multipathing affects and exhibit higher scatter in the vertical component.
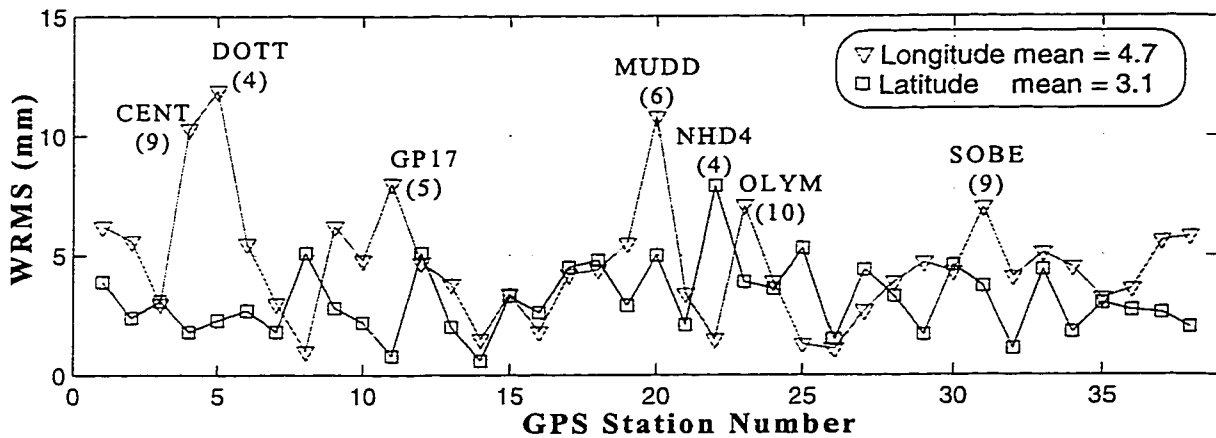
Figure 3.2: Precision of position estimates for the "campaign" GPS stations. Wrms values were calculated using Equation 3.1. Stations with the highest observed rms scatter are plotted with their names next to the estimated values (e.g. CENT). Total number of occupations for these stations are given in parenthesis. See Table D.2 for more details, including station codes and number of occupations. Table A.4 includes occupation history by year.

Long term precision for horizontal components of "campaign" stations calculated with Equation 3.1 is shown in Figure 3.2. Mean values for the north-south and east-west components are equal to 3.1 to 4.7 mm, respectively. Thus, the average achieved precision for the "campaign" stations is approximately 30% worse than for the continuous GPS stations. Considering the fact that the number of occupations in a "campaign" mode is 2 orders of magnitude less than for the continuous sites and the possibility of errors associated with monument stability and antenna/ tripod setup is much higher during the "campaign" measurements, this average precision can be considered satisfactory. However, for approximately one third of the "campaign" stations the achieved precision is worse than the average values between 3 and 5 mm as stated above. It's interesting to note that with the exception of station NHD4, all the other stations with higher than 5 mm wrms values are caused by the degraded precision in the east-west component (Figure 3.2). The worst results are achieved at three stations: CENT, DOTT and MUDD. These stations have

wrms scatters higher than 10 mm in the east-west direction (Figure 3.2). Below I will briefly discuss questions related to monument stability and possible setup errors for these three stations.
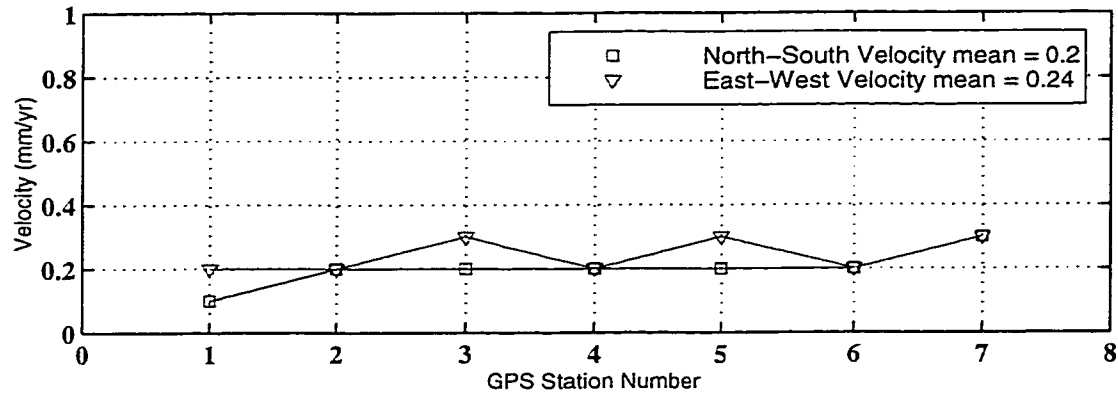
Figure 3.3: Precision of velocity estimates for the continuous GPS stations. The adopted values for the precision equal 1σ errors of the slope in the weighted least squares linear regression of individual station time series (Figures C.1 and C.2). Regression was carried out using the Least Squares Spectral Analysis (LSSA) program by *Pagiatakis* (1997). Table D.1 includes station names corresponding to the plotted numbers.

Station CENT is located along the U.S. Highway 12 in Central Park beneath power lines and next to a sidewalk. It has been occupied twice per year in 1995 and 1996 and 5 times in 1997. In the 1995 campaign, I had problems with one of the tripod legs sinking into the asphalt softened by the sun. However, if we examine CENT time series presented in Figure C.3, occupation of CENT by the USGS in 1995 (Table A.6) represents a bigger outlier. Station DOTT, located along the State Route 6 in Doty, has been surveyed only once per year in 1995 and 1996 (Figure C-3 on page 122) and twice in 1997. Although DOTT campaign data did meet the adopted criteria of station selection (section 2.3.2), if I had discarded the 1995 occupation for DOTT as an outlier (as evidenced by the time series presented in Figure C.3), it would no longer have met the selection criteria. The third station with higher than 10 mm rms scatter in the E-W component is MUDD, located near the Mudd mountain dam. Since this station has only been surveyed by the USGS (Tables A.5 through A.8), I am not familiar with the specifics of its stability and possible setup related errors. In terms of the number of occupations, MUDD has been surveyed twice in each of the three years: 1994, 1995 and 1997. The inspection of time series for MUDD in Figure C.4 shows that the increased wrms value is due to an outlier point in 1995.
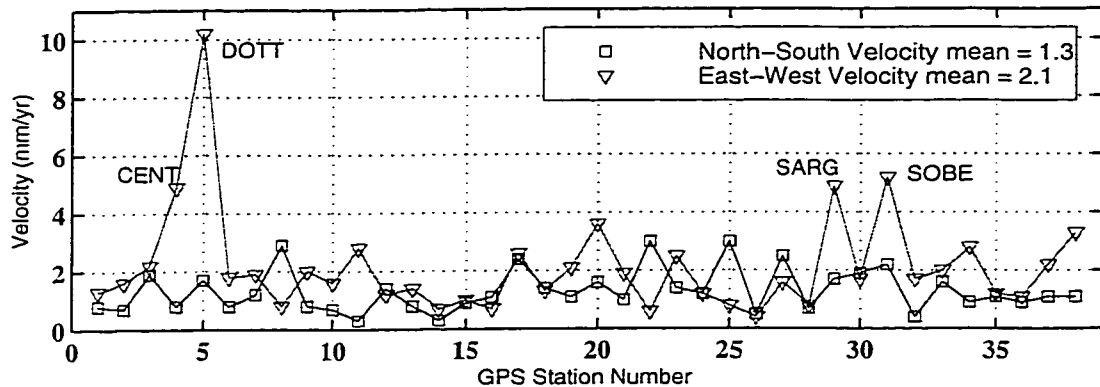
Figure 3.4: Precision of velocity estimates for the "campaign" GPS stations. The adopted values for the precision equal 1σ errors of the slope in the weighted least squares linear regression of individual station time series (Figures C.3 through C.6). Regression was carried out using the Least Squares Spectral Analysis (LSSA) program by *Pagiatakis* (1997). Table D.2 includes station names corresponding to the plotted numbers.

It should be emphasized that the discussion above is concerned with the precision in GPS station *position* estimates and not of their *velocities*. The velocities are determined by linear regression of individual station coordinate components and the uncertainties associated with the velocity estimates are expressed by the standard error of the slope (denoted as 1σ in Tables 3.1, D.1 and D.2). Mean values of 1σ standard errors for the north-south and east-west components of velocity estimates are equal to: 0.20 and 0.24 mm/yr for the continuous stations (Figures 3.3), and to 1.3 and 2.1 mm/yr for the "campaign" stations (Figure 3.4). The reason for almost an order of magnitude difference between the achieved precision for the continuous and the "campaign" stations is due to the fact that throughout this study I have assumed that position estimates are statistically uncorrelated in time and thus, measurement errors can be characterized by a pure white noise model. *Zhang et al.* (1997) have shown that in the case of uncorrelated errors, the velocity uncertainty σ_{wn} can be expressed as follows:

$$\sigma_{wn} = \frac{a_{wn}}{T}\sqrt{\frac{12(N-1)}{N^2 + N}} \approx \frac{2 \cdot a_{wn} \cdot \sqrt{3}}{T \cdot \sqrt{N}} \qquad N \gg 2 \qquad \text{(EQ 3.2)}$$

where a_{wn} is the white noise magnitude (usually of the order 1 mm or less), T is the observation interval (e.g. 2-3 years), and N represents number of measurements.

The presence of the $N^{1/2}$ term in the denominator of Equation 3.2 explains the degraded precision of the velocity estimates from the "campaign" measurements compared to the velocities estimated from observations at continuous GPS stations.

Based on investigations of continuous GPS time series *Zhang et al.* (1997) and *Mao et al.* (1999) concluded that GPS measurements can not be characterized only by the white noise model, and it more appropriate to describe noise characteristics of GPS measurements as a combination of white noise (σ_{wn}) and random walk (σ_{rwn}) models:

$$\sigma = \sigma_{rwn} + \sigma_{rwn} \qquad \text{(EQ 3.3)}$$

In the case of random walk noise *Zhang et al.* (1997) have shown that the velocity uncertainty σ_{rwn} is equal to:

$$\sigma = \frac{b_{rwn}}{\sqrt{T}} \qquad \text{(EQ 3.4)}$$

where b_{rwn} is the magnitude of the random walk noise which can range from 1.3 to 4 mm/yr$^{1/2}$ (e.g. *Langbein and Johnson*, 1997). Since the Equation 3.4 does not include a term N, the velocity uncertainty σ_{rwn} in the presence of random walk noise is independent of number of observations. Hence, even if the GPS observations are made daily for more than two years duration (as is the case with PANGA continuous stations analyzed in this study) the inclusion of colored (time-correlated) noise, such as flicker or random walk models, leads up to factors of 5-11 increase in velocity error estimates as opposed to when only white noise errors are used (*Mao et al.*, 1999). For the continuous GPS station velocity estimates presented in this study this effect would translate to uncertainties of the order of 1-2 mm/yr, which can still be considered as a satisfactory level of precision to study deformations exceeding 2-3 mm/yr.

3.3 Velocity Field

This section includes a presentation of estimated station velocities for the entire set of 44 stations considered in this study (6 continuous and 38 "campaign"). Results in this section are presented in the form of maps where the horizontal velocities are pictured as vectors with error ellipses at their tip. Actual values of the estimated velocities and their 1σ errors and rms scatter are presented in Tables D.1 and D.2.

All the velocities presented in this section and Appendix D are given relative to the IGS station DRAO, located in Penticton, Canada (see Figure 3.5 for its location). Velocity of DRAO, determined by weighted least squares linear regression on position time series shown in Figure C.1, is given in Table 3.1 below. The details of the procedure used to estimate velocities are documented in the *post-processing* part of section 2.4.2.

Table 3.1: Velocity of reference station DRAO in Penticton, Canada.

Reference Frame	North (mm/yr)			East (mm/yr)			Vertical (mm/yr)		
	V	$1\sigma^c$	rms^d	V	1σ	rms	V	1σ	rms
ITRF96[a]	-11.2	0.2	2.3	-11.4	0.2	2.7	1.5	0.3	4.3
NNR-NUVEL-1A[b]	-15.8	--	--	-13.3	--	--	0	0	0

a. Velocity in ITRF96 absolute reference frame estimated as described in the post-processing part of section 2.4.2 and Tables B.2 and B.3
b. Velocity in NNR-NUVEL-1A (*Argus and Gordon*, 1991) reference frame calculated with an euler pole for the North America plate given in Table 2.7.
c. 1σ is an uncertainty of velocity estimates in mm/yr.
d. rms is a weighted root mean square in mm.

First I will present results based on the analysis of the 6 continuous GPS stations located within the study area: ALBH, FTS1, NEAH, RPT1, SEAT and WHDI, plus station DRAO. All 7 stations are listed in shaded cells of Table A.2. As mentioned earlier in chapter II, these stations are part of a larger PANGA network which presently includes more than two dozen continuously recording GPS stations located within the study area (Figure 2.6). However, only 6 of these stations have been operational long enough (more than 2 years) to determine their velocities with a satisfactory precision. Hence, I have limited the discussion only to these 6 continuous GPS stations.

Horizontal velocities estimated for the continuous GPS stations analyzed in this study are shown as red vectors in Figure 3.5. The same figure also includes estimated vertical deformation rates. General features of the observed velocity field are relatively simple: the direction of estimated horizontal velocities is roughly parallel to the JDF/NA relative convergence rate and their magnitude decreases away from the deformation front (Figure 3.5). Maximum horizontal velocities relative to DRAO (i.e. relative to the stable part of the North American continent as discussed in section 2.4.2) are observed at stations along the coast: 10.8±0.3 mm/yr (N57°E±1°) at Neah Bay (NEAH) and 9.4±0.4 mm/yr (N42°E±2°) at Fort Stevens (FTS1). Away from the
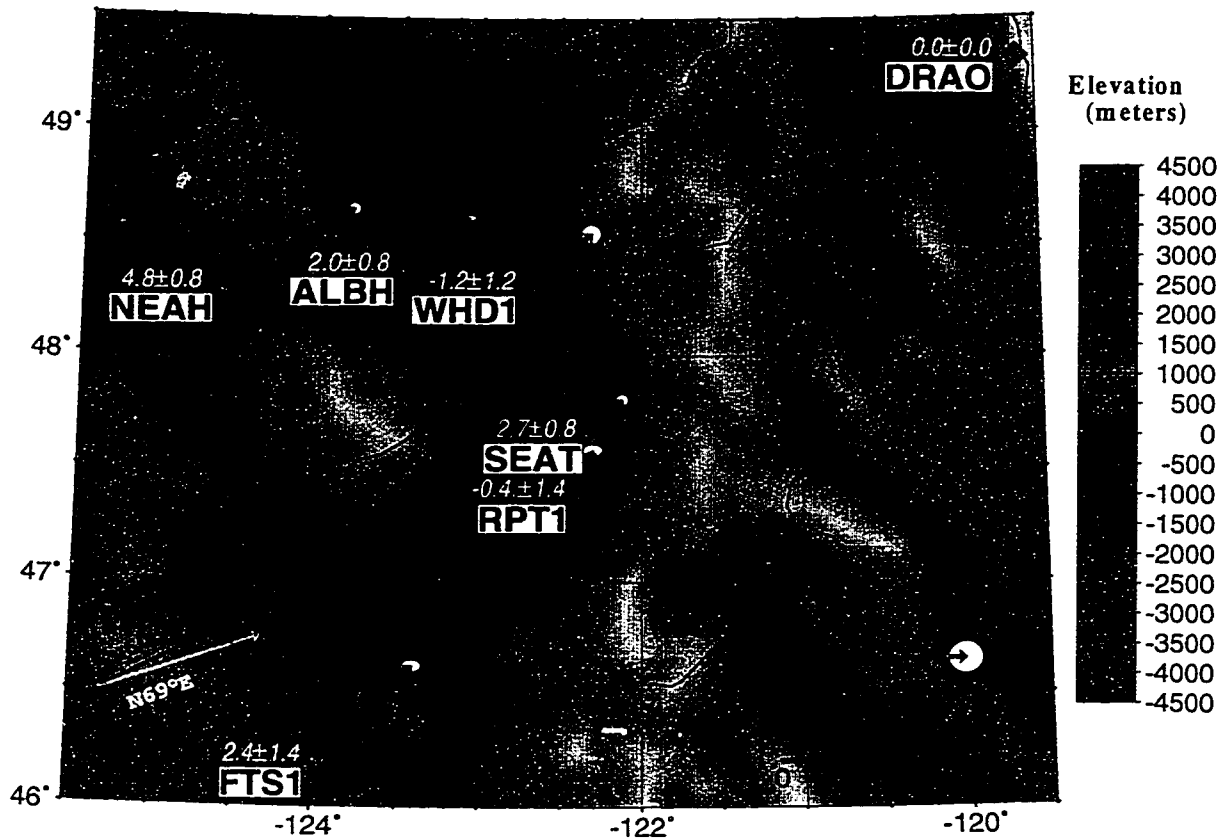
Figure 3.5: Continuous GPS station velocities relative to DRAO. Ellipses   represent   95% confidence limits. Background color depicts surface topography from ETOPO5 (1998) database. Two arrows in the left lower corner of the figure represent the JDF vs. NA plate convergence direction based on: 1) NUVEL-1A (N69°E) model by *DeMets et al.* (1990); 2) *Riddihough* (1984) (N60°E). Note that their scale is different from velocity vectors. Vertical deformation rates with 2σ errors are given above each station name. More information is given in Table D.1.

plate boundary, in the Puget Lowland, velocities decrease to 5.9±0.2 mm/yr (N47°E±4°) at Whidbey Island (WHD1), 3.3±0.3 mm/yr (N39°E±5°) at Seattle (SEAT), and 3.4±0.3 mm/yr (N14°E±6°) at Robinson Point (RPT1). The vertical deformation rates determined by continuous GPS observations presented in Table D.1 (and shown in Figure 3.5), agree reasonably well with the previous measurements of vertical uplift rates discussed in section 1.3.2 *Mitchell et al.*, 1994; *Savage et al.*, 1991) as well as with uplifts predicted by the elastic dislocation model presented in chapter IV (Table D.3). The main discrepancies occur at RPT1 and WHD1, where the model predicts zero uplift, while the data indicate subsidence rates of 2-3 mm/yr. We are not yet certain whether the use of non-choke-ring antennas and/or less stable monumentation at these CORS sites contribute to the above discrepancy.
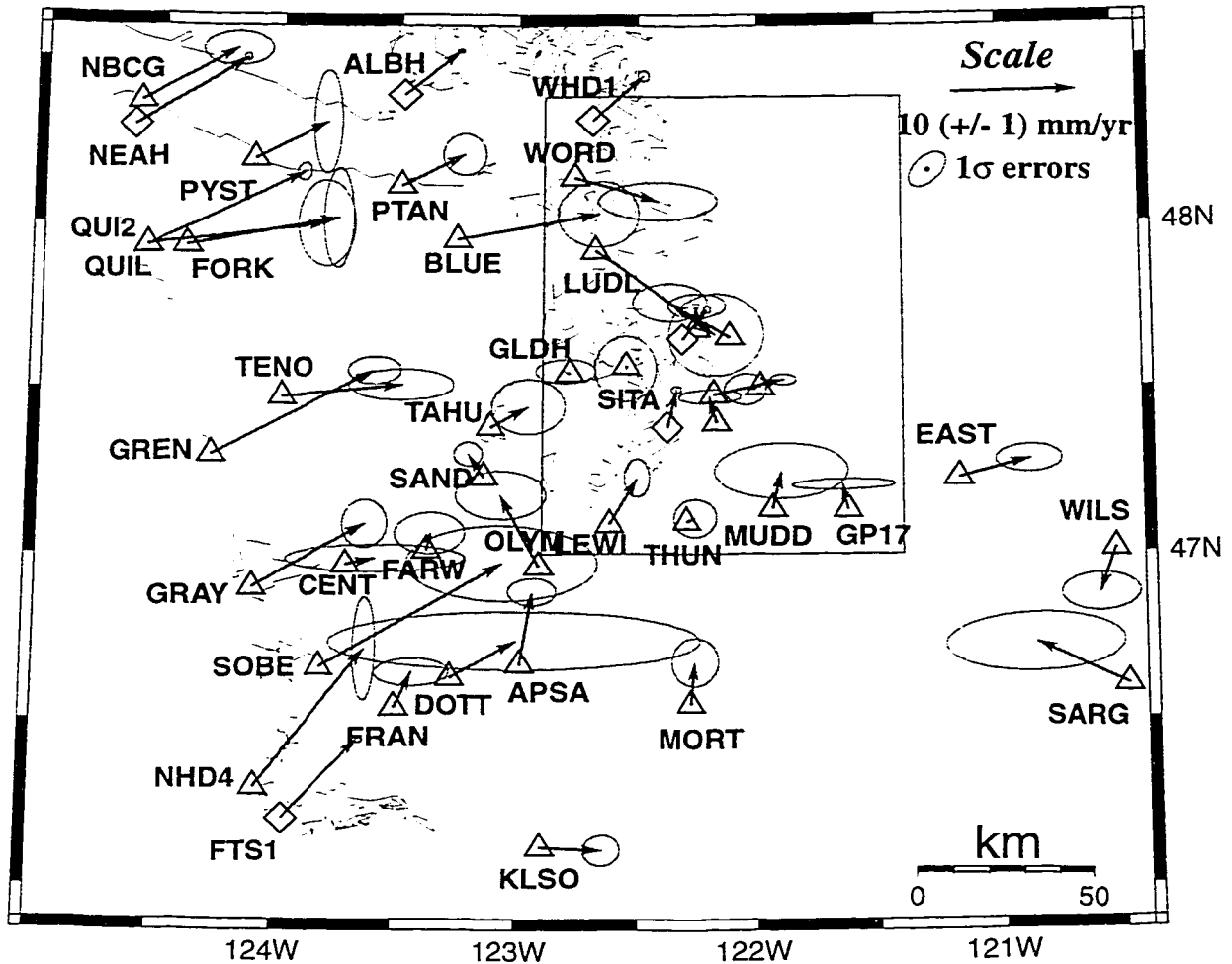
Figure 3.6: Continuous and "campaign" GPS station velocities relative to DRAO. Continuous stations are shown as diamonds and "campaign" stations as triangles. Error ellipses at the tip of each velocity vector represent 68% confidence limits. The box shows the area enlarged in Figure 3.7. Scale of velocity vectors is given in the upper right side of the figure.

Horizontal velocities estimated for the "campaign" and continuous GPS stations are shown in Figures 3.6 and 3.7. General features of the combined velocity field presented in these figures remain the same as for the deformation rates deduced solely from the continuous GPS observations which I have discussed earlier in this section. The biggest difference is in considerably higher errors in velocity estimates for the "campaign" stations which is mainly due to the infrequent observations at these sites (Table A.4), as well as possible problems in site stability and tripod setup errors.
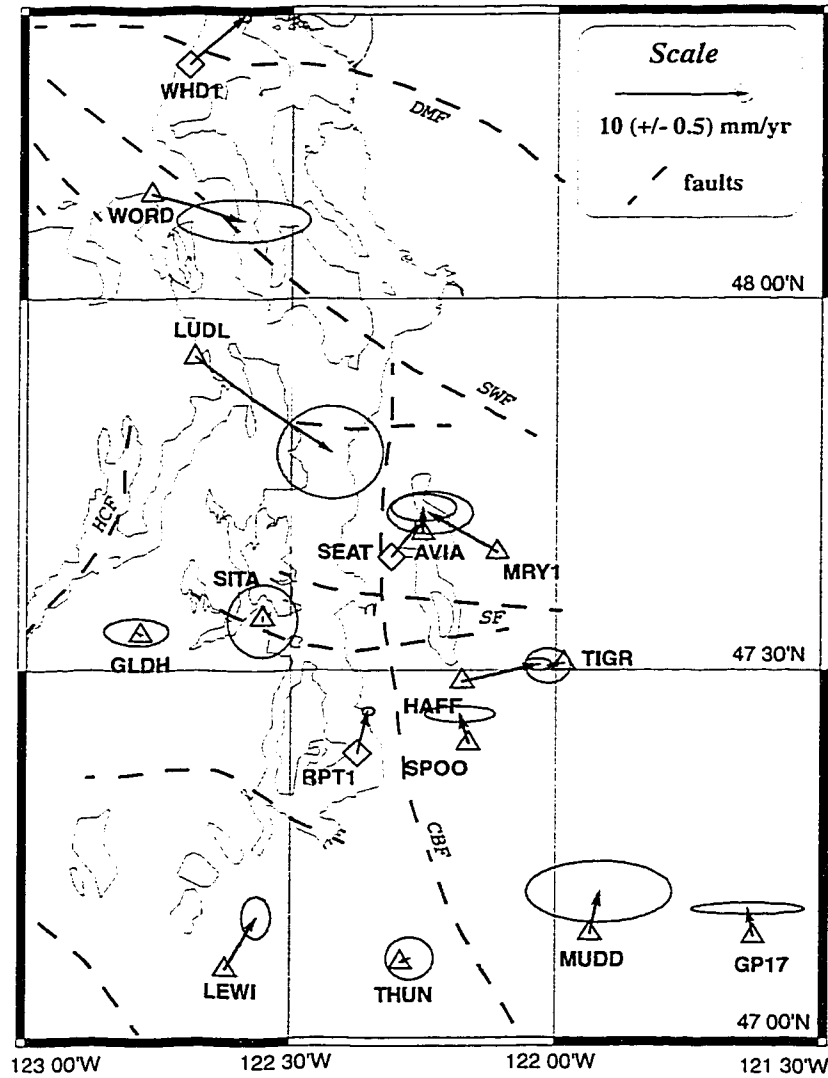
Figure 3.7: Continuous and "campaign" GPS station velocities in the Puget Lowland relative to DRAO. Error ellipses represent 68% confidence limits. Scale for velocity vectors is given in the upper right corner of the figure. Note: scale is different from Figure 3.6. Dashed lines show approximate location of Holocene faults adopted from *Johnson et al.* (1996). Abbreviations for faults in *italics* are the same as in Figure 1.5: *CBF* = Coast Range Boundary Fault; *DMF* = Devils Mountain Fault; *HCF* = Hood Canal Fault; *SF* = Seattle Fault; *SWF* = Southern Whidbey Island Fault.

As mentioned earlier, estimated horizontal velocities decrease away from the coast (i.e. perpendicular to the CSZ deformation front) which indicates the on-going strain accumulation in that direction.

To better illustrate this point, Figure 3.8 shows individual station velocity components plotted as a function of station latitude and longitude. As expected, the highest gradient is observed in plots of the east-west component of velocities versus station longitudes (Figure 3.8d). The calculated slope of -3.39±0.29 mm/yr/degree corresponds to an average east-west strain rate of -0.031±0.003 μstrain/yr (compression[2]). However, since the relative motion between the JDF and NA plates is not oriented east-west but N60°E (*Riddihough*, 1984), relative compression shown in Figure 3.8b might represent an underestimation of the maximum compression. It is more appropriate to plot the component of the horizontal velocity in the direction of the JDF and NA relative plate motion (i.e. N60°E) as a function of distance from the CSZ deformation projected along the same direction. This is illustrated in Figure 3.9. Indeed, the strain rate in the direction of relative plate motion shown in Figure 3.9b is higher than the one estimated for the east-west component of the velocity shown in Figure 3.8. The estimated rate of -0.043±0.006 μstrain/yr also agrees very well with the formal estimate of maximum principal strain rate estimate for the study area presented in the following section.

Regarding the north-south component velocities, no obvious change in the north-south velocity component is observed with increasing latitude: a slope of -0.46±0.34 mm/yr/degree corresponding to approximately -0.004±0.003 μstrain/yr (Figure 3.8a). However, the dependence between the north-south velocities and station longitudes is clear (Figure 3.8b): -1.35±0.21 mm/yr/degree corresponding to approximately -0.012±0.002 μstrain/yr. This trend most likely is due to the not strictly east-west oriented direction of the JDF/NA relative convergence direction and thus, similar to the observed slope in the east-west component velocities, represents the signal of inter-seismic strain across the locked subduction thrust. In chapter V I present a "residual" velocity field (data minus model) in order to investigate the presence of additional north-south compression in the observed velocities, possibly representing a long-term deformation pattern related to margin parallel migration of the forearc (e.g. *Wang*, 1996; *Wells et al.*, 1998).

To summarize, most of the observed crustal deformation in western Washington can be attributed to subduction of the Juan de Fuca plate under North America, where the thrust fault is locked and elastic strain accumulates towards the next subduction earthquake. More detailed discussion of

---

2. Note that this value does not represent a "formal" strain estimate. See section 3.4 for formal calculations of strain.
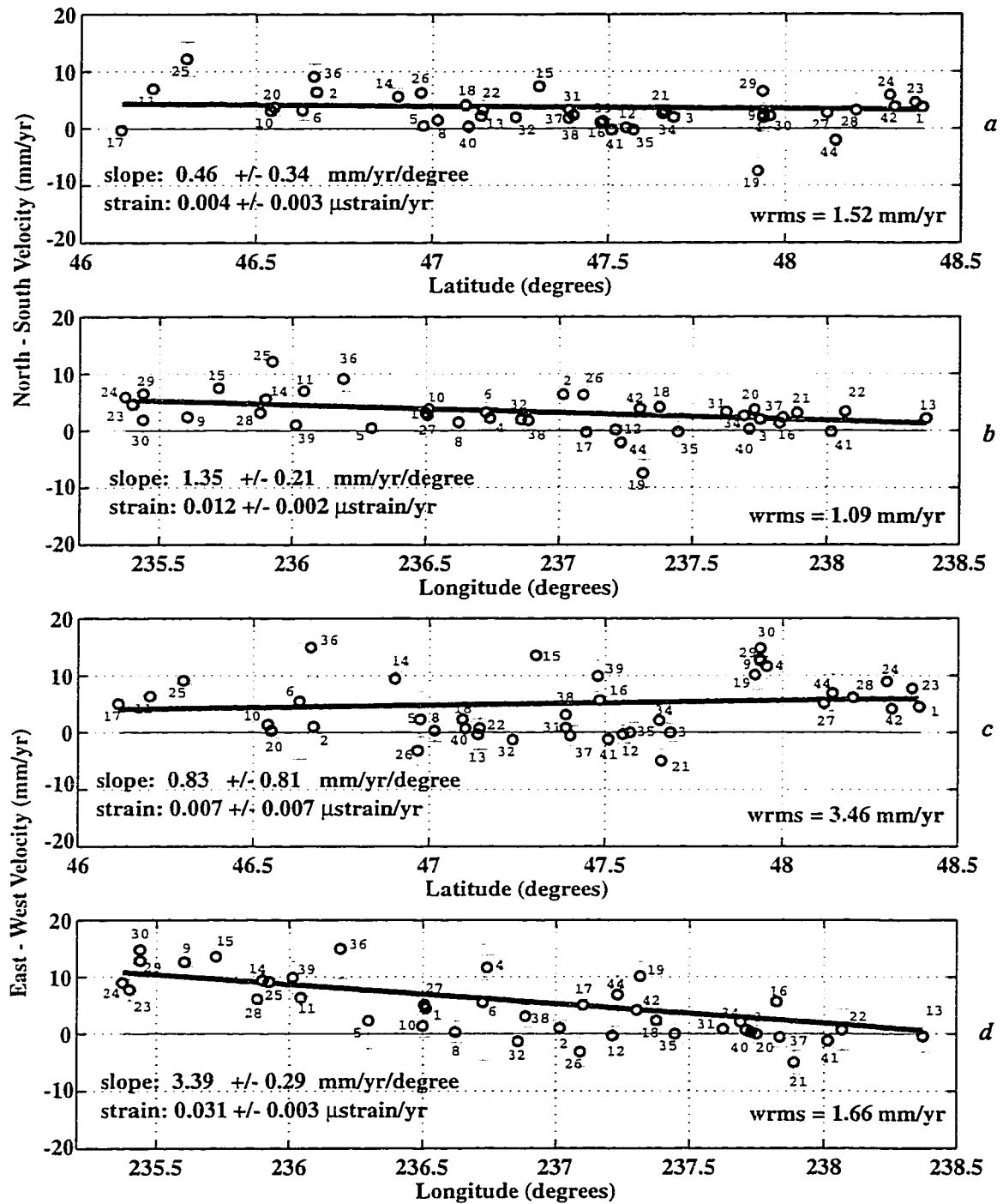
Figure 3.8: North-south and east-west velocity components as a function of station latitude and longitude. Error bars are based on GIPSY formal errors. Error of the slope represents one standard deviation. For station names corresponding to the plotted numbers refer to Table D.3. Regression was carried out using the Least Squares Spectral Analysis (LSSA) program by *Pagiatakis* (1997).

the observed crustal deformation rates will follow in chapter V after I present the elastic dislocation model of the CSZ subduction and its predicted velocities in chapter IV.
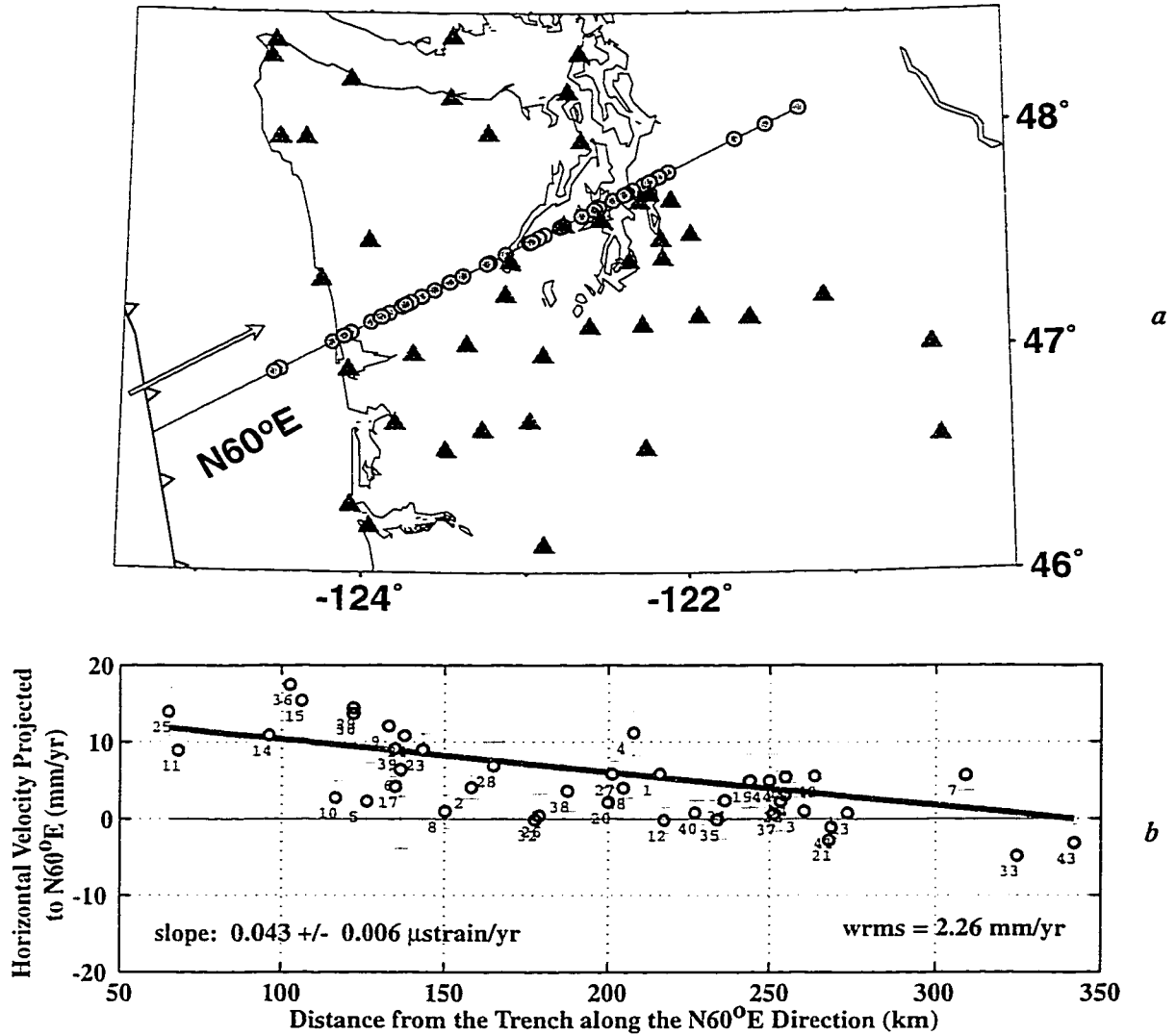
Figure 3.9: Horizontal velocities projected along the JDF/NA relative plate motion direction. Figure *a* includes GPS station locations shown as triangles and the projected points along the profile centered on Seattle and oriented N60°E shown as circles. Error of the slope represents 1σ standard error (units are: μstrain/yr). For station names corresponding to the plotted numbers refer to Table D.3. Regression was carried out using the Least Squares Spectral Analysis (LSSA) program by *Pagiatakis* (1997).

3.4 Strain Determination

3.4.1 Introduction

One of the main advantages of using GPS technology for deformation measurements, as opposed to conventional geodetic techniques (e.g. trilateration), is the ability of determining absolute displacement vectors, consisting of three types of motions: rotation (Θ), translation (C) and strain (ε) (*Dixon*, 1991). In the following two sections I provide an outline of the basic theory behind strain, rotation and translation calculations from velocities and then I present actual estimates of these quantities in the study area based on GPS observations.

3.4.2 Basic Theory

Since this study is mainly concerned with the estimation of horizontal deformation rates, I will limit the discussion to two-dimensions, that is vertical deformation is ignored. Most of the formulation given below is adopted from *McKenzie and Jackson* (1983) and *McCaffrey* (1998). More detailed formulation can be found in *Malvern* (1969).

Displacement vector y between the two points on the earth at time t can be related to the initial vector at t=0 by the following relationship:

$$y(t) = F(t) \cdot y(0) \qquad \text{(EQ 3.5)}$$

where F is a deformation gradient tensor. If we assume that the velocity gradient tensor (L) is constant throughout the deforming region at all times, F can be related to L as follows:

$$\frac{dF}{dt} = L \cdot F \qquad \text{(EQ 3.6)}$$

where L is velocity gradient tensor:

$$L = \begin{bmatrix} \dfrac{\partial V_x}{\partial x} & \dfrac{\partial V_x}{\partial y} \\ \dfrac{\partial V_y}{\partial x} & \dfrac{\partial V_y}{\partial y} \end{bmatrix} \qquad \text{(EQ 3.7)}$$

V_x and V_y in Equation 3.7 are x and y components of the velocity (e.g. North and East). By integrating Equation 3.6 using Equation 3.7 we get expressions for V_x and V_y velocity components:

$$V_x(x, y) = \left(\frac{\partial V_x}{\partial x}\right) \cdot x + \left(\frac{\partial V_x}{\partial y}\right) \cdot y + C_x \qquad \text{(EQ 3.8)}$$

$$V_y(x, y) = \left(\frac{\partial V_y}{\partial x}\right) \cdot x + \left(\frac{\partial V_y}{\partial y}\right) \cdot y + C_y \qquad \text{(EQ 3.9)}$$

where C_x and C_y represent rigid body translation relative to the origin of the coordinate system (i.e. center of mass) in x and y directions, respectively.

Horizontal translation vector C can be expressed in terms of its absolute value C and corresponding angle C_α which can be obtained from C_x and C_y as follows:

$$C = \sqrt{C_x^2 + C_y^2} \qquad \text{(EQ 3.10)}$$

$$C_\alpha = \text{atan}\left(\frac{C_y}{C_x}\right) \qquad \text{(EQ 3.11)}$$

If velocities are known at more than three points, Equations 3.8 and 3.9 can be used to estimate components of the velocity gradient tensor L. Usually, this is achieved by using a weighted least squares procedure, where GPS estimated velocities are weighted by their uncertainties. From L we can find normal ($\dot{\varepsilon}_{xx}$, $\dot{\varepsilon}_{yy}$) and shear ($\dot{\varepsilon}_{xy}$) components of the strain rate as follows:

$$\dot{\varepsilon}_{xx} = \frac{\partial V_x}{\partial x} \qquad \text{(EQ 3.12)}$$

$$\dot{\varepsilon}_{yy} = \frac{\partial V_y}{\partial y} \qquad \text{(EQ 3.13)}$$

$$\dot{\varepsilon}_{xy} = \frac{1}{2}\left(\frac{\partial V_x}{\partial y} + \frac{\partial V_y}{\partial x}\right) = \dot{\varepsilon}_{yx} \qquad \text{(EQ 3.14)}$$

The rigid body rotation rate ($\dot{\omega}$) around the z-axis is related to the velocity gradient tensor components as follows:

$$\dot{\omega} = \frac{1}{2}\left(\frac{\partial V_x}{\partial y} - \frac{\partial V_y}{\partial x}\right) = -\dot{\omega}_{xy} \qquad \text{(EQ 3.15)}$$

Using normal and shear strain rates, $\dot{\varepsilon}_{xx}$, $\dot{\varepsilon}_{yy}$ and $\dot{\varepsilon}_{xy}$, it's possible to find an orientation where no shear forces are exerted on the surface (*Turcotte and Schubert*, 1982). These are called the

principal strain rates and are denoted as: $\dot{\varepsilon}_1$ and $\dot{\varepsilon}_2$. Principal strain rates can be calculated from $\dot{\varepsilon}_{xx}$, $\dot{\varepsilon}_{yy}$ and $\dot{\varepsilon}_{xy}$ as follows:

$$\dot{\varepsilon}_1 = \frac{\dot{\varepsilon}_{xx} + \dot{\varepsilon}_{yy}}{2} + \left[\frac{(\dot{\varepsilon}_{xx} - \dot{\varepsilon}_{xx})^2}{4} + \dot{\varepsilon}_{xy}^2 \right]^{1/2} \qquad \text{(EQ 3.16)}$$

$$\dot{\varepsilon}_2 = \frac{\dot{\varepsilon}_{xx} + \dot{\varepsilon}_{yy}}{2} - \left[\frac{(\dot{\varepsilon}_{xx} - \dot{\varepsilon}_{xx})^2}{4} + \dot{\varepsilon}_{xy}^2 \right]^{1/2} \qquad \text{(EQ 3.17)}$$

The direction of the principal strain rate axis $\dot{\varepsilon}_2$, denoted as Θ, can be obtained from $\dot{\varepsilon}_{xx}$, $\dot{\varepsilon}_{yy}$ and $\dot{\varepsilon}_{xy}$ normal and shear strain rates as follows:

$$\Theta = \frac{1}{2} \text{atan}\left(\frac{2 \cdot \dot{\varepsilon}_{xy}}{\dot{\varepsilon}_{xx} - \dot{\varepsilon}_{yy}} \right) \qquad \text{(EQ 3.18)}$$

In the following section I present calculations of principal strain rates for the study area based on GPS estimated deformation rates, adhering to the same notation as outlined in this section. Equations for calculating normal and shear strain rates from on principal strain rates can be found in *Turcotte and Schubert* (1982).

3.4.3 Regional Strain Calculation

Using GPS estimated velocities for 44 stations in western Washington I have used a computer program called "*strain_m*" (*Wang and Dragert*, 1998) to calculate principal horizontal strain rates in the study area. The "*strain_m*" program is based on equations presented in the previous section. Site positions are first converted into a geocentric (x, y, z) coordinate system assuming a spherical earth. A local two-dimensional coordinate system (x = east and y = north) is established in the plane perpendicular to the center vector of the network. The center of the network is taken as the origin. Using north and south component velocity estimates and errors at three or more stations, a system of linear equations (similar to Equations 3.8 and 3.9 given in the previous section) is formed. In the case of four or more stations, this represents an overdetermined weighted least-squares problem, which is solved using Cramer's rule (*Grossman*, 1991).

The strain calculation is based on the assumption that the estimated velocity at each site remains constant throughout the observation period (i.e. 2-3 years). Calculated strain rates represent an average strain field over the entire net. This approach can only be justified if the entire region deforms uniformally (i.e. the four derivatives constituting the velocity gradient tensor *L* (Equation

Table 3.2: Description of subregions used in strain calculation.

#	Name	Description	N[a]	Center of the Net	
				Latitude	Longitude
1	*ALL*	continuous and "campaign" stations	44	47.356	-122.999
2	*PANGA*	continuous GPS stations only	6	47.708	-123.242
3	*A*	south-west coast; continuous and "campaign"	10	46.801	-123.806
4	*B*	north-west coast; continuous and "campaign"	8	48.148	-124.230
5	*C*	north Puget Lowland; continuous and "campaign"	4	48.083	-122.852
6	*D*	central Puget Lowland; continuous and "campaign"	19	47.227	-122.447

a. Number of GPS stations within the subregion.

3.7) remain constant). Obviously, in an active tectonic region such as western Washington State, this is not necessarily the case. For this reason, I have divided the study area into four subregions: *A*, *B*, *C* and *D*. In addition, I calculated strain rates from velocities estimated for two more subsets of stations: 1) using the entire set of 6 continuous and 38 "campaign" GPS station velocities (ALL); 2) and using only continuous GPS stations (PANGA). Strain estimates and the station locations that constitute each subregion are shown in Figure 3.10. Additional information on subsets of stations is given in Table 3.2. Numerical results of principal strain rates, rigid body rotations and translations with 1σ standard errors are listed in Table 3.3. Below I will discuss the calculations for each of the subregions in detail.

The GPS stations constituting four subregions (*A*, *B*, *C* and *D*) were chosen based on their geographic location. I have excluded three stations, EAST, SARG and WILS, located east of the Cascades mountains from the strain calculations presented in this section, since these three stations lie outside the study area. In addition, the velocity estimates for these stations have relatively high uncertainties which contribute to statistically meaningless strain rate estimates (Table D.2).

Subregions *A* and *B* represent southern and northern coastal regions, respectively. The highest strain rates are observed in these subregions: -0.194±0.109 µstrain/yr N77°E±3° in subregion *A* and -0.088±0.012 µstrain/yr N53°E±3° in subregion *B* (Figure 3.10). Two other subregions include stations located more landward in the Puget Lowland. The stations comprising the subregion *C* (BLUE, LUDL, WHD1 and WORD) were grouped together to investigate their "abnormal" behavior. The inspection of the velocity field, shown in Figure 3.6, clearly illustrates

Table 3.3: Regional strain, rotation and translation from GPS velocities[a].

#	Net Name[b]	Principal Strain Rates (μstrain/yr)			Rotation[f] (degree/Ma)	Translation	
		ε_1[c]	ε_2[d]			mm/yr	degree
		$\varepsilon_1 \pm 1\sigma$	$\varepsilon_2 \pm 1\sigma$	$\Theta^e \pm 1\sigma$	$\omega \pm 1\sigma$	$C^g \pm 1\sigma$	$C_\alpha^h \pm 1\sigma$
1	ALL	-0.004 ± 0.005	**-0.048 ± 0.006**	**75 ± 1**	0.7 ± 0.1	5.5 ± 0.1	45 ± 1
2	PANGA	-0.007 ± 0.006	**-0.042 ± 0.006**	**74 ± 1**	0.7 ± 0.1	6.2 ± 0.1	46 ± 1
3	A	-0.023 ± 0.084	**-0.194 ± 0.109**	**77 ± 3**	3.3 ± 0.5	6.9 ± 0.7	56 ± 5
4	B	0.037 ± 0.023	**-0.088 ± 0.012**	**53 ± 3**	-2.0 ± 0.3	10.8 ± 0.3	60 ± 2
5	C	0.384 ± 0.234	**-0.127 ± 0.258**	**67 ± 5**	2.8 ± 2.5	8.3 ± 1.1	98 ± 6
6	D	0.024 ± 0.045	**-0.005 ± 0.036**	**16 ± 6**	0.1 ± 0.2	3.2 ± 0.2	33 ± 4

a. Note: although variables listed in this table (ε, Θ, ω, C) do not have dots on top of them, they represent time derivatives (i.e. rates).

b. See Table 3.2 for more details.

c. Minimum principal strain rate in μstrain/yr. Positive value is extension represented by outward pointing arrows.

d. Maximum principal strain rate in μstrain/yr. Negative value is compression represented by inward pointing arrows.

e. Azimuth of ε_2 in degrees measured clockwise from North with 1σ errors.

f. Rigid body rotation in degrees/million-years measured clockwise from North with 1σ errors. See Equation 3.15 for the derivation of ω.

g. Rigid body translation with 1σ errors. See Equation 3.10 for the derivation of C.

h. Rigid body translation azimuth in degrees measured clockwise from North with 1σ errors. See Equation 3.11 for the derivation of C_α.

the fact that three (BLUE, LUDL, WORD) out of four stations from subregion C are obvious outliers. The calculated strain rate for the subregion C further illuminates this point. The maximum principal strain rate in this region (0.384±0.234 μstrain/yr N-23°E±5°) is several times higher than in the other subregions and it represents *extension* (positive strain rate), as opposed to the *compression* as in the other subregions (except the subregion D, see the following discussion).

The subregion D includes stations located in the Puget Lowland (excluding stations from the subregion C). The strain rate estimate for this region is somewhat abnormal as well: similar to the subregion C, the largest measured strain rate is *extensional* (i.e. $|\dot{\varepsilon}_1| > |\dot{\varepsilon}_2|$): 0.024±0.045 μstrain/ yr N106°E±6°. However, the large errors in this estimate leaves the actual strain rate essentially unresolved.

Stations constituting the final two subsets, ALL and PANGA were chosen on the basis of the types of observations. The first subset (ALL) includes the entire set of 44 stations: 6 continuous

and 38 "campaign" GPS stations, including three stations located east of the Cascades[3]. The second subset (PANGA) includes only the continuous GPS stations (Table D.1). The strain estimates for the two subsets are very similar. Maximum principal strain rate estimates ($\dot{\varepsilon}_2$) for ALL and PANGA subregions equal -0.048±0.006 μstrain/yr N75°E±1° and -0.042±0.006 μstrain/ yr N74°E±1°, respectively. Minimum principal strain rate ($\dot{\varepsilon}_1$) estimate for the both regions is approximately zero, indicating uniaxial compression.

Comparison of strain rate estimates for individual subregions presented above with rates estimated by previous investigators (Table 1.3) leads to a mixed picture. For example, the strain rate estimates for the subregion B in the south-west corner of the study area (-0.09±0.01 μstrain/yr N53°E±3°) and the Juan de Fuca (*Lisowski et al., 1989*) (-0.18±0.04 μstrain/yr N64°E±5°) and the Olympic (*Savage et al.,* 1991) networks (-0.09±0.03 μstrain/yr N59°E±7°) compare satisfactorily. However, the match further landward, in the Puget Lowland, is less satisfactory: the -0.04±0.01 μstrain/yr N68°±6°E strain rate reported by *Savage et al.* (1991) in the Seattle net does not match well with the strain rate estimate for the subregion D: (-0.01±0.04 μstrain/yr N16°E±6°). The discrepancy is especially large for in the estimated *directions* of the principal strain rates.

Chapter V will include further discussions on the estimated strain rates, including a discussion on estimated rates of rigid body rotations presented in Table 3.3.

---

3. I have performed tests with and without stations to the east of the Cascades, and not surprisingly they do not have a significant influence on the calculated strain parameters.
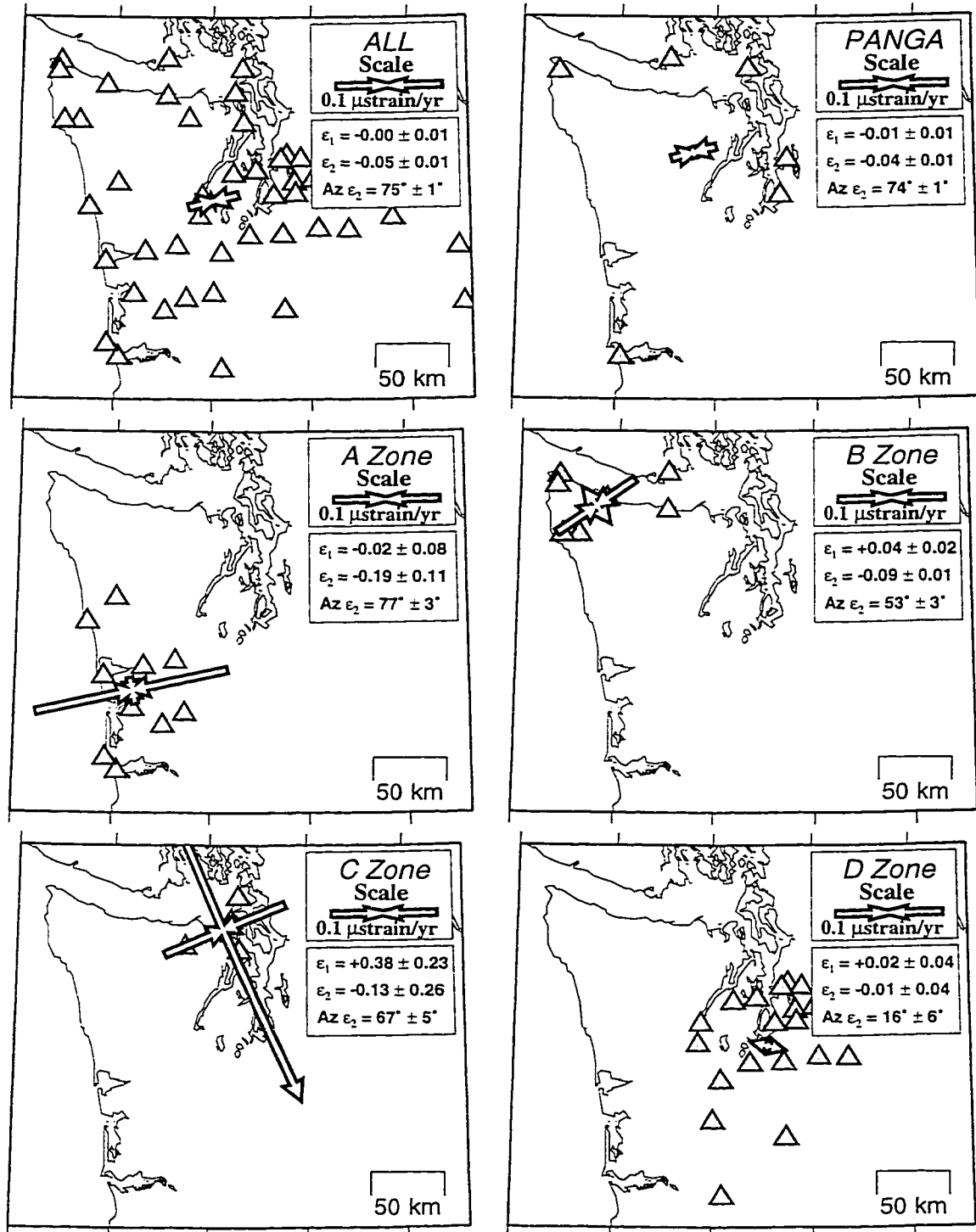
Figure 3.10: Horizontal strain rates in western Washington based on subsets of GPS data. Triangles represent GPS stations constituting the subregion. ε_1 and ε_2 are maximum extensional and compressional strain rates. Strain crosses are located at the center of an individual subregion. See Tables 3.2 and 3.3 for more information.

IV. Dislocation Model

4.1 Introduction

In order to properly interpret the tectonic significance of observed crustal deformation, I have used a three-dimensional model of the Cascadia subduction zone based on elastic dislocation theory. Before I present the details of the modeling technique used in this study and compare predictions of the "preferred" model with the observed velocities in section 4.4, first I will describe the basic theory behind the elastic dislocation modeling of surface deformation (section 4.2), and then present an overview of previous work concerning the surface deformation modeling along the CSZ using elastic dislocation theory (section 4.3).

4.2 Basic Theory

The first application of elastic dislocation theory in modeling of surface displacements is attributed to *Steketee* (1958a; 1958b), who has shown that the displacement field $u_i(x_1, x_2, x_3)$ due to a dislocation $\Delta u_j(\xi_1, \xi_2, \xi_3)$ across a surface Σ in a uniform elastic half-space can be given by Volterra's formula:.

$$u_i = \frac{1}{F} \iint_\Sigma \Delta u_j \left[\lambda \delta_{jk} \frac{\partial u_i^n}{\partial \xi_n} + \mu \left(\frac{\partial u_i^j}{\partial \xi_k} + \frac{\partial u_i^k}{\partial \xi_j} \right) \right] v_k d\Sigma \qquad \text{(EQ 4.1)}$$

where λ and μ are Lamé constants, δ_{jk} is a Kroenecker delta function and v_k is the outward normal vector to surface Σ. u_i^j is the i-th component of displacement at (x_1, x_2, x_3) point due to the j-th point force dislocation of magnitude F at (ξ_1, ξ_2, ξ_3). The coordinate system used in Equation 4.1 is shown in Figure 4.1.

Okada (1985) has presented a comprehensive review of previously conducted work related to elastic dislocation modeling. Using the same Volterra's formula (Equation 4.1) as *Steketee*, he has derived a complete suite of analytic expressions for surface displacements, strains and tilts in three-dimensions for shear and tensile faults. Since then numerous studies have used *Okada's* formulations for modeling surface deformations associated with co-seismic displacements (e.g. *Murray et al.*, 1996), inter-seismic strain accumulation at subduction zones (e.g. *Verdonck*, 1995) or volcanic dyke intrusions (*Okada and Yamamoto*, 1991).
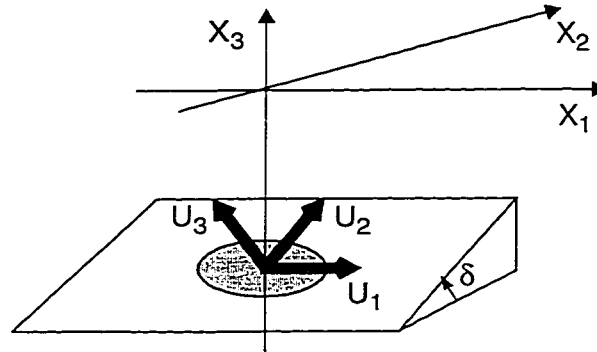
Figure 4.1: Point source representation on a fault surface. U_1, U_2 and U_3 vectors represent the movement of a hanging wall relative to the foot wall for strike-slip, dip-slip and tensile components of elementary dislocations on the fault surface. X_1 is oriented parallel to the strike of the fault. The medium where $X_3 \leq 0$ represents an elastic half-space. δ is the fault dip angle. Figure adopted from *Okada* (1985).

4.3 Previous Dislocation Models for the Cascadia Subduction Zone

The first attempt to model contemporary crustal deformation along the Cascadia subduction zone using elastic deformation theory was by *Savage et al.* (1981). In order to interpret strain measurements from repeated trilateration surveys in Washington State, they used the two-dimensional formulation for surface deformation due to dip-slip faulting by *Freund and Barnett* (1976). Crustal displacement estimates are generated by an *edge dislocation*[1] located at the downdip end of the locked zone with its *Burgers vector*[1] oriented in the direction of the dipping thrust plane with a magnitude equal to the fault slip rate.

Later *Savage* (1983) refined his earlier approach by proposing a generalized model of strain accumulation and release at a subduction zone. He introduced a no-slip (i.e. "locking") condition on a shallow portion of the thrust interface between the subducting and over-riding plates (representing the current condition of the CSZ). This was achieved by representing the overall strain accumulation at a subduction zone as the superposition of *steady state* subduction at a constant rate of plate convergence and a *supplemental solution* equivalent to a normal faulting event in the shallow part of the thrust interface. This is shown schematically in Figure 4.2. The principle of superposition requires that both of these solutions behave linearly. According to the same principle, it is possible to use additional supplemental solutions to introduce a transitional

---

1. See *Turcotte and Schubert* (1982) page 311 for the discussion on edge dislocations and associated Burgers vectors.

steady   supplemental   strain
state   solution   accumulation
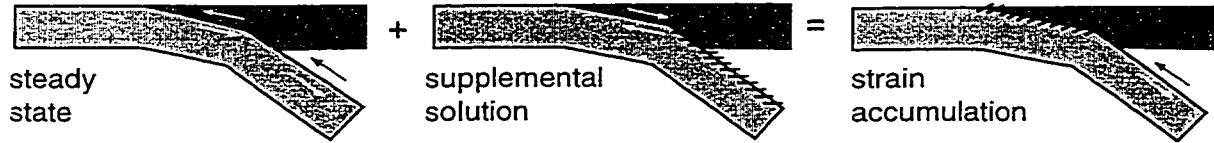
Figure 4.2: Elastic dislocation model of strain accumulation at a subduction zone after *Savage* (1983). Arrows indicate direction of plate movement. Streaked lines represent a hypothetical locked portion of the thrust interface.

zone between the locked and "free" zones on the thrust interface. In this zone, the fault slip increases linearly from zero at the updip end of the transition zone to the plate convergence rate of the steady state subduction at the downdip end of the transition zone (see Figure 4.3 for the schematic illustration). The inclusion of the transition zone eliminates the possibility of an abrupt discontinuity at the downdip end of the locked zone which is physically unrealistic (*Dragert et al.*, 1994).

Savage et al. (1991) included a transition zone in their effort to model subduction related inter-seismic strain accumulation based on the extended set of observations from the Seattle and Olympic Peninsula trilateration networks (see Table 1.3). Their model included the Juan de Fuca plate dipping at 10 degrees and moving towards the NA plate at a rate of 40 mm/yr in the direction of N68°E. The achievement of a reasonably good match with the geodetic data using a dislocation model of subduction with 100 and 75 km wide locked and transition zones respectively, led the authors to the suggestion that subduction along the Cascadia margin is taking place seismically (i.e. is capable of generating large subduction earthquakes).

Later *Hyndman and Wang* (1993), *Dragert et al.* (1994), *Dragert and Hyndman* (1995) and *Hyndman and Wang* (1995) used two dimensional elastic dislocation models to estimate the width and location of the seismogenic zone[2] along several profiles perpendicular to the margin of the CSZ (Figure 4.4). Based on an extended dataset, which included all of the available horizontal and vertical deformation data along the CSZ (summarized in Tables 1.1, 1.2, 1.3 and 1.4) *Hyndman and Wang* (1995) were able to estimate the overall extent of the locked and transition zones along the entire length of the CSZ (shown as dotted lines in Figure 1.4 and as dashed lines in Figure 4.4). This was achieved first by estimating the width of the seismogenic zone for five individual profiles

---

2. *Seismogenic zone* includes locked and transition zones of the plate interface as shown in Figure 4.3.

Volcanic arc

coast

trench

Accretionary prism

Continental crust

100-150C°

350C

450C

Oceanic crust

Mantle

Moho

Seismogenic zone

Seaward free slip zone	Locked zone	Transition zone	Landward free slip zone	
Little motion w.r.t. to NA	No motion accumulation of elastic strain	Rate increases in downdip direction from zero to plate convergence rate	Constant motion at NA vs, JDF plate convergence rate	Interseismic
No seismic initiation most of the total slip deficit is recovered	Earthquake initiation total slip deficit is recovered	Rate decreases in downdip direction from full slip to zero	No motion	Coseismic
Stable sliding	Stick slip, unstable	Stable sliding	Plastic deformation	Mechanism

Figure 4.3: Schematic representation of subduction. The thrust fault is divided into *four* major zones. The main behavioral characteristics of each zone associated with inter-seismic and co-seismic cycles are summarized in the table. The figure is adopted from *Flück* (1996) based on *Hyndman and Wang* (1993).

oriented perpendicular to the deformation front (shown as thin lines in Figure 4.4), and then by interpolating between the individual estimates.

Verdonck (1995) recognized the shortcomings of two-dimensional modeling used in the previous studies and proposed a three-dimensional model using a rectangular source formulation by *Okada* (1985). He used this model to explain the observed north-south variability in vertical uplift rates along the Oregon portion of the CSZ reported by *Mitchell et al.* (1994) (see Figure 1.11). However, since *Verdonck's* (1995) model was based on a rectangular source, it could not account for the complicated geometry of the subducting Juan de Fuca plate. Because the JDF plate arches beneath the Olympic Peninsula (*Weaver and Baker*, 1988), as shown in Figure 4.5, the rectangular source

model cannot be used to further understand the details of contemporary tectonic deformation along the CSZ. With this in mind, *Flück* (1996) and *Flück et al.* (1997) refined the three-dimensional model, and instead of using the rectangular source employed by *Verdonck* (1995), applied *Okada's* (1985) point source solution formulation. This approach enables one to represent the thrust fault more realistically and take into account complications in its geometry. The extent of the locked and transition zones determined by *Flück et al.* (1997) are presented as shaded areas in Figure 4.4. An earlier model of *Hyndman and Wang* (1995) is also shown in this figure for comparison. It is evident that the estimates of the geometry of the seismogenic zone along the CSZ based on two-dimensional (*Hyndman and Wang*, 1995) and three-dimensional models (*Flück et al*, 1997) do not differ significantly from each other. This fact is mainly due to the limited availability of data coverage. However, in the future, as more measurements of crustal deformation (mainly using GPS technology) become available, consequent models may differ greatly. An example of how new data in western Washington affects a "best fitting" model is presented in Figure 4.7 in the next section.

4.4 "Preferred" Model

In this section I present a model of the subducting JDF plate along the western Washington section of the Cascadia subduction zone. I will refer to this model as a "preferred" model, since I have selected it after experimenting with more than a dozen other models by varying various parameters. To calculate deformation rates predicted by the "preferred" model at a given set of GPS stations I have used the program DISL3D, by Kelin Wang of the Pacific Geoscience Centre, Canada. This code represents a modified version of programs written by *Flück* (1996). The main principle of the model (and the code) is based on *Okada's* (1985) formulation for dislocations due to a point source force applied to an infinitesimal surface area Σ as shown in Equation 4.1. The final goal of estimating deformation rates on the surface of the earth is achieved by dividing the fault surface along the thrust interface into numerous small triangular elements (each approximating an infinitesimal surface Σ) and performing summation for all the triangles. Such an approach enables one to account for non-planar fault surfaces, such as the subducting JDF plate, which is known to exhibit upward arching beneath the study area (*Weaver and Baker*, 1988).
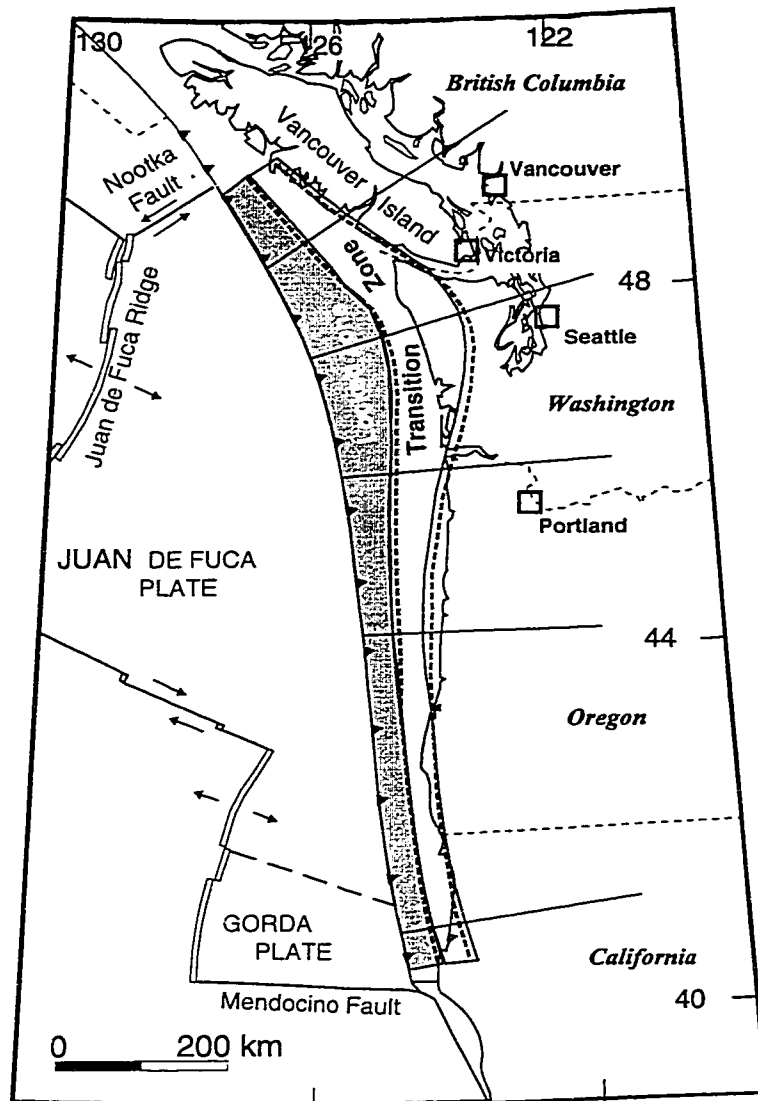
Figure 4.4: The map view of the locked and transition zones along the CSZ. Dashed lines show interpolated boundaries from the previous study by *Hyndman and Wang* (1995) based on two-dimensional elastic dislocation models constructed along the margin-perpendicular profiles shown as thin lines. Figure is adopted from *Flück et al.* (1997).

In the following sections I will first outline the main assumptions (section 4.4.1) and parameters (section 4.4.2) behind the use of elastic dislocation theory in modeling inter-seismic crustal deformation rates. Then I will describe the procedure involved in the construction of the "preferred" model (section 4.4.3). Finally, I will present the comparison of deformation rates predicted by the "preferred" model with the GPS determined tectonic deformation rates reported in chapter III (section 4.4.4).

4.4.1 Main Assumptions

The main assumptions in using elastic dislocation theory to model crustal deformation during the inter-seismic period were summarized by *Flück et al.* (1997). Since these assumptions are valid for the modeling technique presented in this study as well, I re-iterate them below with minor corrections. For some of the assumptions I also provide additional justifications to support their validity.

The main assumptions are:

- Earthquake cycles can be approximated by elastic behavior.

   Although, the real earth is surely not elastic and its visco-elastic properties should also be taken into account for more realistic modeling of surface deformation throughout the earthquake cycle, it has been shown that for modeling deformation rates at the later stages of the inter-seismic period, as is the case for the CSZ (see the discussion in section 1.2.4), elastic dislocation models are adequate (e.g. *Dragert et al.*, 1994; *Wang et al.*, 1994).

- Net permanent deformation throughout the entire earthquake cycle is equal to zero. This implies that all of the strain accumulated throughout the inter-seismic period is released during an abrupt co-seismic rupture on the fault, followed by rapid post-seismic relaxation (see Figure 5.1).

   This assumption is supported by the results of modeling surface deformation along the Nankai subduction zone in southwest Japan, where the geodetic data span the entire seismic cycle (e.g. *Savage and Thatcher*, 1992; *Hyndman et al.*, 1995). In addition, studies of wave-cut shore platforms along the CSZ show that the long-term (~100,000 years) uplift rates average 0.2 mm/yr and do not exceed 1 mm/yr (*Kelsey*, 1990; *Kelsey and Bockheim*, 1994; *Kelsey et al.*, 1994). These rates are an order of magnitude less than present day uplift rates determined from leveling and tide gauge records (see Tables 1.11.2) and continuous GPS observations reported in this study (Table D.1).

- Surface deformation depends directly on fault slip rates which are equal to the plate convergence velocity at the seaward and landward free slip zones (see Figure 4.3).

- Fault slip rates are zero at the locked zone (i.e. plates are fully coupled) and increase landward from zero to the full slip rate (i.e. plate convergence rate) within the transition zone (Figure 4.3).

- Surface deformation rates remain constant throughout the inter-seismic period (i.e. plate convergence rate remains constant).

   See discussion in the "Plate Motions" part of section 4.4.2.

- Widths of the locked and transition zones remain constant throughout the inter-seismic period.

4.4.2 Main Parameters

In my modeling efforts I have incorporated a number of independent geophysical observations. The main independent constraints for the construction of an initial model of the subducting Juan de Fuca plate include: 1) the geometry of the subducting Juan de Fuca plate (i.e. slab geometry) 2) the convergence direction and rate between the JDF and NA plates. In addition, it's important to keep in mind that although I have constrained the width of the seismogenic zone (its updip and downdip limits) along the thrust interface directly from the GPS data, I have also adhered to the constraints imposed by thermal and compositional characteristics of rocks at the thrust interface. Below I will discuss each of the above parameters individually.

JDF Slab Geometry

The geometry of the subducting JDF plate can be divided into *shallow, intermediate* and *deep* parts. The shallow part of the JDF plate extends from the deformation front down to a depth of about 30 km. The location of the deformation front is determined by the studies of ocean floor bathymetry (e.g. *Goldfinger et al.*, 1997).The geometry of the slab is determined from off-shore and onshore seismic reflection/refraction studies (*Taber and Lewis*, 1986; *Stanley et al.*, 1994; *Parsons et al.*, 1998). For the northern part of the CSZ at the latitude of southern Vancouver Island, the geometry of the shallow part of the JDF plate is relatively well constrained by LITHOPROBE deep seismic reflection studies (e.g. *Clowes et al.*,1987; *Clowes et al,* 1995). Along the Washington section of the CSZ the geometry of the shallow part of the JDF subducting slab is not as well known, due to the limited number of offshore and onshore seismic reflection studies conducted in this area (e.g. *Stanley et al.*, 1994). However, in the last year new constraints on the structure of the shallow part of the JDF plate were reported, based on a 530 km long wide-angle onshore-offshore seismic transect at the latitude of Grays Harbour (*Flueh et al.*, 1998; *Parsons et al.*, 1998). The "preferred" model agrees well with the $12°$ dip of the JDF plate beneath the Washington coast reported by *Parsons et al.* (1998).

The intermediate part of the slab, from 30 km to 100 km depth is mainly constrained by locations of intra-slab earthquakes determined by the Pacific Northwest Seismograph Network (*Ludwin et al.*, 1991) (Figures 1.9, 1.10 and 4.5) and by teleseismic receiver function analysis (*Crosson and Owens*, 1987; *Lapp et al.*, 1990; *Cassidy*, 1991; 1995). The latter are summarized in Figure 4.5. The same figure also includes interpolated slab depth contour lines, where the arching of the JDF
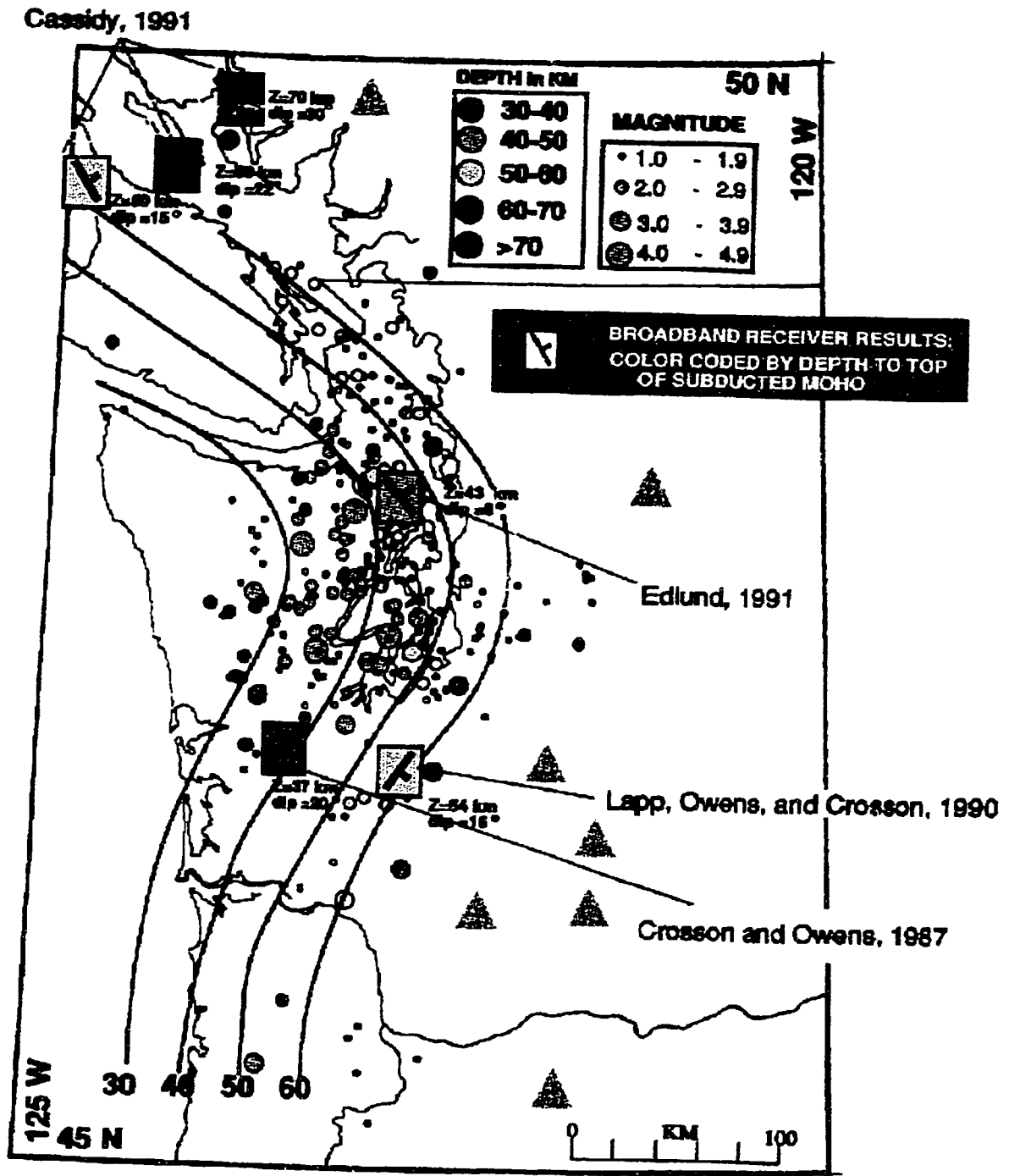
Figure 4.5: Juan de Fuca slab geometry beneath western Washington. 30, 40, 50 and 60 km depth contour lines are based on intra-plate seismicity (shown as circles) and broadband receiver function analysis results (shown as small boxes). Triangles indicate Cascade volcanoes. Figure is a courtesy of Dr. R. S. Crosson (Geophysics Program, University of Washington).

plate beneath the Olympic mountains and the Puget Lowland is apparent (e.g. *Weaver and Baker*, 1988). The intermediate structure of the slab (down to 50 km depth) has also been imaged by wide-angle seismic profiling as reported by *Parsons et al.* (1998).

The deep part of the JDF plate (below ~100 km) can be imaged only with seismic tomography, since earthquakes are not observed below 100 km depth (see Figure 1.10). Tomographic inversion of *P*-wave teleseismic waves have provided evidence that the JDF slab reaches 400-600 km depth beneath Washington (*Rasmussen and Humphreys*, 1988; *Bostock and VanDecar*, 1995). However, for this study the deep structure of the JDF plate is not very important, since the seismogenic zone of the thrust interface does not extend below 50 km, and thus, tectonic deformation of the earth's crust is not influenced by the geometry of the slab below this depth.

Plate Motions

The convergence *rate* and *direction* between the JDF and NA plates represents an important constraint on the dislocation model. Predicted crustal deformation rates and directions depend directly on JDF and NA plate convergence parameters. Unfortunately, the exact value of relative motion between the JDF and NA plates is not known, as evidenced from the following discussion.

Geological estimates of the relative convergence *rate* between the JDF and NA plates, averaged over the past 0.5-6 million years, is approximately 40 mm/yr (*Wilson*, 1983; *Riddihough*, 1984; *DeMets et al.*, 1990; 1994). However, there is a discrepancy in the *direction* of convergence between the estimates proposed by different authors. According to the NUVEL-1A global plate motions model by *DeMets et al.* (1990; 1994), based on spreading rate, transform fault orientation and earthquake slip vector estimates for 12 globally distributed rigid plates, the relative convergence direction between the JDF and NA plates is oriented in the direction N69°E. On the other hand, the direction estimated by *Riddihough* (1984) based on orientation and spacing of magnetic anomalies from the JDF plate system is oriented on average 10° more northward (e.g. N60°E). Figure 1.2 illustrates this discrepancy by presenting the JDF/NA convergence vectors predicted by the two models[3] at a selected set of GPS stations.

---

3. I have used an instantaneous pole of rotation estimated by *Riddihough* (1984) for the last 1 million years (epoch 0.5 Ma in Table 1 on page 6986 of his paper): 29.4°N, 111.7°W and 1.09 °/m.y clockwise.
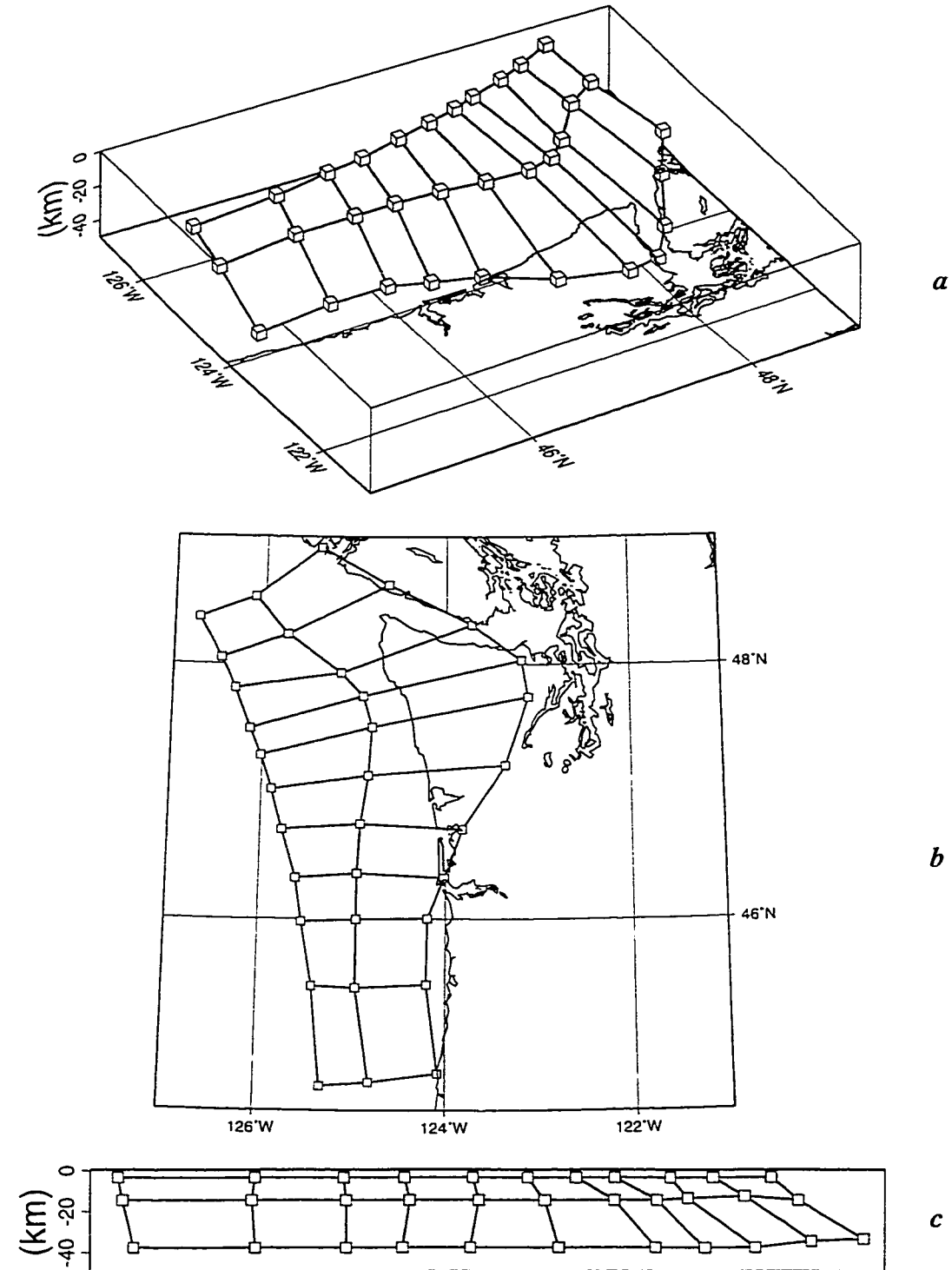
Figure 4.6: "Preferred" model of the seismogenic zone along the western Washington section of the CSZ. *a*: 3-D view; *b*: map view; *c*: North-South cross-section. Nodes of the initial grid are shown as cubes in *a* and squares in *b* and *c*. Dark shaded region is the locked zone and lighter shaded region represents the transition zone.

When considering geologically estimated relative plate motions, one has to keep in mind that the estimates imply a steady plate motion for long periods of time, which is not always the case. For example, *Riddihough* (1984) has shown that in the past 7 million years (Ma), the relative motion of the JDF and NA plates has undergone significant changes. According to his findings, the biggest jump occurred approximately 3 Ma ago and, since then, convergence between the two plates has stayed relatively constant. The location of the instantaneous pole of rotation for the JDF/NA plates estimated by *Riddihough* (1984) for the last 1 Ma agrees well with the location of the NUVEL-1A pole of rotation, even though the latter represents an average over the past 3 Ma (Figure 1.2). This observation suggests that relative motion between the JDF and NA plates for the past 3 Ma has not changed significantly and most likely represents the *present-day* state of plate convergence.

One could test this hypothesis relatively simply if the JDF plate had an island where a continuously recording GPS station could be deployed. But since this is not the case, more sophisticated means of measuring present-day convergence rate between the two plates have to be used. Since 1991 a pilot project has been in progress with the participation of scientists from JPL, SIO and GSC[4] having as its main goal the measurement of the present-day convergence rate of the JDF/NA plates. This is achieved by measuring periodically distances (similar to the "campaign" style GPS observations) between the continuous GPS stations on-land (e.g. ALBH) and special acoustic transponders placed on the sea-floor of the JDF plate (*Chadwell et al.*, 1998). Preliminary results based on observations conducted in 1994, 1995 and 1996 indicate 42±11 mm/yr convergence in the direction of N15°E±38° (*Chadwell et al.*, 1998). This *rate* agrees remarkably well with the geologically estimated rates. However, the *direction* estimated by *Chadwell et al.* (1998) is oriented considerably more northward than suggested by *Riddihough* (1984) and *DeMets et al.* (1990).

In the construction of the "preferred" elastic slip-dislocation model (see section 4.4.3), *Riddihough*'s (1984) convergence parameters have been used for two reasons: 1) The use of convergence parameters estimated directly from local magnetic anomalies in the Juan de Fuca plate is felt to be more accurate than the use of parameters based on global reconstructions of plate

---

4. JPL: Jet Propulsion Laboratory; SIO: Scripps Institute of Oceanography; GSC: Geological Survey of Canada.
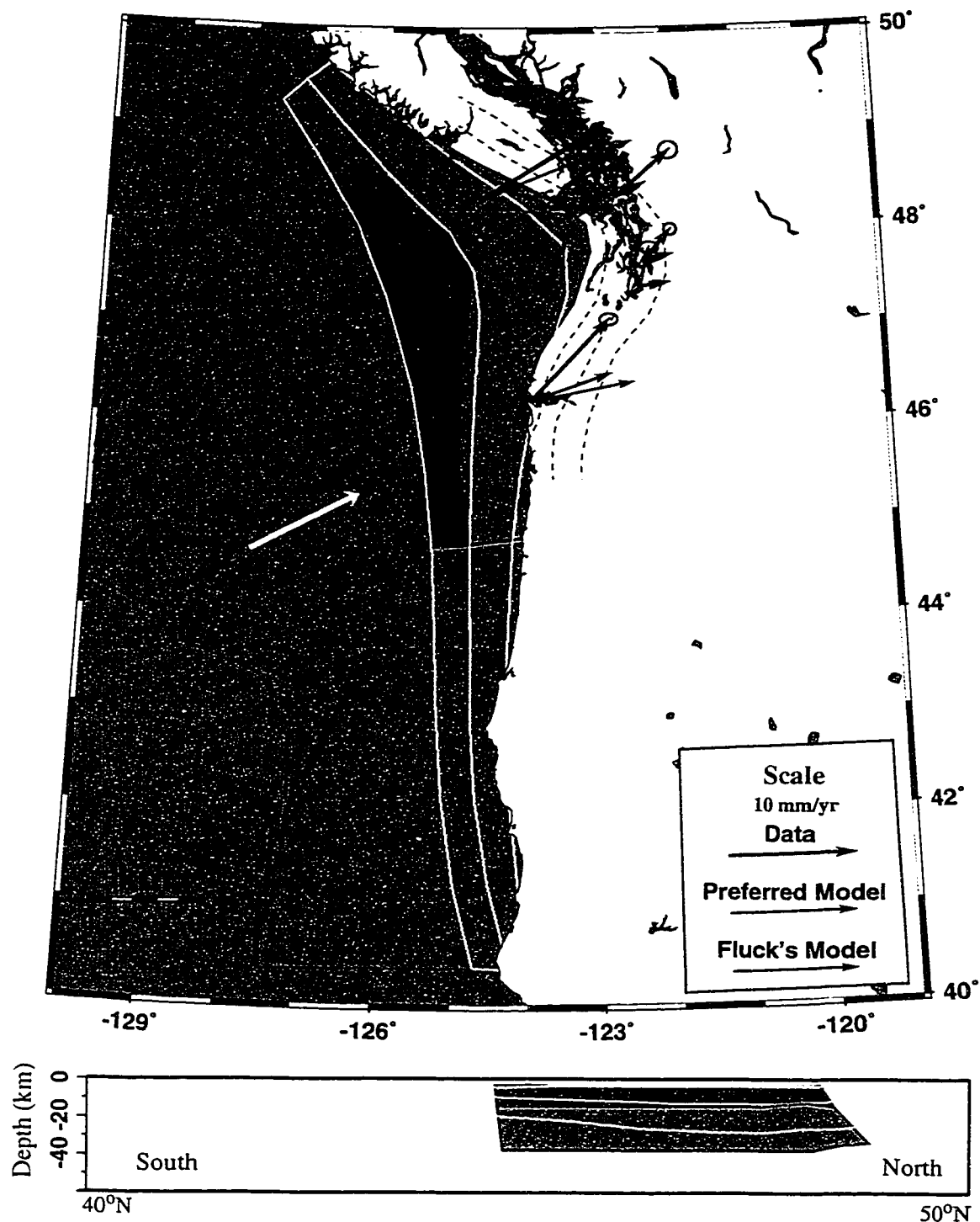
Figure 4.7: Comparison of the "preferred" and *Flück et al.*'s (1997) models. *Flück* model is outlined by yellow lines. Dark and light green shaded areas, outlined by red lines, depict the "locked" and the "transition" zones of the "preferred" model. Thin dashed lines represent an approximate location of the upper surface of the JDF slab at 30 to 60 km depths, based on the data presented in Figure 4.5.

motions of the major crustal plates (e.g. NUVEL-1A model by *DeMets et al.* (1990)); 2) Preliminary modeling results for the Cascadia locked subduction zone presented by *Dragert et al.* (1998) show better agreement between observed and modeled velocities with a convergence azimuth of N60°E as opposed to N69°E.

Width of the Seismogenic Zone

The width of the seismogenic zone along the subduction thrust interface is defined by the updip and downdip limits of the coupled zone. Studies of great subduction earthquakes and their aftershocks from around the world have shown that ruptures associated with this type of event are generally limited to a depth not exceeding 50 km and do not extend all the way to the sea-floor (i.e. trench axis) (*Byrne et al.*, 1988; *Pacheco et al.*, 1993; *Tichelaar and Ruff*, 1993). Thus, the seaward portion of the thrust interface is aseismic. Most commonly, this observation has been attributed to the presence of unconsolidated and semi-consolidated sediments on the incoming oceanic plate (*Tichelaar and Ruff*, 1993; *Hyndman and Wang*, 1993), and specifically to the presence of smectite rich clays (*Vrolijk*, 1990) which exhibit stable-sliding properties until they undergo transformation to illite and chlorite at higher temperatures and pressures. *Hyndman and Wang* (1993) suggest that this transformation and consequently the "locking" of the subduction thrust interface takes place at a depth where temperature reaches 100-150°C (see Figure 4.3). For the purpose of our studies the exact location of the updip limit of the seismogenic zone is not very important, since the deformation rates observed farther landward are not sensitive to this parameter. However, as shown by *Flück*, (1996) and *Flück et al.* (1997) the location of the updip limit is important in modeling co-seismic displacements and associated tsunamis.

The downdip limit of the seismogenic zone of the thrust interface can be described by *two* depth limits as shown in the schematic diagram of subduction in Figure 4.3. The *first* one is the maximum depth of the fully locked portion of the seismogenic zone, which is characterized by stick-slip behavior (i.e. earthquakes nucleate in this zone). This downdip limit of the locked zone (i.e. depth of seismic coupling) is most commonly attributed to thermal effects taking place at 350°C temperature (*Tichelaar and Ruff*, 1993; *Hyndman and Wang*, 1993). At this critical temperature crustal rocks are known to undergo transformation from velocity weakening to velocity strengthening (i.e. seismic to aseismic transition) (*Scholz*, 1990). The *second* downdip limit corresponds to a temperature of approximately 450°C. The zone between the downdip limits

corresponding to 350°C and 450°C temperatures is often referred to as a transition zone. Although earthquakes probably nucleate within the locked zone, the rupture may propagate deep into the transition zone (*see Hyndman et al.*, 1997 and references therein). The physical mechanism for transition zone behavior has been attributed to conditional sliding (*Marone and Scholz*, 1988; *Scholz*, 1988), where transition from unstable to stable sliding takes place (*Hyndman and Wang*, 1993; *Tichelaar and Ruff*, 1993).

More detailed discussion on thermal constraints of the depth of seismogenic portion of subduction zones can be found in papers by *Tichelaar and Ruff* (1993), *Hyndman et al.* (1997), and references therein.

4.4.3 Construction of the Model

The mathematical representation of the subduction thrust fault by numerous triangular elements is generated almost automatically in Wang's DISL3D program. The user defines the spatial locations of 3 points: the up-dip and down-dip limits of the locked zone and the down-dip limit of the transition zone along several profiles normal to the trench (I have used 11 profiles). The program then fits a smooth arc through the three points defining each profile, and subdivides each arc into a user-defined number of segments. Commensurate points along each arc are then joined by trench-parallel line segments which are also subdivided into a user-defined number of sub-segments. This results in a mathematical grid consisting of the triangular elements representing the fault interface.

In this study an initial grid of 33 points (shown in Figure 4.6) was used to define boundaries of the locked and transition zones. For the final integration, this grid is divided into 100,000 triangular elements, each with an area of ~1 km^2. The assigned slip rate on the fault in the model is based on the plate convergence rate estimated by *Riddihough* (1984) of 42 mm/yr and a convergence direction of N60°E (the justification for using the convergence direction estimated by *Riddihough*'s (1984) as opposed to the NUVEL-1A (*DeMets et al.*, 1990; 1994) estimated direction of N69°E is given in section 4.4.2 at the end of the subsection "Plate Motions").

In the "preferred" model, the updip and downdip limits of the locked and transition zones were constrained to 15 and 38 km depth, respectively (Figure 4.6c). These values were intentionally kept constant along the strike of the fault (i.e. in the north-south direction) as is evident from Figure 4.6. This was done in order to avoid divergence from the seismically determined geometry of the JDF slab (shown as dashed contour lines in at Figure 4.7). The adopted downdip depth of

the seismogenic zone of the "preferred" model is consistent with a depth of seismic coupling of 40±5 km suggested by *Tichelaar and Ruff* (1993). In addition, the depth of the locked zone of the "preferred" model agrees well with the location of the 350°C isotherm predicted by thermal models (e.g. *Hyndman and Wang*, 1993). However, the agreement between the depths of the transition zones predicted by the thermal models (corresponding to the 450°C isotherm) and the "preferred" model is not as good. Nevertheless, if the higher levels of uncertainties predicted by thermal models for the location of the 450°C isotherm (compared to 350°C) (e.g. *Hyndman et al.*, 1997) are taken into account and are combined with the uncertainties in the "true" location of the thrust interface, the observed difference of 10 km could be easily accommodated. The difference between models are shown in a cross-sectional plot in Figure 4.7, where the "preferred" model is overlaid by the model of *Flück et al.* (1997). They constructed their initial three-dimensional grid of the CSZ by interpolation of a model by *Hyndman and Wang* (1995) based on two-dimensional thermal and elastic dislocation models constructed along the margin-perpendicular profiles (shown as dashed lines in Figure 4.4).

To summarize, the main differences between the "preferred" model and the model of *Flück et al.* (1997) include:

- The north-south extent of the "preferred" model along the CSZ is reduced but is sufficient to model the stations in the study area.

- Slab dip is increased slightly to match the seismically determined geometry of the slab (Figure 4.5). This helps to reduce the magnitude of predicted horizontal deformation rates at the coast.

- The width of the locked and transition zones has been re-adjusted, reaching maximum widths of 100 and 130 km respectively, under the Olympic Peninsula.

- The increase in the width of the transition zone is dictated by the low rate at which observed station velocities decrease with distance away from the trench.

The numerical values of velocities predicted by the "preferred" model are given in Table D.3.

4.4.4 Comparison with GPS Measurements

Figures 4.8 and 4.9 below include maps where GPS station velocities predicted by the "preferred" dislocation model are displayed together with observed velocities (section 3.3). These maps illustrates the fact that objectively evaluating the "goodness-of-fit" of the model by visually inspecting the predicted and the observed velocity vectors is not trivial. In my case, this task was

somewhat simpler, since I have constrained the "preferred" model based on velocities estimated for continuous GPS stations only (shown in Figure 3.5). This was done mainly for two reasons: 1) the precision of velocity estimates for the continuous sites is an order magnitude better than for the "campaign" stations (see the discussion in section 3.2); 2) the majority of the modeling efforts were carried out prior to the completion of the analysis of the "campaign" data.
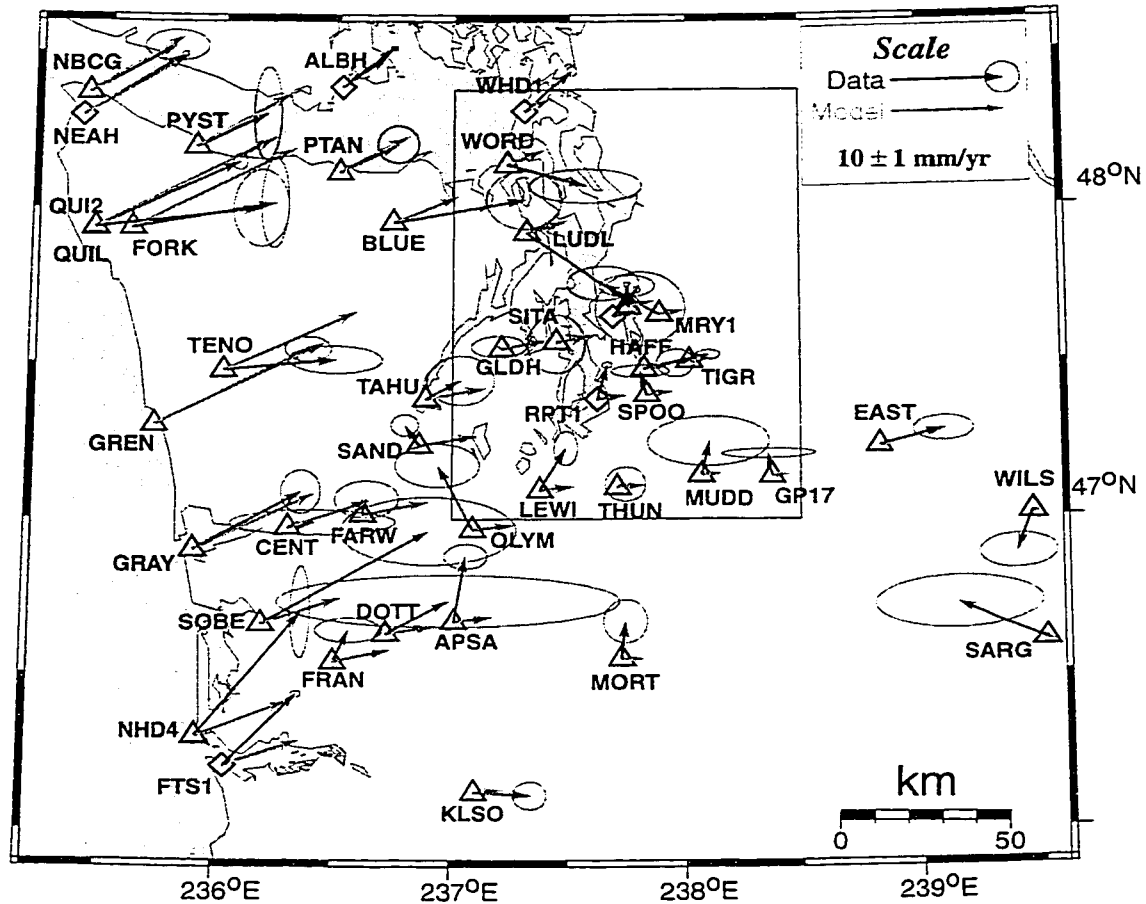
Figure 4.8: Map of model predicted and observed velocity vectors. Continuous stations are shown as diamonds and "campaign" stations as triangles. Error ellipses at the tip of each velocity vector represents 68% confidence limits. The box shows the area enlarged in Figure 4.9. Scale of velocity vectors is given in the upper right side of the figure.

Besides the visual examination of the predicted and observed velocities the L1 norm minimization method has also been used to quantitatively evaluate the "goodness" of various versions of models. Specifically, this was done by subtracting the model predicted velocities from the observed velocities (component-wise) and then summing up the differences for all the stations (i.e.
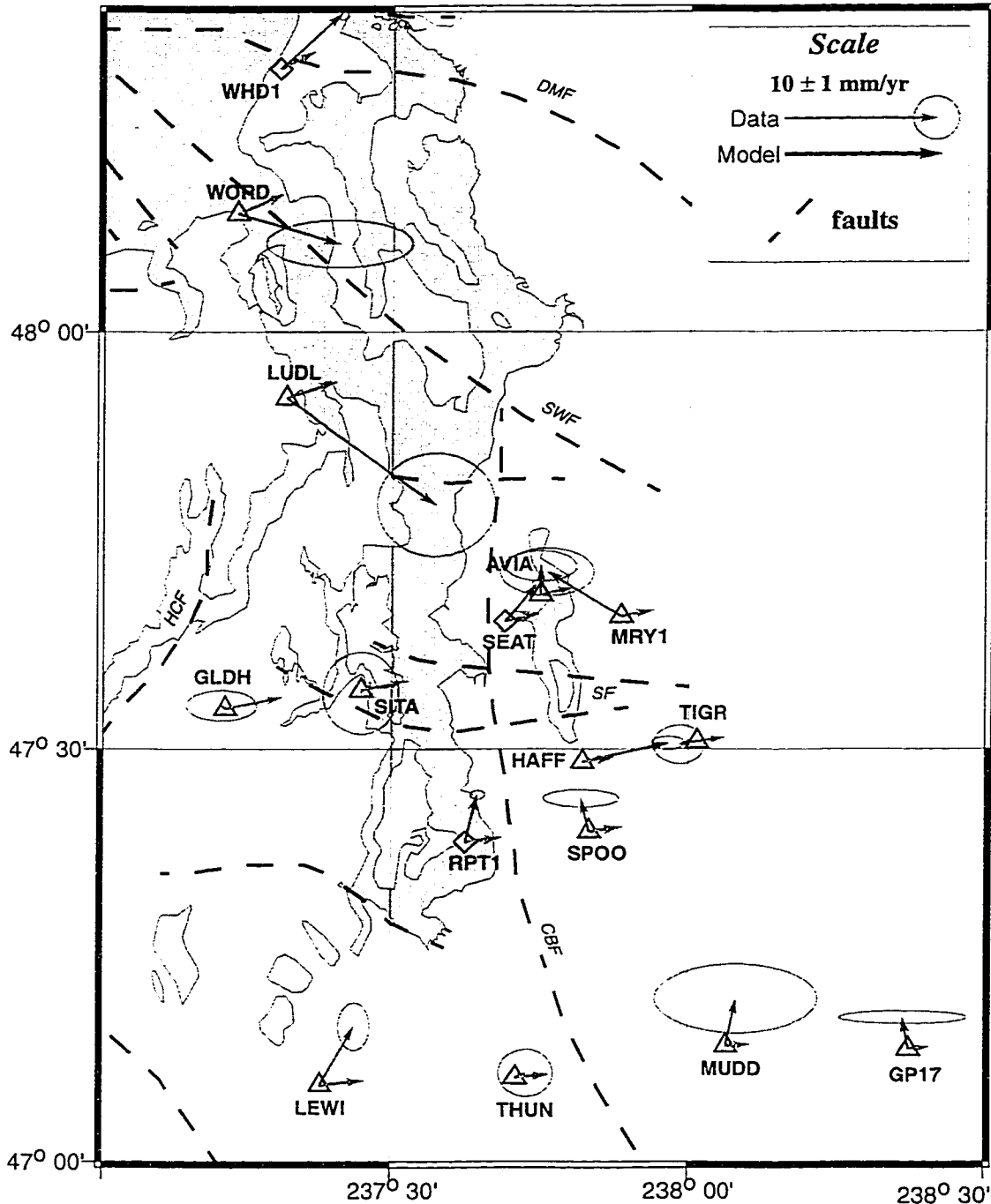
Figure 4.9: Map of model predicted and observed velocity vectors in the Puget Lowland. Velocities are relative to station DRAO. Error ellipses represent 68% confidence limits. Scale for velocity vectors is given in the upper right corner of the figure. Note: the scale is different from Figure 4.8. Dashed lines show approximate location of Holocene faults adopted from *Johnson et al.* (1996). Abbreviations for faults in *italics* are the same as in Figure 1.5: *CBF* = Coast Range Boundary Fault; *DMF* = Devils Mountain Fault; *HCF* = Hood Canal Fault; *SF* = Seattle Fault; *SWF* = Southern Whidbey Island Fault.

6 continuous GPS stations). The L1 norm obtained for the north-south component is approximately twice as big as for the east-west component (2.2 mm/yr versus 0.9 mm/yr). This result indicates that the dislocation model is less successful in explaining the north-south component of the observed crustal deformation rates. The explanation for this observation will be discussed in the following chapter.

V. Discussion

5.1 Main Observations

The contemporary crustal deformation rates in western Washington, based on more than three years of continuous and "campaign" GPS measurements, indicate that the direction of maximum compression is roughly parallel to the relative convergence direction between the Juan de Fuca and the North America plates and that the observed station velocities decrease away from the trench (Figures 3.5, 3.6 and 3.7). This main observation can be explained by the inter-seismic strain accumulation due to the locking of the thrust interface between the subducting JDF and overriding NA plates (shown schematically in Figure 5.1) and can be predicted by the dislocation model (as presented in chapter IV).
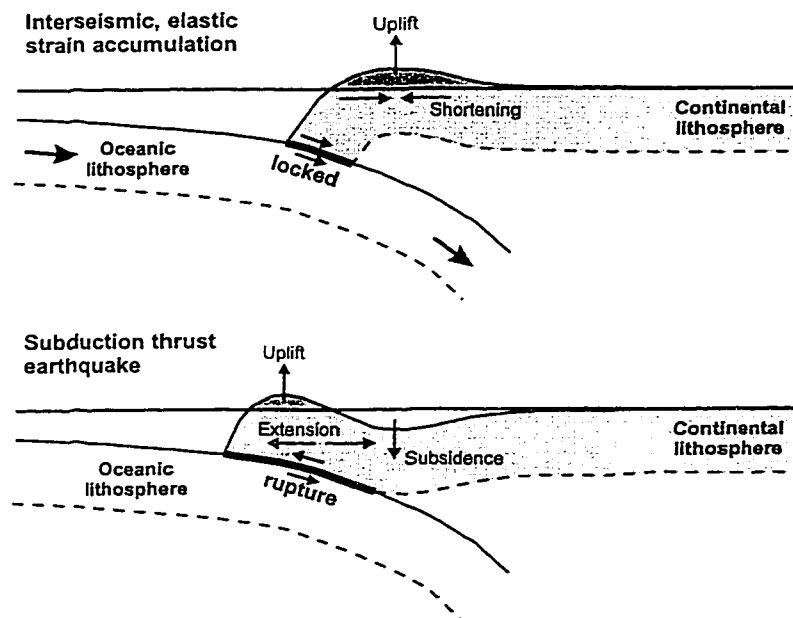
Figure 5.1: Simplified picture of an earthquake cycle at the subduction zone after *Dragert et al.* (1994). Sense of motion during the inter-seismic strain accumulation (i.e. vertical uplift and horizontal compression) is reversed during the earthquake. Net deformation throughout the earthquake cycle is assumed to equal zero (see the discussion in section 4.4.1).

This result is in agreement with previous geodetic measurements (*Savage et al.*, 1991; *Dragert et al.*, 1994) and confirms the hypothesis that geodetic measurements in the Pacific Northwest (including the GPS measurements presented in this study) are mainly sensitive to short term[1]

stress variations, reflecting elastic strain accumulation during the inter-seismic period between large megathrust earthquakes on the CSZ (*Sbar*, 1983; *Wang*, 1995).
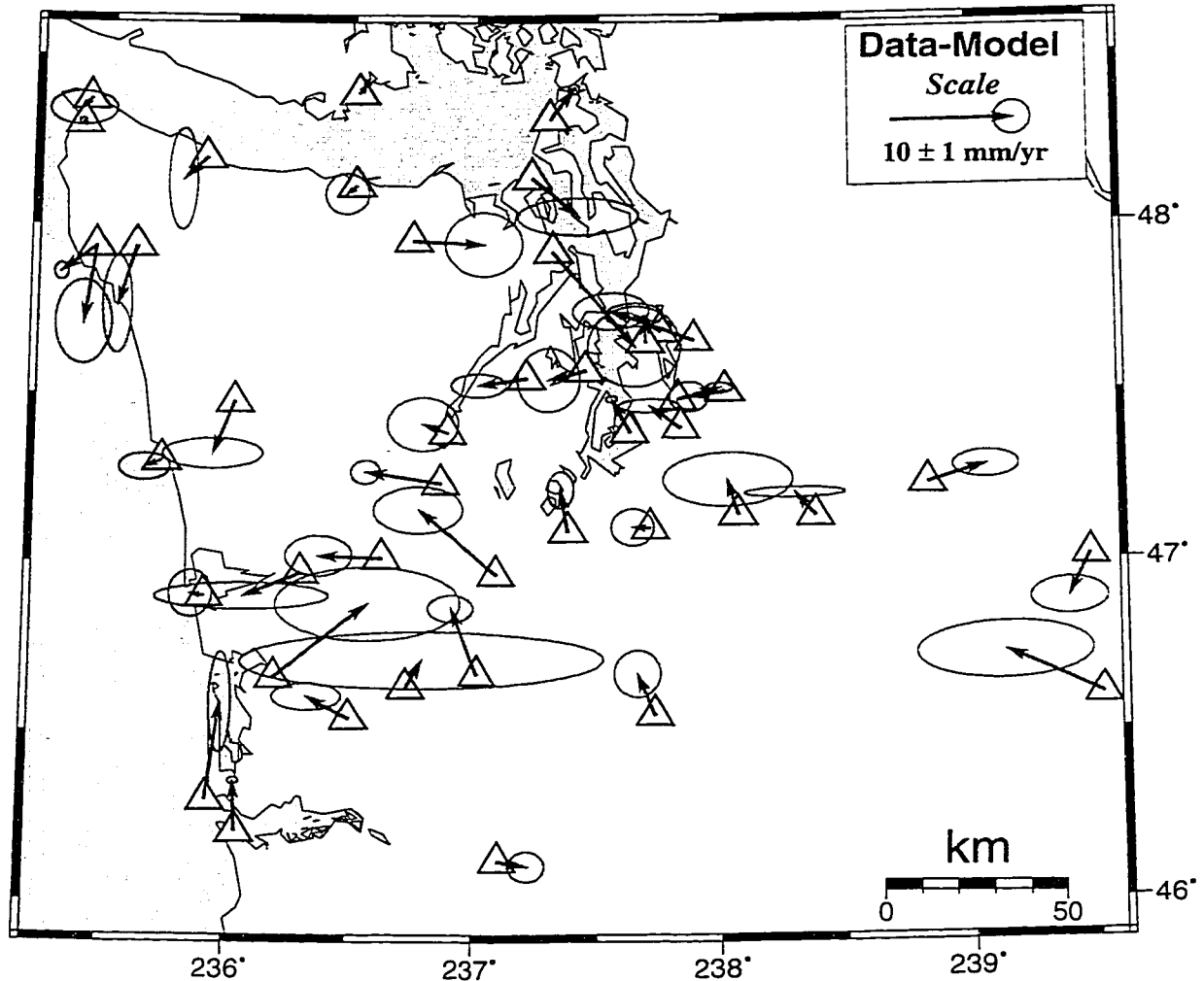
Figure 5.2: Map of the GPS station "residual" velocities. Residual velocities were obtained by subtracting component-wise the "preferred" model predicted values (Table D.3) from the velocities deduced by GPS observations (Tables D.1 and D.2).

The data also suggest an additional north-south oriented compression in western Washington at a rate of ~4 mm/yr over a north-south distance of approximately 250 km, presumably representing a more long-term deformation pattern than the periodic accumulation and release of strain connected with subduction earthquakes. This may be caused by the presence of dextral shear

---

1. Here, "short term" means approximately 500 years, the repeat time for great subduction type earthquakes along the CSZ (*Atwater et al.*, 1996).
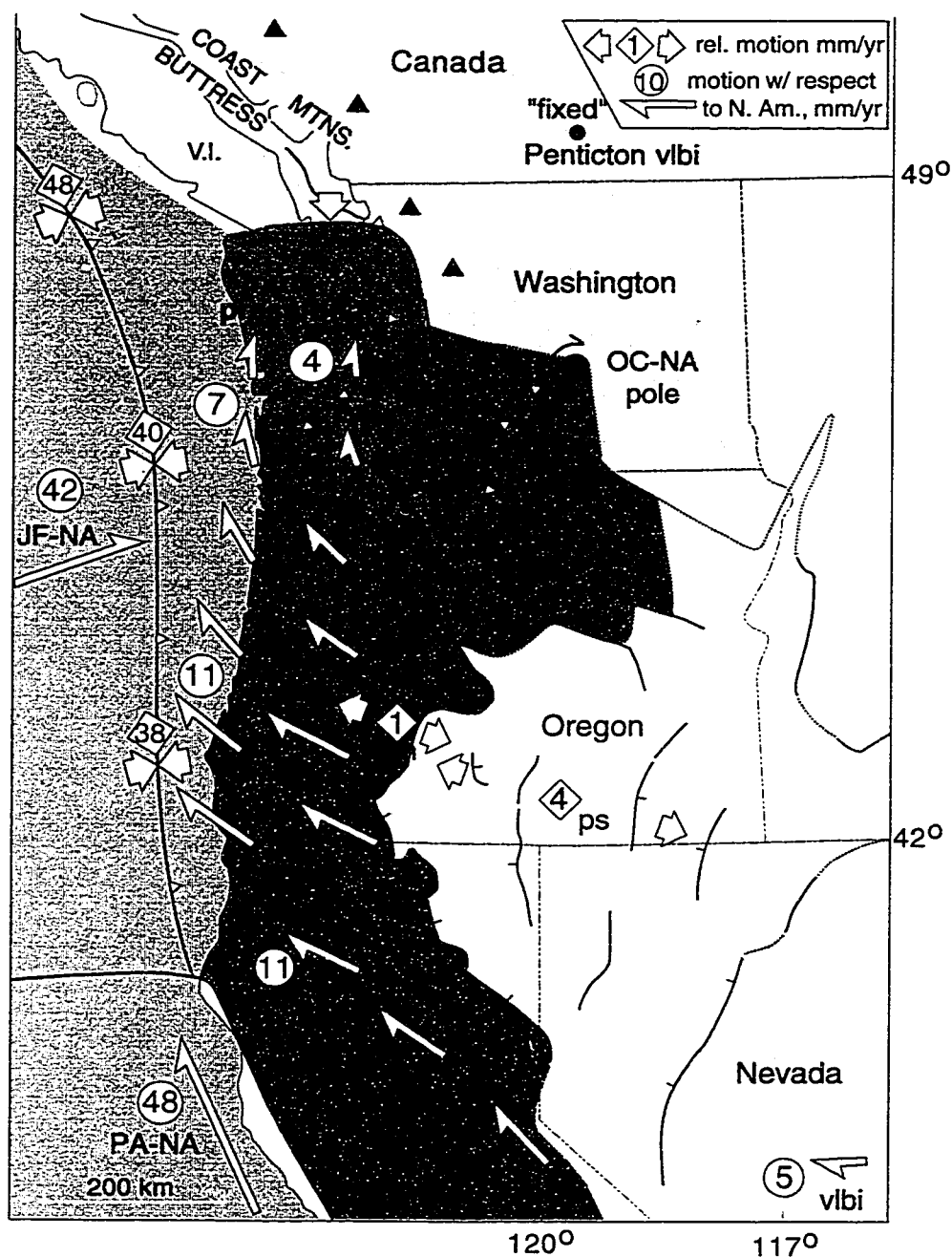
Figure 5.3: Kinematic model of the Cascadia forearc blocks from *Wells et al.* (1998). From south to north, the forearc is divided into three tectonic blocks/segments: Sierra-Nevada (SN) shown in purple; Oregon Coastal (OC) shown in pink and Washington (W) shown in green. Thick arrows indicate observed relative rates from very long baseline interferometry, paleoseismology and magmatic spreading. Thin yellow arrows represent velocities w.r.t. North America (fixed to Penticton) calculated from OC-NA and OC-SN Euler poles of rotation shown as circles filled with black color. Note that the location of the pole of rotation for the OC-NA blocks shown in this figure is different from the one published in *Wells et al.* (1998). The location used here supersedes the earlier published position by *Wells* (pers. comm.).

between the Pacific and North America plates that dominates tectonics in California (*Pezzopane and Weldon*, 1993; *Wells et al.*, 1998), and/or by changes in the rates of margin parallel translation of the forearc sliver (*McCaffrey*, 1992; *Wang*, 1996) due to the obliqueness of subduction across the CSZ. Further discussion regarding the north-south compression detected in the observed GPS velocities will be provided in the following sections.

5.2 Tectonic Implications

A closer examination of the observed velocity field in Figure 3.6 reveals a trend showing that stations in the southern part of the study area have a larger northward component than stations located in the north. To further investigate this matter, it is convenient to subtract the JDF/NA subduction related deformation rates (predicted by the dislocation model and shown in Figures 4.84.9) from the observed velocities (shown in Figure 3.6). The resulted velocity field is shown in Figure 5.2 and from here on I will refer to it as "residual" velocities.

If I plot the north and the east components of the "residual" velocities versus station latitude and longitude, a trend of decreasing north velocities with increasing station latitudes is apparent (Figure 5.4a). The slope of the fitted line for N "residual" velocities versus station latitude calculated by the linear regression and converted to units of strain rate, equals -0.013±0.003 μstrain/yr, which is identical to the maximum principal strain rate value estimated from "residual" velocities presented later (Table 5.1). On the other hand, linear regression slopes in the east component of "residual" velocities or the north-south versus longitude plots points to near zero strain rates in these directions (Figure 5.4b-d). Thus, we can interpret the slope of the fitted line for the north component of the "residual" velocities as compression in the north-south direction which is not accounted for by the "preferred" dislocation model of inter-seismic strain accumulation due to locking along the subduction thrust interface.

Such a "residual compression" agrees well with the north-south shortening rate predicted by the kinematic model of the Cascadia forearc blocks proposed recently by *Wells et al.* (1998) (see Figure 5.3). According to this model, the Washington block (shown as a green shaded area), which is located in the forearc of the CSZ and more or less coincides with the study area, is characterized by the presence of several broken sub-blocks squeezed against the Canadian Coast mountains buttress[2] in the north. This squeezing is most likely due to the northward translation of

the central Oregon block (shown as a pink shaded area in Figure 5.3) driven by the Pacific-North America dextral shear that dominates tectonics in California (*Pezzopane and Weldon*, 1993; *Wells et al.*, 1998) and/or by the margin-parallel translation of the forearc segments driven by oblique subduction across the CSZ (*McCaffrey*, 1992; *Wang*, 1996). The rates of northward motion predicted by the *Wells*'s kinematic model agree almost exactly with the estimates of northward compression deduced from the north-south "residual" velocity field. Both the model and the data suggest approximately 4-5 mm/yr northward motion at the southern edge of the Washington block, which decreases to zero in the north where the Washington block encounters the Canadian Coast mountains which arrest its motion. This is surely a very intriguing observation and will require further verification by additional GPS observations.

Table 5.1: Strain, rotation and translation from "residual" GPS velocities.

#	Net Name[a]	Principal Strain Rates (μstrain/yr)			Rotation[e] (degree/ m.yr)	Translation	
		ε_1[b]	ε_2[c]			mm/yr	degree
		$\varepsilon_1 \pm 1\sigma$	$\varepsilon_2 \pm 1\sigma$	Θ[d] $\pm 1\sigma$	$\omega \pm 1\sigma$	C[f] $\pm 1\sigma$	C_α[g] $\pm 1\sigma$
1	ALL	0.004 ± 0.006	-0.013 ± 0.005	-12 ± 2	0.1 ± 0.0	2.2 ± 0.1	-8 ± 3
2	PANGA	0.003 ± 0.006	-0.017 ± 0.005	-17 ± 2	0.0 ± 0.1	2.1 ± 0.1	0 ± 3
3	A	-0.045 ± 0.041	-0.090 ± 0.065	59 ± 15	-0.1 ± 0.5	2.4 ± 0.7	-74 ± 10
4	B	0.076 ± 0.040	-0.011 ± 0.030	-67 ± 4	1.7 ± 0.3	1.5 ± 0.3	-128 ± 11
5	C	0.372 ± 0.232	-0.060 ± 0.257	67 ± 6	2.6 ± 2.5	5.4 ± 1.3	121 ± 13
6	D	0.062 ± 0.049	-0.007 ± 0.040	7 ± 3	-0.2 ± 0.2	2.4 ± 0.2	-17 ± 5

a. See Table 3.3 for more details.

b. Minimum principal strain rate in μstrain/yr. Positive value is extension represented by outward pointing arrows.

c. Maximum principal strain rate in μstrain/yr. Negative value is compression represented by inward pointing arrows.

d. Azimuth of ε_2 in degrees measured clockwise from North with 1σ errors.

e. Rigid body rotation in degrees/million-years measured clockwise from North with 1σ errors. See Equation 3.15 for the derivation of ω.

f. Rigid body translation with 1σ errors. See Equation 3.10 for the derivation of C.

g. Rigid body translation azimuth in degrees measured clockwise from North with 1σ errors. See Equation 3.11 for the derivation of C_α.

---

2. See *Beck* (1993) for the description of the buttressing effect in the margin-parallel strike-slip fault systems.

Instead of estimating a "residual" north-south strain rate via linear regression of "residual" velocities (Figure 5.4a), one can also estimate "residual strain rates" directly from the "residual" velocities (as carried out previously in chapter III from the observed velocities). Table 5.1 and Figure 5.5 show the results for the "residual strain rate" estimates commensurate with the same site groupings used in the calculation of "observed" strain rates presented in section 3.4 (Table 3.3 and Figure 3.10).

The principal "residual" strain rates for estimates #1 and #2 (*ALL* and *PANGA*) given in Table 5.1 are in excellent agreement with the regression estimates above (Figure 5.4a). A comparison of these quantities with the strain rate estimates presented in Table 3.3, also shows that the maximum "residual" principal strain rate (-0.013±0.005 μstrain/yr N12°W±2°) is close to the minimum "observed" principal strain rate (-0.004±0.006 μstrain/yr N12°W±1). This shows that it is predominantly the margin-parallel strain that is not accounted for by the "preferred" slip-dislocation model. The corresponding "residual" rigid block translation estimates (Table 5.1) also agree with an *average* northward motion of 2 mm/yr for the Washington Block (Figure 5.3). The rather large errors for estimates #3 through #6 (*A*, *B*, *C* and *D*) show that no meaningful principal "residual" strain estimates can be resolved for these subsets of sites.

5.2.1 Rigid Body Rotations

One of the main advantages of using GPS technology for deformation measurements, as opposed to conventional geodetic techniques (e.g. trilateration), is the ability of determining absolute displacement vectors, consisting of three types of motion: rotation (Θ), translation (C) and strain (ε). Until now I have been focusing on estimates of strain rates. However, rigid body translation and rotation rates can be at least as important as strain rate estimates to interpret deformation processes within active tectonic regions. In particular, the rigid body parameters might be very useful in testing the hypothesis that the short term (3-4 years in this study) geodetically observed displacements of crustal blocks are representative of long-term (>1 Ma) tectonic motion obtained from geologic observations. Here I will discuss the relationship between the observed "instantaneous"[3] and paleomagnetically determined rotation rates. The following discussion is quite speculative in nature and the main goal of presenting it is to point out possible links between

---

3. "instantaneous" term is used to emphasize the fact that the time-scale of GPS observations is a "snap-shot" of events evolving through millions of years of geologic time.
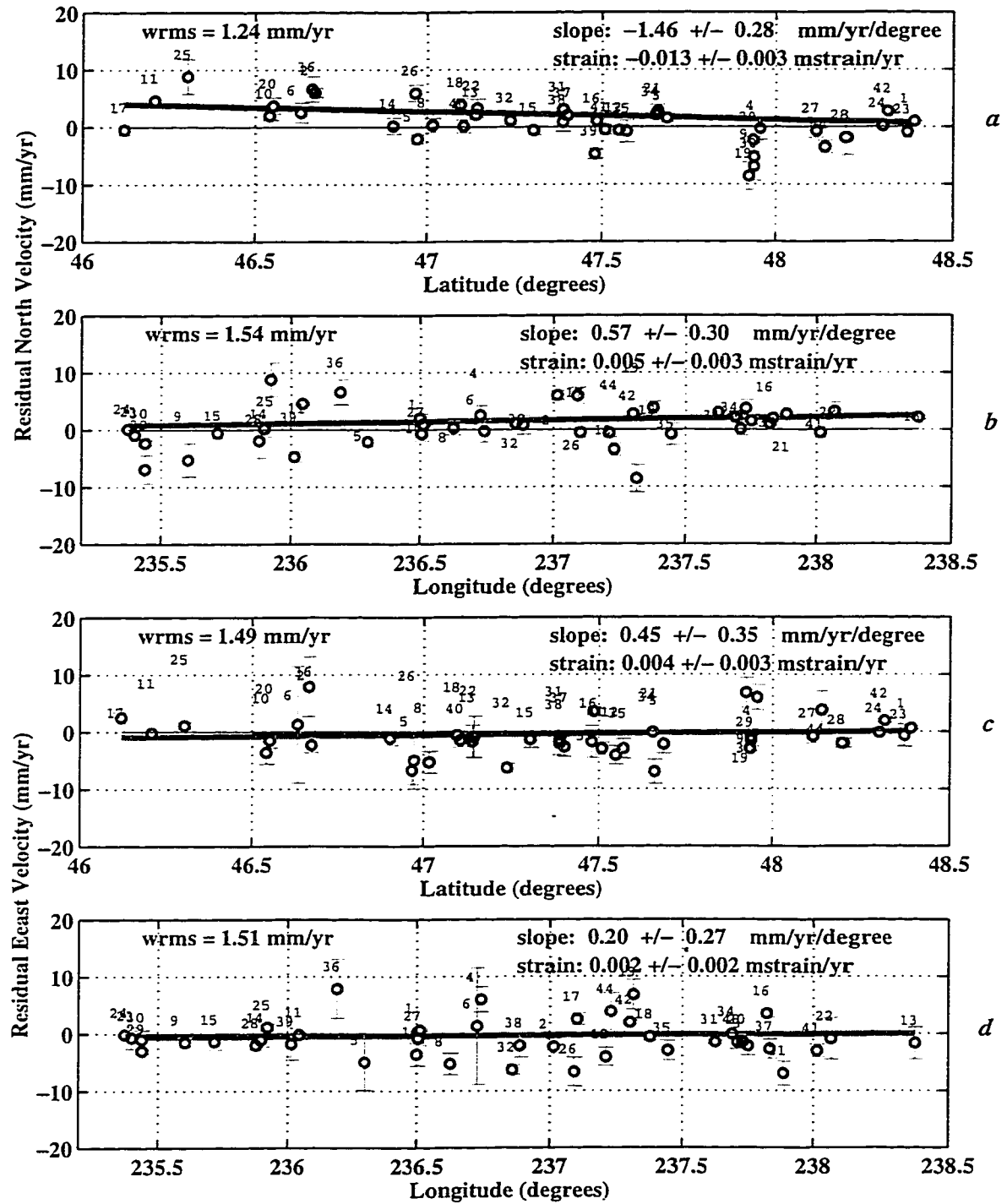
Figure 5.4: North and east "residual" velocity components as a function of station latitude and longitude. Error bars are based on GIPSY formal errors. Error of the slope represents 1 standard deviation. For station names corresponding to the plotted numbers refer to Table D.3. Regression was carried out using the Least Squares Spectral Analysis (LSSA) program by *Pagiatakis* (1997).
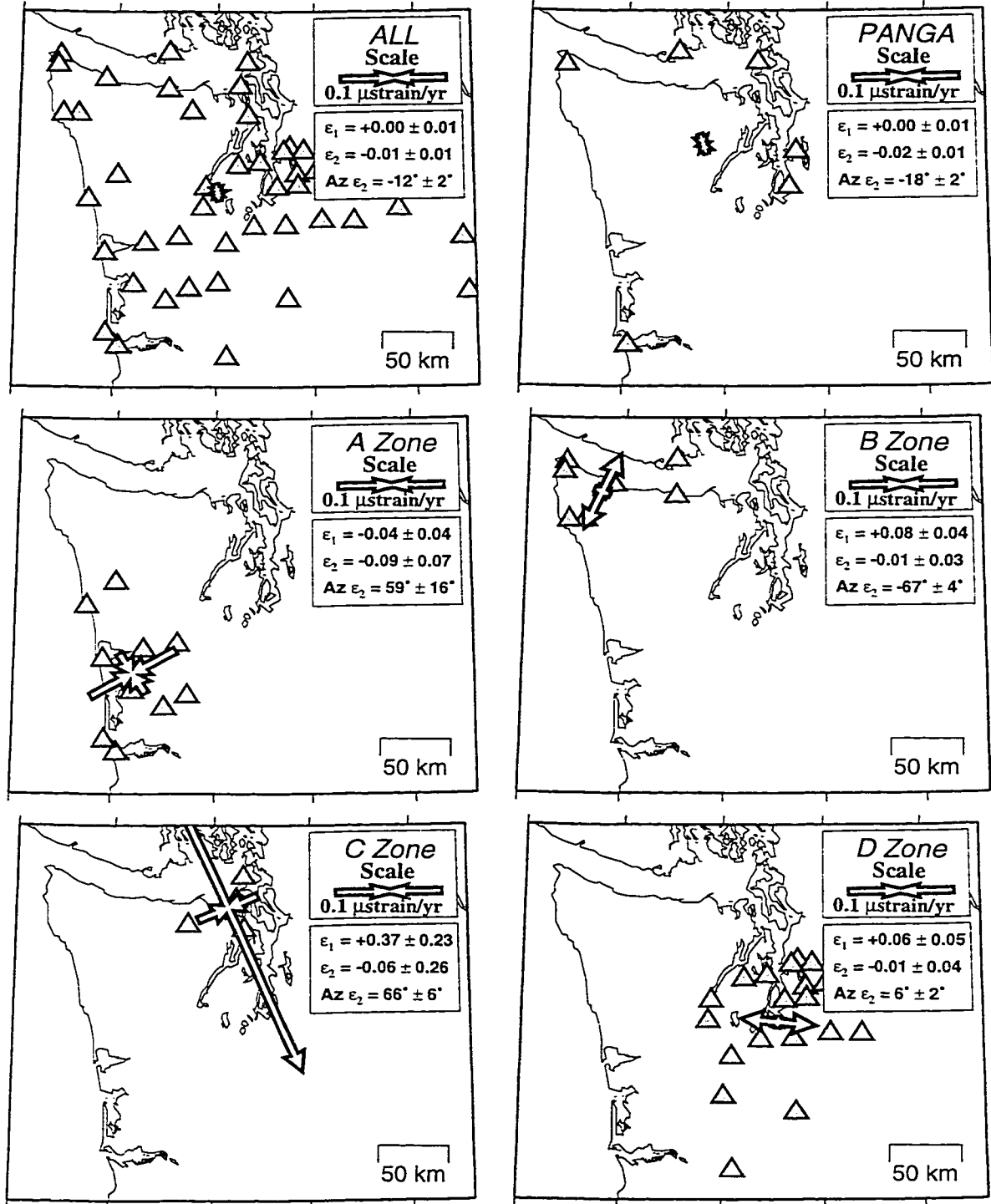
Figure 5.5: Horizontal "residual" strain rates in western Washington. Rates were calculated from "residual" velocities shown in Figure 5.2. ε_1 and ε_2 are maximum extensional and contractional strain rates. Strain crosses are located at the center of individual nets. See the caption to Figure 3.10 for more information.

the GPS observed and geologically estimated deformation rates in western Washington and to underline the power of GPS to make tectonic interpretations based on the calculation of absolute displacement vectors.

The measurements of remnant magnetization in rocks of the forearc, arc and the backarc blocks of the CSZ indicate a persistent picture of clockwise rotations in Cenozoic (<62 Ma) rocks from these regions (Figure 5.3). These paleomagnetically determined rotations exhibit the following *two* main characteristics (*Magill et al.*, 1982; *Beck et al.*, 1986; *Wells*, 1990; *England and Wells*, 1991):

- rotation rates decrease from West to East

    The youngest paleomagnetic rotations, estimated for Miocene age (12-15 Ma) Columbia River basalts which flowed for hundreds of kilometers west through the Cascade arc, show a clear trend of decreasing rotation away from the CSZ deformation front (i.e. West to East): from $-30°$ along the coast to $-6°$ 300 km away from the plate boundary (*England and Wells*, 1991). These estimates translate to rotation rates of -2.2 and -0.4 °/Ma, respectively.

- rotation rates decrease from South to North

    Maximum rotation ($-80°$) is found in the Paleocene (-60 Ma) rocks of south-west Oregon (see *Coastal Oregon* block in Figure 1.3) which is equivalent to rotation rate of -1.5 °/Ma (*Wells*, 1990).

We can test whether GPS estimated rotation rates for individual subregions within the study area (Table 3.3) can be directly related to paleomagnetically determined rotations described above. However, comparison of these rotations is not straightforward. As applied here, geodetically estimated rigid body rotations are relative to a rotation axis located at the center of mass of the subset of stations being analyzed where the strain arrows are shown in Figures 3.10 and 5.5). The exact location of paleomagnetically determined poles of rotation is less clear. Based on observed differential rotations over distances of less than 10 km in the paleomagnetic data from Columbia River basalts, *Wells* (1990) suggested that the length of an individual rotating rigid block does not exceed -10 km. This would imply that the rotation takes place around an axis located in the center of this relatively small block. However, the driving forces behind these rotations could lie much farther away. For example, *Wells et al.* (1998) suggest that the paleomagnetic rotations observed in Washington State (discussed above) can be explained by a pole of rotation located in Central Washington State (marked PC-NA in Figure 5.3). This situation is schematically illustrated in Figure 5.6.
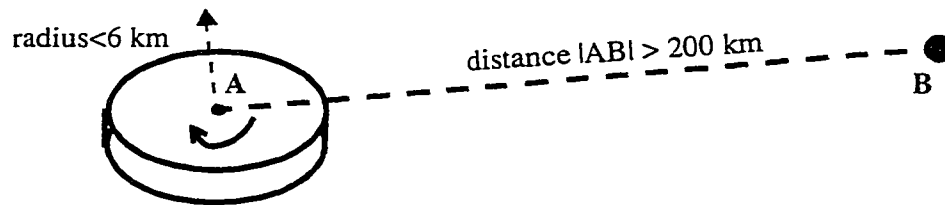
Figure 5.6: Example of a rotating block around two axes. Solid and dashed arrows indicate the direction of rotation due to rotation poles located at points A and B, respectively. If we assume that the rotating body does not deform internally (i.e. has zero strain) then the rigid body rotations and translations calculated from GPS determined velocities should reflect the rotation around the A and B poles, respectively (assuming point B is fixed).

Keeping in mind the potential problems just discussed, I proceed to a comparison of geodetically and paleomagnetically estimated rotation rates for individual subsets of stations based on GPS determined crustal deformation velocities (Table 3.3). The comparison of geodetic rotation rates estimated for regions A and D can be used to check the dependence of rotation rate on longitude. The coastal regions A and B can be used to test the dependence of rotation rate on latitude. The results of these comparisons are summarized in Table 5.2 below.

Table 5.2: Comparison of GPS estimated rigid body rotation rates with paleomagnetic rotations.

Direction	GPS Estimated Rotation Rates[a]			Paleomagnetic Rotation Rates[a]		
	Subregion[b]	ω (West→East)	Δω	Ω (West→East)	ΔΩ	Ref.[c]
West→East	A→D	3.3 → 0.1	3.2	2.2 → 0.4	1.8	1, 2
South→North	A→B	3.3 → -2.0	5.3	1.5 → 0.0	1.5	1, 3

a. Rotation rates are given in °/Ma (degrees/million-years); positive values indicate the clockwise rotation; axis of rotation is vertical.
b. See Table 3.2 for the location of subregions and further details.
c. (1) *Magill et al.* (1982); (2) *England and Wells* (1991); (3) *Wells* (1990).

The estimated rotation rate (3.3±0.5 °/Ma) for the southwestern part of the study area (i.e. subregion A) matches reasonably well the Neogene rotation rate of 2.2 °/Ma estimated by *England and Wells* (1991). The match is also good farther inland. The rotation rate estimated for subregion D is 0.1±0.2 °/Ma and the Neogene deformation rate estimated approximately 300 km away from the deformation front is ~0.4 °/Ma. The largest discrepancy occurs in the northwest corner of Washington (subregion B). GPS measured rotation rates indicate -2.0±0.3 °/Ma anti-clockwise motion, while paleomagnetic results suggest zero rotation rates (e.g. *Wells*, 1990). This

discrepancy could be due to the fact that the observed GPS velocities in this area reach their maximum (Figure 3.6), while paleomagnetic rotations are at their minimum. Thus, the anti-clockwise rotations measured in the subregion *B* could be related to the locking of the subduction thrust interface. In addition, one has to keep in mind that this area is characterized by a complex geologic setting in which north dipping thrust faults separate the Olympic Subduction Complex from the adjacent Crescent Formation (Figures 1.51.6).

Remarkably, geodetically determined rotation rates agree fairly well with paleomagnetically determined rotation rates. If we assume that the GPS estimated rigid body rotation rates presented above are indeed real and they do not represent an artifact of reference frame related problems in the processing of GPS data (*J. Klotz*, pers. comm) we can speculate that these "instantaneous" rotation rates reflect the same forces that cause long-term tectonic deformation. As mentioned earlier, the main driving forces behind the margin parallel translation and rotation of the forearc blocks along the CSZ include: *1)* dextral shear along the coast due to the PA/NA plate interaction (e.g. *Pezzopane and Weldon*, 1993); *2)* the tangential component of JDF/NA oblique subduction (e.g. *Beck*, 1993; *Wang*, 1995) (Both of these forces are contributing to the margin parallel translation of the forearc); *3)* intra-continental extension in the Basin and Range (Figure 5.3), causing the clockwise rotations observed in the forearc of the CSZ (e.g. *Walcott*, 1993; *Wells et al.*, 1998).

5.3 Seismic Hazard Implications

5.3.1 Estimates of Magnitude along the CSZ

Basic Theory

The most commonly used way to describe the size of an earthquake is in terms of its magnitude, which is usually estimated by measuring maximum amplitudes of various types of seismic waves recorded at a seismographic station (*Bolt*, 1993). However, it is more appropriate to relate the size of an earthquake to the moment released during the event. For this purpose, *Kanamori* (1977) has proposed yet another type of earthquake magnitude, called moment magnitude (M_w) which he empirically related to the fundamental parameter describing the size and the strength of an earthquake, its seismic moment (M_o):

$$M_w = \frac{2}{3}\log M_o - b \qquad \text{(EQ 5.1)}$$

where the coefficient b in Equation 5.1 equals 10.7 when M_0 is given in CGS units of dyne·cm or 6.0 when M_0 is in SI units of N·m. Note: 1 N·m (Newton·meters) = 10^7 dyne·cm.

The scalar seismic moment M_0 (in N·m) can be estimated from the following fault rupture parameters (*Aki and Richards*, 1980):

$$M_0 = \mu u A \qquad \qquad (EQ\ 5.2)$$

where, μ is the shear modulus[4] (in N/m^2), u is the average slip on the fault (in meters) and A is the ruptured fault area (in meters^2).

Previous Estimates

Previous estimates of the maximum hypothetical size of a subduction earthquake along the CSZ varies between $7<M_w<9.2$. The lower limit of $M_w<8$ is suggested by *McCaffrey and Goldfinger* (1995) based on the analysis of subduction zones around the world. They interpret the presence of active strike-slip faults in the submarine forearc of the CSZ (*Goldfinger* et al., 1997) as an indicator of the weakness of the forearc and its ability to deform anelastically. Based on these observations, *McCaffrey and Goldfinger* (1995) argue that the CSZ is not necessarily due for the next great ($M_w>9.0$) subduction earthquake and suggest that smaller $M_w<8$ earthquakes can be more characteristic for Cascadia.

The upper limit ($M_w\approx9.2$) for CSZ great subduction earthquakes is based on the results of dislocation and thermal models (e.g. *Hyndman and Wang*, 1995; *Verdonck*, 1995; *Flück*, 1996). Since these estimates were based on the models that assume purely elastic behavior of the crust, the amount of strain accumulated during the inter-seismic cycle and subsequently released in an earthquake is higher than during the mechanism proposed by *McCaffrey and Goldfinger* (1995) which included the presence of anelastic (i.e. permanent) deformation.

Magnitude Estimation

On the basis of the "preferred" model of the seismogenic zone (presented in chapter IV) and the moment/magnitude relationship given above, I have calculated the maximum expected magnitude of the future inter-plate earthquake along the Cascadia subduction zone.

---

4. Shear modulus μ (which is often referred to as elastic modulus) has units of stress (1 Pascal= 1 Newton/m^2) and can be related to seismic shear wave velocities V_s and density ρ as follows: $\mu=V_s^2\cdot\rho$.

The average value of the shear modulus μ in the upper crustal layers of the earth is approximately $3.35 \cdot 10^{10}$ N/m^2 (*Stacey*, 1992). The other parameters on the right hand side of Equation 5.2 are calculated from elastic dislocation model results. The average slip u is estimated by multiplying the seismic slip rate on the fault ($\bar{v}$) by the repeat time of megathrust earthquakes (τ). The slip rate $\bar{v}$ is a fraction of plate convergence rate (i.e. ~42 mm/yr), depending on the width of the locked and the transition zones. Using the "preferred" elastic dislocation model presented in section 4.4 I have estimated that the average slip deficit over the entire seismogenic zone equals ~25 mm/yr. However, ±5 mm/yr variation in $\bar{v}$ does not significantly affect the computed values of moment magnitude. The repeat time (τ) of megathrust earthquakes for the CSZ is thought to be ~500 years (see Figure 1.8) (e.g. *Atwater*, 1996). Using the above values for $\bar{v}$ and τ the average slip on the fault u equals ~12.5 meters. The second parameter needed to estimate M_0 using Equation 5.2 is the area of the fault. Since the three-dimensional elastic dislocation model is based on a geometrical grid representing the seismogenic zone along the CSZ (as shown in Figure 4.6), the estimation of its area is relatively simple.

In Table 5.3 below I provide estimates of maximum possible size (seismic moment M_0 and magnitude M_w) of a subduction type earthquake which can occur along the CSZ based on *three* different models calculated using Equation 5.2. The *first* estimate is based on the "preferred" model (discussed in section 4.4) which covers the Washington portion of the CSZ. The *second* estimate is based on *Flück et al.*'s (1997) model which spans the CSZ along its entire length. And finally, the *third* estimate is based on a "composite" model between the "preferred" and the *Flück et al.*'s (1997) models. The latter model essentially represents a summation of fault areas for the "preferred" model and the southern and northern segments of the *Flück et al.*'s (1997) model which fall outside the "preferred" model (shown in Figure 4.7 by yellow lines filled with the same color as the ocean).

Table 5.3: Maximum possible size of a subduction type earthquake along the CSZ.

Model	Fault Area			Average Slip			M_0 (dyne·cm)	M_w	$M_w{}^d$	$m_w{}^e$
	Locked (km^2)	Trans. (km^2)	L+T^a (km^2)	τ^b (yr)	V^c (mm/yr)	u (m)				
"preferred"	26000	42000	68000	500	25	12.5	$2.86 \cdot 10^{29}$	8.9	8.8	8.8
Flück et al. (1997)	55000	58000	113000	500	25	12.5	$4.72 \cdot 10^{29}$	9.1	9.0	9.0
"composite"	50000	66000	116000	500	25	12.5	$4.88 \cdot 10^{29}$	9.1	9.0	9.0

a. L+T means the surface area of the locked and the transition zones combined. This area represnts maximum rupture surface of the fault.

b. τ is a recurrence time of earthquakes in years. See Figure 1.8 for the CSZ earthquake reccurence times.

c. V is a slip deficit rate in mm/yr predicted by the model and averaged over the fault area. M_w is not very sensitive to this parameter. Using 20 or 30 mm/yr did not affect the estimated magnitudes.

d. This magnitude was calculated for the area of the fault comprised by the entire Locked zone (L) and one half of the Transition zone (T/2) (e.g. the "preferred" model Area=26000+42000/2=47000 km^2).

e. m_w is a moment magnitude calculated using Wells and Coppersmith's (1994) empirical relationship between the magnitude and the rupture area of the fault A : m_w=4.07+0.98·log(A); Note: I have used the coefficients derived by Wells and Coppersmith (1994) for earthquakes with all types of slip (i.e. normal, strike-slip and reverse).

A moment magnitude of M_w=9.1 estimated from Flück et al.'s model (1997) and the "composite" model represents the maximum hypothetical size of the CSZ earthquake, since it was calculated based on the assumption that the entire seismogenic zone (i.e. locked and transition zones) ruptures in a single event. In reality, it is more common that earthquakes along the subduction interface rupture only parts of the fault. For example, along the Nankai subduction zone in southwest Japan, the thrust interface ruptured in two individual events separated by 2 years: the 1944 Tonankai M_s=8.1 and 1946 Nankaido M_s=8.2 earthquakes (Kanamori, 1972). However, even if the future great earthquake along the CSZ follows the scenario of the southwest Japanese events, the seismic hazard remains very significant. This is illustrated by the fact that the maximum expected magnitude calculated for the fault area corresponding to the "preferred" model (68000 km^2) is M_w=8.9, which is not much less than M_w=9.1 calculated for the two other models with fault areas approximately twice as large (116000 km^2).

Table 5.3 also includes estimates of M_w based on the assumption that only half of the transition zone ruptures (i.e. fault area = locked zone + 1/2 transition zone). This reduction in the fault area results in a reduction of calculated M_w magnitudes by 0.1 units. The latter are identical to magnitudes (denoted by m_w in Table 5.3) calculated using the following relationship between magnitude and the rupture area of the fault (A) given by Wells and Coppersmith (1994):

$$m_\omega = 4.07 + 0.98 \cdot \log A \qquad \text{(EQ 5.3)}$$

Coefficients in Equation 5.3 were derived for earthquakes with all types of slip (i.e. normal, strike-slip and reverse).

Another important finding of this study concerns the geographic location of the seismogenic zone relative to the coast. As can be seen from Figure 4.7 the only place where the transition portion of

the seismogenic zone overlaps the land is in western Washington where the subducting JDF plate arches upward (*Weaver and Baker*, 1988). Although this observation has been pointed out in previous publications (e.g. *Dragert et al.*, 1994; *Hyndman and Wang*, 1995; *Flück et al.*, 1997), the estimated width for the seismogenic zone (specifically the transition zone) based on the "preferred" model is approximately 30 km wider than the previously estimated values (see Figure 4.7). However, this difference is within the uncertainties associated with the data and the model. The fact that the "preferred" model (which is based on the newest estimates of crustal deformation rates in western Washington) agrees so well with the previous estimates of the dimension and the location of the seismogenic zone is significant because it validates previous models which were based on very few data for this section of the CSZ. The slightly increased width of the seismogenic zone in the "preferred" model can theoretically cause higher levels of ground shaking in western Washington, and in particular in the densely populated Puget Sound area (*Qamar et al.*, 1998). Further investigations are necessary to quantify this effect and its implications on the seismic hazard estimate for the area.

5.3.2 Comparison with Seismic Strain Estimates

Basic Theory

To evaluate the significance of the contemporary crustal deformation rates obtained in this study and examine their implications to the seismic hazard estimates for the study area, one can relate the geodetically estimated strain rates ($\dot{\varepsilon}$) to seismic strain rates $(\bar{\varepsilon})$[5]. The main principle of estimating seismic strain rate is based on its dependence on the seismic moment tensor of an earthquake (M_{ij}). The latter can be calculated as shown in Equation 5.4.

$$M_{ji} = M_0(u_j n_i + n_i u_j) = M_{ij}$$

(EQ 5.4)

where M_0 is a scalar seismic moment related to the fault parameters as shown in Equation 5.2, u is a unit vector in the direction of slip, and n is a unit vector normal to the fault plane (*Aki and Richards*, 1980).

---

5. Note, that although $\bar{\varepsilon}$ represents a time derivative of strain (i.e. strain rate) the bar instead of the dot on top of ε is used to differentiate it from geodetically estimated strain rate ($\dot{\varepsilon}$).

There are *two* main methods for calculating average seismic slip and strain rates from seismicity data. The *first* method was derived by *Brune* (1968) for estimating seismic slip rates ($\bar{u}$) along major fault zones (Equation 5.5), for example the San Andreas fault in California.

$$\bar{u}_{ij} = \frac{1}{\mu A \tau} \sum_{n=1}^{N} M^{n}_{ij}$$

(EQ 5.5)

The *second* method, derived by *Kostrov* (1974), provides a seismic strain rate ($\bar{\varepsilon}$) estimate and is applicable to the areas where deformation and earthquakes are distributed over broad areas (Equation 5.6). It is more appropriate to use *Kostrov*'s formulation to calculate seismic strain rates in the Pacific Northwest, since earthquakes there are distributed over broad areas covering hundreds of square kilometers (e.g. Figure 1.9).

$$\bar{\varepsilon}_{ij} = \frac{1}{2\mu V \tau} \sum_{n=1}^{N} M^{n}_{ij}$$

(EQ 5.6)

Parameters in Equations 5.5 and 5.6 are as follows: μ is the shear modulus, A is the area of the fault and V is the volume of the deforming zone, τ is the duration of the seismic catalogue, M_{ij}^{n} is the seismic moment tensor for the n-th earthquake and the summation is performed for all the events, denoted by number N.

The main assumptions implicit in Equation 5.6 are linear elasticity and the presence of homogenous strain within the deforming zone of volume V. For further details regarding the relationship between plate motions and seismic moment tensors the reader is referred to *Jackson and McKenzie* (1988).

Seismic Strain Estimates

The only published values (known to me) of seismic strain (or slip) estimates in the vicinity of the study area are attributed to *Hyndman and Weichert* (1983); *Weichert and Hyndman* (1983) and *Pezzopane and Weldon* (1993).

A summary of seismic slip estimates by *Hyndman* (pers. comm, 1997) along the northern part of the CSZ forearc is shown in Figure 5.7. These estimates are based on seismicity records by integration of magnitude-recurrence relations (*Hyndman and Weichert*, 1983). The upper limit of the estimated seismic slip rate (9.0 mm/yr) by *Hyndman* (pers. comm, 1997) results from
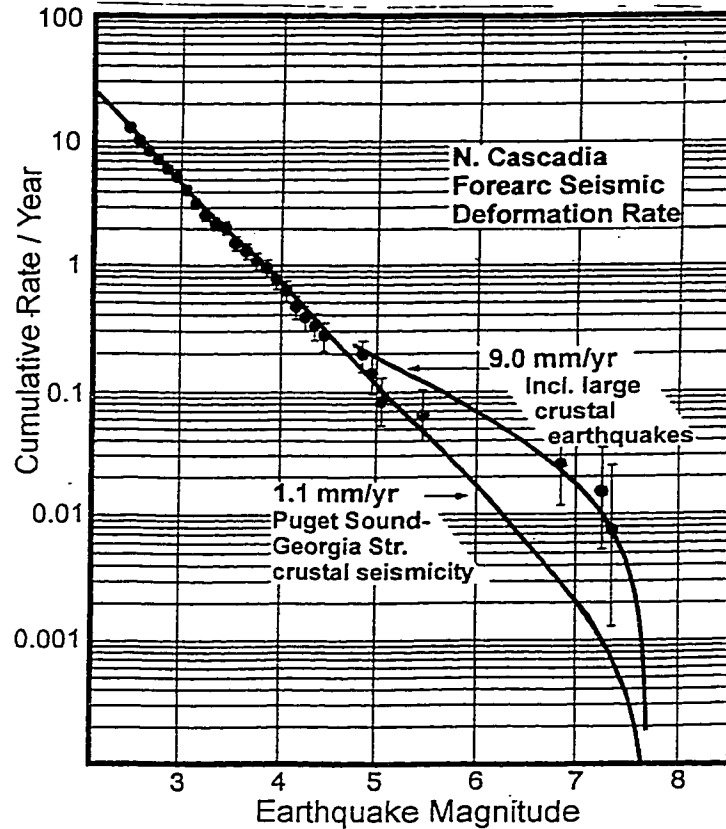
Figure 5.7: Cumulative recurrence plot for the northern Cascadia forearc seismicity from *Hyndman* (pers. comm, 1997). *9.0* mm/yr represents an *upper limit* of the seismic slip rate that is based on the seismicity record which includes *two* large crustal earthquakes from northern Vancouver Island in 1918 (M7.0) and 1943 (M7.3) and *one* event from Washington in 1872 (M7.4). *1.1* mm/yr represents a *lower limit* for the seismic slip rate based on the seismicity in the Puget Lowland and Georgia Strait only. The latter is more representative for the area considered in this study. See *Hyndman and Weichert* (1983) and *Weichert and Hyndman* (1983) for the details of estimating seismic slip rates from seismic moment, magnitude and recurrence relationships.

including *two* large crustal earthquakes from northern Vancouver Island in 1918 (M7.0) and 1943 (M7.3) and *one* earthquake from northern Washington State in 1872 (M7.4). The lower limit of the estimated seismic slip (1.1 mm/yr) is based on seismicity in the Puget Lowland and Georgia Strait only and excludes these three large crustal events. The area used to calculate the latter estimate more closely resembles the study area and, hence, the 1.1 mm/yr seismic slip rate calculated by *Hyndman* (pers. comm, 1997) is deemed to be more representative for this study. Uncertainties in the seismic slip rate estimates quoted by *Hyndman and Weichert* (1983) may be

up to twice as large as the estimated values. At the time of publication (i.e 1983) *Hyndman and Weichert* (1983) argued that "a gross discrepancy" between the seismic slip rates along the CSZ (i.e. 1.1 to 9 mm/yr) and the relative plate convergence rate of ~40 mm/yr is either due to the presence of aseismic creep or elastic strain accumulation not yet released during the period of seismicity catalog.

Another estimate of the seismic strain in the vicinity of the study area is given by *Pezzopane and Weldon* (1993), who based their calculation on the moment tensor summation method outlined in the previous section. They have estimated components of the cumulative moment tensor and consequently the seismic strain rates in the four separate zones along the western margin of North America (Figure 5.8). This method of estimating seismic slip rates has an advantage over the method used by *Hyndman and Weichert* (1983) because the preferred orientation of earthquake slip vectors can be determined as well as the slip rate.

None of the regions used by *Pezzopane and Weldon* (1993) overlap the study area exactly (Figure 5.8). Nevertheless, region b which the authors refer to as the "Central Washington" region does cover approximately 2/3 of the study area and can be considered representative for a seismic strain rate estimate in the study area as well. *Pezzopane and Weldon* (1993) estimated that there is a factor of 2 or 3 uncertainty for the estimates of cumulative moment tensors. Therefore, there is the same factor of uncertainty in seismic strain and slip estimates.

The cumulative moment tensor of $\Sigma M_{total} = 11.8 \cdot 10^{19}$ N·m was obtained by *Pezzopane and Weldon* (1993) by summation of moment tensors for 20 earthquakes, including the 1872 North Cascades earthquake (M7.3) discussed in section 1.2.4 and the 1936 Milton-Freewater, Oregon earthquake (M6.4) (*Ludwin et al.*, 1991) (both events are indicated by arrows in Figure 5.8). The 1936 event was not considered in the seismicity section of chapter I, since it occurred outside the study area. Unless these two historic events are included in the estimation of the cumulative moment tensor for the region b, the cumulative moment tensor calculated by *Pezzopane and Weldon* (1993) is only $0.06 \cdot 10^{19}$ N·m, which results in insignificant estimated slip rates (<0.1 mm/yr).

Below I present estimates for the seismic strain rate $\bar{\varepsilon}$ calculated using Equation 5.6 and the slip rate $\bar{v}$ which is obtained by multiplying $\bar{\varepsilon}$ by the length of the deforming zone L. I used L=450 km which is the width of the deforming zones chosen by *Pezzopane and Weldon* (1993). Table
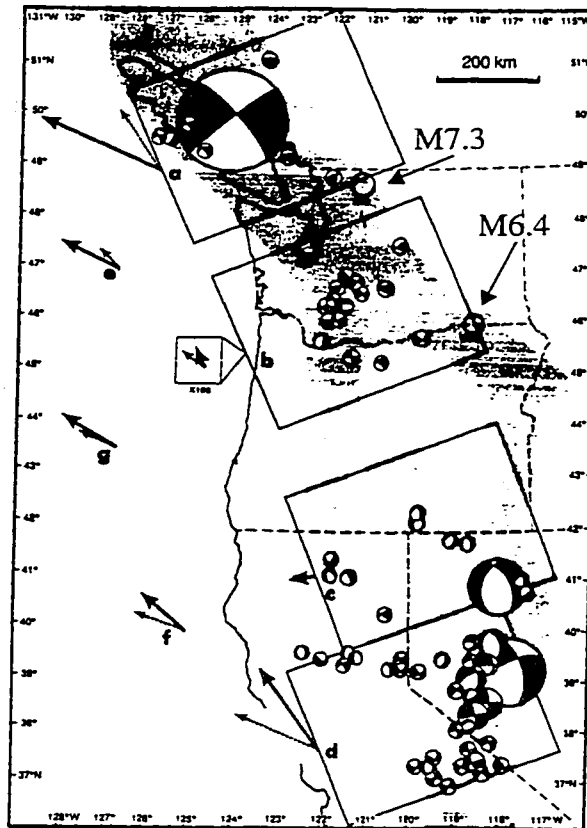
Figure 5.8: Deforming zones and earthquakes used in seismic strain calculation by *Pezzopane and Weldon* (1993). The dimension of each zone equals 350 km (in direction N20°W) by 450 km (in direction N70°E).

5.4 below includes the estimates of seismic strain and slip rates integrated to three different depths of seismicity (i.e. the depth of the seismogenic volume): 10, 15 and 30 km. Discussion of estimated seismic rates follows in the next section.

Table 5.4: Seismic strain and slip estimates after *Pezzopane and Weldon* (1993).

Seismogenic Volume Depth (km)	Strain Rate (μstrain/yr) $\overline{\varepsilon}$	Slip Rate (mm/yr) $\underline{u}$	Azimuth[a] (degrees)
10	-0.009	4.3	
15	-0.006	2.8	338°±30
30	-0.003	1.4	

a. Indicates the overall direction of deformation measured clockwise from North.

Comparing Seismic and Geodetic Strains

The estimate of the seismic strain rate presented in Table 5.4, although crude, makes a useful comparison against the geodetic strain rate estimates presented earlier. The comparison of the seismic strain rate estimates to the geodetic strain rates based not only on the "raw"[6] GPS estimated velocities (shown in Figure 3.10 and listed in Table 3.3) but also to the strain rates calculated from the "residual" velocity field (shown in Figure 5.5 and listed in Table 5.1).

Table 5.5: Comparison of seismic and geodetic strain estimates.

Geodetic Strain Rate					Seismic Strain Rate (µstrain/yr)	
"raw"			"residual"			
$\varepsilon_2{}^a \pm 1\sigma$	$\varepsilon_1{}^b \pm 1\sigma$	$\Theta^c \pm 1\sigma$	$\varepsilon_2 \pm 1\sigma$	$\Theta \pm 1\sigma$	$\overline{\varepsilon} \pm 2\overline{\varepsilon}{}^d$	Θ^b
-0.048±0.006	-0.004±0.005	75 ± 1	-0.013±0.005	-12±2	-0.003±0.006	-22±30

a. Maximum principal strain rate in µstrain/yr. Negative value is compression represented by inward pointing arrows.
b. Minimum principal strain rate in µstrain/yr. Negative value is compression represented by inward pointing arrows.
c. Azimuth of ε_2 and $\overline{\varepsilon}$ in degrees measured clockwise from North with 1σ errors.
d. I use factor of 2 uncertainty for the seismic strain estimates as suggested by *Pezzopane and Weldon* (1993).

If we concentrate our attention on the estimates of the geodetic strain for the subregion ALL^7 and the seismic strain rates for a seismogenic depth of 30 km^8 it is evident that the seismic strain rate estimate ($\overline{\varepsilon}$ = -0.003 µstrain/yr) is an order of magnitude less than the estimate of *maximum* principal strain rate based on the "raw" geodetic observations (ε_2 = -0.048 µstrain/yr). In addition, the orientation of the two strain estimates differs from each other by ~100° (N75°E and N22°W respectively), which remains a significant discrepancy even if we take into account the high level of uncertainty associated with the seismic strain rate direction (±30°). However, the

---

6. "raw" here is used to denote the observed velocity field, which represents a snapshot of contemporary crustal deformation.
7. ALL includes the entire set of 6 continuous and 38 "campaign" GPS stations. Thus, when considering strain rate estimates for this region, one has to keep in mind that the strain is assumed to be uniform within the entire area which is a gross simplification of the actual strain field. This is illustrated by the range of calculated strain rate values for different subregions (see section 3.4 for detailed discussion).
8. 30 km depth for the seismogenic zone is the preferred value, since crustal seismicity in western Washington extends to this depth (see Figure 1.10).

corresponding *minimum* principal strain rate estimate ($\dot{\varepsilon}_1$ = -0.004 μstrain/yr), determined from the "raw" GPS velocities, agrees with the seismic strain rate estimate much better (Table 5.5).

Thus, I conclude that the seismic strain rate estimates within the study area do not resemble geodetically estimated maximum principal strain rates and tend to grossly underestimate the average rate of shortening in the crust compared to the rates deduced from the GPS observations (as well as the previous geodetic results discussed in section 1.3.3). This discrepancy in the seismic and geodetic strain rate estimates (often referred to as "seismic slip deficit") in western Washington State, can be explained either by the presence of a significant component of aseismic strain accumulation due to locking of the subduction thrust interface or the existence of overdue earthquake(s) (e.g. *Norabuena et al.*, 1998). However, this explanation is not appropriate for the CSZ, since the geodetically determined maximum principal strain rate reflects the NE inter-seismic elastic strain accumulation of the subduction process, whereas the seismic strain rate estimate, since it is based on crustal seismicity data, reflects the N-S oriented state of stress within the crust of the overriding NA plate. Thus, it is not surprising that the two estimates of strain rate are not similar and hence, a presence of the "seismic slip deficit" is not justified.

To achieve further insight into the relationship between the geodetic and seismic strain rates in western Washington and its effect on seismic hazard, it is necessary to examine either the minimum principal strain rate (discussed above) or the "residual" geodetic strain estimates obtained by subtracting component-wise the "preferred" model predicted values (Table D.3) from the observed velocities (Tables D.1 and D.2). The estimated value for the "residual" maximum principal strain rate, -0.013±0.005 μstrain/yr in the direction N12°W±2°, agrees well with the seismic strain rate estimates (-0.006±0.012 μstrain/yr in the direction N22°E±30°) as well as with the minimum principal strain rate estimate based on "raw" GPS velocities (-0.004±0.005 μstrain/ yr in the direction N15°W±1°). These comparisons are summarized in Table 5.5.

Based on the above discussion, it can be concluded that the major part of the GPS measured crustal deformation rates in western Washington State is mainly due to inter-seismic elastic strain accumulation caused by locking of the thrust interface along the CSZ. However, there is a suggestion of a north-south oriented secondary signal in the GPS measured deformation rates which can be related to present day crustal seismicity (through the seismic strain rate estimates presented in Table 5.4), known to be characterized by predominantly north-south oriented

maximum principal stress direction (*Ma*, 1988; *Qamar and Ludwin*, 1992; *Ma et al.*, 1996). This stress orientation has been suggested to reflect an absolute state of stress field in the crust of western Washington (*Sbar*, 1983; *Wang*, 1995) which most likely represents a long-term deformation pattern directed parallel to the plate margin (i.e. north-south).

5.3.3 Calculating the Size of a Crustal Earthquake from Geodetic Strain Rates

In section 5.3.1 I have provided an estimate for the maximum magnitude of a *subduction* type earthquake along the CSZ. However, this type of earthquake is only one of the three different types of earthquakes that occur in western Washington (see section 1.2.4). Crustal earthquakes on major shallow faults in Washington and Oregon (e.g Seattle fault) may pose a more direct threat to populated regions than megathrust type earthquakes on the CSZ. GPS estimated crustal deformation rates presented in this study can be used to estimate the seismic hazard in western Washington associated with crustal earthquakes.

This type of seismic hazard estimate is based on the idea that, besides the subduction related short-term deformation, GPS determined velocities in western Washington also include long-term signal of deformation (i.e. north-south oriented compression). This effect has been illustrated in Figure 5.4a, where I presented the evidence for the existence of north-south directed strain (approximately -0.013 μstrain/yr) in the "residual" velocities which were obtained by subtracting effects of the subduction related elastic strain accumulation from the observed velocities. If we assume that this shortening rate is indeed real and represents an average geodetic strain rate accumulated in the crust of western Washington, we can reverse the procedure followed by *Pezzopane and Weldon* (1993) and calculate a maximum possible earthquake magnitude in a given time period based on the geodetically estimated strain rate.

We can do so if we rewrite *Kostrov's* formula given in Equation 5.6 as follows:

$$\sum_{n=1}^{N} M_{22}^{n} = 2\mu V \tau \bar{e} = \frac{2\mu V \tau \bar{u}}{L} \qquad \text{(EQ 5.7)}$$

where V is the volume of the deforming zone; τ represents a hypothetical observation time (here I use 80-120 years); $\bar{v}$ represents the slip rate; choice of i and j indices for the moment tensor in Equation 5.7 is based on the assumption that all the deformation occurs in the N-S direction and

the coordinate frame, x_1 and x_2, is oriented in E-W and N-S directions, respectively (*Jackson and McKenzie*, 1988).

Using the approximate dimensions of the study area the following dimensions for the deforming zone V were chosen: north-south length L=250 km, east-west width W=330 km and depth of the seismogenic zone D=30 km (see Footnote 8). For the slip rate ($\bar{u}$) I assumed that only the north-south oriented "raw' or "residual" strain rates are related to the crustal seismicity and thus, I used three different values ranging from 1 to 4 mm/yr, which correspond to the "raw" minimum principal strain rate estimate of -0.004 µstrain/yr (see ALL in Table 3.3) and the "residual" maximum principal strain rate estimate of -0.013 µstrain/yr (see ALL in Table 5.1), calculated over the N-S extent of the study area (i.e. 250 km).

If we assume that the cumulative moment tensor calculated using Equation 5.7 is due to only one big earthquake[9] and use the parameters described above in Equation 5.1, we can calculate the size and recurrence time of the hypothetical earthquake in the crust of Washington (Figure 5.9).
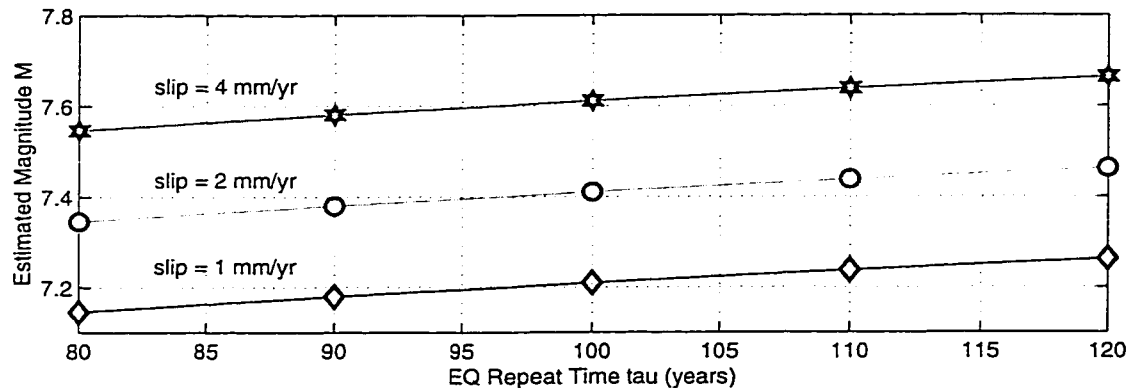
Figure 5.9: Maximum size of a crustal type earthquakes calculated based on geodetically estimated slip rates. Considered geodetic slip rates included: $\bar{v}$ = 1, 2 and 4 mm/yr. Considered τ recurrence times ranged from 80 to 120 years. Adopted dimensions of the deforming zone approximating the study area were: E-W width: 330 km; N-S length 250 km; seismogenic zone depth: 30 km.

The upper curve in Figure 5.9 suggests that one ~M7.6 earthquake every 100 years is required in western Washington to account for the 4 mm/yr slip rate estimated from the "residual" maximum

---

9. This is a reasonable assumption since no more than one M6-7 event has occurred in western Washington since 1900. The last M7.3 event occurred in 1872.

principal strain rate of -0.013 μstrain/yr oriented roughly north-south in the direction N12°W±2° (Table 5.1). The seismic moment for this slip rate calculated using Equation 5.7 is $2.6 \cdot 10^{20}$ N·m. Alternatively, the same amount of seismic moment (and the corresponding seismic slip) can be released in the same amount of time (i.e. 100 years) either in *8* M7.0 or *250* M6.0 earthquakes.

On the other hand, the lower curve in Figure 5.9 suggests that one M7.2 earthquake every 100 years is required in western Washington to account for the 1 mm/yr slip rate estimated from the "raw" minimum principal strain rate of -0.004 μstrain/yr oriented roughly north-south in the direction N16°W±1° (Table 3.3). The seismic moment for this slip rate calculated using Equation 5.7 is $6.5 \cdot 10^{19}$ N·m. Alternatively, the same amount of seismic moment (and the corresponding seismic slip) can be released in the same amount of time (i.e. 100 years) either in *2* M7.0 or *63* M6.0 earthquakes.

Regardless, whether we adopt the seismic slip rate estimates based on "raw" or "residual" strain rates (corresponding to the lower and the upper curves in Figure 5.9, respectively), if we assume that these rates are representative of the crustal seismicity in western Washington, then at least one M7+ event or half a dozen M6.0 earthquakes should have been recorded within the study area in the past century. Since not more than *one* event larger than M6 (*Noson et al.*, 1988) has been recorded within the crust of western Washington in this time period[10], it can be suggested that the observed geodetic strain rates require the occurrence of at least one M7+ earthquake each century. This type of event(s) could cause significant damage to the densely populated areas in the Puget Sound area. Earthquakes of this size are not completely uncommon in western Washington. Besides the M7.4 1872 North Cascades Earthquake, there is also evidence that 1100 years ago an earthquake exceeding M7.0 occurred on the Seattle fault (e.g. *Bucknam et al.*, 1992). However, the recurrence time of such events on the Seattle fault is probably at least 1000 years. The geologically determined rate of seismic slip accumulation on the Seattle fault is of the order of 0.1 mm/yr (*Johnson et al.*, 1994). That leaves us with a deficit of more than 3 mm/yr in the geodetically estimated N-S slip rates. To account for the observed slip rate would require the

---

10. Note that the given discussion is concerned with *crustal* earthquakes and not the *deep* (intra-slab) earthquakes, like the 1949 M7.1 Olympia and 1965 M6.6 Seattle earthquakes, which occurred within the subducting JDF plate at more than 50 km depth (see section 1.2.4 for references and further details). It is not clear how geodetic measurements on the surface could be used to determine seismic hazard associated with these type of events.

existence of 30 other faults similar to the Seattle fault. However, less than a dozen faults have been identified in the Puget Lowland (e.g *Johnson et al.,* 1994; 1996).

It is possible that part of the geodetically observed slip is accommodated by It is also possible that my approach of first subtracting the JDF/NA subduction related signal from the observed velocities and then analyzing the "residual" field is contaminated by a transient signal, perhaps associated with irregularities in the along-strike coupling properties of the locked zone (*K. Creager*, pers. comm.).

The alternative explanations for the absence of sufficient number of strong earthquakes required by the measured geodetic strain rates include: *1)* the significant portion of the crust deforms aseismically (e.g. by creeping); *2)* geodetically estimated "instantaneous" (i.e. 2-3 years for the given study) strain rates are nor representative for rates averaged over recurrence times of crustal earthquakes on individual faults (>1000years); *3)* the adopted approach of first subtracting the JDF/NA subduction related signal from the observed velocities and then analyzing the "residual" field is contaminated by a transient signal, perhaps associated with irregularities in the along-strike coupling properties of the locked zone (*K. Creager*, pers. comm.)

Unfortunately, at this stage I am not able to provide a definitive answer to the above questions but the ground has been laid for further investigations. With more data and increased precision in geodetic measurements these crucial problems can be resolved.

VI. Conclusions

6.1 Main Conclusions

More that three years of continuous and "campaign" style GPS measurements indicate that contemporary crustal deformation rates in western Washington are mainly influenced by the convergence of the Juan de Fuca and North America plates. These results confirm earlier findings that the thrust interface between the JDF and NA plates is locked and elastic strain accumulates towards the next great subduction earthquake (e.g. *Dragert et al.*, 1994). The GPS measurements show that 1) the directions of the observed horizontal velocities are roughly parallel to the direction of JDF/NA relative plate convergence and 2) velocities decrease away from the deformation front (i.e. from west to east). These two observations do not come as a surprise and are in agreement with previous geodetic measurements (e.g. *Savage et al.*, 1991; *Dragert et al.*, 1994). These conclusions support the hypothesis that the geodetic estimate of crustal deformation in the Pacific Northwest (including the GPS measurements presented in this study) are mainly sensitive to short term stress variations, reflecting elastic strain accumulation during the inter-seismic period between large megathrust earthquakes on the Cascadia Subduction Zone (CSZ) (*Sbar*, 1983; *Wang*, 1995).

Three-dimensional elastic dislocation modeling results presented in chapter IV support the conclusions drawn above. In addition, elastic dislocation modeling provides a refined estimate for the extent of the seismogenic zone (i.e. locked and transition zones) along the JDF/NA thrust interface that is still consistent with a maximum hypothetical size for a subduction type earthquake along the CSZ of $M_w9.1$. However, the greater seismogenic width of the "preferred" dislocation model brings the potential rupture zone about 30 km closer to Puget Lowland. Theoretically, this could cause stronger ground motions and, consequently, increase the seismic hazard associated with the great subduction type earthquakes in the Seattle-Olympia metropolitan area. Further studies are needed in order to quantify this important suggestion.

Although the subduction related signal dominates the observed GPS velocity field, there is also evidence for an additional north-south oriented compression in the observed velocities. To isolate this signal from the subduction related signal the dislocation model predictions must be subtracted from the observed velocities, yielding the "residual" velocity field. However, since the "residual"

velocity field has the dislocation model predictions imbedded in it, errors in the model will be transferred directly to the "residual" field. Therefore, one has to exercise caution when talking about the north-south oriented strain deduced from the "residual" velocities. These values should not be confused with strain rates calculated directly from the observed velocities.

The "residual" velocity field in western Washington suggests the presence of north-south oriented compression at a rate of ~4 mm/yr over a north-south distance of approximately 250 km, or about -0.013 μstrain/yr. This signal presumably represents a more long-term deformation pattern than the periodic accumulation and release of elastic strain connected with subduction earthquakes and most likely is related to the occurrence of shallow earthquakes in western Washington, which are characterized by predominantly north-south oriented maximum principal stress directions (e.g. Ma et al., 1996). The main driving forces behind this N-S deformation could be ascribed to: 1) the dextral shear along the coast due to the PA/NA plate interaction; 2) the tangential component of JDF/NA oblique subduction and 3) intra-continental extension in the Basin and Range province.

To release all of the geodetically observed "residual" strain rate of -0.013 μstrain/yr (oriented roughly north-south) by earthquakes within the crust of western Washington would require one ~M7.6 or more than 200 ~M6.0 earthquakes every hundred years. This represents a significant seismic hazard. Obviously, further investigations are required to make sure that this additional signal in the observed GPS velocities is indeed real.

6.2 Future Work

The most intriguing and controversial finding of this dissertation is the hypothesis of a secondary, north-south oriented signal in the observed GPS velocities. This can be tested by the analysis of data from new PANGA continuous GPS stations located within the forearc of the CSZ and as far away from the deformation front as possible so that the subduction related signal is damped out (e.g. CHWK, SEDR and JRO1 in Figure 2.6).

By conducting one more GPS "campaign" it will be possible to increase the number of stations meeting the selection criteria used in this study (Figure 2.9) by ~50%. And thus, substantially improve the spatial resolution of the velocity field. It is recommended that GPS "campaigns" consist of at least three daily occupations (>8 hours) at each site. This would significantly

increase the precision in achieved position (and velocity) estimates. Also, it would be beneficial to survey simultaneously with the main marker a nearby located reference point, which would provide a useful constraint on the question of geodetic marker stability.

The use of antenna phase elevation dependence calibration results will increase the precision of position (and velocity) estimates and will eventually make it possible to measure tectonic uplift rates using GPS technology.

The suggestion of higher levels of ground shaking in the Puget Lowland due to ~30 km more landward extent of the seismogenic zone, as compared to previous models, has to be further quantified by ground motion modeling.

Dislocation modeling results can benefit from a refined and updated geometry for the Juan de Fuca slab.

The seismic strain estimate should be done for the study area using the most recent seismicity data and moment tensor solutions.

Subregions for strain tensor determination should be chosen based on the best geologic and tectonic information. This would facilitate the interpretation of the measurements especially with regard to rigid body motion parameters.

Bibliography

Aki, K., and P.G. Richards, *Quantitative Seismology*, 557 pp., W. H. Freeman and Company, New York, USA, 1980.

Ando, M., and E.I. Balazs, Geodetic evidence for aseismic subduction of the Juan de Fuca Plate, *J. Geophys. Res.*, 84 (6), 3023-3028, 1979.

Argus, D.F., and M.B. Heflin, Plate motion and crustal deformation estimated with geodetic data from the Global Positioning System, *Geophys. Res. Lett.*, 22 (15), 1973-1976, 1995.

Argus, D.E., and R.G. Gordon, Tests of the rigid-plate hypothesis and bounds on intraplate deformation using geodetic data from very long baseline interferometry, *J. Geophys. Res.*, 101 (6), 13,555-13,572, 1996.

Atwater, B.F., M. Stuiver, and D.K. Yamaguchi, Radiocarbon test of earthquake magnitude at the Cascadia subduction zone, *Nature*, 353 (6340), 156-158, 1991.

Atwater, B.F., Geologic evidence for earthquakes during the past 2000 years along the Copalis River, southern coastal Washington, *J. Geophys. Res.*, 97 (2), 1901-1919, 1992.

Atwater, B.F., A.R. Nelson, J.J. Clague, G.A. Carver, D.K. Yamaguchi, P.T. Bobrowsky, J. Bourgeois, M.E. Darienzo, W.C. Grant, E. Hemphill-Haley, H.M. Kelsey, G.C. Jacoby, S.P. Nishenko, S.P. Palmer, C.D. Peterson, and M.A. Reinhart, Summary of coastal geologic evidence for past great earthquakes at the Cascadia subduction zone, *Earthquake Spectra*, 11 (1), 1-18, 1995.

Atwater, B.F., Coastal evidence for great earthquakes in western Washington, *U. S. Geological Survey Professional Paper*, 1560, 77-90, 1996.

Babcock, R.S., R.F. Burmester, D.C. Engebretson, A. Warnock, and K.P. Clark, A rifted margin origin for the Crescent basalts and related rocks in the northern Coast Range volcanic province, Washington and British Columbia, *J. Geophys. Res.*, 97 (5), 6799-6821, 1992.

Bar-Sever, Y.E., P.M. Kroger, and J.A. Borjesson, Estimating horizontal gradients of tropospheric path delay with a single GPS receiver, *J. Geophys. Res.*, 103 (3), 5019-5035, 1998.

Beck, M.E., Jr., R.F. Burmester, D.E. Craig, C.S. Gromme, and R.E. Wells, Paleomagnetism of middle Tertiary volcanic rocks from the Western Cascade Series, Northern California, *J. Geophys. Res.*, 91 (8), 8219-8230, 1986.

Beck, M. E. Jr., On the nature of buttressing in margin-parallel strike-slip fault systems, *Geology*, 21 (8), 755-758, 1993.

Beutler, G., I.I. Mueller, and R.E. Neilan, The International GPS Service for Geodynamics (IGS): development and start of official service on January 1, 1994, Bulletin Geodésiqué, 68, 1, 1994.

Bierman, G.J., *Factorization methods for discrete sequential estimation*, Academic Press, New York, NY, 1977.

Blackwell, D.D., J.L. Steele, S. Kelley, and M.A. Korosec, Heat flow in the state of Washington and thermal conditions in the Cascade Range, *J. Geophys. Res.*, 95 (12), 19,495-19,516, 1990.

Blakely, R.J., and R.C. Jachens, Volcanism, isostatic residual gravity, and regional tectonic setting of the Cascade volcanic province, *J. Geophys. Res.*, 95 (12), 19, 1990.

Blewitt, G., Carrier phase ambiguity resolution for the Global Positioning System applied to geodetic baselines up to 2000 km, *J. Geophys. Res.*, 94 (8), 10,187-11,203, 1989.

Blewitt, G., An automatic editing algorithm for GPS data, *Geophys. Res. Lett.*, 17 (3), 199-202, 1990.

Blewitt, G., M.B. Heflin, F.H. Webb, U.J. Lindqwister, and R.P. Malla, Global coordinates with centimeter accuracy in the International Terrestrial Reference Frame using GPS, *Geophys. Res. Lett.*, 19 (9), 853-856, 1992.

Blewitt, G., Advances in Global Positioning System technology for geodynamics investigations: 1978-1992, in *Contributions of Space Geodesy to Geodynamics Technology*, Geodyn. Ser., edited by D.E. Smith, and D.L. Turcotte, pp. 195-213, AGU, Washington, D.C., 1993.

Blewitt, G., M.B. Heflin, K.J. Hurst, D.C. Jefferson, F.H. Webb, and J.F. Zumberge, Absolute far-field displacements from the 28 June 1992 Landers earthquake sequence, *Nature*, 361 (6410), 340-342, 1993.

Bock, Y., D.C. Agnew, P. Fang, J.F. Genrich, B.H. Hager, T.A. Herring, K.W. Hudnut, R.W. King, S. Larsen, J.B. Minster, K. Stark, S. Wdowinski, and W.F. K., Detection of crustal deformation from the Landers earthquake sequence using continuous geodetic measurements, *Nature*, 361 (6410), 337-340, 1993.

Bolt, B.A., *Earthquakes*, 331 pp., W. H. Freeman and Company, New York, USA, 1993.

Bostock, M.G., and J.C. Van Decar, Upper mantle structure of the northern Cascadia subduction zone, *Can. J. Earth Sci.*, *32* (1), 1-12, 1995.

Brandon, M.T., and A.R. Calderwood, High-pressure metamorphism and uplift of the Olympic subduction complex, *Geology*, 18 (12), 1252-1255, 1990.

Brandon, M.T., and J.A. Vance, Tectonic evolution of the Cenozoic Olympic subduction complex, Washington State, as deduced from fission track ages for detrital zircons, *Amer. J. of Sci.*, 22 (8), 565-636, 1992.

Brandon, M.T., M.K. Roden, and J.I. Garver, Late Cenozoic exhumation of the Cascadia accretionary wedge in the Olympic Mountains, Northwest Washington State, *Geol. Soc. Am. Bull.*, 110 (8), 985-1009, 1998.

Brune, J.N., Seismic moment, seismicity, and rate of slip along major fault zones, *J. Geophys. Res.*, *73* (2), 777-784, 1968.

Bucknam, R.C., H.E. Hemphill, and E.B. Leopold, Abrupt uplift within the past 1700 years at southern Puget Sound, Washington, *Science*, 258 (5088), 1611-1614, 1992.

Byrne, D.E., D.M. Davis, and L.R. Sykes, Loci and maximum size of thrust earthquakes and the mechanics of the shallow region of subduction zones, *Tectonics, 7* (4), 833-857, 1988.

Cassidy, J.F., Teleseismic receiver function analysis of the crust and upper mantle of southwestern British Columbia, *Ph. D. Thesis*, University of British Columbia, Vancouver, BC, Canada, 1991.

Cassidy, J.F., A comparison of the receiver structure beneath stations of the Canadian National Seismograph Network, *Can. J. Earth Sci.*, 32, 938-951, 1995.

Chadwell, C.D., F.N. Spiess, L.E. Young, G.H. Purcell, and H. Dragert, Present-day Convergence of the Juan de Fuca and North American plates measured with GPS/Acoustic positioning of a Seafloor Reference Point, *EOS, Trans. AGU*, 1998.

Clowes, R.M., M.T. Brandon, A.G. Green, C.J. Yorath, A. Sutherland Brown, E.R. Kanasewich, and C. Spencer, LITHOPROBE-southern Vancouver Island: Cenozoic subduction complex imaged by deep seismic reflections, *Can. J. Earth Sci.*, *24*, 31-51, 1987.

Clowes, R.M., C.A. Zelt, J.R. Amor, and E.R. M., Lithospheric structure in the southern Canadian Cordillera from a network of seismic refraction lines, *Can. J. Earth Sci.*, *32* (10), 1485-1513, 1995.

Cox, A., and R.B. Hart, *Plate tectonics: how it works*, 392 pp., Blackwell Scientific Publications, Palo Alto, California, USA, 1986.

Crosson, R.S., Small earthquakes, structure, and tectonics of the Puget Sound region, *Bull. Seismol. Soc. Amer.*, 62 (5), 1133-1171, 1972.

Crosson, R.S., and T.J. Owens, Slab geometry of the Cascadia subduction zone beneath Washington from earthquake hypocenters and teleseismic converted waves, *Geophys. Res. Lett.*, 14 (8), 824-827, 1987.

Dana, P.H., The Geographer's Craft Project, Department of Geography, The University of Texas at Austin, 1998.

Davis, J.L., T.A. Herring, T.A. Shapiro, A.E. Rogers, and G. Elgered, Geodesy by radio interferometry: Effects of modelling errors on estimates of baseline length, *Radio Science*, 20, 1593-1607, 1985.

DeMets, C., R.G. Gordon, D.F. Argus, and S. Stein, Current plate motions, *Geophys. J. Int.*, 101 (2), 425-478, 1990.

DeMets, C., R.G. Gordon, D.F. Argus, and S. Stein, Effect of recent revisions to the geomagnetic reversal time scale on estimates of current plate motions, *Geophys. Res. Lett.*, 21 (20), 2191-2194, 1994.

Dewberry, S.R., and R.S. Crosson, The M (sub D) 5.0 earthquake of 29 January 1995 in the Puget Lowland of western Washington; an event on the Seattle Fault?, *Bull. Seismol. Soc. Amer.*, 86 (4), 1167-1172, 1996.

Dixon, T.H., An introduction to the Global Positioning System and some geological applications, *Rev. Geophys.*, 29 (2), 249-276, 1991.

Douglas, B.C., Global sea level rise, *J. Geophys. Res*, 96, 6891-6992, 1991.

Dragert, H., R.D. Hyndman, R.G. C., and K Wang, Current deformation and the width of the seismogenic zone of the northern Cascadia subduction thrust, *J. Geophys. Res.*, 99 (1), 653-668, 1994.

Dragert, H., and R.D. Hyndman, Continuous GPS monitoring of elastic strain in the northern Cascadia subduction zone, *Geophys. Res. Lett.*, 22 (7), 755-758, 1995.

Dragert, H., X. Chen, and J. Kouba, GPS monitoring of crustal strain in Southwest British Columbia with the Western Canada deformation array, *Geomatica*, 49 (3), 301-313, 1995.

Dragert, H., M. Schmidt, and Y. Lu, The Western Canada Deformation Array: Measuring Crustal Motions in Coastal British Columbia with Continuous GPS, *EOS, Trans. AGU*, 79 (45), F191, 1998.

Dragert, H., J.A. Henton, and G. Khazaradze, Present-day strain variations along the north Cascadia margin, *EOS, Trans. AGU*, 79 (45), F982, 1998.

Duncan, R.A., and K.D. LeVerne, Plate tectonic evolution of the Cascades arc-subduction complex, in *Neotectonics of North America*, edited by D.B. Slemmons, E.R. Engdahl, M.D. Zoback, and D.D. Blackwell, pp. 413-438, Geological Society of America, Boulder, CO, United States., 1991.

Engebretson, D.C., A. Cox, and R.G. Gordon, Relative motions between oceanic plates of the Pacific Basin, *J. Geophys. Res.*, 89 (12), 10,291-210,310, 1984.

England, P.C., and R.E. Wells, Neogene rotations and quasicontinuous deformation of the Pacific Northwest continental margin, *Geology*, 19 (10), 978-981, 1991.

Essen, L., and K.D. Froome, The refractive indices and dielectric constants of air and its principal constituents at 24000 Mc/s, *Proceedings of Physical Society of London*, 64, 862-875, 1951.

ETOPO5, Digital relief of the Surface of the Earth, NOAA, National Geophysical Data Center, Boulder, Colorado, USA, 1998.

Finn, C.A., Geophysical constraints on Washington convergent margin structure, *J. Geophys. Res.*, 95 (12), 19, 1990.

Flueh, E.R., M.A. Fisher, J. Bialas, J.R. Childs, D. Klaeschen, N. Kukowski, T. Parsons, D.W. Scholl, U. ten Brink, A.M. Trehu, and N. Vidal, New seismic images of the Cascadia subduction zone from Cruise SO108: ORWELL, *Tectonophysics*, 293, 69-84, 1998.

Flück, P., 3-D dislocation model for great earthquakes of the Cascadia subduction zone, *Diploma Thesis*, Swiss Federal Institute of Technology (ETH), Zürich, Switzerland, 1996.

Flück, P., R.D. Hyndman, and K. Wang, Three-dimensional dislocation model for great earthquakes of the Cascadia subduction zone, *J. Geophys. Res.*, 102 (9), 20,539-20,550, 1997.

Freund, L.B., and D.M. Barnett, A two-dimensional analysis of surface deformation due to sip-slip faulting, Bulletin of Seismological Society of America, 66 (3), 667-675, 1976.

Freymueller, J., *PhasEdit: and automatic data editing program for dual-frequency codeless GPS receivers*, Stanford University, 1992.

Gendt, G., IGS combination of tropospheric estimates, in *IGS 1997 annual report*, edited by R.E. Neilan, pp. 38, Jet Propulsion Laboratory, California Institute of Technology, JPL Publication 400-786, Pasadena, California, United States, 1998.

Goldfinger, C., L.D. Kulm, R.S. Yeats, L. McNeill, and C. Hummon, Oblique strike-slip faulting of the central Cascadia submarine forearc, *J. Geophys. Res.*, *102* (4), 8217-8243, 1997.

Gower, H.D., J.C. Yount, and R.S. Crosson, Seismotectonic map of the Puget Sound region, Washington, U. S. Geological Survey, Reston, VA, United States., 1985.

Gregorius, T., *GIPSY-OASIS II: How it works*, 109 pp., University of Newcastle upon Tyne, Newcastle upon Tyne, U.K., 1996.

Grossman, S.I., *Elementary Linear Algebra*, 503 pp., Saunders College Publishing, Orlando, FL, USA, 1991.

Guffanti, M., and C.S. Weaver, Distribution of late Cenozoic volcanic vents in the Cascade Range; volcanic arc segmentation and regional tectonic considerations, *J. Geophys. Res.*, 93 (6), 6513-6529, 1988.

Gurtner, W., G. Mader, and D. MacArthur, A common exchange format for GPS data, in *GPS Bulletin*, pp. 1-11, National Geodetic Survey, Rockville, Maryland, 1989.

Heaton, T.H., and H. Kanamori, Seismic potential associated with subduction in the Northwestern United States, *Bull. Seismol. Soc. Amer.*, 74 (3), 933-941, 1984.

Heflin, M., W. Bertiger, G. Blewitt, A. Freedman, K. Hurst, S. Lichten, U. Lindqwister, Y. Vigue, F. Webb, T. Yunck, and J. Zumberge, Global geodesy using GPS without fiducial sites, *Geophys. Res. Lett.*, 19 (2), 131-134, 1992.

Heller, P.L., R.W. Tabor, and C.A. Siczek, Paleogeographic evolution of the United States Pacific Northwest during Paleogene time, *Can. J. Earth Sci.*, 24, 1652-1667, 1987.

Henton, J.A., H. Dragert, R.D. Hyndman, M. Schmidt, and P. Flück, Recent crustal deformation constraints for modelling the locked portion of the Cascadia subduction zone, *Eos Trans. AGU*, 77 (46), 147-148, 1996.

Henton, J.A., H. Dragert, R.D. Hyndman, and K. Wang, Geodetic Monitoring of Crustal Deformation on Vancouver Island, *EOS, Trans. AGU*, 79 (45), F192, 1998.

Herring, T.A., and D. Dong, Measurement of diurnal and semidiurnal rotation variations and tidal parameters of Earth, *J. Geophys. Res.*, 99 (9), 18,051-018,071, 1994.

Holdahl, S.R., F. Faucher, and H. Dragert, Contemporary vertical crustal motion in the Pacific Northwest, in *Slow Deformation and Transmission of Stress in the Earth, Geophys. Monogr. Ser.*, edited by S.C. Cohen, and P. Vanicek, pp. 17-29, AGU, Washington, D.C., USA, 1989.

Hyndman, R.D., and D.H. Weichert, Seismicity and rates of relative motion on the plate boundaries of western North America, *Geophys. J. R. astr. Soc.*, 72 (1), 59-82, 1983.

Hyndman, R.D., and K. Wang, Thermal constraints on the zone of major thrust earthquake failure; the Cascadia subduction zone, *J. Geophys. Res.*, 98 (2), 2039-2060, 1993.

Hyndman, R.D., K. Wang, and M. Yamano, Thermal constraints on the seismogenic portion of the southwestern Japan subduction thrust, *J. Geophys. Res.*, 1000 (8), 15,373-315,392, 1995.

Hyndman, R.D., and K. Wang, The rupture zone of Cascadia great earthquakes from current deformation and the thermal regime, *J. Geophys. Res.*, 100 (11), 22,133-122,154, 1995.

Hyndman, R.D., M. Yamano, and D.A. Oleskevich, The seismogenic zone of subduction thrust faults, *The Island Arc*, 6 (3), 244-260, 1997.

Jackson, J., and D. McKenzie, The relationship between plate motions and seismic moment tensors, and the rates of active deformation in the Mediterranean and Middle East, *Geophysical Journal*, 93, 45-73, 1988.

James, T., Postglacial rebound in the Cascadia subduction zone, *Program with Abstracts Geological Association of Canada*, 20 (117), 1995.

Johnson, S.Y., C.J. Potter, and J.M. Armentrout, Origin and evolution of the Seattle Fault and Seattle Basin, Washington, *Geology*, 22 (1), ages 71-74, 1994.

Johnson, S.Y., C.J. Potter, J.M. Armentrout, J.J. Miller, C.A. Finn, and C.S. Weaver, The southern Whidbey Island Fault; an active structure in the Puget Lowland, Washington, *Geol. Soc. Am. Bull.*, 108 (3), 334-354, 1996.

Kanamori, H., The energy release in great earthquakes, *J. Geophys. Res.*, *82*, 2981-2987, 1977.

Kanamori, H., Tectonic implications of the 1944 Tonankai and the 1946 Nankaido earthquakes, *Phys. Earth Planet. Inter.*, *5*, 129-139, 1972.

Kato, T.,.G.S. El Fiky, E.N. Oware, and S. Miyazaki, Crustal strains in the Japanese islands as deduced from dense GPS array, *Geophys. Res. Lett.*, 25 (18), 3445-3448, 1998.

Kelsey, H.M., D.C. Engebretson, C.E. Mitchell, and R.L. Ticknor, Topographic form of the Coast Ranges of the Cascadia Margin in relation to coastal uplift rates and plate subduction, *J. Geophys. Res.*, 99 (6), 12,245-12,255, 1994.

Kelsey, H.M., Late Quaternary deformation of marine terraces on the Cascadia subduction zone near Cape Blanco, Oregon, *Tectonics*, 9 (5), 983-1014, 1990.

Kelsey, H.M., and J.G. Bockheim, Coastal landscape evolution as a function of eustasy and surface uplift rate, Cascadia margin, southern Oregon; with Suppl. Data 9426, *Geol. Soc. Am. Bull.*, 106 (6), 840-854, 1994.

Khazaradze, G., A. Qamar, and H. Dragert, Permanent GPS network in Washington, *EOS Transactions AGU*, 76 (46), F150, 1995.

Khazaradze, G., and A. Qamar, Strain accumulation rates inferred from GPS measurements in western Washington, *Seismol. Res. Lett.*, 68 (2), 316, 1997.

Kostrov, V.V., Seismic moment and energy of earthquakes, and seismic flow of rock, *Izv. Acad. Sci. USSR Phys. Solid Earth*, English Transl., 1, 13-21, 1974.

Langbein, J., and H. Johnson, Correlated errors in geodetic time series; implications for time-dependent deformation, *J. Geophys. Res.*, *102* (1), 591-604, 1997.

Lanyi, G.E., Tropospheric propagation delay effects in radio interferometric measurements, *EOS Trans. AGU*, 64 (18), 210, 1983.

Lanyi, G.E., Tropospheric delay effects in radio interferometry, pp. 152-159, Jet Propulsion Laboratory, Pasadena, USA, 1984.

Lapp, D.B., R.S. Crosson, and T.J. Owens, *P* waveform analysis for local subduction geometry south of Puget Sound, *Pure Appl. Geoph.*, *133*, 349-365, 1990.

Larson, K.M., F.H. Webb, and D.C. Agnew, Application of the Global Positioning System to crustal deformation measurement; 1, Precision and accuracy, *J. Geophys. Res.*, 96 (10), 16,547-16,565, 1991.

Leick, A., GPS satellite surveying, 560 pp., John Wiley and Sons, New York, NY, United States, 1995.

Lichten, S.M., Estimation and filtering for high-precision GPS positioning applications, *Manuscripta Geodaetica*, 15 (3), 159-176, 1990.

Lisowski, M., W.H. Prescott, H. Dragert, and S.R. Holdahl, Results from 1986 and 1987 GPS survey across the Strait of Juan de Fuca, Washington and British Columbia, *Seismol. Res. Lett.*, 60, 1, 1989.

Ludwin, R.S., C.S. Weaver, and R.S. Crosson, Seismicity of Washington and Oregon, in *Neotectonics of North America*, edited by D.B. Slemmons, E.R. Engdahl, M.D. Zoback, and D.D. Blackwell, pp. 77-97, Geological Society of America, Boulder, CO, United States., 1991.

Ma, L., R.S. Crosson, and R. Ludwin, Regional tectonic stress in western Washington from focal mechanisms of crustal and subcrustal earthquakes, *Seismol. Res. Lett.*, *59* (1), 16, 1988.

Ma, L., R.S. Crosson, and R. Ludwin, Western Washington earthquake focal mechanisms and their relationship to regional tectonic stress, *U. S. Geological Survey Professional Paper*, *1560*, 257-283, 1996.

Mader, G.L., Calibration of GPS antennas, *www.grdl.noaa.gov/GRD/GPS/Projects/ANTCAL/*, Office of Ocean and Earth *Sciences*, NGS, NOAA, Silver Spring, Maryland, USA, 1999.

Magill, J.R., R.E. Wells, R.W. Simpson, and A.V. Cox, Post 12 m.y. rotation of southwest Washington, *J. Geophys. Res.*, 87 (5), 3761-3776, 1982.

Malone, S.D., and S.S. Bor, Attenuation patterns in the Pacific Northwest based on intensity data and the location of the 1872 North Cascades earthquake, *Bull. Seismol. Soc. Amer.*, 69 (2), 531-546, 1979.

Malvern, L.E., *Introduction to the mechanics of a continuous medium*, 713 pp., Prentice-Hall, Englewood Cliffs, N.J., USA, 1969.

Mao, A., C.G.A. Harrison, and T.H. Dixon, Noise in GPS coordinate estimates, *J. Geophys. Res.*, *104*, 2797-2816, 1999.

Marone, C., and C.H. Scholz, The depth of seismic faulting and the upper transition from stable to unstable slip regimes, *Geophys. Res. Lett.*, *15* (6), 621-624, 1988.

McCaffrey, R., Oblique plate convergence, slip vectors, and forearc deformation, *J. Geophys. Res.*, 97 (6), 8905-8915, 1992.

McCaffrey, R., and C. Goldfinger, Forearc deformation and great subduction earthquakes: Implications for Cascadia offshore earthquake potential, *Science, 267*, 856-859, 1995.

McCaffrey, R., Lecture Notes: Introduction to Geophysics, *http://www.rpi.edu/~mccafr/igeoph.htm*, Rensselaer Polytechnic Institute, Troy, N.Y., USA, 1998.

McKenzie, D., and J. Jackson, The relationship between strain rates, crustal thickening, palaeomagnetism, finite strain and fault movements within a deforming zone, Earth Planet. Sci. Lett., 65 (1), 182-202, 1983.

Miller, M.M., H. Dragert, E. Endo, J.T. Freymueller, C. Goldfinger, H.M. Kelsey, E.D. Humphreys, D.J. Johnson, R. McCaffrey, J.S. Oldow, A. Qamar, and C.M. Rubin, Precise measurements help gauge Pacific Northwest's earthquake potential, EOS, Trans. AGU, 79 (23), 269, 1998.

Milne, W.G., G.C. Rogers, R.P. Riddihough, G.A. McMechan, and R.D. Hyndman, Seismicity of western Canada, *Can. J. Earth Sci.*, 15, 1170-1193, 1978.

Mitchell, C.E., P. Vincent, R.J. Weldon, and M.A. Richards, Present-day vertical deformation of the Cascadia margin, Pacific Northwest, United States, *J. Geophys. Res.*, 99 (6), 12,257-212,277, 1994.

Monger, J.W.H., R.A. Price, and D.J. Tempelman-Kluit, Tectonic accretion and the origin of the two major metamorphic and plutonic welts in the Canadian Cordillera, *Geology*, 10 (2), 70-75, 1982.

Murray, M.H., J.C. Savage, M. Lisowski, and W.K. Gross, Coseismic displacements: 1992 Landers, California, Earthquake, *Geophys. Res. Lett.*, 20 (7), 623-626, 1993.

Murray, M.H., and M. Lisowski, Strain accumulation along the Cascadia subduction zone from triangulation, trilateration, and GPS measurements, EOS, Trans. AGU, 75 (44), 178, 1994.

Murray, M.H., G.A. Marshall, M. Lisowski, and R.S. Stein, The 1992 M = Cape Mendocino, California, earthquake; coseismic deformation at the south end of the Cascadia Megathrust, *J. Geophys. Res.*, 101 (8), 17,707-17,725, 1996.

Norabuena, E., L. Leffler-Griffin, A. Mao, T. Dixon, S. Stein, S.I. Sacks, L. Ocola, and M. Ellis, Space geodetic observations of Nazca-South America convergence across the central Andes, *Science*, 279, 358-362, 1998.

Okada, Y., Surface deformation due to shear and tensile faults in a half-space, *Bull. Seismol. Soc. Amer.*, 75, 1135-1154, 1985.

Okada, Y., and E. Yamamoto, Dyke intrusion model for the 1989 seismovolcanic activity off Ito, central Japan, *J. Geophys. Res.*, 96 (6), 10,361-310,376, 1991.

Pacheco, J.F., L.R. Sykes, and C.H. Scholz, Nature of seismic coupling along simple plate boundaries of the subduction type, *J. Geophys. Res.*, 98 (8), 14,133-114,159, 1993.

Pagiatakis, S., *LSSA: Least Squares Spectral Analysis*, Geomatics Canada, Natural Resources Canada, Ottawa, Ontario, 1997.

Parsons, T., A.M. Trehu, J.H. Luetgert, K. Miller, F. Kilbride, R.E. Wells, M.A. Fisher, E. Flueh, U.S. ten Brink, and N.I. Christensen, A new view into the Cascadia subduction zone and

volcanic arc; implications for earthquake hazards along the Washington margin, *Geology, 26* (3), 199-202, 1998.

Pezzopane, S.K., and R.J. Weldon, II, Tectonic role of active faulting in central Oregon, *Tectonics,* 12 (5), 1140-1169, 1993.

Pratt, T.L., S. Johnson, C. Potter, W. Stephenson, and C. Finn, Seismic reflection images beneath Puget Sound, western Washington State; the Puget Lowland thrust sheet hypothesis, *J. Geophys. Res.,* 102 (12), 27, 1997.

Qamar, A., and R.S. Ludwin, Stress directions in Washington and northern Oregon inferred from earthquake focal mechanisms, *Seismol. Res. Lett.,* 63 (1), 28, 1992.

Qamar, A., G. Khazaradze, and H. Dragert, Crustal Deformation in Western Washington from Continuously Recording GPS, *EOS, Trans. AGU, 79* (45), F191, 1998.

Rasmussen, J., and E.D. Humphreys, Tomographic image of the Juan de Fuca Plate beneath Washington and western Oregon using teleseismic P-wave travel times, *Geophys. Res. Lett.,* 15 (12), 1417-1420, 1988.

Reilinger, R., and J. Adams, Geodetic evidence for active landward tilting of the Oregon and Washington coastal ranges, *Geophys. Res. Lett.,* 9, 401-403, 1982.

Riddihough, R.P., Recent movements of the Juan de Fuca plate system, *J. Geophys. Res,* 89 (8), 6980-6994, 1984.

Satake, K., K. Shimazaki, Y. Tsuji, and K. Ueda, Time and size of a giant earthquake in Cascadia inferred from Japanese tsunami records of January 1700, *Nature,* 379 (6562), 246-249, 1996.

Savage, J.C., M. Lisowski, and W.H. Prescott, Geodetic strain measurements in Washington, *J. Geophys. Res.,* 86, (6), 4929-4940, 1981.

Savage, J.C., A dislocation model of strain accumulation and release at a subduction zone, *J. Geophys. Res.,* 88 (6), 4984-4996, 1983.

Savage, J.C., M. Lisowski, and W.H. Prescott, Strain accumulation in western Washington, *J. Geophys. Res.*, 96 (9), 14,493-414,507, 1991.

Savage, J.C., and W. Thatcher, Interseismic deformation at the Nankai Trough, Japan, subduction zone, *J. Geophys. Res.*, *97* (7), 11,117-11,135, 1992.

Sbar, M.L., An explanation for contradictory geodetic strain and fault plane solution data in western North America, *Geophys. Res. Lett.*, *10* (3), 177-180, 1983.

Scholz, C.H., The brittle-plastic transition and the depth of seismic faulting, *Geologische Rundschau*, *77* (1), 319-328, 1988.

Scholz, C.H., *The mechanics of earthquakes and faulting*, 439 pp., Cambridge Univ. Press. Cambridge, United Kingdom., Press, 1990.

Schultz, A.P., and R.S. Crosson, Seismic velocity structure across the central Washington Cascade Range from refraction interpretation with earthquake sources, *J. Geophys. Res.*, 101 (12), 27,899-827,915, 1996.

Schupler, B.R., R.L. Allshouse, and T.A. Clark, Signal characteristics of GPS user antennas, *Navigation*, 41, 277-295, 1994.

Sillard, P., Z. Altamini, and C. Boucher, The ITRF96 realization and its associated field, *Geophys. Res. Lett.*, 25 (17), 3223-3226, 1998.

Snavely, P.D., Jr., Tertiary geologic framework, neotectonics, and petroleum potential of the Oregon-Washington continental margin, in *Geology and resource potential of the continental margin of western North America and adjacent ocean basins-Beaufort sea to Baja California*, edited by D.V. Scholl, A. Grantz, and J.G. Vedder, pp. 305-335, Circum Pacific Council for Energy and Mineral Resources, Earth *Science* Series, 1987.

Snay, R.A., and T. Matsikari, Horizontal deformation in the Cascadia subduction zone as derived from serendipitous geodetic data, *Tectonophysics*, 194, 59-67, 1991.

Sovers, O.J., and J.S. Border, Observation model and parameter partials for the JPL geodetic GPS modeling software "GPSOMC", pp. 37, Jet Propulsion Laboratory, California Institute of Technology, JPL Publication 87-21, Pasadena, California, USA, 1990.

Stanley, W.D., S.Y. Johnson, and V.F. Nuccio, Analysis of deep seismic reflection and other data from the southern Washington Cascades, in *Open File Report*, U. S. Geological Survey, Reston, VA, United States, 1994.

Stacey, F.D., *Physics of the Earth*, 513 pp., Brookfield Press, Brisbane, Australia, 1992.

Steketee, L.A., On Volterra's dislocations in a semi-infinite elastic medium, *Can. J. Phys.*, 36, 192-205, 1958a.

Steketee, L.A., Some geophysical applications of the elasticity theory of dislocations, *Can. J. Phys.*, 36, 1168, 1958b.

Strange, W.E., A national spatial data system framework continuously operating GPS reference stations., *GIS World*, 1, 37-41, 1994.

Taber, J.J., and Lewis, B.T.R., Crustal structure of the Washington continental margin from refraction data, *Bull. Seismol. Soc. Amer.*, 76 (4), 1011-1024, 1986.

Tabor, R.W., and W.M. Cady, The structure of the Olympic Mountains, Washington; analysis of a subduction zone., in *U. S. Geological Survey Professional Paper*, pp. 38, 1978.

Tichelaar, B.W., and L.J. Ruff, Depth of seismic coupling along subduction zones, *J. Geophys. Res.*, 98 (2), 2017-2037, 1993.

Tralli, D.M., T.H. Dixon, and S.A. Stephens, Effect of wet tropospheric path delays on estimation of geodetic baselines in the Gulf of California using the Global Positioning System, *J. Geophys. Res.*, 93 (6), 6545-6557, 1988.

Tralli, D.M., and S.M. Lichten, Stochastic estimation of tropospheric path delays in Global Positioning System geodetic measurements, *Bulletin Geodesique*, 64 (2), 127-159, 1990.

Tralli, D.M., M. Lichten, and T.A. Herring, Comparison of Kalman filter estimates of zenith atmospheric path delays using the Global Positioning System and very long baseline interferometry, Radio *Science*, 27 (6), 999-1007, 1992.

Tranquilla, J.M., J.P. Carr, and R.H.M. Al, Analysis of a choke ring groundplane for multipath control in Global Positioning System (GPS) applications, *IEEE Transactions on Antennas and Propagation*, 42 (7), 905-911, 1994.

Trehu, A.M., I. Asudeh, T.M. Brocher, J.H. Luetgert, W.D. Mooney, J.L. Nabelek, and Y. Nakamura, Crustal architecture of the Cascadia forearc, *Science*, 266 (5183), 237-243, 1994.

Turcotte, D.T., and G. Schubert, *Geodynamics, Applications of Continuum Physics to Geological Problems*, 450 pp., John Wiley & Sons, New York, N.Y., USA, 1982.

Tushingham, A.M., and W.R. Peltier, Ice-3G: A new global model of late Pleistocene deglaciation based upon geophysical predictions of postglacial relative sea level change, *J. Geophys. Res*, 96, 4497-4523, 1991.

Vanicek, P., and E.J. Krakiwsky, *Geodesy, the concepts*, 696 pp., Elsevier Science Publishers, Amsterdam, Netherlands, 1986.

Verdonck, D., Three-dimensional model of vertical deformation at the southern Cascadia subduction zone, Western United States, *Geology*, 23 (3), 261-264, 1995.

Vincent, P., Geodetic deformation of the Oregon Cascadia margin, *M. Sc. Thesis*, University of Oregon, Eugene, 1989.

Vrolijk, P., On the mechanical role of smectite in subduction zones, *Geology*, *18*, 703-707, 1990.

Walcott, D., Neogene tectonics and kinematics of western North America, *Tectonics*, *12* (2), 326-333, 1993.

Wang, K., H. Dragert, and H.J. Melosh, Finite element study of uplift and strain across Vancouver Island, *Can. J. Earth Sci.*, 31 (10), 1510-1522, 1994.

Wang, K., T. Maulder, G.C. Rogers, and R.D. Hyndman, Case for very low coupling stress on the Cascadia subduction fault, *J. Geophys. Res.*, 100 (7), 12,907-912,918, 1995.

Wang, K., Simplified analysis of horizontal stresses in a buttressed forearc sliver at an oblique subduction zone, *Geophys. Res. Lett.*, 23 (16), 2021-2024, 1996.

Wang, K., and H. Dragert, Strain_M: computer program to calculate average strain tensor, Pacific Geoscience Centre, Geological Survey of Canada, 1998.

Weaver, C.S., and G.E. Baker, Geometry of the Juan de Fuca plate beneath Washington and northern Oregon from seismicity, *Bull. Seismol. Soc. Amer.*, 78 (1), 264-275, 1988.

Webb, F.H., and J.F. Zumberge, *An introduction to GIPSY/OASIS II*, Jet Propulsion Laboratory, Pasadena, USA, 1997.

Wells, D.L., and K.J. Coppersmith, New empirical relationships among magnitude, rupture length, rupture width, rupture area, and surface displacements, *Bull. Seismol. Soc. Amer.*, *84* (4), 974-1002, 1994.

Wells, R.E., D.C. Engebretson, P.D.J. Snavely, and R.S. Coe, Cenozoic plate motions and the volcano-tectonic evolution of western Oregon and Washington, *Tectonics*, 3 (2), 275-294, 1984.

Wells, R.E., and R.S. Coe, Paleomagnetism and *geology* of Eocene volcanic rocks of Southwest Washington, implications for mechanisms of tectonic rotation, *J. Geophys. Res.*, 90 (2), 1925-1947, 1985.

Wells, R.E., and P.L. Heller, The relative contribution of accretion, shear, and extension to Cenozoic tectonic rotation in the Pacific Northwest, *Geol. Soc. Am. Bull.*, 100 (3), 325-338, 1988.

Wells, R.E., Paleomagnetic rotations and the Cenozoic tectonics of the Cascade arc, Washington, Oregon, and California, *J. Geophys. Res.*, 95 (12), 19,409-19,417, 1990.

Wells, R.E., C.S. Weaver, and R.J. Blakely, Fore-arc migration in Cascadia and its neotectonic significance, *Geology*, 26 (8), 759-762, 1998.

Wilson, D.S., Confidence intervals for motion and deformation of the Juan de Fuca plate, *J. Geophys. Res.*, *98* (B9), 16,053-16,071, 1993.

Weichert, D.H., and R.D. Hyndman, A comparison of the rate of seismic activity and several estimates of deformation in the Puget Sound area, *Open File Report, U. S. Geological Survey*, 105-130, 1983.

Wu, J.T., S.C. Wu, G.A. Hajj, W.I. Bertiger, and S.M. Lichten, Effects of antenna orientation on GPS carrier phase, *Manuscripta Geodaetica*, 18 (2), 91-98, 1993.

Wyatt, F.K., D.C. Agnew, and M. Gladwin, Continuous measurements of crustal deformation for the 1992 Landers earthquake sequence, *Bull. Seismol. Soc. Amer.*, 84 (3), 768-779, 1994.

Yamaguchi, D.K., B.F. Atwater, D.E. Bunker, B.E. Benson, and M.S. Reid, Tree-ring dating the 1700 Cascadia earthquake, *U. S. Geological Survey Professional Paper*, 389 (6654), 922-923, 1997.

Yunck, T.P., GPS data, acquisition, environmental effects, *Rev. Geophys.*, Supplement, 349-352, 1995.

Zhang, J., Y. Bock, H. Johnson, P. Fang, S. Williams, J. Genrich, S. Wdowinski, and J. Behr, Southern California Permanent GPS Geodetic Array: error analysis of daily position estimates and site velocities, *J. Geophys. Res.*, *102*, 18,035-18,055, 1997.

Zumberge, J.F., M.B. Heflin, D.C. Jefferson, M.M. Watkins, and F.H. Webb, Precise point positioning for the efficient and robust analysis of GPS data from large networks, *J. Geophys. Res.*, 102 (3), 5005-5017, 1997.

Appendix A - Analyzed GPS Station Information

Table A.1: IGS global GPS stations included in the analysis

#	Location	ID	Latitude	Longitude	Height	Plate
1	Algonquin Park, Ontario, Canada	ALGO	48.38978	281.92863	200.89	NOAM[a]
2	Penticton, B.C., Canada	DRAO	49.32262	240.37502	541.87	NOAM
3	Fairbanks, Alaska, USA	FAIR	64.97800	212.50076	318.99	NOAM
4	Kokee Park, Kauai, Hawaii, USA	KOKB	22.12626	200.33508	1167.36	PAC[b]
5	North Liberty, Iowa, USA	NLIB	41.77159	268.42511	207.04	NOAM

a. North America plate.
b. Pacific plate.

Table A.2: Pacific Northwest Geodetic Array (PANGA) stations.

#[a]	Location	ID	Latitude	Longitude	DATE	Agency[b]
1	Albert Head, B.C.	ALBH	48.3898	123.4875	05/04/92	GSC
2	Appleton, WA	GWEN	45.7826	121.3276	05/15/97	USCG/NGS
3	Holberg, B.C.	HOLB	50.6404	128.1350	24/06/92	GSC
4	Whistler, B.C.	WSLR	50.1265	122.9212	12/09/96	GSC
5	Penticton, B.C.	DRAO	49.3226	119.6250	27/02/91	GSC
6	Nanoose, B.C.	NANO	49.29481	124.0865	13/05/95	GSC
7	Uclulet, B.C.	UCLU	48.9256	125.5416	05/05/94	GSC
8	Chilliwack, B.C.	CHWK	49.1566	122.0084	17/10/98	GSC
9	Burns Junction, OR	BURN	42.7795	117.8435	10/09/97	UW
10	Cape Blanco, OR	CABL	42.8361	124.5633	08/09/97	CWU
11	Corvallis, OR	CORV	44.5855	123.3046	05/30/96	OSU/RPI
12	Ellensburg, WA	LIND	47.0003	120.5385	07/26/98	CWU
13	Fort Stevens, OR	FTS1	46.2049	123.9561	01/19/96	USCG/NGS
14	Goldendale, WA	GOBS	45.8388	120.8147	08/01/97	CWU
15	Johnston Ridge, WA	JRO1	46.2751	122.2176	06/01/97	CVO
16	Kelso, WA	KELS	46.1181	122.8959	10/09/97	UW
17	Neah Bay, WA	NEAH	48.2979	124.6249	07/14/95	UW/GSC
18	Newport, OR	NEWP	44.5850	124.0618	06/04/96	OSU/RPI
19	Pacific Beach, WA	PABH	47.2128	124.2046	08/01/97	CWU
20	Redmond, OR	REDM	44.2597	121.1478	07/24/98	CWU
21	Robinson Point, WA	RPT1	47.3875	122.3748	09/20/95	USCG/NGS
22	Satsop, WA	SATS	46.9657	123.5412	06/01/97	CVO
23	Seattle, WA	SEAT	47.6540	122.3095	06/14/95	UW
24	Sedro Woolley, WA	SEDR	48.5216	122.2238	10/07/97	UW
25	Whidbey Island, WA	WHD1	48.3127	122.6961	09/20/95	USCG/NGS

a. Stations included in the analysis are shown in shaded cells.

b. Abreviations for agencies and institutions responsible for station installation and maintenance: \
  UW: University of Washington;
  CWU: Central Washington University;
  GSC: Geological Survey of Canada;
  RPI: Rensselaer Polytechnic Institute;
  CVO: Cascades Volcano Observatory;
  USCG: United States Coast Guard;
  NGS: National Geodetic Survey.

Table A.3: Description of "campaign" GPS stations.

#	Code	Location	Stamping	Latitude	Longitude
1	APSA	Chehalis Airp.	STA.A_AP_1956_USCGS	46.6708	-122.9853
2	AVIA	Seattle	Aviation_2_1982_NGS	47.6857	-122.2491
3	BLUE	Blue Mtn.	Blue_Mt_1955_1981_NGS	47.9550	-123.2596
4	CENT	Central	Central_1990_NGS	46.9727	-123.7032
5	DOTT	Dotty	F64_1934	46.6312	-123.2756
6	EAST	Easton	Easton_1958_USCGS	47.2318	-121.1711
7	FARW	Elma Fairgrounds	Fair_1990_NGS	47.2701	-122.1011
8	FORK	Forks Airport	FORKS 1954 1989	47.9367	-124.3956
9	FRAN	Frances	Frances_1991_NGS	46.5414	-123.5002
10	GLDH	Gold Hill	Gold_Hill_1954_USC&GS	47.5486	-122.7867
11	GP17	Green Water	GP_17_410-8_1986_NGS	47.1375	-121.6253
12	GRAY	Grays Harbor	Grays_Harbor_E_B_2_1940_USC&GS	46.9003	-124.0997
13	GREN	Point Grenville	Grenville_XXVII_USC&GS	47.3042	-124.2787
14	HAFF	Renton	Haff_HCR_1990_NGS	47.4841	-122.1761
15	KLSO	Kelso	Kelso_KLS_1990_NGS	46.1181	-122.8959
16	LEWI	Fort Lewis	Lewis_GP_1990_USE	47.0943	-122.6207
17	LUDL	Port Ludlow	Port_Ludlow_1990	47.9216	-122.6825
18	MORT	Morton	Morton_Air_1990	46.5506	-122.2704
19	MRY1	Marymoor Park	Marymoor_Rm1_1972_NCER	47.6605	-122.1111
20	MUDD	Mud Mtn.	Mud_unreadable_USCE	47.1418	-121.9335
21	NBCG	Neah Bay	NBCG_1991_USGS	48.3669	-124.6210
22	NHD4	North Head	North_Head_No_4_1942_1987_NGS	46.3004	-124.0760
23	OLYM	Olympia	Olympia_1110_unstamped_NGS	46.9667	-122.9074
24	PTAN	Port Angeles Airp.	PORT ANGELES 1994	48.1170	-123.4945
25	PYST	Pyst	N_469_1974	48.1979	-124.1190
26	QUI2	Quillayute Airp.	QUIL AIR, 1994 CVO/USGS	47.9397	-124.5613
27	QUIL	Quillayute Airp.	FAA UIL A 1992	47.9368	-124.5614
28	SAND	Sanderson Airp.	Sanderson_1987_NGS	47.2366	-123.1413
29	SARG	Yakima	Sarg_1990_NGS	46.6024	-120.4778
30	SITA	Manchester	Sitar_Rm1_1974_NGS	47.5710	-122.5526
31	SOBE	South Bend	South_Bend_1990	46.6631	-123.8102
32	SPOO	Kent	Spoon_C_1936_King_Co.	47.4008	-122.1640
33	TAHU	Tahuya	Tahuya_1990_NGS	47.3870	-123.1128
34	TENO	Ten O'clock	TEN OCLOCK 1954	47.4789	-123.9858
35	THUN	Thun Field Airp.	THUN FIELD RESET 1994	47.1028	-122.2897
36	TIGR	Tiger Mtn.	Tiger_Ecc_1981_USGS	47.5086	-121.9851
37	WILS	Ellensburg	Wilson_1957_USCGS	47.0115	-120.5213
38	WORD	Fort Worden	Worden_USC&GS	48.1408	-122.7682

Table A.4: Occupation history of "campaign" GPS stations.

#	STA	1994	1995	1996	1997	All Years
1	APSA	7	4	4	3	18
2	AVIA	2	1	4	2	9
3	BLUE	0	1	5	2	8
4	CENT	0	3	2	4	9
5	DOTT	0	1	1	2	4
6	EAST	2	3	1	3	9
7	FARW	0	2	0	2	4
8	FORK	0	1	2	2	5
9	FRAN	4	0	1	2	7
10	GLDH	5	0	0	2	7
11	GP17	2	1	0	2	5
12	GRAY	2	3	1	4	10
13	GREN	0	2	1	4	7
14	HAFF	0	1	2	2	5
15	KLSO	0	2	15	13	30
16	LEWI	0	2	1	4	7
17	LUDL	0	1	1	2	4
18	MORT	3	0	8	2	13
19	MRY1	2	0	0	2	4
20	MUDD	2	2	0	2	6
21	NBCG	1	1	6	2	10
22	NHD4	2	0	1	1	4
23	OLYM	0	4	2	4	10
24	PTAN	1	1	8	4	14
25	PYST	0	1	1	2	4
26	QUI2	2	0	0	2	4
27	QUIL	0	1	1	2	4
28	SAND	4	5	2	11	22
29	SARG	0	1	1	1	3
30	SITA	1	1	1	2	5
31	SOBE	0	1	6	2	9
32	SPOO	1	0	2	2	5
33	TAHU	1	0	2	2	5
34	TENO	0	1	2	2	5
35	THUN	1	2	2	4	9
36	TIGR	3	0	0	2	5
37	WILS	0	2	1	3	6
38	WORD	0	1	3	2	6
	Total	48	52	90	110	300

Table A.5: 1994 "campaign" occupation history sorted by date.

#	Code	Date	DOY	Agency	AntH	Mm[a]	AntType[b]
1	APSA	08/09/94	221	CVO	1.0186	C	TRIM_SST
2	EAST	08/09/94	221	CVO	1.2786	C	TRIM_SST
3	MORT	08/09/94	221	CVO	1.4285	C	TRIM_SST
4	NBCG	08/09/94	221	UW	1.6679	C	TRIM_SST
5	PTAN	08/09/94	221	UW	1.7423	C	TRIM_SST
6	THUN	08/09/94	221	CVO	1.6265	D	ASH_GDP
7	APSA	08/10/94	222	CVO	1.0010	C	TRIM_SST
8	EAST	08/10/94	222	CVO	1.2720	C	TRIM_SST
9	FRAN	08/10/94	222	CVO	1.7800	D	ASH_GDP
10	GLDH	08/10/94	222	USGS	1.3170	B	ASH_GDP
11	NBCG	08/10/94	222	UW	1.6679	C	TRIM_SST
12	PTAN	08/10/94	222	UW	1.7507	C	TRIM_SST
13	SAND	08/10/94	222	USGS	0.5220	B	ASH_GDP
14	THUN	08/10/94	222	CVO	1.7892	D	ASH_GDP
15	APSA	08/11/94	223	CVO	0.9425	C	TRIM_SST
16	FRAN	08/11/94	223	CVO	1.8730	D	ASH_GDP
17	GLDH	08/11/94	223	USGS	1.3170	B	ASH_GDP
18	MUDD	08/11/94	223	CVO	1.4196	C	TRIM_SST
19	SAND	08/11/94	223	USGS	0.5220	B	ASH_GDP
20	APSA	08/12/94	224	CVO	0.9600	C	TRIM_SST
21	GLDH	08/12/94	224	USGS	1.3170	B	ASH_GDP
22	MORT	08/12/94	224	CVO	1.3815	C	TRIM_SST
23	SAND	08/12/94	224	USGS	0.5220	B	ASH_GDP
24	GLDH	08/13/94	225	USGS	1.3180	B	ASH_GDP
25	HAFF	08/13/94	225	USGS	1.5290	B	ASH_GDP
26	SAND	08/13/94	225	USGS	0.5220	B	ASH_GDP
27	AVIA	08/14/94	226	UW	1.6305	C	TRIM_SST
28	GLDH	08/14/94	226	USGS	1.3180	B	ASH_GDP
29	MRY1	08/14/94	226	USGS	1.5260	B	ASH_GDP
30	SAND	08/14/94	226	USGS	0.5220	B	ASH_GDP
31	SPOO	08/14/94	226	USGS	1.7100	B	ASH_GDP
32	TAHU	08/14/94	226	UW	1.5636	C	TRIM_SST
33	TIGR	08/14/94	226	USGS	1.3860	B	ASH_GDP
34	AVIA	08/15/94	227	UW	1.6265	C	TRIM_SST
35	GLDH	08/15/94	227	USGS	1.3180	B	ASH_GDP

Table A.5: 1994 "campaign" occupation history sorted by date.

#	Code	Date	DOY	Agency	AntH	Mm[a]	AntType[b]
36	MRY1	08/15/94	227	USGS	1.5410	B	ASH_GDP
37	SAND	08/15/94	227	USGS	0.5220	B	ASH_GDP
38	SITA	08/15/94	227	UW	1.7827	C	TRIM_SST
39	TIGR	08/15/94	227	USGS	1.3480	B	ASH_GDP
40	APSA	08/16/94	228	CVO	1.0400	C	TRIM_SST
41	FRAN	08/16/94	228	USGS	1.7330	B	ASH_GDP
42	GLDH	08/16/94	228	USGS	1.3160	B	ASH_GDP
43	GP17	08/16/94	228	CVO	1.4810	C	TRIM_SST
44	GRAY	08/16/94	228	CVO	1.2380	D	ASH_GDP
45	MORT	08/16/94	228	UW	1.6712	C	TRIM_SST
46	QUI2	08/16/94	228	CVO	1.4350	C	TRIM_SST
47	TIGR	08/16/94	228	USGS	1.4010	B	ASH_GDP
48	APSA	08/17/94	229	CVO	1.1096	C	TRIM_SST
49	GP17	08/17/94	229	CVO	1.4760	C	TRIM_SST
50	GRAY	08/17/94	229	CVO	1.2380	D	ASH_GDP
51	MUDD	08/17/94	229	CVO	1.6495	C	TRIM_SST
52	QUI2	08/17/94	229	CVO	1.4340	C	TRIM_SST
53	APSA	08/18/94	230	USGS	0.6120	B	ASH_GDP
54	FRAN	08/18/94	230	USGS	1.6520	B	ASH_GDP
55	NHD4	08/18/94	230	UW	1.7392	C	TRIM_SST
56	NHD4	08/19/94	231	UW	1.6951	C	TRIM_SST
57	SITA	09/13/94	256	UW	1.7513	A	TRIM_SST

a. Antenna height measuring method. See Table A.9 for details.
b. Antenna type codes are listed in Table 2.4.

Table A.6: 1995 "campaign" occupation history sorted by date.

#	Code	Date	DOY	Agency	AntH	Mm[a]	AntType[b]
1	NBCG	06/13/95	165	UW	1.5358	A	TRIM_SST
2	PYST	06/13/95	165	UW	1.5997	A	TRIM_SST
3	QUIL	06/14/95	166	UW	1.6268	A	TRIM_SST
4	FORK	06/15/95	166	UW	1.5484	A	TRIM_SST
5	GREN	06/20/95	172	UW	1.2108	A	TRIM_SST
6	TENO	06/20/95	172	UW	1.4244	A	TRIM_SST
7	CENT	06/21/95	173	UW	1.2763	A	TRIM_SST
8	GRAY	06/21/95	173	UW	1.6325	A	TRIM_SST
9	DOTT	06/22/95	173	UW	1.5712	A	TRIM_SST
10	SOBE	06/23/95	173	UW	1.4418	A	TRIM_SST
11	LEWI	06/26/95	177	UW	1.7189	A	TRIM_SST
12	HAFF	06/27/95	178	UW	1.5875	A	TRIM_SST
13	THUN	06/27/95	178	UW	1.8113	A	TRIM_SST
14	SAND	06/30/95	181	UW	1.3868	A	TRIM_SST
15	SITA	06/30/95	181	UW	1.7693	A	TRIM_SST
16	EAST	07/04/95	185	UW	1.3557	A	TRIM_SST
17	EAST	07/04/95	186	UW	1.3552	A	TRIM_SST
18	WILS	07/04/95	186	UW	1.3840	A	TRIM_SST
19	SARG	07/05/95	187	UW	1.5711	A	TRIM_SST
20	WORD	07/11/95	193	UW	1.4947	A	TRIM_SST
21	BLUE	07/12/95	193	UW	1.5644	A	TRIM_SST
22	PTAN	07/12/95	194	UW	1.6298	A	TRIM_SST
23	AVIA	07/30/95	211	UW	1.6185	A	TRIM_SST
24	APSA	08/05/95	217	USGS	0.6440	B	ASH_WHP
25	CENT	08/05/95	217	USGS	1.4060	B	ASH_GDP
26	FARW	08/05/95	217	USGS	1.4210	B	ASH_WHP
27	LEWI	08/05/95	217	USGS	1.6200	B	ASH_GDP
28	OLYM	08/05/95	217	USGS	0.4950	B	ASH_WHP
29	SAND	08/05/95	217	USGS	0.5070	B	ASH_GDP
30	APSA	08/06/95	218	USGS	0.6440	B	ASH_WHP
31	EAST	08/06/95	218	USGS	1.3400	B	ASH_GDP
32	FARW	08/06/95	218	USGS	1.4570	B	ASH_GDP
33	GRAY	08/06/95	218	USGS	1.2220	B	ASH_GDP
34	MUDD	08/06/95	218	USGS	1.6900	B	ASH_WHP
35	OLYM	08/06/95	218	USGS	0.4950	B	ASH_WHP

Table A.6: 1995 "campaign" occupation history sorted by date.

#	Code	Date	DOY	Agency	AntH	Mm [a]	AntType[b]
36	SAND	08/06/95	218	USGS	0.5070	B	ASH_GDP
37	THUN	08/06/95	218	USGS	1.6220	B	ASH_GDP
38	APSA	08/07/95	219	USGS	0.6440	B	ASH_WHP
39	CENT	08/07/95	219	USGS	1.3220	B	ASH_GDP
40	EAST	08/07/95	219	USGS	1.4090	B	ASH_GDP
41	GP17	08/07/95	219	USGS	1.4780	B	ASH_GDP
42	GRAY	08/07/95	219	USGS	1.2840	B	ASH_GDP
43	GREN	08/07/95	219	USGS	1.1960	B	ASH_GDP
44	MUDD	08/07/95	219	USGS	1.6900	B	ASH_WHP
45	OLYM	08/07/95	219	USGS	0.4950	B	ASH_WHP
46	SAND	08/07/95	219	USGS	0.5070	B	ASH_GDP
47	APSA	08/08/95	220	USGS	0.6440	B	ASH_WHP
48	OLYM	08/08/95	220	USGS	0.4950	B	ASH_WHP
49	SAND	08/08/95	220	USGS	0.5070	B	ASH_GDP
50	WILS	08/08/95	220	USGS	1.3740	B	ASH_GDP
51	Z478	08/08/95	220	USGS	1.4530	B	ASH_GDP

a. Antenna height measuring method. See Table A.9 for details.
b. Antenna type codes are listed in Table 2.4.

Table A.7: 1996 "campaign" occupation history sorted by date.

#	Code	Date	DOY	Agency	AntH	Mm[a]	AntType[b]
1	FORK	05/29/96	151	UW	1.4193	A	TRIM_SST
2	PYST	05/29/96	151	UW	1.6208	A	TRIM_SST
3	FORK	05/30/96	152	UW	1.4186	A	TRIM_SST
4	QUIL	05/30/96	152	UW	1.4148	A	TRIM_SST
5	TENO	05/31/96	153	UW	1.2501	A	TRIM_SST
6	GREN	06/01/96	153	UW	1.1536	A	TRIM_SST
7	GREN	06/01/96	154	UW	1.1517	A	TRIM_SST
8	CENT	06/02/96	155	UW	1.2223	A	TRIM_SST
9	SITA	06/06/96	158	UW	1.9625	A	TRIM_SST
10	APSA	06/10/96	162	CVO	1.4820	A	TRIM_CGP
11	MORT	06/10/96	162	CVO	1.4975	A	TRIM_CGP
12	PTAN	06/10/96	162	CVO	1.6560	B	TRIM_CHK
13	SOBE	06/10/96	162	CVO	1.4770	B	TRIM_CHK
14	TAHU	06/10/96	162	CVO	1.4820	A	TRIM_CGP
15	APSA	06/11/96	163	CVO	1.4380	A	TRIM_CGP
16	MORT	06/11/96	163	CVO	1.5113	A	TRIM_CGP
17	PTAN	06/11/96	163	CVO	1.6560	B	TRIM_CHK
18	SOBE	06/11/96	163	CVO	1.4857	B	TRIM_CHK
19	TAHU	06/11/96	163	CVO	1.6143	A	TRIM_CGP
20	AVIA	06/12/96	164	UW	1.6977	A	TRIM_SST
21	MORT	06/12/96	164	CVO	1.5103	A	TRIM_CGP
22	OLYM	06/12/96	164	CVO	1.3698	A	TRIM_CGP
23	PTAN	06/12/96	164	CVO	1.6560	B	TRIM_CHK
24	SOBE	06/12/96	164	CVO	1.4817	B	TRIM_CHK
25	SPOO	06/12/96	164	UW	1.8226	B	TRIM_CHK
26	AVIA	06/13/96	165	UW	1.7305	A	TRIM_SST
27	MORT	06/13/96	165	CVO	1.5057	A	TRIM_CGP
28	OLYM	06/13/96	165	CVO	1.4360	A	TRIM_CGP
29	PTAN	06/13/96	165	CVO	1.6560	B	TRIM_CHK
30	SOBE	06/13/96	165	CVO	1.4900	B	TRIM_CHK
31	SPOO	06/13/96	165	UW	1.8133	B	TRIM_CHK
32	HAFF	06/14/96	166	UW	1.4147	B	TRIM_CHK
33	MORT	06/14/96	166	CVO	1.5050	A	TRIM_CGP
34	PTAN	06/14/96	166	CVO	1.6560	B	TRIM_CHK
35	SAND	06/14/96	166	CVO	1.2213	A	TRIM_CGP
36	SOBE	06/14/96	166	CVO	1.4750	B	TRIM_CHK
37	HAFF	06/15/96	167	UW	1.3762	B	TRIM_CHK
38	MORT	06/15/96	167	CVO	1.5030	A	TRIM_CGP
39	PTAN	06/15/96	167	CVO	1.6560	B	TRIM_CHK
40	SAND	06/15/96	167	CVO	1.1520	A	TRIM_CGP

Table A.7: 1996 "campaign" occupation history sorted by date.

#	Code	Date	DOY	Agency	AntH	Mm[a]	AntType[b]
41	SOBE	06/15/96	167	CVO	1.4510	B	TRIM_CHK
42	LEWI	06/17/96	169	UW	1.5969	B	TRIM_CHK
43	THUN	06/17/96	169	UW	1.6941	A	TRIM_SST
44	WORD	06/17/96	170	UW	1.4943	A	TRIM_SST
45	THUN	06/18/96	170	UW	1.7638	A	TRIM_SST
46	APSA	06/20/96	172	CVO	1.4190	B	TRIM_CHK
47	MORT	06/20/96	172	CVO	1.5137	B	TRIM_CHK
48	PTAN	06/20/96	172	CVO	1.5150	B	TRIM_CHK
49	APSA	06/21/96	173	CVO	1.4190	B	TRIM_CHK
50	MORT	06/21/96	173	CVO	1.5110	B	TRIM_CHK
51	PTAN	06/21/96	173	CVO	1.5150	B	TRIM_CHK
52	TENO	06/24/96	177	UW	1.3832	A	TRIM_SST
53	CENT	06/25/96	177	UW	1.4073	A	TRIM_SST
54	GRAY	06/25/96	177	UW	1.3755	A	TRIM_SST
55	NHD4	06/25/96	178	UW	1.5260	A	TRIM_SST
56	NHD4	06/26/96	178	UW	1.5260	A	TRIM_SST
57	DOTT	06/27/96	179	UW	1.4675	A	TRIM_SST
58	FRAN	06/27/96	179	UW	1.7278	A	TRIM_SST
59	SARG	06/27/96	180	UW	1.5717	A	TRIM_SST
60	EAST	06/28/96	180	UW	1.3868	A	TRIM_SST
61	WILS	06/28/96	180	UW	1.3954	A	TRIM_SST
62	AVIA	08/04/96	217	USGS	1.6390	B	ASH_GDP
63	NBCG	08/04/96	217	USGS	1.3270	B	ASH_WHP
64	AVIA	08/05/96	218	USGS	1.5740	B	ASH_GDP
65	NBCG	08/05/96	218	USGS	1.3270	B	ASH_WHP
66	BLUE	08/06/96	219	USGS	1.5745	B	ASH_GDP
67	NBCG	08/06/96	219	USGS	1.3270	B	ASH_WHP
68	BLUE	08/07/96	220	USGS	1.4900	B	ASH_WHP
69	NBCG	08/07/96	220	USGS	1.3270	B	ASH_WHP
70	WORD	08/07/96	220	USGS	1.3150	B	ASH_GDP
71	NBCG	08/08/96	221	USGS	1.3270	B	ASH_WHP
72	NBCG	08/09/96	222	USGS	1.3270	B	ASH_WHP
73	WORD	08/09/96	222	USGS	1.3210	B	ASH_GDP
74	NBCG	08/10/96	223	USGS	1.3270	B	ASH_WHP
75	BLUE	09/06/96	250	USGS	1.4460	B	ASH_GDP
76	BLUE	09/07/96	251	USGS	1.4460	B	ASH_GDP
77	BLUE	09/10/96	254	USGS	1.4600	B	ASH_WHP

a. Antenna height measuring method. See Table A.9 for details.
b. Antenna type codes are listed in Table 2.4.

Table A.8: 1997 "campaign" occupation history sorted by date.

#	Code	Date	DOY	Agency	AntH	Mm[a]	AntType[b]
1	NBCG	05/10/97	130	UW	1.4965	B	TRIM_CHK
2	NBCG	05/11/97	131	UW	1.4965	B	TRIM_CHK
3	LEWI	06/07/97	158	UW	1.6912	B	TRIM_CHK
4	SAND	06/07/97	158	UW	1.2053	B	TRIM_CHK
5	THUN	06/07/97	158	UW	1.1000	V	TRIM_CHK
6	Z478	06/07/97	158	UW	1.4885	A	TRIM_SST
7	LEWI	06/08/97	159	UW	1.7046	B	TRIM_CHK
8	SAND	06/08/97	159	UW	1.2048	B	TRIM_CHK
9	THUN	06/08/97	159	UW	1.1000	V	TRIM_CHK
10	Z478	06/08/97	159	UW	1.4741	A	TRIM_SST
11	PTAN	06/12/97	163	UW	1.3293	B	TRIM_CHK
12	WORD	06/12/97	163	UW	1.4679	B	TRIM_CHK
13	PTAN	06/13/97	164	UW	1.3293	B	TRIM_CHK
14	WORD	06/13/97	164	UW	1.4840	B	TRIM_CHK
15	AVIA	06/16/97	167	UW	1.6888	B	TRIM_CHK
16	AVIA	06/17/97	168	UW	1.6140	B	TRIM_CHK
17	HAFF	06/18/97	169	UW	1.1000	V	TRIM_CHK
18	MRY1	06/18/97	169	UW	1.5242	A	TRIM_SST
19	SPOO	06/18/97	169	UW	1.8779	B	TRIM_CHK
20	TIGR	06/18/97	169	UW	1.4532	B	TRIM_CHK
21	HAFF	06/19/97	170	UW	1.1000	V	TRIM_CHK
22	MRY1	06/19/97	170	UW	1.5218	A	TRIM_SST
23	SPOO	06/19/97	170	UW	1.9144	B	TRIM_CHK
24	TIGR	06/19/97	170	UW	1.4528	B	TRIM_CHK
25	PTAN	06/20/97	172	UW	1.4726	B	TRIM_CHK
26	FORK	06/21/97	172	UW	1.5017	B	TRIM_CHK
27	PYST	06/21/97	172	UW	1.5983	A	TRIM_SST
28	QUI2	06/21/97	172	UW	1.5620	B	TRIM_CHK
29	QUIL	06/21/97	172	UW	1.4424	A	TRIM_SST
30	FORK	06/22/97	173	UW	1.6591	B	TRIM_CHK
31	PTAN	06/22/97	173	UW	1.4726	B	TRIM_CHK
32	PYST	06/22/97	173	UW	1.5371	A	TRIM_SST
33	QUI2	06/22/97	173	UW	1.4831	B	TRIM_CHK
34	QUIL	06/22/97	173	UW	1.5616	A	TRIM_SST
35	SITA	06/30/97	181	UW	2.1947	B	TRIM_CHK
36	TAHU	06/30/97	181	UW	1.5193	B	TRIM_CHK
37	SITA	07/01/97	182	UW	2.1909	B	TRIM_CHK

Table A.8: 1997 "campaign" occupation history sorted by date.

#	Code	Date	DOY	Agency	AntH	Mm a	AntType[b]
38	TAHU	07/01/97	182	UW	1.5247	B	TRIM_CHK
39	EAST	07/03/97	184	UW	1.1840	A	TRIM_SST
40	MORT	07/03/97	185	UW	1.6600	B	TRIM_CHK
41	MORT	07/03/97	184	UW	1.6603	B	TRIM_CHK
42	SARG	07/04/97	185	UW	1.6310	A	TRIM_SST
43	WILS	07/04/97	185	UW	1.3629	A	TRIM_SST
44	APSA	07/08/97	189	UW	1.5180	B	TRIM_CHK
45	DOTT	07/08/97	189	UW	1.4806	B	TRIM_CHK
46	FRAN	07/08/97	189	UW	1.8805	B	TRIM_CHK
47	OLYM	07/08/97	189	UW	1.5010	B	TRIM_CHK
48	APSA	07/09/97	191	UW	1.5185	B	TRIM_CHK
49	APSA	07/09/97	190	UW	1.5181	B	TRIM_CHK
50	DOTT	07/09/97	190	UW	1.3877	B	TRIM_CHK
51	FRAN	07/09/97	190	UW	1.8087	B	TRIM_CHK
52	OLYM	07/09/97	190	UW	1.5010	B	TRIM_CHK
53	NHD4	07/10/97	191	UW	1.5483	B	TRIM_CHK
54	CENT	07/14/97	195	UW	1.4223	B	TRIM_CHK
55	GRAY	07/14/97	195	UW	1.3295	B	TRIM_CHK
56	SOBE	07/14/97	195	UW	1.5972	B	TRIM_CHK
57	CENT	07/15/97	196	UW	1.3588	B	TRIM_CHK
58	GRAY	07/15/97	196	UW	1.3365	B	TRIM_CHK
59	SOBE	07/15/97	196	UW	1.5970	B	TRIM_CHK
60	GREN	07/16/97	197	UW	1.3360	B	TRIM_CHK
61	TENO	07/16/97	197	UW	1.3868	B	TRIM_CHK
62	GREN	07/17/97	198	UW	1.2532	B	TRIM_CHK
63	TENO	07/17/97	198	UW	1.3791	B	TRIM_CHK
64	BLUE	07/30/97	211	UW	1.3865	B	TRIM_CHK
65	GLDH	07/30/97	211	UW	1.3667	B	TRIM_CHK
66	BLUE	07/31/97	212	UW	1.3885	B	TRIM_CHK
67	GLDH	07/31/97	212	UW	1.3662	B	TRIM_CHK
68	SAND	08/12/97	224	USGS	1.2930	B	ASH_CHK
69	GRAY	08/13/97	225	USGS	1.3490	B	ASH_CHK
70	GREN	08/13/97	225	USGS	1.3810	B	ASH_CHK
71	OP25	08/13/97	225	USGS	1.4550	B	ASH_CHK
72	SAND	08/13/97	225	USGS	1.2930	B	ASH_CHK
73	GREN	08/14/97	226	USGS	1.3810	B	ASH_CHK
74	OP25	08/14/97	226	USGS	1.5130	B	ASH_CHK

Table A.8: 1997 "campaign" occupation history sorted by date.

#	Code	Date	DOY	Agency	AntH	Mm a	AntType[b]
75	SAND	08/14/97	226	USGS	1.2930	B	ASH_CHK
76	CENT	08/15/97	227	USGS	1.3660	B	ASH_CHK
77	FARW	08/15/97	227	USGS	1.4250	B	ASH_CHK
78	GRAY	08/15/97	227	USGS	1.5000	B	ASH_CHK
79	SAND	08/15/97	227	USGS	1.2930	B	ASH_CHK
80	FARW	08/16/97	228	USGS	1.5130	B	ASH_CHK
81	SAND	08/16/97	228	USGS	1.2930	B	ASH_CHK
82	CENT	08/17/97	229	USGS	1.3180	B	ASH_CHK
83	SAND	08/17/97	229	USGS	1.2930	B	ASH_CHK
84	OLYM	08/18/97	230	USGS	1.2398	V	ASH_CHK
85	SAND	08/18/97	230	USGS	1.2930	B	ASH_CHK
86	THUN	08/18/97	230	USGS	1.5800	B	ASH_CHK
87	OLYM	08/19/97	231	USGS	1.2398	V	ASH_CHK
88	SAND	08/19/97	231	USGS	1.2930	B	ASH_CHK
89	THUN	08/19/97	231	USGS	1.7950	B	ASH_CHK
90	Z478	08/19/97	231	USGS	1.3820	B	ASH_CHK
91	GP17	08/20/97	232	USGS	1.2330	B	ASH_CHK
92	LEWI	08/20/97	232	USGS	1.5690	B	ASH_CHK
93	MUDD	08/20/97	232	USGS	1.2530	B	ASH_CHK
94	OLYM	08/20/97	232	USGS	1.2398	V	ASH_CHK
95	SAND	08/20/97	232	USGS	1.2930	B	ASH_CHK
96	Z478	08/20/97	232	USGS	1.5700	B	ASH_CHK
97	GP17	08/21/97	233	USGS	1.4570	B	ASH_CHK
98	LEWI	08/21/97	233	USGS	1.5650	B	ASH_CHK
99	MUDD	08/21/97	233	USGS	1.2530	B	ASH_CHK
100	SAND	08/21/97	233	USGS	1.2930	B	ASH_CHK
101	EAST	08/22/97	234	USGS	1.2520	B	ASH_CHK
102	SAND	08/22/97	234	USGS	1.2930	B	ASH_CHK
103	WILS	08/22/97	234	USGS	1.1930	B	ASH_CHK
104	EAST	08/23/97	235	USGS	1.1980	B	ASH_CHK
105	SAND	08/23/97	235	USGS	1.2930	B	ASH_CHK
106	WILS	08/23/97	235	USGS	1.4020	B	ASH_CHK
107	SAND	08/24/97	236	USGS	1.2930	B	ASH_CHK

a. Antenna height measuring method. See Table A.9 for details.
b. Antenna type codes are listed in Table 2.4.

Table A.9: Listing of codes of GPS antenna height measuring methods.

Code	Measuring Method	Notes
A	SLANT Height to BOTTOM of INSIDE of NOTCH on Ground Plane	For antennas without notches the equivalent measurement method would be type B (i.e. for choke ring antennas).
B	SLANT Height to BOTTOM of OUTSIDE EDGE of ground plane.	Used for choke ring antennas. This is the USGS, Manly Park standard procedure (*J. Svarc*, pers. comm).
C	SLANT Height to TOP of INSIDE of NOTCH on Ground Plane.	Not Standard procedure.
D	SLANT Height to TOP of OUTSIDE EDGE of Ground Plane.	Used when no notches exist on ground plane (not a standard method of measurement).
V	VERTICAL height to the bottom of preamplifier (e.g. Antenna Reference Point)	UW owns only one setup with a fixed vertical height: UNAVCO's design grey tripod with 1.100 m height.

Appendix B - GPS Data Analysis Strategy

Table B.1: The GIPSY/OASIS II analysis strategy used for the GPS data analysis.

Measurement Models		
Pre-processing	outlier editing and cycle slip detection/fixing	
Basic observables	carrier Phase (L)	
	pseudo-ranges (P) for P-code receivers (e.g. TurboRogue)	
	elevation angle cutoff	10°
	sampling rate	5 min
	weighting: carrier-phase	1 cm
	pseudorange	1 m
Modeled Observable	undifferenced, corrected for ionosphere (LC, PC), CA pseudoranges not corrected for CA-P1 biases.	
RHC polar phase rotation correction		applied
Ground antenna	phase center elevation dependence not applied. Used NGS calibration results for vertical offsets (*Mader*, 1999).	
Troposphere	zenith delay adjusted as random walk process with noise:	1.7 cm/ sqrt(hr)
	mapping Function by *Lanyi* (1984)	
Ionosphere	not modeled (accounted for by forming LC and PC combinations)	
Plate motions		not used
Tidal displacements	Solid earth tides: model by Wahr	applied
	Pole tides:	not applied
	Ocean loading:	not applied
Atmospheric loading		not applied
Earth orientation model (EOP)	~24h and ~12h variations in X, Y and UT1 from VLBI based model by *Herring and Dong* (1994)	
Satellite center mass correction	Block I: x, y, z: (0.210, 0, 0.854 meters)	
	Block II/IIA: x, y, z: (0.279, 0, 1.0229 m)	
Satellite phase center calibration		not applied
Satellite clock correct.	relativistic corrections applied	
GPS attitude model	kinematic model measurement corrections based on apriori yaw rates (made available by JPL)	applied

Table B.1: The GIPSY/OASIS II analysis strategy used for the GPS data analysis.

Orbit Models used by JPL in their precise orbit determination	
Geopotential	GEM T3 + C21+S21 model up to degree and order 8
	GM=398600.4415 km**3/sec**2
	AE = 6378.137 km
Third-body	Sun, Moon and planets regarded as point masses
	ephemeris: JPL DE200
	GMsun = 132712439935.4842 km**3/sec**2
	GMmoon = 4902.7991 km**3/sec**2
Solar radiation pressure	direct radiation: T10 and T20 models of Block I and Block II satellites, respectively
	x, z scale and y radiation biases: taken into account
	Earth shadow model includes: penumbra and atmospheric refraction/ attenuation effects
Tidal forces	Solid earth tides: frequency independent Love number K2= 0.300
	Ocean tides: UT CSR model from Schwiderski
Numerical integration	variable (high) order Adams predictor-corrector integration with direct integration of second-order equations
	integration step: variable (typically < 1000s)
	starter procedure: Runge-Kutta
	arc length: 30 hours
Estimated Parameters	
Adjustment	Weighted least squares using square-root information filter (SRIF) (*Bierman*, 1977)
Station coordinates	No station is held fixed (*Heflin et al.*, 1992). 6 IGS stations used: ALBH, ALGO, DRAO, FAIR, KOKB, NLIB
Satellite clock biases	fixed to JPL computed values (YYYY-MM-DD.tdpc)
Receiver clock biases	modeled as white noise process and solved for at each bias epoch.
Orbital parameters	fixed to JPL computed fiducual precise orbits (YYYY-MM-DD.eci)
Tropospheric correction	estimated as a random walk process with 0.017 m/sqrt(hr) sigma.
Ionospheric correction	not estimated
Ambiguity fixing	Applied (*Blewitt*, 1989)
Reference Frames	

Table B.1: The GIPSY/OASIS II analysis strategy used for the GPS data analysis.

Inertial	Geocentric; mean equator and equinox of 2000 Jan 1.5 (J2000.0)
Terrestrial	ITRF96 reference frame (*Sillard et al.*, 1998)
Interconnection	Precession: IAU 1976 Precession Theory
	Nutation: IAU 1980 Nutation Theory + CP corr.(Bull.A)
	Earth Orientation models (EOP): from IERS Bull A
	Tidal variations in UT1: applied for periods <= 32 days

Table B.2: GPS data analysis post-processing procedure using the GIPSY/OASIS II software[a]

```
# declare daily stacov files sorted by date (e.g. 96jan02.stacov)
set STACOVS = 'ls 9??????.stacov I sort -b +0.0 -0.2 +0.2M -0.5'

# declare epoch for which positions are calculated
setenv VEL_MOD 97JAN01

# declare a reference frame (e.g. ITRF96)
set REF_FRAME = /goa/ITRF/96/itrf96.stacov

# adjust antenna heights
heightfix -r /goa/sta_info/antenna.truth -i $STACOVS > & heightfix.log

# combine daily stacov files to estimate positions and velocities for epoch $VEL_MOD
stamrg -i $STACOVS -o all.stacov -v $VEL_MOD

# apply internal constraints to the combined covariance matrix
project -i all.stacov -o project.stacov -r -t -s

transform estimates into an appropriate reference frame
transform -f $REF_FRAME -i project.stacov -o final.stacov -r -t -s

# start creating time series for each daily solution
foreach file ($STACOVS)
   set TAIL = $file:t; set FILE = $file:r
   set DATE = ('echo $FILE I awk '{print substr($0,0,7)}'") # declare day (e.g. 95JAN05)

   # apply internal constraints to the position estimates
   project -i $file -o "$FILE"_project.stacov -r -t -s

   # map the position and velocity estimates to day $DATE
   stamrg -i final.stacov -o "$FILE"_frame.stacov -v $FILE

   transform estimates into an appropriate reference frame
   transform -i "$FILE"_project.stacov -f "$FILE"_frame.stacov -o "$FILE"_series.stacov -r -t -s
end

# calculate final geodetic coordinates for each day
statistics -r final.stacov -i *_series.stacov -gds
```

a. based on JPL recommended procedure in the GIPSY/OASIS II manual (*Webb and Zumberge*, 1997).

Table B.3: Procedure for calculating GPS station velocities relative to a given point.

The following three steps describe the procedure of conversion of GPS station velocities from NA fixed reference frame to a reference frame fixed to a specific point (e.g. station DRAO):

- Convert NA fixed reference frame velocity vector $V_L = (V_n, V_e, V_d)$ from local (n=north; e=east; d=down) coordinate system to a vector $V = (V_x, V_y, V_z)$ in global cartesian (x, y, z) coordinate system.

- Subtract component-wise velocity of the fixed point (e.g. DRAO) from the rest of the velocities:

$$V_{fixed} = V - V_{DRAO} = \begin{bmatrix} V_x - V_{x(DRAO)} \\ V_y - V_{x(DRAO)} \\ V_z - V_{x(DRAO)} \end{bmatrix} \qquad \text{(EQ B.1)}$$

- Convert obtained velocities (e.g. V_{fixed}) from cartesian (x, y, z) coordinate system back to (n=north; e=east; d=down) coordinate system.

Cox and Hart (1986) provide analytic expressions on how to convert from local to cartesian coordinate system and reverse, which were used in the steps described above.

If the global cartesian components of a vector $V = (V_x, V_y, V_z)$ are known, than the vector in local coordinates $V_L = (V_n, V_e, V_d)$ at point A with λ latitude and ϕ longitude can be found by the matrix multiplication:

$$V_L = T \cdot V = \begin{bmatrix} T_{nx} & T_{ny} & T_{nz} \\ T_{ex} & T_{ey} & T_{ez} \\ T_{dx} & T_{dy} & T_{dz} \end{bmatrix} \begin{bmatrix} V_x \\ V_y \\ V_z \end{bmatrix} \qquad \text{(EQ B.2)}$$

where the components of the T transformation matrix are $T_{nx} = n \cdot x$, $T_{ey} = e \cdot y$, $T_{dz} = d \cdot z$, etc.

It can be shown that individual term of matrix T can be expressed in terms of latitude (λ) and longitude (ϕ) of the fixed point A as follows:

$$T = \begin{bmatrix} -\sin\lambda\cos\phi & -\sin\lambda\sin\phi & \cos\lambda \\ -\sin\phi & -\cos\phi & 0 \\ -\cos\lambda\cos\phi & -\cos\lambda\sin\phi & -\sin\lambda \end{bmatrix} \qquad \text{(EQ B.3)}$$

To convert the velocity vector in local coordinate system V_L to cartesian coordinates V we use the inverse of the transformation matrix T:

$$V = T^{-1} \cdot V_L \qquad \text{(EQ B.4)}$$

Appendix C - GPS Station Time Series
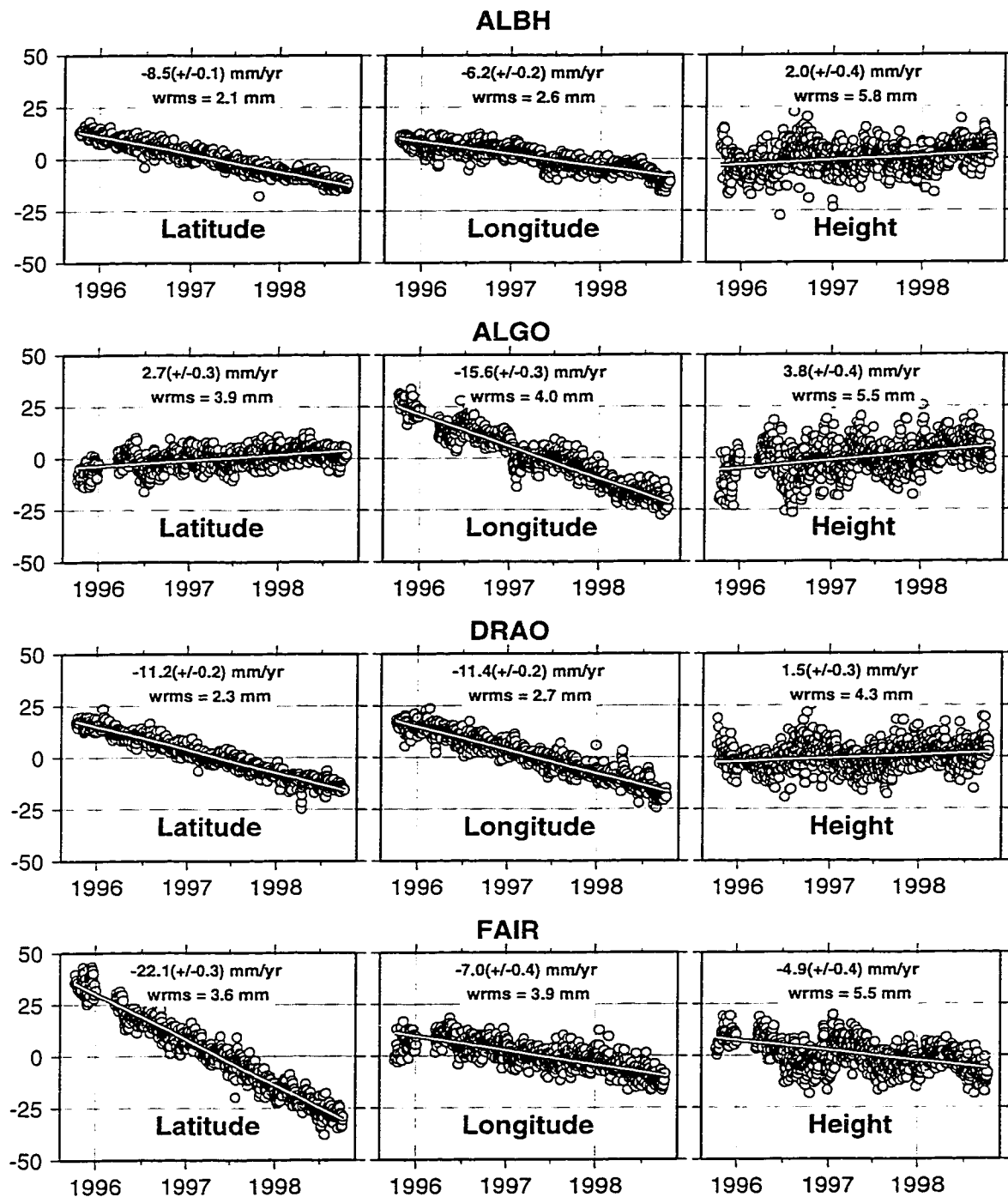
ALBH

ALGO

DRAO

FAIR

Figure C.1: Time series of continuous GPS stations: ALBH, ALGO, DRAO and FAIR. Deviations for local North, East and Up components in ITRF96 reference frame epoch 01/01/ 1997. See Figures 2.5 and 2.6 for station maps. Tables A.1 and A.2 contain absolute positions. The Y-scale is in *mm* and the X-scale in in *years*.

Figure C.2: Time series of continuous GPS stations: FTS1 to WHD1. See the caption to Figure C.1 for more information.

Figure C.3: Time series of "campaign" GPS stations: APSA to GLDH. See the caption to Figure C.1 for more information.
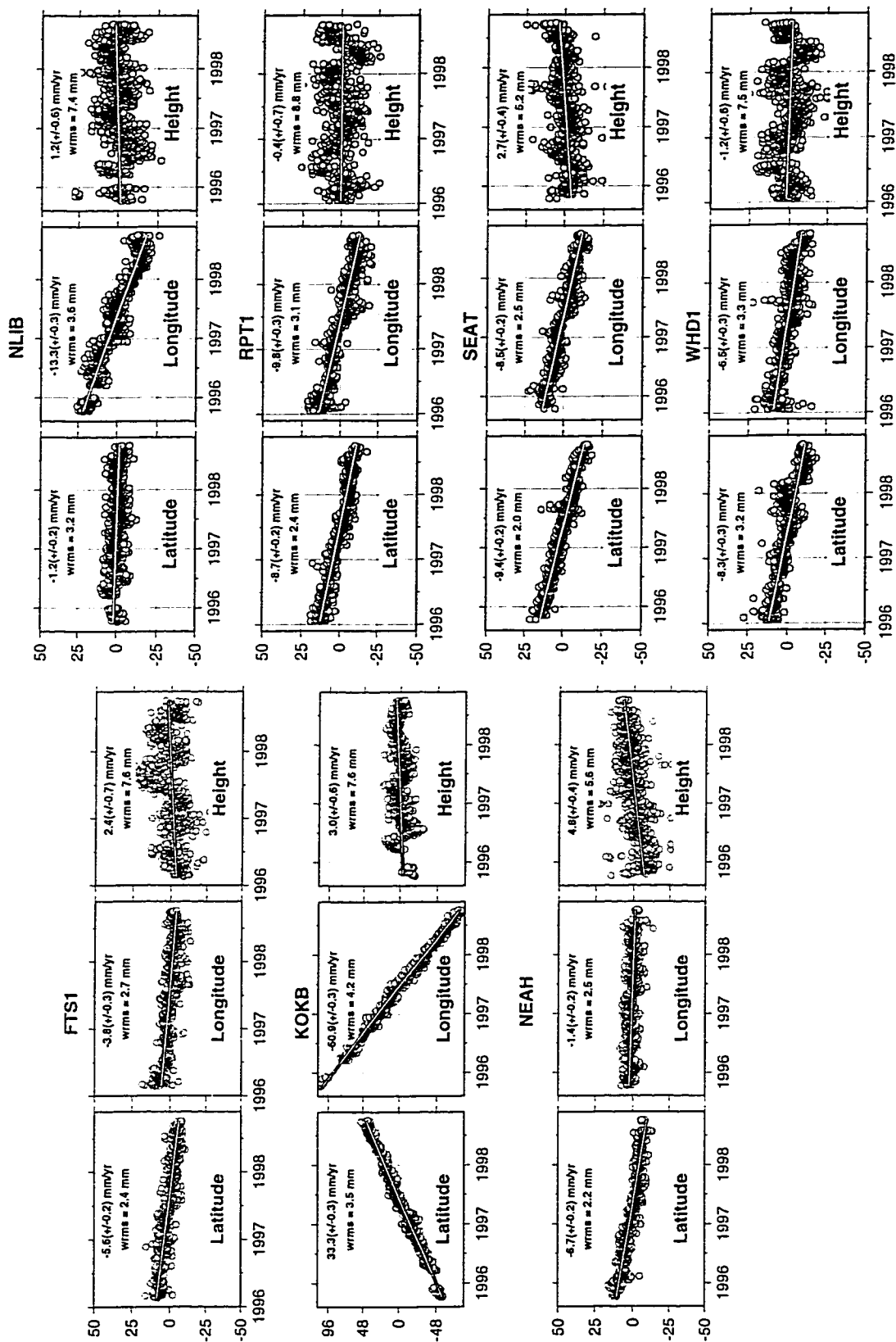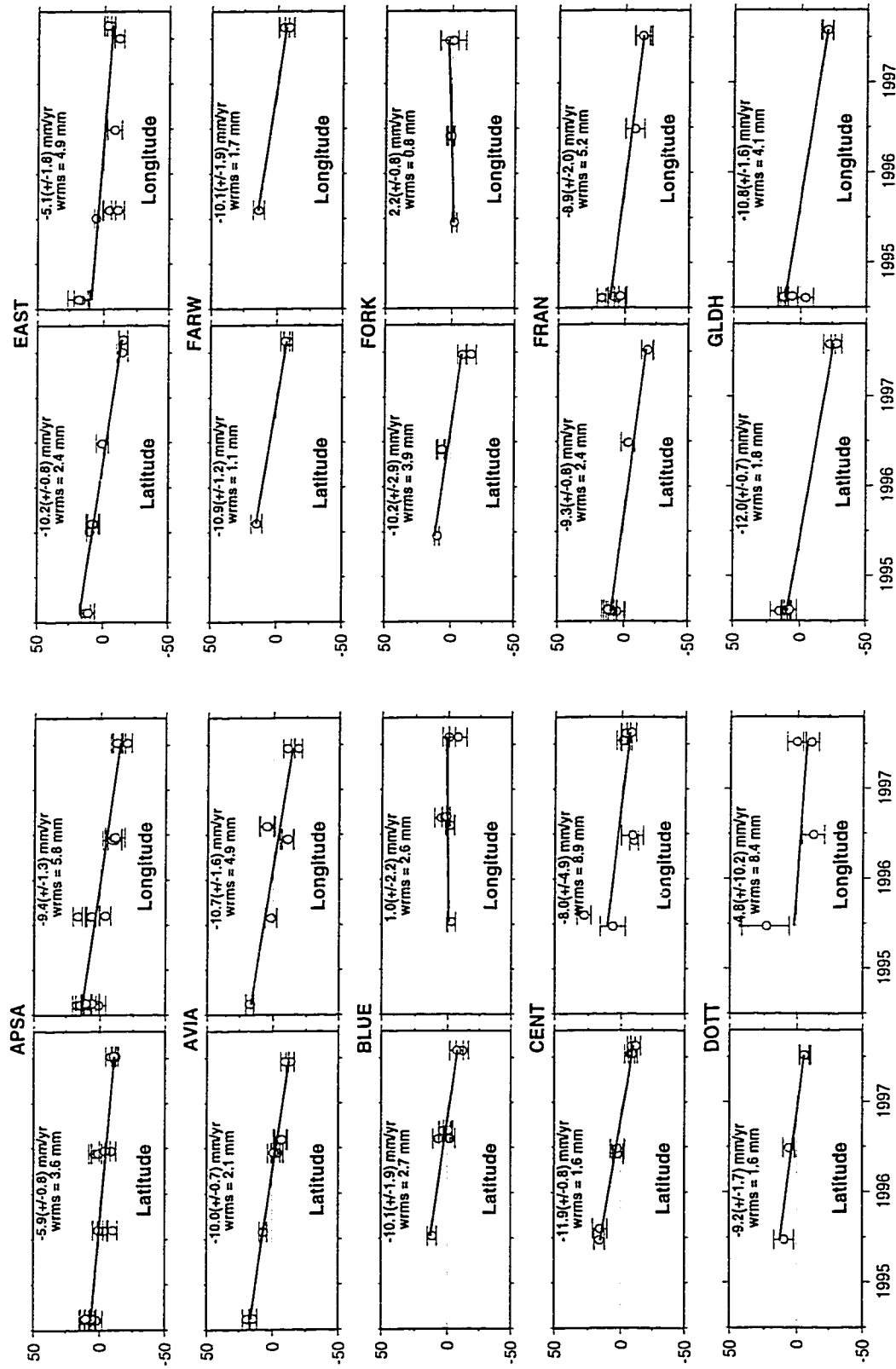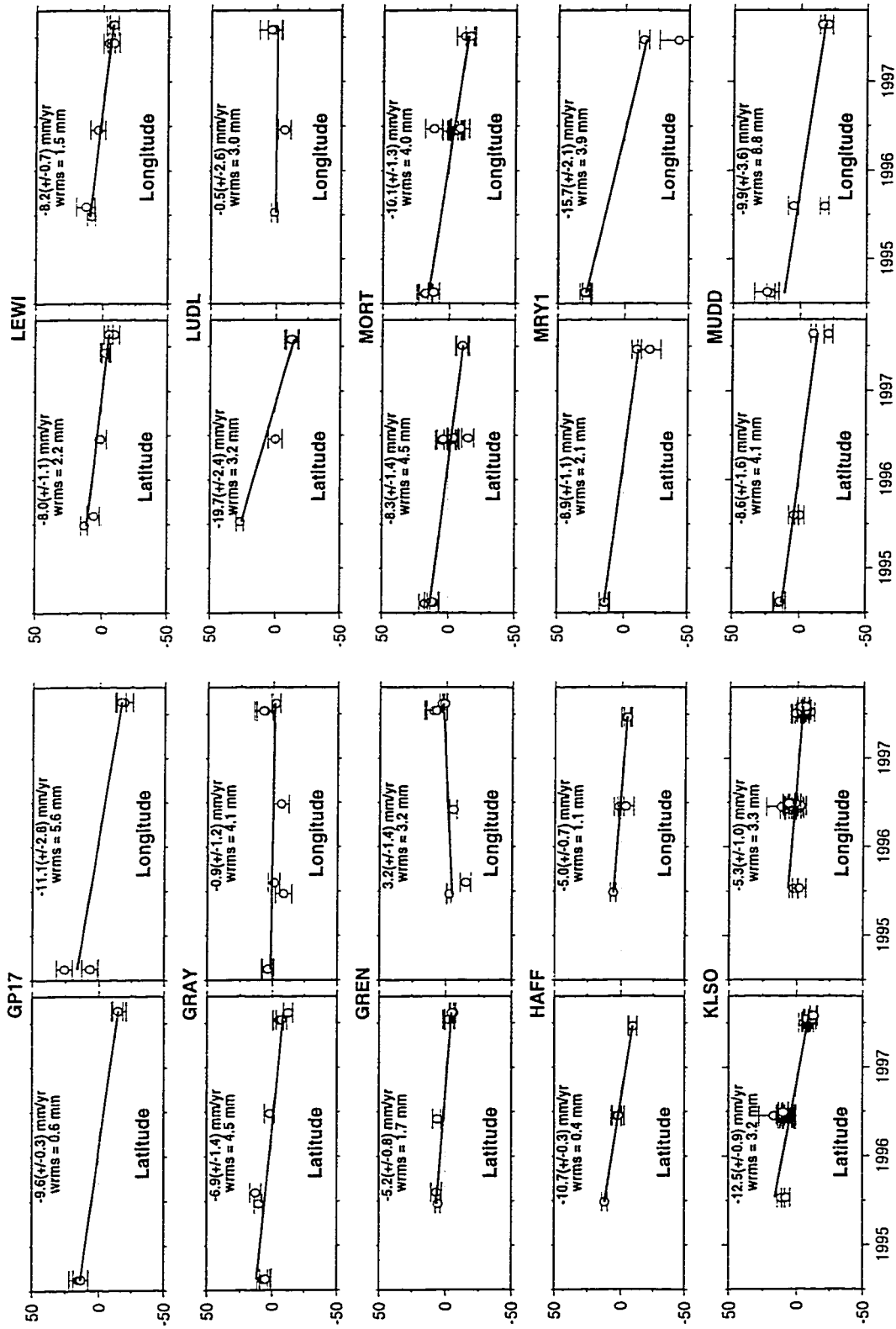
154

Figure C.4: Time series of "campaign" GPS stations: GP17 to MUDD. See the caption to Figure C.1 for more information.
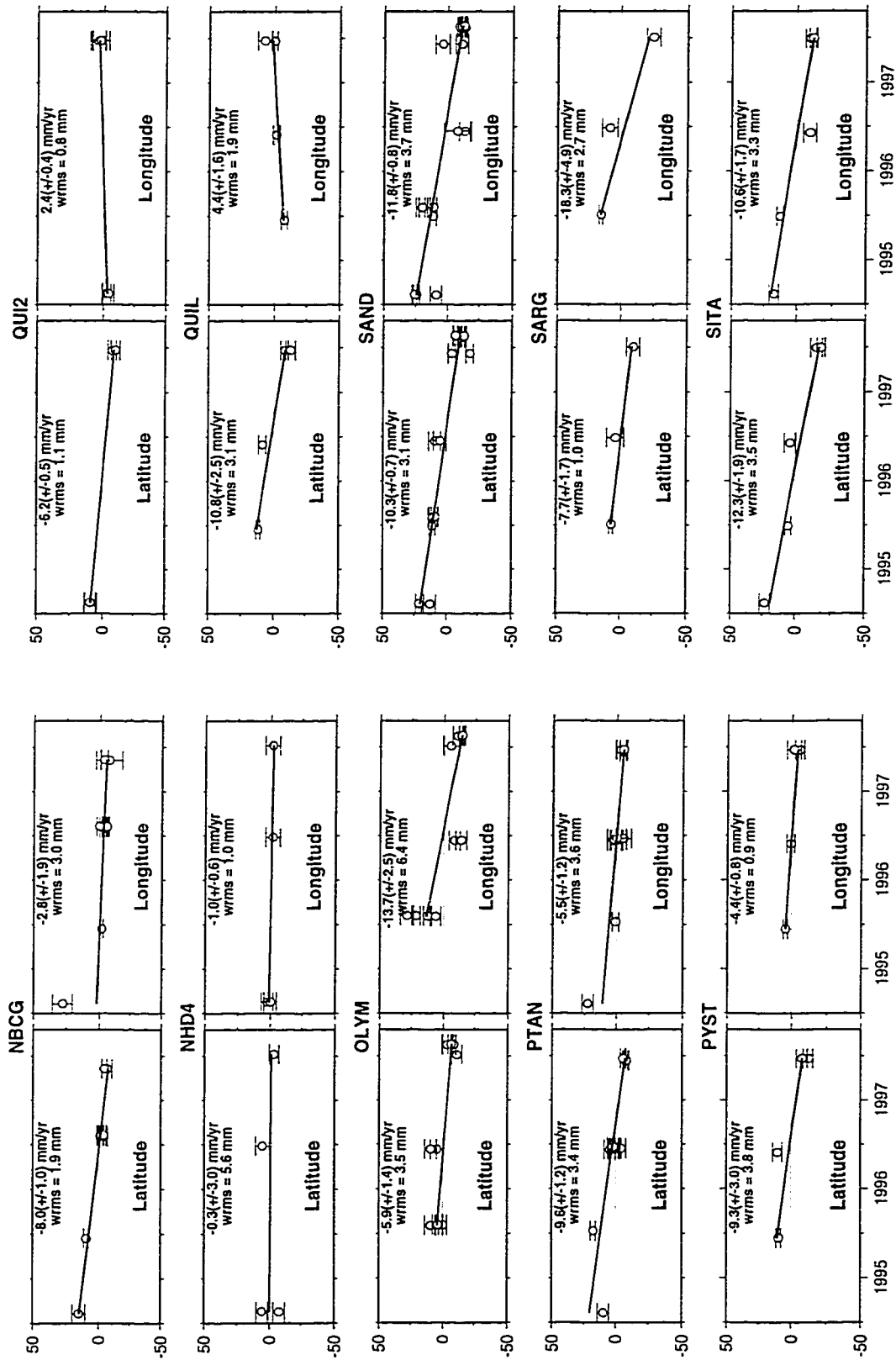
Figure C.5: Time series of "campaign" GPS stations: NBCG to SITA. See the caption to Figure C.1 for more information.
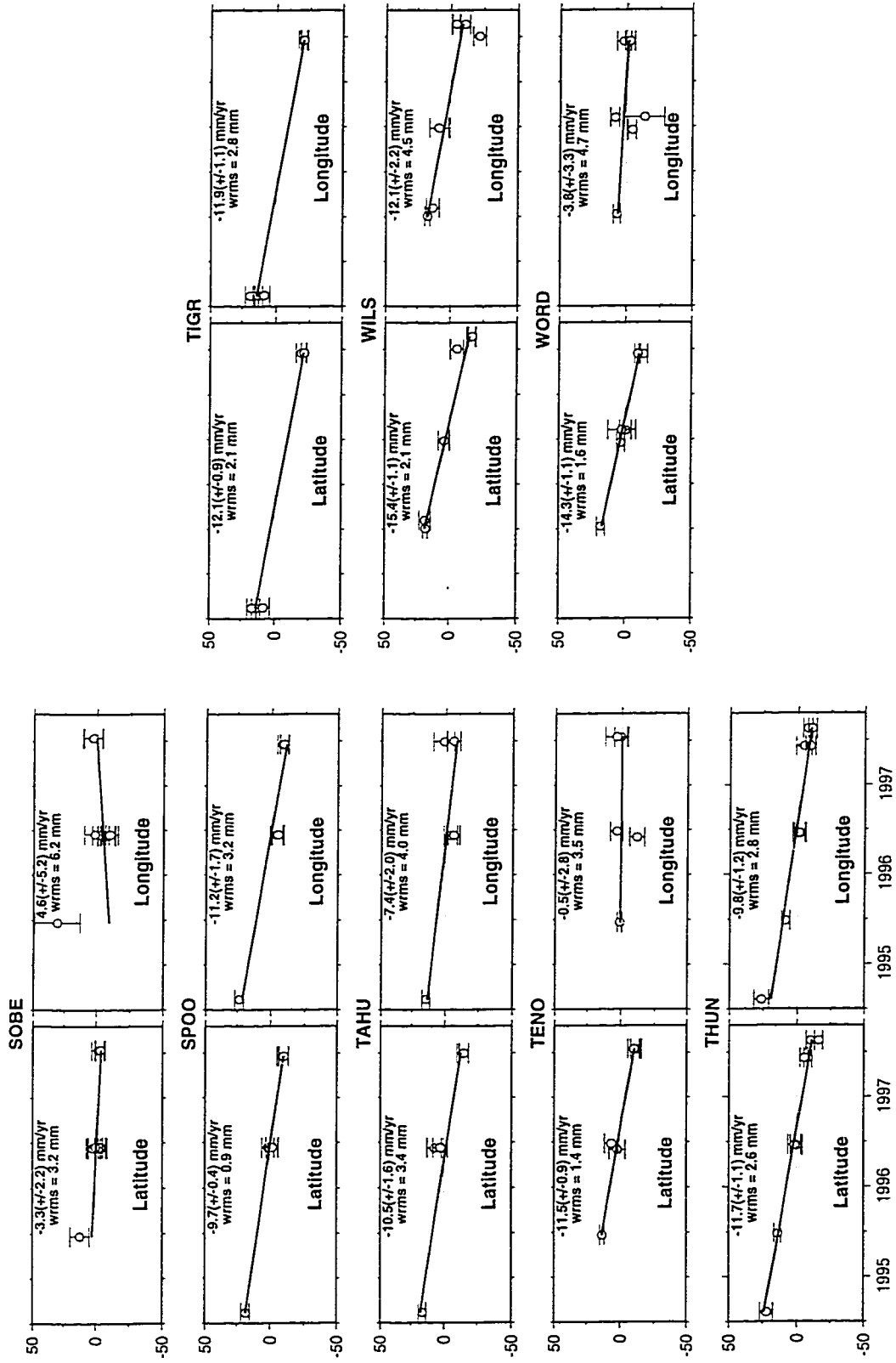
Figure C.6: Time series of "campaign" GPS stations: SOBE to WORD. See the caption to Figure C.1 for more information.

Appendix D - Estimated and Predicted GPS Station Velocities

Table D.1: Continuous GPS station velocities relative to station DRAO[a].

#	NAME	North (mm/yr)			East (mm/yr)			Vertical (mm/yr)			Horizontal (mm/yr)			
		V	1σ	rms	V	1σ	rms	V	1σ	rms	V	1σ	Az	1σ
1	ALBH	3.8	0.1	2.1	4.5	0.2	2.6	2.0	0.4	5.8	5.9	0.2	50	2
2	FTS1	7.0	0.2	2.4	6.3	0.3	2.7	2.4	0.7	7.6	9.4	0.4	42	2
3	NEAH	5.9	0.2	2.2	9.0	0.2	2.5	4.8	0.4	5.6	10.8	0.3	57	1
4	RPT1	3.3	0.2	2.4	0.8	0.3	3.1	-0.4	0.7	8.8	3.4	0.4	14	6
5	SEAT	2.6	0.2	2.0	2.1	0.2	2.5	2.7	0.4	5.2	3.3	0.3	39	5
6	WHD1	3.9	0.3	3.2	4.2	0.3	3.3	-1.2	0.6	7.5	5.7	0.4	47	4

a. See footnotes to Table D.2 for further details, including explanations of 1σ and rms. Distance between the stations and CSZ deformation fronts is given in Table D.3.

Table D.2: Campaign GPS station velocities relative to station DRAO[a].

#	NAME	# of occupations	North (mm/yr)			East (mm/yr)			Horizontal (mm/yr)			
			V	1σ[b]	rms[c]	V	1σ	rms	V[d]	1σ	Az[e]	1σ
1	APSA	18	6.4	0.8	3.6	1.0	1.3	5.8	6.5	1.5	9	12
2	AVIA	9	2.0	0.7	2.1	0.0	1.6	4.9	2.0	1.7	0	46
3	BLUE	8	2.2	1.9	2.7	11.6	2.2	2.6	11.8	2.9	79	11
4	CENT	9	0.5	0.8	1.6	2.3	4.9	8.9	2.4	5.0	78	44
5	DOTT	4	3.2	1.7	1.6	5.5	10.2	8.4	6.4	10.3	60	59
6	EAST	9	1.5	0.8	2.4	5.7	1.8	4.9	5.9	2.0	75	12
7	FARW	4	1.5	1.2	1.1	0.3	1.9	1.7	1.5	2.2	11	79
8	FORK	5	2.4	2.9	3.9	12.6	0.8	0.8	12.8	3.0	79	13
9	FRAN	7	3.1	0.8	2.4	1.4	2.0	5.2	3.4	2.2	24	36
10	GLDH	7	0.2	0.7	1.8	-0.3	1.6	4.1	0.4	1.7	204	48
11	GP17	5	2.2	0.3	0.6	-0.4	2.8	5.6	2.2	2.8	350	69
12	GRAY	10	5.6	1.4	4.5	9.4	1.2	4.1	10.9	1.8	59	10
13	GREN	7	7.4	0.8	1.7	13.5	1.4	3.2	15.4	1.6	61	5
14	HAFF	5	1.3	0.3	0.4	5.6	0.7	1.1	5.7	0.8	77	4
15	KLSO	30	-0.3	0.9	3.2	5.0	1.0	3.3	5.0	1.3	93	10
16	LEWI	7	4.1	1.1	2.2	2.3	0.7	1.5	4.7	1.3	29	14

Table D.2: Campaign GPS station velocities relative to station DRAO[a].

#	NAME	# of occupa-tions	North (mm/yr)			East (mm/yr)			Horizontal (mm/yr)			
			V	1σ b	rm s[c]	V	1σ	rm s	V[d]	1σ	Az[e]	1σ
17	LUDL	4	-7.5	2.4	3.2	10.1	2.6	3.0	12.6	3.5	127	2
18	MORT	13	3.7	1.4	4.5	0.3	1.3	4.0	3.7	1.9	5	22
19	MRY1	4	3.1	1.1	2.1	-5.0	2.1	3.9	5.9	2.4	302	2
20	MUDD	6	3.3	1.6	4.1	0.7	3.6	8.8	3.4	3.9	12	65
21	NBCG	10	4.6	1.0	1.9	7.7	1.9	3.0	9.0	2.1	59	12
22	NHD4	4	12.2	3.0	5.6	9.1	0.6	1.0	15.2	3.1	37	9
23	OLYM	10	6.3	1.4	3.5	-3.2	2.5	6.4	7.1	2.9	323	13
24	PTAN	14	2.7	1.2	3.4	5.1	1.2	3.6	5.8	1.7	62	16
25	PYST	4	3.2	3.0	3.8	6.1	0.8	0.9	6.9	3.1	62	25
26	QUI2	4	6.5	0.5	1.1	12.8	0.4	0.8	14.4	0.6	63	3
27	QUIL	4	1.9	2.5	3.1	14.8	1.6	1.9	14.9	3.0	83	10
28	SAND	22	2.0	0.7	3.1	-1.3	0.8	3.7	2.4	1.1	327	7
29	SARG	3	3.8	1.7	1.0	-7.7	4.9	2.7	8.6	5.2	-64	4
30	SITA	5	-0.2	1.9	3.5	0.0	1.7	3.3	0.2	2.5	180	487
31	SOBE	9	9.1	2.2	3.2	14.9	5.2	6.2	17.5	5.6	59	15
32	SPOO	5	2.3	0.4	0.9	-0.6	1.7	3.2	2.4	1.7	-15	37
33	TAHU	5	1.8	1.6	3.4	3.1	2.0	4.0	3.6	2.6	60	38
34	TENO	5	1.0	0.9	1.4	9.9	2.8	3.5	10.0	2.9	84	7
35	THUN	9	0.3	1.1	2.6	0.7	1.2	2.8	0.8	1.6	67	112
36	TIGR	5	-0.2	0.9	2.1	-1.2	1.1	2.8	1.2	1.4	261	50
37	WILS	6	-3.9	1.1	2.1	-1.4	2.2	4.5	4.1	2.5	200	34
38	WORD	6	-2.1	1.1	1.6	6.9	3.3	4.7	7.2	2.8	107	1

a. DRAO station (Figure 3.5) is presumed to be located on a stable North American continent. Velocities in North, East and Vertical components for each station relative to DRAO were calculated by subtracting the corresponding DRAO velocity in an absolute ITRF96 reference frame (Table 3.1). Further details are described in the *post-processing* part of section 2.4. Distance between the stations and CSZ deformation fronts is given in Table D.3

b. 1σ represents a slope error (e.g. velocity uncertainty) in mm/yr from weighted least squares regression.

c. rms is a weighted root mean square of the regression in mm computed with equation Equation 3.5. GIPSY output formal errors were re-scaled (multiplied by factor of 2-4) in order to equate the reduced chi-square to one.

d. Horizontal velocity based on an individual station's north and east component of velocity.

e. Azimuth in degrees for the horizontal velocties, measured clockwise from North.

Table D.3: Model predicted velocities relative to DRAO[a].

#	Station Information				Predicted Velocities (mm/yr)			Horizontal Velocity (mm/yr)	
	Code	Latitude	Longitude	Dist.[b]	North	East	Vertical	V[c]	Az[d]
1	ALBH	48.3898	236.5125	216	3.0	4.1	1.2	5.1	54
2	APSA	46.6708	237.0150	177	0.4	3.3	0.4	3.3	83
3	AVIA	47.6857	237.7510	270	0.5	2.2	0.2	2.3	77
4	BLUE	47.9550	236.7400	207	2.5	5.6	2.0	6.1	66
5	CENT	46.9727	236.2970	129	2.6	7.3	2.0	7.7	70
6	DOTT	46.6313	236.7250	155	0.7	4.2	0.7	4.3	81
7	EAST	47.2317	238.8290	330	0.0	0.9	-0.1	0.9	90
8	FARW	47.0146	236.6240	154	1.2	5.6	1.4	5.7	78
9	FORK	47.9367	235.6040	122	7.7	14.1	1.9	16.1	61
10	FRAN	46.5414	236.5000	136	1.1	5.0	1.0	5.1	78
11	FTS1	46.2049	236.0439	94	2.5	6.9	1.9	7.3	70
12	GLDH	47.5486	237.2130	223	0.8	3.8	0.7	3.9	78
13	GP17	47.1375	238.3750	292	0.1	1.3	-0.0	1.3	86
14	GRAY	46.9028	235.9000	97	5.4	10.5	1.9	11.8	63
15	GREN	47.3042	235.7210	100	8.0	14.9	1.4	16.9	62
16	HAFF	47.4848	237.8240	266	0.3	2.1	0.1	2.1	82
17	KLSO	46.1181	237.1040	174	0.2	2.5	0.2	2.5	85
18	LEWI	47.0942	237.3790	215	0.3	2.9	0.3	2.9	84
19	LUDL	47.9216	237.3170	248	1.1	3.3	0.6	3.5	72
20	MORT	46.5506	237.7300	230	0.0	1.8	0.0	1.8	90
21	MRY1	47.6605	237.8890	279	0.4	2.0	0.1	2.0	79
22	MUDD	47.1419	238.0660	269	0.1	1.6	0.0	1.6	86
23	NBCG	48.3702	235.4010	133	5.5	8.4	2.0	10.0	57
24	NEAH	48.2979	235.3751	126	6.1	9.7	1.9	11.5	58
25	NHD4	46.3004	235.9240	87	3.4	8.0	2.3	8.7	67
26	OLYM	46.9669	237.0920	189	0.4	3.5	0.5	3.5	83
27	PTAN	48.1170	236.5060	199	3.4	5.9	2.2	6.8	60
28	PYST	48.1979	235.8810	157	5.1	8.1	2.1	9.6	58

Table D.3: Model predicted velocities relative to DRAO[a].

#	Station Information				Predicted Velocities (mm/yr)			Horizontal Velocity (mm/yr)	
	Code	Latitude	Longitude	Dist.[b]	North	East	Vertical	V[c]	Az[d]
29	QUI2	47.9346	235.4400	109	8.8	15.8	1.9	18.1	61
30	QUIL	47.9368	235.4390	109	8.8	15.8	1.9	18.1	61
31	RPT1	47.3875	237.6252	247	0.4	2.5	0.2	2.5	81
32	SAND	47.2366	236.8590	182	0.9	5.0	1.2	5.1	80
33	SARG	46.6024	239.5230	367	-0.2	0.5	-0.1	0.5	112
34	SEAT	47.6540	237.6905	264	0.5	2.4	0.2	2.5	78
35	SITA	47.5710	237.4470	242	0.6	3.0	0.4	3.1	79
36	SOBE	46.6630	236.1900	114	2.5	7.0	1.9	7.4	70
37	SPOO	47.4008	237.8360	263	0.3	2.1	0.1	2.1	82
38	TAHU	47.3870	236.8870	191	1.0	5.2	1.4	5.3	79
39	TENO	47.4789	236.0140	130	5.7	11.7	1.9	13.0	64
40	THUN	47.5086	238.0150	240	0.2	2.2	0.1	2.2	85
41	TIGR	47.1025	237.7100	282	0.3	1.8	0.1	1.8	81
42	WHD1	48.3127	237.3039	270	1.3	2.5	0.3	2.8	63
43	WILS	47.0121	239.4790	370	-0.1	0.5	-0.1	0.5	101
44	WORD	48.1408	237.2320	254	1.4	3.1	0.5	3.4	66

a. DRAO velocities predicted by the model are: North: 0.3 mm/yr; East: 0.5 mm/yr and Vertical: 0 mm/yr.
b. Distance from the station to the deformation front (i.e. trench) in kilometers.
c. Horizontal velocity based on an individual station's north and east component of velocity.
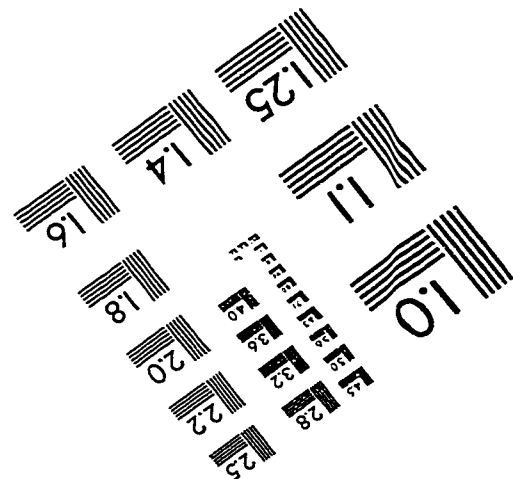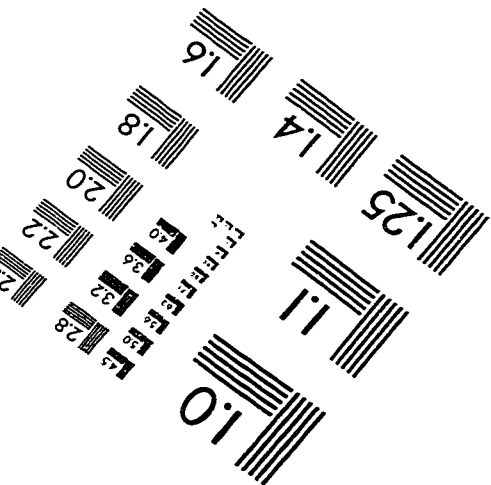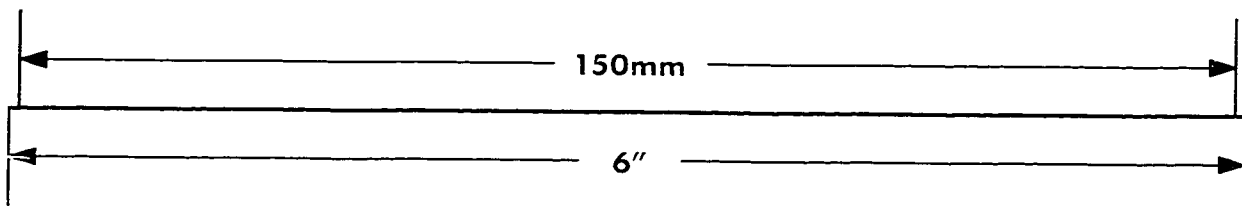d. Azimuth in degrees for the horizontal velocites, measured clockwise from north.
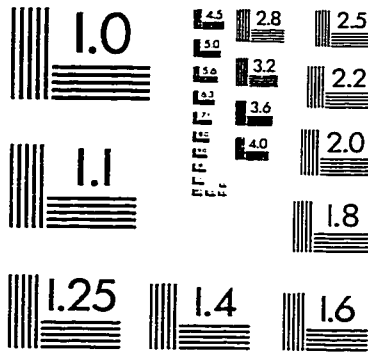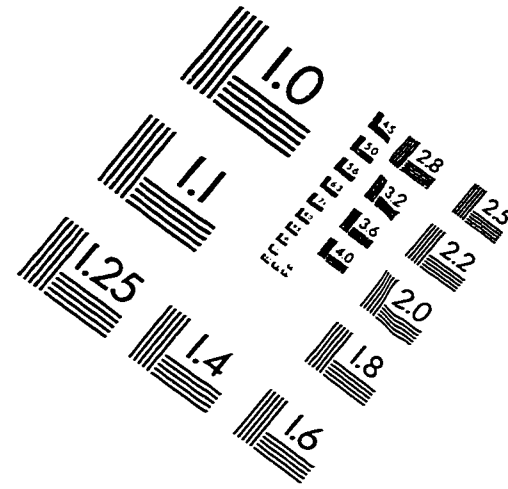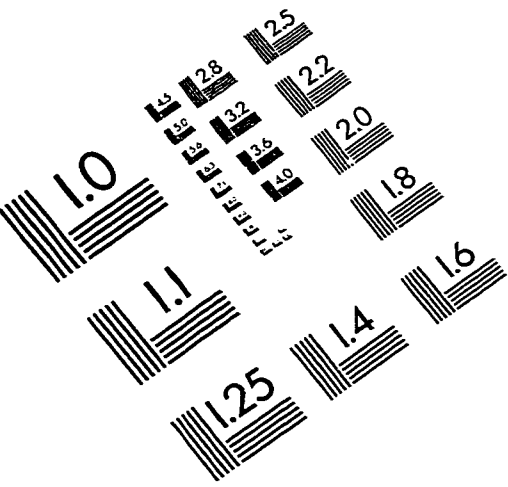
Vita

Giorgi Khazaradze

Born: April 7, 1966 Tbilisi, Georgia

Education

- Diploma in Geophysics, Tbilisi State University, Tbilisi, Georgia, 1990.
- Ph. D. in Geophysics, University of Washington, Seattle, USA, 1999.

IMAGE EVALUATION
TEST TARGET (QA-3)

1.0

1.1

1.25

1.4

1.6

1.8

2.0

2.2

2.5

2.8

3.2

3.6

4.0

4.5

5.0

150mm

6"